

**ENCLOSURE 5**

Copy of the non-proprietary WCAP-17091-NP, Rev. 0 dated June 2009,  
H\*: Alternate Repair Criteria for the Tubesheet Expansion Region in Steam Generators with  
Hydraulically Expanded Tubes (Model 44F).

(WCAP-17091-NP is 356 Pages)

Westinghouse Non-Proprietary Class 3

WCAP-17091-NP  
Revision 0

June 2009

H\*: Alternate Repair Criteria for  
the Tubesheet Expansion Region  
in Steam Generators with  
Hydraulically Expanded Tubes  
(Model 44F)



WCAP-17091-NP

Revision 0

## **H\*: Alternate Repair Criteria for the Tubesheet Expansion Region in Steam Generators with Hydraulically Expanded Tubes (Model 44F)**

June 2009

Author: \*  
\_\_\_\_\_  
H. O. Lagally  
Steam Generator Management Programs

Author: \*  
\_\_\_\_\_  
G. W. Whiteman  
Regulatory Compliance and Plant Licensing

Reviewer: \*  
\_\_\_\_\_  
C. D. Cassino  
Steam Generator Management Programs

Approved: \*  
\_\_\_\_\_  
D. A. Testa, Manager  
Steam Generator Management Programs

\* Electronically Approved Records Are Authenticated in the Electronic Document Management System

---

Westinghouse Electric Company LLC  
P.O. Box 355  
Pittsburgh, PA 15230-0355

© 2009 Westinghouse Electric Company LLC  
All Rights Reserved

---

**TABLE OF CONTENTS**

1.0	INTRODUCTION .....	1-1
1.1	H*/B* Background Information .....	1-1
1.2	Discussion of the Calculation Processes .....	1-2
1.2.1	Structural Integrity Analysis .....	1-3
1.2.2	Leakage Integrity Approach .....	1-4
1.3	Summary of Changes from Prior H* Submittals .....	1-4
1.3.1	Structural Integrity Analysis .....	1-4
1.3.2	Leakage Integrity Analysis .....	1-6
1.3.3	Probabilistic Analysis .....	1-7
1.4	Conservatisms in the H* Analysis .....	1-7
1.5	Report Overview .....	1-8
1.6	References .....	1-8
2.0	RESOLUTION OF TECHNICAL ISSUES AND NRC REQUEST FOR ADDITIONAL INFORMATION (RAI) FROM PRIOR H* SUBMITTALS .....	2-1
2.1	Categorization of Technical Issues and Resolution Road Map .....	2-1
2.2	Review of Prior NRC Requests for Information .....	2-1
2.3	References .....	2-2
3.0	TEST PROGRAM IN SUPPORT OF H* .....	3-1
3.1	Coefficient of Thermal Expansion (CTE) of Alloy 600 and SA508 Steel .....	3-1
3.1.1	Review of Industry Data .....	3-2
3.2	CTE Tests .....	3-2
3.2.1	Description of the CTE Tests .....	3-2
3.2.2	CTE Tests .....	3-4
3.3	CTE Test Results .....	3-5
3.4	Discussion .....	3-5
3.5	Conclusions .....	3-6
3.6	References .....	3-7
4.0	STRUCTURAL AND LEAKAGE INTEGRITY ACCEPTANCE CRITERIA .....	4-1
4.1	Structural Integrity Acceptance Criteria .....	4-2
4.2	Primary-to-Secondary Leakage Acceptance Criteria .....	4-3
4.3	References .....	4-5

---

5.0	PLANT OPERATING CONDITIONS AND LOADINGS (MODEL 44F).....	5-1
5.1	Normal Operating Conditions and Loadings .....	5-1
5.2	Faulted Conditions.....	5-1
5.2.1	Steam Line Break.....	5-1
5.2.2	Locked Rotor .....	5-1
5.2.3	Control Rod Ejection .....	5-2
5.3	Calculation of Applied End Cap Loads .....	5-3
5.4	References.....	5-4
6.0	Structural Analysis of the Tube-to-Tubesheet Joint .....	6-1
6.1	Results Summary .....	6-1
6.1.1	Introduction.....	6-2
6.1.2	Evolution and Development of the H* Structural Model .....	6-3
6.2	3D Finite Element Tubesheet Displacement Analysis.....	6-7
6.2.1	Description of the Tubesheet Complex Model .....	6-7
6.2.2	Inputs to the Model and Their Variability .....	6-16
6.2.3	Bounding Sector Analysis .....	6-34
6.2.4	Radius Dependent Tubesheet Stiffness Analysis.....	6-38
6.2.5	Tubesheet Tube Bore Dilation.....	6-59
6.2.6	Divider Plate Modeling.....	6-79
6.3	Tubesheet Rotation Effects .....	6-80
6.3.1	Topical White Paper: Relationship Between Tubesheet Tube Bore Eccentricity and Contact Pressure at Lower Temperatures and Pressures .....	6-82
6.4	Calculation of Tube-to-Tubesheet Contact Pressure .....	6-90
6.4.1	Calculation of Local Effects Due to Interaction of the Tube and Tubesheet Hole.....	6-90
6.4.2	General Description of 3D FEA Model Results .....	6-94
6.4.3	General Description of 3D FEA Post-Processing.....	6-99
6.4.4	Determination of Limiting Model 44F SG Plant in the H* Fleet .....	6-99
6.4.5	Sample Mean H* and Contact Pressure Calculation .....	6-101
6.4.6	Validation of Calculated Contact Pressures and Supporting Models .....	6-103
6.4.7	Distribution of Tube-to-Tubesheet Contact Pressure as a Function of Tubesheet Elevation.....	6-106

6.4.8	Effect of Excluding Specimen 7 Crevice Pressure Data on Contact Pressure Results .....	6-110
6.5	Conclusions.....	6-112
6.6	References.....	6-115
7.0	RESIDUAL CONTACT PRESSURE .....	7-1
7.1	Pull out Test Program .....	7-2
7.2	Analysis for Uncertainties in RCP .....	7-2
7.2.1	Variables that Affect the Value of RCP.....	7-2
7.2.2	Structural Analysis Model .....	7-3
7.2.3	Structural Analysis Results.....	7-4
7.2.4	RCP Uncertainty Evaluation.....	7-4
7.2.5	Application to H* Calculation .....	7-5
7.3	References.....	7-6
8.0	DETERMINATION OF H* AT THE REQUIRED PROBABILITY AND CONFIDENCE .....	8-1
8.1	Process .....	8-1
8.1.1	Effect of Crevice Pressure on H*.....	8-1
8.1.2	Definition of Variables and Their Variability.....	8-2
8.1.3	Interaction Among the Applicable Variables .....	8-3
8.1.4	Influence Factor Distributions .....	8-5
8.2	Calculation of Probabilistic H* .....	8-18
8.2.1	Square Root of the Sum of the Squares (SRSS) Approach.....	8-18
8.2.2	Monte Carlo Sampling Approach to Calculating the Probabilistic Value of H* .....	8-20
8.3	Summary and Conclusions .....	8-23
8.4	References.....	8-24
9.0	LEAK RATE ANALYSIS OF CRACKED TUBE-TO-TUBESHEET JOINTS .....	9-1
9.1	Leakage Analysis Methodology .....	9-1
9.1.1	Development of Overall Leakage Factor.....	9-1
9.1.2	Viscosity Subfactor.....	9-3
9.1.3	Discussion on Porous Medium .....	9-3
9.2	Determination of Limiting Conditions for H* Leakage Calculation .....	9-4
9.2.1	Background.....	9-4

9.2.2	Pressure-Time Histories for Accidents that Model Primary-to-Secondary Leakage.....	9-4
9.2.3	Limiting Temperature Conditions.....	9-5
9.3	Leak Rate Testing.....	9-6
9.3.1	Description of Testing.....	9-6
9.3.2	Leak Test Results.....	9-9
9.3.3	Loss Coefficient Evaluation.....	9-9
9.4	Development of Final Leakage Factors.....	9-10
9.5	Condition Monitoring/Operational Assessment Impact.....	9-11
9.6	Final Leakage Factor Determination.....	9-12
9.7	Ligament Tearing Discussion.....	9-12
9.7.1	Circumferential Cracks.....	9-13
9.7.2	Axial Cracks.....	9-14
9.8	Review of Leak Rate Susceptibility to Tube Slippage.....	9-17
9.8.1	Background.....	9-17
9.8.2	Assessment of the Potential for Tube Slippage.....	9-17
9.8.3	Assessment of Leakage Potential Under Postulated Tube Slippage.....	9-18
9.8.4	Conclusions Regarding Tube Slippage.....	9-19
9.9	References.....	9-20
10.0	SUMMARY AND CONCLUSIONS.....	10-1
10.1	Recommended Value of $H^*$ .....	10-1
10.2	$H^*$ Concept and Evolution.....	10-1
10.3	Design Requirements.....	10-2
10.4	Design Conditions.....	10-2
10.5	Material Properties.....	10-3
10.6	Residual Contact Pressure.....	10-3
10.7	Structural Analysis.....	10-3
10.8	Leakage Analysis.....	10-4
10.9	Probabilistic Analysis.....	10-5
10.10	Tube Slippage.....	10-6
APPENDIX A	Tube Pull Out Testing Data.....	A-1
APPENDIX B	An Evaluation of the Statistical Variability in Coefficient of Thermal Expansion Properties of SA-508 and Alloy-600.....	B-1

## LIST OF TABLES

Table 1-1	List of Conservatisms in the H* Structural and Leakage Analysis.....	1-11
Table 2-1	NRC Technical Issue Response Road Map .....	2-3
Table 2-2	List of NRC RAI on H* and Resolution Status .....	2-4
Table 3-1	Chemical Certifications (in Weight Percent) for A508 Pressure Vessel Steel Used in the CTE Test Program .....	3-9
Table 3-2	Mechanical Certifications for A508 Pressure Vessel Steel in the CTE Test Program .....	3-9
Table 3-3	Summary of the A600 Tubes Used in the CTE Test Program.....	3-10
Table 3-4	Chemical Certifications (in Weight Percent) of the A600 Tubes Used in the CTE Test Program.....	3-10
Table 3-5	Mechanical Certifications of the A600 Tubes Used in the CTE Test Program .....	3-11
Table 3-6	Matrix for Coefficient of Thermal Expansion Tests.....	3-12
Table 3-7	Listing of the Test Results and Their Corresponding Figure Numbers .....	3-13
Table 5-1	Operating Conditions – Model 44F/51F Plants .....	5-5
Table 5-2	Steam Line Break Conditions .....	5-6
Table 5-3	Locked Rotor Event Conditions.....	5-7
Table 5-4	Control Rod Ejection Event Conditions .....	5-8
Table 5-5	H* Design End Cap Loads for Normal Operating Plant Conditions, Locked Rotor and Control Rod Ejection for Model 44F Plants.....	5-9
Table 6-1	List of Lower SG Complex Materials.....	6-16
Table 6-2	Summary of Material Properties for Alloy 600 Tube and Divider Plate Material.....	6-19
Table 6-3	Summary of Material Properties for SA-508 Class 2a Tubesheet Material.....	6-19
Table 6-4	Summary of Material Properties for SA-533 Grade A Class 2 Shell Material .....	6-20
Table 6-5	Summary of Material Properties for SA-216 Grade WCC Channelhead Material.....	6-20
Table 6-6	Summary of H* Point Beach Unit 1 Analysis Mean Input Properties.....	6-21
Table 6-7	List of SG Models and H* Plants With Tubesheet Support Ring Structures.....	6-22
Table 6-8	Conservative Generic NOP Pressures and Temperatures for 4-Loop Model F .....	6-29
Table 6-9	Generic NOP Low $T_{avg}$ Pressures and Temperatures for 4-Loop Model F.....	6-29
Table 6-10	Generic NOP High $T_{avg}$ Pressures and Temperatures for 4-Loop Model F.....	6-29
Table 6-11	Generic SLB Pressures and Temperatures for 4-Loop Model F.....	6-30
Table 6-12	Generic FLB Pressures and Temperatures for 4-Loop Model F.....	6-30
Table 6-13	Conservative Generic SLB Pressures and Temperatures for 4-Loop Model F.....	6-30
Table 6-14	Analysis Results of Model 1 Inside Hole Deflection for Multiple Pressure Load Combinations .....	6-54
Table 6-15	Comparison of FEA Results and Thick Shell Results .....	6-57
Table 6-16	Calculation of Adjusted $d$ .....	6-57
Table 6-17	Comparison of Thick Shell Results for Initial $d$ and Adjusted $d$ Values .....	6-58
Table 6-18	Contact Pressure for Square Displacement Model .....	6-67
Table 6-19	Contact Pressure for Diagonal Displacement Model.....	6-68
Table 6-20	Scale Factor as a Function of Initial Eccentricity .....	6-82
Table 6-21	Initial Mean H* Values.....	6-102
Table 6-22	Mean H* Values Adjusted for Thermal Distribution Effect.....	6-102
Table 6-23	Mean H* Values Including BET Offset.....	6-103
Table 6-24	Final Mean H* Values .....	6-103
Table 6-25	Mean Contact Pressure Distributions for NOP, Low $T_{avg}$ Condition.....	6-113
Table 6-26	Mean Contact Pressure Distributions for SLB Condition.....	6-114
Table 7-1	Variables That Affect Residual Contact Pressure.....	7-7
Table 7-2	Residual Contact Stress Model F Steam Generator .....	7-7
Table 7-3	Residual Contact Stress Model D5 Steam Generator .....	7-8
Table 7-4	Residual Contact Mode 44F Steam Generator.....	7-9

---

Table 7-5	Weibull Parameters for Residual Contact Pressure Variation .....	7-10
Table 8-1	H* Input Variables and Their Applications .....	8-7
Table 8-2	H* Variables and Influence Factors.....	8-8
Table 8-3	Matrix of Variable Interaction Study for H* .....	8-8
Table 8-4	Summary of Probabilistic Analysis .....	8-26
Table 9-1	Reactor Coolant System Temperature Increase Above Normal Operating Temperature Associated With Design Basis Accidents.....	9-22
Table 9-2	Reactor Coolant Systems Peak Pressures During Design Basis Accidents .....	9-23
Table 9-3	Model F Room Temperature Leak Rate Test Data .....	9-24
Table 9-4	Model F Elevated Temperature Leak Rate Test Data.....	9-25
Table 9-5	H* Plants Operating Conditions Summary <sup>1</sup> .....	9-26
Table 9-6	H* Plant Maximum Pressure Differentials During Transients that Model Primary-to-Secondary Leakage .....	9-27
Table 9-7	Final H* Leakage Analysis Leak Rate Factors.....	9-28
Table A-1	Model F Test Specimen Pull Out Data (11/16 Inch Diameter Tubes).....	A-2
Table A-2	Model 44F and 51F Test Specimen Pull Out Data (7/8 Inch Diameter Table).....	A-3
Table A-3	Model D5 Test Specimen Pull Out Data (3/4 Inch Diameter Tubes) .....	A-4

## TABLE OF FIGURES

Figure 1-1	Analysis Process for H*.....	1-10
Figure 3-1	Model F Steam Generator Split Collar Used to Strain Harden A600 Tubing .....	3-14
Figure 3-2	Model D5 Steam Generator Split Collar Used to Strain Harden A600 Tubing.....	3-15
Figure 3-3	Model 44F Steam Generator Split Collar Used to Strain Harden A600 Tubing .....	3-16
Figure 3-4	Heat-Up Test on A508 Gr. 3 Cl. 1 Material .....	3-17
Figure 3-5	Heat-Up Test on A508 Gr. 3 Cl. 2 Material .....	3-17
Figure 3-6	Heat-Up Test on A508 Gr. 3 Cl. 2 Material .....	3-18
Figure 3-7	Heat-Up Test on A508 Gr. 3 Cl. 2 Material .....	3-18
Figure 3-8	A508 Mean Curves Versus the ASME Code Curves .....	3-19
Figure 3-9	Heat-Up Test on A600, Model F Tube, Heat NX9749.....	3-19
Figure 3-10	Heat-Up Test on A600, Model F Tube, Heat NX0419.....	3-20
Figure 3-11	Heat-Up Test on A600, Model F Tube, Heat NX9821.....	3-20
Figure 3-12	Summary of Heat-Up Testing of All Heats of A600 Model F Tube .....	3-21
Figure 3-13	Mean Curves of Heats of A600 Model F Tube Versus the ASME Code Curve .....	3-21
Figure 3-14	Heat-Up Test of A600, Model D5 Tube, Heat NX1002.....	3-22
Figure 3-15	Heat-Up Test of A600, Model D5 Tube, Heat NX1019.....	3-22
Figure 3-16	Heat-Up Test of A600, Model D5 Tube, Heat NX1145.....	3-23
Figure 3-17	Summary of Heat-Up Testing of All Heats of A600 Model D5 Tube.....	3-23
Figure 3-18	Mean Curves of Heats of A600 Model D5 Tube Versus the ASME Code Curve.....	3-24
Figure 3-19	Heat-Up Tests of A600, Model 44F Tube, Heat NX9180.....	3-24
Figure 3-20	Heat-Up Tests of A600, Model 44F Tube, Heat NX9292.....	3-25
Figure 3-21	Heat-Up Tests of A600, Model 44F Tube, Heat NX1518.....	3-25
Figure 3-22	Summary of Heat-Up Testing of All Heats of A600 Model 44F Tube .....	3-26
Figure 3-23	Mean Curves of Heats of A600 Model 44F Tube Versus the ASME Code Curve.....	3-26
Figure 3-24	Mean Curves of All A600 Steam Generator Model Data Versus the ASME Code Curve.....	3-27
Figure 3-25	A508, Heat 97D258-1-1, Sample 8 Multiple Testing.....	3-27
Figure 3-26	A600, Heat NX1019, Sample 3 Multiple Testing.....	3-28
Figure 3-27	Heat-Up Tests of Strain Hardened A600 Model F Tubing, Heat NX9749.....	3-28
Figure 3-28	Heat-Up Tests of Strain Hardened A600 Model F Tubing, Heat NX0419.....	3-29
Figure 3-29	Heat-Up Tests of Strain Hardened A600 Model F Tubing, Heat NX9821.....	3-29
Figure 3-30	Heat-Up Tests of Strain Hardened A600 Model D5 Tubing, Heat NX1002.....	3-30
Figure 3-31	Heat-Up Tests of Strain Hardened A600 Model D5 Tubing, Heat NX1019.....	3-30
Figure 3-32	Heat-Up Tests of Strain Hardened A600 Model D5 Tubing, Heat NX1145.....	3-31
Figure 3-33	Heat-Up Tests of Strain Hardened A600 Model 44F Tubing, Heat NX9180.....	3-31
Figure 3-34	Heat-Up Tests of Strain Hardened A600 Model 44F Tubing, Heat NX9292.....	3-32
Figure 3-35	Heat-Up Tests of Strain Hardened A600 Model 44F Tubing, Heat NX1518.....	3-32
Figure 3-36	A600 Model F Tube, Heat NX0419, Repeat Test.....	3-33
Figure 3-37	A600 Model D5 Tube, Heat NX1019, Repeat Test.....	3-33
Figure 3-38	A600 Model 44F Tube, Heat NX9180, Repeat Test.....	3-34
Figure 3-39	A600 Model D5 Tube, Heat NX1145, Repeat Test.....	3-34
Figure 6-1	Mean H* Values for the Limiting Model 44F Plant (w/o crevice pressure adjustment) .....	6-2
Figure 6-2	Solid 3D Model of a Typical 44F SG.....	6-11
Figure 6-3	3D Model Mesh Screen Shot .....	6-11
Figure 6-4	Close-Up of Tubesheet Junction Mesh .....	6-12
Figure 6-5	Typical Finite Element Mesh for a Prior Axisymmetric Tubesheet-Channelhead- Stub Barrel Model.....	6-13
Figure 6-6	3D Tubesheet Mesh Close-Up Screen Shot.....	6-14
Figure 6-7	Top Plane View of Perforated Tubesheet Mesh .....	6-14

Figure 6-8	Rear View of 3D Model Mesh.....	6-15
Figure 6-9	Important Structures in the Lower SG Complex .....	6-17
Figure 6-10	Top View of Tubesheet Showing Different Tubesheet Structures .....	6-17
Figure 6-11	Surface Groups for a Typical SG FEM.....	6-24
Figure 6-12	Important Edges in a Typical SG FEM With a Tubesheet Support Ring .....	6-24
Figure 6-13	Important Edges in a Typical SG FEM Without a Tubesheet Support Ring .....	6-25
Figure 6-14	Typical Structural Model Applied Loads .....	6-26
Figure 6-15	Typical Thermal Model Applied Loads.....	6-26
Figure 6-16	Typical Thermal Model Tubesheet Boundary Conditions Shown on Top View SG.....	6-27
Figure 6-17	Typical Structural Model Tubesheet Boundary Conditions Shown on Top View of Typical SG.....	6-27
Figure 6-18	Comparison of Different Temperature Distributions Through the Tubesheet due to Varying Boundary Conditions .....	6-32
Figure 6-19	Top View of Model 44F Tubesheet Showing Sector Regions for Displacement Analysis .....	6-35
Figure 6-20	Radial TS Displacement due to Pressure at TTS and BTS for TS Radius ~ 55 Inches During NOP.....	6-36
Figure 6-21	Relative Change in Tubesheet Displacement as a Function of Sector Angle During NOP for a Model F SG .....	6-37
Figure 6-22	FEA Model Orientations as Shown From a Top View of a Typical Tubesheet .....	6-41
Figure 6-23	Model 1 Geometry, Region of Tubesheet Perpendicular to Tube Lane .....	6-42
Figure 6-24	Model 2 Geometry, Region of Tubesheet Parallel to Tube Lane .....	6-42
Figure 6-25	Model 1 Applied Boundary Conditions - Perpendicular to Divider Lane .....	6-43
Figure 6-26	Model 2 Applied Boundary Conditions - Parallel to Divider Lane .....	6-43
Figure 6-27	Relative Location of the Three Tube Holes of Interest in Model 1 and Model 2 .....	6-44
Figure 6-28	Close-Up of Inside Hole Location .....	6-44
Figure 6-29	Close-Up of Middle Hole Location .....	6-44
Figure 6-30	Close-Up of Outside Hole Location .....	6-45
Figure 6-31	Reference Configuration for Tube Bore Deflection Plots .....	6-47
Figure 6-32	Inside Hole Results for NOP Conditions, $P_{pri} = 2250$ psi, for Model 1 .....	6-47
Figure 6-33	Middle Hole Results for NOP Conditions, $P_{pri} = 2250$ psi, for Model 1 .....	6-48
Figure 6-34	Outside Hole Results for NOP Conditions, $P_{pri} = 2250$ psi, for Model 1 .....	6-48
Figure 6-35	Inside Hole Results for SLB Conditions, $P_{pri} = 2560$ psi, for Model 1 .....	6-49
Figure 6-36	Middle Hole Results for SLB Conditions, $P_{pri} = 2560$ psi, for Model 1 .....	6-49
Figure 6-37	Outside Hole Results for SLB Conditions, $P_{pri} = 2560$ psi, for Model 1 .....	6-50
Figure 6-38	Comparison of FEA Results and Thick Shell Equations for NOP and SLB Using Equations (6-1) and (6-2).....	6-51
Figure 6-39	Typical Result for Including the Tube Cross Section Within the Tube Bore, for the Outside Hole, When All of the Tube Bores are Pressurized.....	6-51
Figure 6-40	Graphic of Applied Pressure Regions in Separate Pressure Combination Study .....	6-53
Figure 6-41	Tube Bore ID Deflection due to a Constant Applied Internal Pressure as a Function of Outer Collar Radius.....	6-55
Figure 6-42	Linear Relationships Between Applied Effective Outer Radius ( $d$ ) and TS Radius for the NOP and SLB Conditions .....	6-58
Figure 6-43	Finite Element Model .....	6-69
Figure 6-44	Boundary Conditions for Square Displacement Model .....	6-69
Figure 6-45	Displaced Shape for S.1.1 Through S.1.6 Computer Runs.....	6-70
Figure 6-46	Displaced Shape for S.2.1 Through S.2.6 Computer Runs.....	6-70
Figure 6-47	Boundary Conditions for Diagonal Displacement Model.....	6-71
Figure 6-48	Displaced Shape for D.1.1 Through D.1.6 Computer Runs .....	6-71
Figure 6-49	Displaced Shape for D.2.1 Through D.2.6 Computer Runs .....	6-72

Figure 6-50	Computer Run S.1.5, Step 1, Stress Intensity .....	6-72
Figure 6-51	Computer Run S.1.5, Step 2, Stress Intensity .....	6-73
Figure 6-52	Computer Run S.1.5, Step 2, Contact Pressure.....	6-73
Figure 6-53	Computer Run S.1.5, Step 3, Stress Intensity .....	6-74
Figure 6-54	Computer Run S.1.5, Step 3, Contact Pressure.....	6-74
Figure 6-55	Computer Run S.1.5, Step 4, Stress Intensity .....	6-75
Figure 6-56	Computer Run S.1.5, Step 4, Contact Pressure.....	6-75
Figure 6-57	Computer Run S.1.5, Step 5, Stress Intensity .....	6-76
Figure 6-58	Computer Run S.1.5, Step 5, Contact Pressure.....	6-76
Figure 6-59	Computer Run S.1.5, Step 6, Stress Intensity .....	6-77
Figure 6-60	Computer Run S.1.5, Step 6, Contact Pressure.....	6-77
Figure 6-61	Computer Run S.1.5, Step 7, Stress Intensity .....	6-78
Figure 6-62	Computer Run S.1.5, Step 7, Contact Pressure.....	6-78
Figure 6-63	Comparison Between H* Values for a Degraded Divider Plate (DPF = [ ] <sup>a,c,e</sup> ) and an Intact Divider Plate (DPF = [ ] <sup>a,c,e</sup> ) .....	6-80
Figure 6-64	Calculated T/TS Contact Pressure as a Function of Tube Bore Eccentricity .....	6-88
Figure 6-65	Reduction in T/TS Contact Pressure Based on Limiting Fit from Figure 1.....	6-89
Figure 6-66	Typical Model 44F Pressure Displacement Results for 3D Model.....	6-96
Figure 6-67	Typical Model 44F Pressure Displacement Results for 3D Model During SLB.....	6-96
Figure 6-68	Combined Thermal and Pressure Tubesheet Radial Displacement for Point Beach Unit 1 at the Bottom of the Tubesheet, DPF = [ ] <sup>a,c,e</sup> .....	6-97
Figure 6-69	Combined Thermal and Pressure Tubesheet Radial Displacement for Point Beach Unit 1 at the Neutral Axis of the Tubesheet, DPF = [ ] <sup>a,c,e</sup> .....	6-97
Figure 6-70	Combined Thermal and Pressure Tubesheet Radial Displacement for Point Beach Unit 1 at the Top of the Tubesheet, DPF = [ ] <sup>a,c,e</sup> .....	6-98
Figure 6-71	Comparison of Tube-to-Tubesheet Contact Pressure for Point Beach Unit 1 at the Limiting Tubesheet Radius of [ ] <sup>a,c,e</sup> inches .....	6-98
Figure 6-72	Comparison of Contact Pressures for Model 44F Fleet Including Specimen 8 Crevice Pressure Data At Limiting TS Radius [ ] <sup>a,c,e</sup> BTS = 21.81 inches, TTS = 0.0 inches .....	6-100
Figure 6-73	Tube-to-Tubesheet Contact Pressure for the Limiting Model 44F Plant (Point Beach Unit 1) at the Limiting TS Radius Using Only the Specimen 8 Crevice Pressure Data .....	6-101
Figure 6-74	TS Radial Displacement Under Combined Thermal and Pressure Loads During SLB TTS = TS Elevation 21.0 inches, BTS = TS Elevation 0.0 inches .....	6-106
Figure 6-75	TS Radial Displacement Under Combined Thermal and Pressure Loads for NOP TTS = TS Elevation 21.0 inches, BTS = TS Elevation 0.0 inches .....	6-107
Figure 6-76	Combined Thermal and Pressure Load Tubesheet Radial Displacements for NOP TTS = TS Elevation 21.0 inches, BTS = TS Elevation 0.0 inches .....	6-108
Figure 6-77	Combined Thermal and Pressure Load Tubesheet Radial Displacements for SLB TTS = TS Elevation 21.0 inches BTS = TS Elevation 0.0 inches .....	6-109
Figure 6-78	Mean Contact Pressure Distribution Case for Point Beach Unit 1 Conditions at a TS Radius of [ ] <sup>a,c,e</sup> inches TTS = TS Elevation 0.0 inches BTS = TS Elevation 21.03 inches .....	6-110
Figure 6-79	Comparison of the Average Crevice Pressure Data as a Function of Depth Ratio for t he Entire Crevice Pressure Data Set and the Data Set When Only Specimen 8 is Considered .....	6-111
Figure 6-80	Comparison of H* for Different Crevice Pressure Data Input.....	6-111
Figure 7-1	Finite Element Model – Overall View.....	7-11
Figure 7-2	Finite Element Model – Node Constraints.....	7-12
Figure 7-3	Cumulative Distribution Functions of RCP Variables Factors .....	7-13

Figure 7-4	Compositive Variability of Residual Contact Pressure.....	7-14
Figure 7-5	Illustration of Adjustment to H* for Positive RCP .....	7-14
Figure 8-1	Model 44F: Adjustment to H* for Distributed Crevice Pressure Referenced to Initial Prediction of H* .....	8-9
Figure 8-2	H* Variation of H* with Individual Input Variables .....	8-10
Figure 8-3	Variability of H* with All Relevant Parameters .....	8-11
Figure 8-4	Expected Variation of H* When Both $\alpha_T$ and $\alpha_{TS}$ are Varied and are Independent.....	8-12
Figure 8-5	Interaction Between $\alpha_{TS}$ and $\alpha_T$ .....	8-13
Figure 8-6	Interaction Between $\alpha_{TS}$ and $E_{TS}$ .....	8-14
Figure 8-7	Interaction Between $\alpha_{TS}$ and $E_T$ .....	8-14
Figure 8-8	Interaction Between $\alpha_T$ and $E_T$ .....	8-15
Figure 8-9	Interaction Between $E_{TS}$ and $\alpha_T$ .....	8-15
Figure 8-10	Interaction Between $E_{TS}$ and $E_T$ .....	8-16
Figure 8-11	Illustration of Biased Influence Factors.....	8-17
Figure 8-12	Single Tube Required Reliability, Expressed as Number of Standard Deviations from the Mean to Meet a Whole-Bundle (3214 Tubes) Reliability of 95% .....	8-27
Figure 9-1	Dynamic Viscosity as a Function of Temperature.....	9-29
Figure 9-2	Plot of Model D and Model F Total Data Set for 70°F and 600°F.....	9-30
Figure 9-3	Model 44F SLB RCS Pressure-Time History Graph for a 2 Loop Plant.....	9-31
Figure 9-3a	Model 44F SLB RCS Temperature-Time History Graph for a 2 Loop Plant (Hot Leg).....	9-32
Figure 9-3b	Model 44F SLB RCS Temperature-Time History Graph for a 2 Loop Plant (Cold Leg).....	9-33
Figure 9-4	Model 44F SLB RCS Pressure-Time History Graph For a 3 Loop Plant.....	9-34
Figure 9-4a	Model 44F SLB RCS Temperature-Time History Graph for a 3 Loop Plant (Hot Leg).....	9-35
Figure 9-4b	Model 44F SLB RCS Temperature-Time History Graph for a 3 Loop Plant (Cold Leg).....	9-36
Figure 9-5	This Figure Intentionally Left Blank .....	9-37
Figure 9-6	This Figure Intentionally Left Blank .....	9-38
Figure 9-7	Example Leakage Test Schematic (Model F Testing Only).....	9-39
Figure 9-8	Schematic for the Test Autoclave Systems for Leak Rate Testing (Model D5 Testing Only).....	9-40
Figure 9-9	Example Tube Joint Leakage Test Configuration.....	9-41
Figure 9-10	Model F Room Temperature Leak Rate Test Results.....	9-42
Figure 9-11	Model F Elevated Temperature Leak Rate Test Results.....	9-43
Figure 9-12	Model F Room Temperature Leak Rate Ratio Versus Differential Pressure Ratio Comparison.....	9-44
Figure 9-13	Model F Elevated Temperature Leak Rate Ratio Versus $\Delta P$ Ratio Comparison (600°F).....	9-45
Figure 9-14	Results of Test-by-Test Loss Coefficient (K) Regression on Contact Pressure for Model D5 Test Specimens.....	9-46
Figure 9-15	Results of Test-by-Test Loss Coefficient (K) Regression on Contact Pressure for Model F Test Specimens.....	9-47
Figure 9-16	Typical Reactor Coolant Pump Locked Rotor and Control Rod Ejection Delta P for Model 44F SGs .....	9-48

## 1.0 INTRODUCTION

### 1.1 H\*/B\* BACKGROUND INFORMATION

In response to the detection of crack-like indications within the tube expansion region of steam generators (SGs) with Alloy 600 thermally-treated (A600TT) tubing, the NRC issued GL-2004-01 (Reference 1-14) which reiterated the requirement to inspect the full length of the tubes with probes capable of detecting potential degradation in all the areas of the steam generator (SG) unless a technical argument was available to demonstrate that specific types of degradation are not expected. Indications interpreted as primary water system stress corrosion cracking (PWSCC) were reported from the nondestructive, eddy current examination of the SG tubes during the fall 2004 outage at the Catawba Unit 2 Nuclear Power Plant (References 1-1, 1-2, and 1-3). The indications at Catawba Unit 2 were reported about 7.6 inches from the top of the tubesheet in one tube, and just above the tube-to-tubesheet welds in a region of the tube known as the tack expansion (TE) in several other tubes. The Catawba Unit 2 plant has Westinghouse designed, Model D5 SGs fabricated with A600TT tubes of 3/4 inch outside diameter. Subsequently, one indication was reported in each of two SG tubes at the Vogtle Unit 1 Plant (Reference 1-4). The Vogtle Unit 1 SGs are of the Westinghouse Model F design with 11/16 inch outside diameter A600TT tubes. The indication locations in both Catawba Unit 2 and Vogtle Unit 1 were coincident with geometric variations, termed "bulges" (BLG), in the expansion region. It was concluded from those observations that there is the potential for similar tube indications to be reported during future inspections of all SGs with hydraulically expanded A600TT tubes since geometric variations in the tubesheet expansion region are common. Since that time, several plants that have inspected through the entire thickness of the tubesheet with rotating pancake coil (RPC) have reported indications near the tube-to-tubesheet welds, in the tack expansion region.

The findings in the Catawba Unit 2 and Vogtle Unit 1 SG tubes present two distinct issues with regard to future inspections of A600TT SG tubes which have been hydraulically expanded into the tubesheet:

1. Indications may occur at internal bulges (BLG) or overexpansions (OXF) in the tubes within the tubesheet that were created as an artifact of the manufacturing process.
2. Indications may occur at the elevation of the tack expansion transition because it represents a stress riser in the tube.

Although some of the indications at Catawba were reported to be in the tube end weld, subsequent studies using a prototypic tube end test section concluded that the eddy current techniques were not capable of distinguishing the interface between the tube and weld, and further, that the indications likely were in the tube material. However, it could not be ruled out that the indications may extend into the weld. The indications were located within the tack expansion length, which, at Catawba, was made using a hard-rolling process. Thus, it was concluded that the indications that were observed all occurred in areas of potentially elevated residual stress in the tube material.

A technical evaluation is presented in this report that considers the requirements of the American Society of Mechanical Engineers (ASME) Code, Regulatory Guides, NRC Generic Letters, NRC Information Notices, the Code of Federal Regulations, NEI 97-06, and responses to NRC Request for Additional Information (RAI). The two major conclusions of the technical evaluation are that:

1. The structural integrity of the primary-to-secondary pressure boundary is unaffected by tube degradation of any magnitude below a specific depth of 13.31 inches, designated as  $H^*$ , and,
2. The accident condition leak rate integrity is bounded by an overall leakage increase of 2.03 during the limiting design basis accident (DBA) relative to normal operating plant conditions. This is known as the leakage factor. Although an increase in contact pressure at accident conditions relative to normal operating conditions is not a basis for the leakage evaluation, for conservatism, it is shown that, for the Model 44F SG, the contact pressure between the tube and the tubesheet is greater at accident conditions than at normal operating conditions (NOP) for all relevant accidents.

The determination of the required engagement depth is based on the use of finite element model structural analyses and of a bounding leak rate evaluation for normal operation and postulated accident conditions. The results provide the technical rationale to exempt inspection of the region of the tube below the calculated  $H^*$  elevation. Such an approach is interpreted as a redefinition of the primary-to-secondary pressure boundary relative to the original design of the SG, which requires the approval of a license amendment by the NRC Staff.

The  $H^*$  values are determined to assure meeting the structural performance criteria for the operating SG tubes as delineated in NEI 97-06, Revision 2 (Reference 1-5). The leakage factors are determined based on meeting the accident condition leak rate performance criteria for all DBA that model primary-to-secondary leakage. The leakage analysis is based on a first principles application of the Darcy model for leakage through a porous medium, supported by empirical test results that show that there is no correlation between loss coefficient and contact pressure for the conditions of interest. The leakage analysis is supported by the structural analysis (Section 6.0) that shows for the Model 44F SG that the contact pressure between the tubes and tubesheet is always greater at accident conditions than at normal operating conditions.

Tests have shown that all full-depth expanded tube-to-tubesheet joints in Westinghouse-designed SGs have a residual radial preload interface pressure between the tube and the tubesheet. Residual contact pressure is not an essential element for determining a value of  $H^*$  for hydraulically expanded tubes. The reference approach in this document is to assume zero contribution from residual contact pressure; however, when the existing residual contact pressure is more firmly established through additional testing, the value of  $H^*$  presented in this report will be significantly smaller. Thus, the assumption of zero residual contact pressure is a conservative assumption.

## 1.2 DISCUSSION OF THE CALCULATION PROCESSES

The current candidate plants for  $H^*$  are those plants whose SGs have Alloy 600TT tubes that are hydraulically expanded into the tubesheet. Among these are plants with Model F SGs, Model D5 SGs, Model 44F SGs and Model 51F SGs. Except for the Model 51F SGs, there are multiple plants with each of the other models of SGs. To reduce the analysis burden, a bounding plant was determined for each model of SG as discussed in Section 6.0. The value of  $H^*$  determined for each of the bounding plants is the recommended  $H^*$  for each of the models of SG, respectively.

This report is specifically based on the properties of the Model 44F SGs. Separate reports will be provided for the other models of SGs. While specific geometric and operating conditions are different among the various models of SGs, the methodology for the H\* calculations are common to all models of SGs represented among the population of H\* candidate plants.

### 1.2.1 Structural Integrity Analysis

The H\* technical analysis consists of two essentially independent processes; the structural evaluation to define the value of H\*, and the leakage analysis for the tubesheet expansion region. The structural analysis for H\* is a complex analysis that involves the use of four different models as shown on the flowchart on Figure 1-1.

- A finite element structural model is used to calculate the deflections and rotations of the tubesheet complex components which include the tubesheet, channelhead, stub barrel and divider plate. The finite element model is a three-dimensional finite element model (3D FEA) using the ANSYS computer code. This model is described in detail in Section 6.0.
- An Excel<sup>®</sup>(<sup>1</sup>) spreadsheet model utilizes the deflection and rotation output from the 3D FEA model (Reference 1-7) and a crevice pressure input based on test data to calculate the radially and axially distributed contact pressures between the tube and tubesheet for the various operating conditions. The spreadsheet also axially integrates the forces resisting tube pull out based on the contact pressures and a conservative value of coefficient of friction to define the mean value of H\*. H\* is defined as the distance from the top of the tubesheet at which the integrated pull out resisting force equals the applied end cap loads. The Excel<sup>®</sup> model is described in Section 6.0. The end cap force calculation applied to the tubes is described in Section 5.0.
- The third model is an Excel<sup>®</sup> spreadsheet that calculates the mean residual contact pressure based on pull out test data, and provides the residual contact pressure to the H\* integrating spreadsheet discussed above. Residual contact pressure is defined as the contact pressure between the tube and the tubesheet at room temperature that results from the hydraulic expansion process. The use of this model is optional for the justification of H\*; the reference calculation in this report assumes that residual contact pressure is zero.
- The variability of the residual contact pressure, also an input to the probabilistic analysis, is determined from a two-dimensional finite element model (2D FEA) (Reference 1-9). The variability of the inputs used to calculate the residual contact pressures are determined individually using an influence factor approach and combined into a single residual contact pressure variability distribution using different approaches including a Monte Carlo sampling technique. This is discussed in Section 7.0.

---

(1) Microsoft, MSN, and Windows Vista are trademarks of the Microsoft group of companies.

## 1.2.2 Leakage Integrity Approach

As discussed in Section 9.0 of this report, the expression used to predict the leak rate from tube cracks through the tube-to-tubesheet crevice is the Darcy expression for flow rate,  $Q$ , through porous media, i.e.,

$$Q = \frac{\Delta p}{12\mu Kl}$$

where

- $\mu$  = the viscosity of the fluid
- $\Delta p$  = the driving pressure differential
- $l$  = the physical dimension in the direction of the flow (effective crevice length)
- $K$  = the leakage "loss coefficient" which can also be termed the flow resistance.

The leakage analysis utilizes a ratio approach, based on the Darcy equation, to determine the ratio of leakage at accident conditions to that at normal operating conditions. It is shown in Section 9.0 that the loss coefficient is not a function of contact pressure; therefore, the loss coefficient ratio has a value of 1. It is also shown that the tube and the tubesheet are in contact for the total length of the tubesheet thickness. Therefore, the ratio of the length of the porous medium also has a value of 1. The ratio of the viscosity at accident conditions to that at normal operating conditions is also conservatively shown to be 1. Consequently, the leakage ratio is a function of only the ratio of the driving heads, that is, the ratio of the accident condition  $\Delta p$  to that at normal operating conditions.

## 1.3 SUMMARY OF CHANGES FROM PRIOR H\* SUBMITTALS

### 1.3.1 Structural Integrity Analysis

All prior submittals of the H\* technical justification (e.g., Reference 1-9) utilized the same analysis approach summarized in Section 1.2.1. However, since the last submittal by Wolf Creek Nuclear Operating Corporation (Reference 1-8, with Reference 1-9 enclosed) significant changes have been made in the structural models. The original structural model utilized a two-dimensional (2D) axisymmetric model for the tubesheet complex. A number of RAIs were issued by the NRC (see Section 2.1) that questioned the details of the application of this model. Further, questions were raised regarding the efficacy of the superpositioning approach employed with this model because it was noted that different results were obtained when the model input was condition-specific compared to the superposition results based on temperature and pressure. The process of benchmarking the 2D model utilized state-of-the-art three-dimensional (3D) finite element capabilities inherent to the ANSYS computer code. Ultimately, a new 3D model of the tubesheet complex was developed and adopted as the reference model for the structural analysis. The 2D axisymmetric model is no longer used in the current tubesheet deflection calculations supporting the analysis of H\*.

Prior calculations assumed that contact pressure from the tube would expand the tubesheet bore uniformly without considering the restoring forces from adjacent pressurized tubesheet bores. In the structural model, a tubesheet radius dependent stiffness effect is applied by modifying the representative collar thickness (see Section 6.2.4) of the tubesheet material surrounding a tube based on the position of the tube in the bundle. The basis for the radius dependent tubesheet stiffness effect is similar to the previously mentioned “beta factor” approach. The “beta factor” was a coefficient applied to reduce the crevice pressure to reflect the expected crevice pressure during normal operating conditions in some prior H\* calculations and is no longer used in the structural analysis of the tube-to-tubesheet joint. The current structural analysis consistently includes a radius dependent stiffness calculation described in detail in Section 6.2.4. The application of the radius dependent stiffness factor has only a small effect on the ultimate value of H\* but rationalizes the sensitivity of H\* to uncertainties throughout the tubesheet.

The contact pressure analysis methodology has not changed since 2007 (Reference 1-9). However, the inputs to the contact pressure analysis and how H\* is calculated have changed in that period of time. The details describing the inputs to the contact pressure analysis are discussed in Section 6.0.

The calculation for H\* includes the summation of axial pull out resistance due to local interactions between the tube bore and the tube. Although tube bending is a direct effect of tubesheet displacement, the calculation for H\* conservatively ignores any additional pull out resistance due to tube bending within the tubesheet or Poisson expansion effects acting on the severed tube end. In previous submittals, the force resisting pull out acting on a length of a tube between any two elevations  $h_1$  and  $h_2$  was defined in Equation (1-1):

$$\left[ \dots \right]^{a,c,e} \tag{1-1}$$

where:

- $F_{HE}$  = Resistance per length to pull out due to the installation hydraulic expansion,
- $d$  = Expanded tube outer diameter,
- $P$  = Contact pressure acting over the incremental length segment  $dh$ , and,
- $\mu$  = Coefficient of friction between the tube and tubesheet, conservatively assumed to be 0.2 for the pull out analysis to determine H\*.

The current H\* analysis generally uses the following equation to determine the axial pull out resistance of a tube between any two elevations  $h_1$  and  $h_2$ :

$$\left[ \dots \right]^{a,c,e} \tag{1-2}$$

Where the other parameters in Equation (1-2) are the same as in Equation (1-1) and [

]<sup>a,c,e</sup>. A detailed explanation of the

revised axial pull out equation are included in Section 6.0 of this report. However, the reference basis for the H\* analysis is the assumption that residual contact pressure contributes zero additional resistance to tube pull out. Therefore, the equation to calculate the pull out resistance in the H\* analysis is:

$$\left[ \quad \quad \quad \right]^{a,c,e} \quad (1-3)$$

### 1.3.2 Leakage Integrity Analysis

Prior submittals of the technical justification of H\* (Reference 1-9) argued that  $K$  was a function of the contact pressure,  $P_c$ , and, therefore, that resistance was a function of the location within the tubesheet. The total resistance was found as the average value of the quantity  $\mu K$ , the resistance per unit length, multiplied by  $L$ , or by integrating the incremental resistance,  $dR = \mu K dL$  over the length  $L$ , i.e.,

$$R = \mu \bar{K} (L_2 - L_1) = \mu \int_{L_1}^{L_2} K dL \quad (1-4)$$

Interpretation of the results from multiple leak rate testing programs suggested that the logarithm of the loss coefficient was a linear function of the contact pressure, i.e.,

$$\ln K = a_0 + a_1 P_c, \quad (1-5)$$

where the coefficients,  $a_0$  and  $a_1$  of the linear relation were based on a regression analysis of the test data; both coefficients are greater than zero. Simply put, the loss coefficient was determined to be greater than zero at the point where the contact pressure is zero and it was determined that the loss coefficient increases with increasing contact pressure. Thus,

$$K = e^{a_0 + a_1 P_c}, \quad (1-6)$$

and the loss coefficient was an exponential function of the contact pressure.

The B\* distance ( $L_B$ ) was defined as the depth at which the resistance to leak during SLB was the same as that during normal operating conditions (NOP) (using Equation 1-4, the B\* distance was calculated setting  $R_{SLB} = R_{NOP}$  and solving for  $L_B$ ). Therefore, when calculating the ratio of the leak rate during the design basis accident condition to the leak rate during normal operating conditions, the change in magnitude of leakage was solely a function of the ratio of the pressure differential between the design basis accident and normal operating plant conditions.

The NRC Staff raised several concerns relative to the credibility of the existence of the loss coefficient versus contact pressure relationship used in support of the development of the B\* criterion:

1. The Model F SG loss coefficient versus contact pressure plot exhibits a higher slope than the case for the Model D5 SG (Reference 1-10).
2. Although the mean of the regression fits for the loss coefficient data for the Model F and the Model D5 SGs are within a factor of three (3) of each other, the slope and intercept properties remain highly divergent (Reference 1-11).
3. The Model D5 loss coefficient data is spread out in range and results in a slightly negative log-linear correlation (Reference 1-11).

The current approach to the leakage analysis shows that there is no significant correlation between loss coefficient and contact pressure based on the available test data. A ratio approach, using the Darcy formulation as noted above and as described in detail in Section 9.0, is the current reference basis for leakage ratio calculations.

### 1.3.3 Probabilistic Analysis

At a meeting in July 2008, the NRC requested a probabilistic evaluation of  $H^*$ . Probabilistic evaluations of  $H^*$  had not been performed. Previously, a limiting worst-case analysis was provided (Reference 1-11) that was based on an  $H^*$  variability study on individual inputs parameters. The worst-case values of the variables were then combined into an integrated case that resulted in a high probability value of  $H^*$ . This approach was not accepted as noted in the remaining technical concerns issued in Reference 1-12.

Because of the complexity of the  $H^*$  calculations (see Section 1.2.1) that involve the combined use of four different models, a pure Monte Carlo approach was not possible. The current analysis of  $H^*$  is based principally on the semi-statistical approach outlined in the EPRI Integrity Assessment Guidelines (Reference 1-13), in which the uncertainties are combined using a square root of sum of squares (SRSS) approach. Further, to support the SRSS approach, a Monte Carlo approach to the  $H^*$  calculation was developed that utilized influence factors. For the influence factor approach, a distribution of  $H^*$  in a single input variable is determined while maintaining all other input variables at their nominal values. This process is completed for each input variable, resulting in  $H^*$  distributions in every input variable. Monte Carlo sampling is performed from these distributions to develop the integrated variability of  $H^*$  in all variables. The probabilistic analysis for  $H^*$  is included in Section 8.0 of this report.

In response to the residual technical issues identified by the Staff, the capability to provide residual contact pressure variability as an input to the  $H^*$  integration model was developed. The mean value of residual contact pressure is based on test data, and the variability around the mean value is determined for each relevant input variable based on analysis. The individual variability distribution for residual contact pressure is combined in the same manner as discussed above for the probabilistic  $H^*$  determination. It is noted that the reference  $H^*$  calculation provided in this report assumes residual contact pressure to be zero. Any positive value of residual contact pressure will decrease the final value of  $H^*$ .

## 1.4 CONSERVATISMS IN THE $H^*$ ANALYSIS

A conservative approach was taken for the calculation of  $H^*$ . Notwithstanding that the underlying structural integrity and leakage requirements are inherently conservative, e.g., application of a factor of

three (3) on expected normal operating pressure differentials, other conservative assumptions were made that provide significant confidence in the predicted value of  $H^*$  and the leakage factors. Table 1-1 summarizes the significant conservative assumptions and approaches included in the calculations for  $H^*$ .

## 1.5 REPORT OVERVIEW

Section 1.0 provides an introduction to WCAP-17091-P. Section 2.0 provides information on the resolution of all technical issues and NRC requests for additional information on this topic. Section 3.0 addresses the test programs in support of the technical justification of  $H^*$ . Section 4.0 addresses the structural and leakage analysis acceptance criteria. Section 5.0 discusses the plant operating conditions at the  $H^*$  plants with Model 44F SGs. Section 6.0 discusses the structural analyses of the tube-to-tubesheet joint. Section 7.0 addresses residual contact pressure and its variability. Section 8.0 uses the results provided in Section 6.0 and Section 7.0 to define the  $H^*$  values as a function of tubesheet radial location for each of the  $H^*$  plants for normal operating, postulated steam line break, and feedwater line break conditions to provide a probabilistic assessment of the  $H^*$  value. Section 9.0 discusses the details of the leakage analysis. Finally, Section 10.0 provides the conclusion of this report.

## 1.6 REFERENCES

- 1-1 OE19662 (Restricted & Confidential), "Steam Generators (Catawba Nuclear Power Station)," Institute of Nuclear Power Operations (INPO), Atlanta, GA, USA, December 13, 2004.
- 1-2 IN 2005-09, "Indications in Thermally-Treated Alloy 600 Steam Generator Tubes and Tube-to-Tubesheet Welds," United States Nuclear Regulatory Commission, Washington, DC, April 7, 2005.
- 1-3 SGMP-IL-05-01, "Catawba Unit 2 Tubesheet Degradation Issues," EPRI, Palo Alto, CA, March 4, 2005.
- 1-4 OE20339, "Vogtle Unit 1 Steam Generator Tube Crack Indications," Institute of Nuclear Power Operations (INPO), Atlanta, GA, USA, April 4, 2005.
- 1-5 NEI 97-06, Rev. 2, "Steam Generator Program Guidelines," Nuclear Energy Institute, Washington, DC, May 2005.
- 1-6 LTR-SST-05-19, Rev. 1, "System State Equivalency Testing Not Required for Windows XP SP-2," June 20, 2005.
- 1-7 LTR-SST-08-16, "ANSYS 10.0 for HP-UX 11.23i Release Letter," March 28, 2009.
- 1-8 WCNOC Letter ET-06-0004, "Revision to Technical Specification 5.5.9, Steam Generator Tube Surveillance Program," February 21, 2006.

- 
- 1-9 LTR-CDME-05-209-P, "Steam Generator Tube Alternate Repair Criteria for the Portion of Tube Within the Tubesheet at the Wolf Creek Generating Station," January 2006.
  - 1-10 LTR-CDME-07-72, "Response to NRC Request for Additional Information Relating to LTR-CDME-05-209-P of the Wolf Creek Generating Station (WCGS) Permanent B\* License Amendment Request," April 24, 2007 (Enclosure to WCNOG Letter WO 07-0012, dated May 3, 2007).
  - 1-11 LTR-CDME-07-198, "Response to NRC Request for Additional Information Relating to LTR-CDME-07-72 P-Attachment and LTR-CDME-05-209-P of the Wolf Creek Generating Station (WCGS) Permanent B\* License Amendment Request," September 24, 2007 (Enclosure to WCNOG Letter ET07-0043, dated September 27, 2007).
  - 1-12 NRC Letter, "Wolf Creek Generating Station – Withdrawal of License Amendment Request on Steam Generator Tube Inspections (TAC No. MD1097)," February 28, 2008.
  - 1-13 Steam Generator Integrity Assessment Guidelines, Revision 2, EPRI, Palo Alto, CA, July 2006, 1012987.
  - 1-14 NRC Generic Letter 2004-01, "Requirements for Steam Generator Tube Inspections," August 30, 2004.

a,c,e



**Figure 1-1 Analysis Process for H\***

Table 1-1 List of Conservatisms in the H\* Structural and Leakage Analysis

Assumption/Approach	Why Conservative?
The NEI 97-06 performance criteria, which address tube burst, are applied by equating failure to meet the H* distance with tube burst.	Tube burst cannot occur within the tubesheet (see Section 4.1), thus application of the same criteria designed to prevent tube burst in an area where tube burst cannot occur is inherently conservative. Prevention of tube burst is a necessity for preventing excessive leakage, and accident-induced leakage in the tubesheet expansion region is shown to be limited, independent of the H* distance. Therefore, equating failure to meet H* with tube burst, and application of the same criteria to prevent tube burst to H*, is inherently conservative.
H* distances are based on analysis of the worst tube in the bundle.	The distribution of the contact pressure between the tube and the tubesheet varies as a function of radial position in the tubesheet; <i>the worst-case tube location is used to establish the H* distance</i> (see Section 6.2.3). All other tubes have lower H* values.
Structural support from the divider plate is ignored.	The H* distances for a severely degraded divider plate (no connection between the tubesheet and the divider plate) bound the H* distances for a non-degraded divider plate (see Section 6.2.6).
Residual Contact Pressure Assumed to be Zero.	All pull out tests to date have shown that there is residual contact pressure from the hydraulic expansion; any non-zero value will decrease H* (see Section 7.0 and Appendix A).
Calculation of Pull out Force.	Assumes mean plus 2 sigma tubesheet bore diameter as basis for tube cross-sectional area (see Section 5.3).
Coefficient of Thermal Expansion.	Use of ASME Code mean is conservative relative to test data for both tubesheet and tubing material (see Section 3.5 and Appendix B).
Coefficient of Friction.	Lower bound value of [ ] <sup>a,c,e</sup> is used in the determination of the H* distance (see Section 6.2.2.3.3). Standard reference values suggest a reasonable value of coefficient of friction is [ ] <sup>a,c,e</sup> .
Darcy equation used to model leakage analysis.	The assumed linear relationship between leak rate and differential pressure is conservative relative to alternate models such as Bernoulli or orifice models which assume the leak rate to be proportional to the square root of the pressure differential (see Section 9.1.1 and Reference 9-5 of Section 9.0).

Table 1-1 List of Conservatisms in the H\* Structural and Leakage Analysis (Continued)

Assumption/Approach	Why Conservative?
Use of different plant temperature and pressure conditions for structural and leakage calculations.	<p>The conditions that maximize H* are different from those that maximize leakage conditions. Separate maximizing assumptions are made for structural and leakage analysis (see Section 6.4.5 for the structural analysis assumptions and Section 9.4 for the leakage analysis assumptions).</p> <p>Bounding limit values for the most limiting plant operating pressure and temperatures which include maximum licensed steam generator tube plugging levels (i.e., in numbers of tubes plugged) are used to establish the H* distances for the Model 44F SGs (see Section 5.0).</p> <p>A combination of [ ]<sup>a,c,e</sup> are used for the structural evaluation (see Section 6.2.2.2 and Section 6.2.2.5).</p> <p>[ ]<sup>a,c,e</sup> conditions are used for evaluating the overall leakage factors (to maximize the pressure difference ratio between design basis accident conditions and normal operating conditions) (see Section 9.4).</p>
H* distances based on hot leg temperatures and pressure.	The results described in this report conservatively bound the requirements for both the hot leg and the cold leg in any Model 44F SG (see Section 6.2.2.3).
Stiffening effect of the presence of tubes ignored in the structural analysis.	Equivalent properties of the tubesheet are calculated without taking credit for the stiffening effect in the tubes, which results in a conservatism in the calculations regarding tubesheet deflection (see Section 6.2.1).
Some local interactions between the tube bore and the tube are ignored.	Additional pull out resistance due to tube bending within the tubesheet or Poisson expansion effects on the severed tube end are ignored (see Section 1.3.1).
Peak reactor coolant system pressures and temperatures are assumed to exist during the entire design basis accidents.	Time varying, or transient pressures and temperatures would reduce the pressure and thermal loads on the tube and the tubesheet (see Section 6.2.2).

Table 1-1 List of Conservatism in the H\* Structural and Leakage Analysis (Continued)

Assumption/Approach	Why Conservative?
A [ ] <sup>a,c,e</sup>	This is conservative because it reduces the stiffness of the solid and perforated regions of the tubesheet to the lowest level for each operating condition (see Section 6.2.2.2.2).
Pressure is not applied to the [ ] <sup>a,c,e</sup>	Applying pressure to the [ ] <sup>a,c,e</sup> (see Section 6.2.2.4).
The radius dependent stiffness analysis ignores the presence of the [ ] <sup>a,c,e</sup>	Including these structures in the analysis would reduce the tubesheet displacement and limit the local deformation of the tubesheet hole ID (see Section 6.2.4.4).
The tubesheet bore dilation [ ] <sup>a,c,e</sup>	Thermal expansions under operating loads were [ ] <sup>a,c,e</sup> (see Section 6.2.5).

## **2.0 RESOLUTION OF TECHNICAL ISSUES AND NRC REQUEST FOR ADDITIONAL INFORMATION (RAI) FROM PRIOR H\* SUBMITTALS**

### **2.1 CATEGORIZATION OF TECHNICAL ISSUES AND RESOLUTION ROAD MAP**

The open technical issues identified by the NRC Staff are included in Reference 2-1. Generally, the significant remaining technical issues are in the following categories:

1. Determination of residual contact pressures and variability of residual contact pressure.
2. Adequacy of the existing tube pull out data to justify residual contact pressure when potentially larger values of H\* may be determined.
3. Justification of the mean values and variability of the coefficient of thermal expansion for the tubesheet material (SA508) and the tubing material (A600).
4. Leakage loss coefficient as a function of tube-to-tubesheet contact pressure.
5. Consideration of the potential for incremental tube slippage during pressure and temperature cycles.

Table 2-1 provides a listing of the remaining technical issues related to steam generator (SG) tube inspections based on the H\*/B\* methodology that were identified in Reference 2-1 and a road map to where these issues are addressed within this report. Since the issuance of Reference 2-1, four additional issues have been identified during NRC/Industry meetings. These issues are labeled as A\*\*, B\*\*, C\*\*, and D\*\* and are also resolved in this report.

### **2.2 REVIEW OF PRIOR NRC REQUESTS FOR INFORMATION**

Wolf Creek Nuclear Operating Corporation (WCNOC) submitted a license amendment request on February 21, 2006 (Reference 2-4) proposing changes to the Technical Specifications for the Wolf Creek Generating Station. The proposed changes were to revise the Technical Specification to exclude portions of the SG tube for a distance from the top of the tubesheet in the SGs from periodic tube inspections based on the application of structural analysis and leak rate evaluation results to re-define the primary-to-secondary pressure boundary. The NRC Staff provided an initial Request for Additional Information (RAI) on June 27, 2006 (Reference 2-5). Subsequently, a second NRC Staff RAI was received by WCNOC via electronic mail on June 22, 2007. The second NRC Staff RAI was documented in Reference 2-6. Responses to these two sets of NRC RAI are included in References 2-2 and 2-3.

All previously issued NRC RAI are identified in Table 2-2 below along with a summary of either the resolution of the issues or identification of where the previous NRC RAI are addressed in this report.

**2.3 REFERENCES**

- 2-1 NRC Letter, "Wolf Creek Generating Station – Withdrawal of License Amendment Request on Steam Generator Tube Inspections (TAC No. MD0197)," February 28, 2008.
- 2-2 LTR-CDME-07-72, "Response to NRC Request for Additional Information Relating to LTR-CDME-05-209-P of the Wolf Creek Generating Station (WCGS) Permanent B\* License Amendment Request," Westinghouse Electric Company LLC, Pittsburgh, PA, April 24, 2007 (Enclosure to WCNO Letter WO 07-0012, dated May 3, 2007).
- 2-3 LTR-CDME-07-198, "Response to NRC Request for Additional Information Relating to LTR-CDME-07-72 P-Attachment and LTR-CDME-05-209-P of the Wolf Creek Generating Station (WCGS) Permanent B\* License Amendment Request," Westinghouse Electric Company LLC, Pittsburgh, PA, September 24, 2007 (Enclosure to WCNO Letter ET 07-0043, dated September 27, 2007).
- 2-4 WCNO Letter ET 06-0004, "Revision to Technical Specification 5.5.9, Steam Generator Tube Surveillance Program," February 21, 2006.
- 2-5 NRC Letter, "Wolf Creek Generating Station – Request for Additional Information (RAI) Related to License Amendment Request (LAR) to Revise the Steam Generator Program (TAC No. MD0197)," June 27, 2007.
- 2-6 NRC Letter, "Meeting with Representatives of Wolf Creek Nuclear Operating Corporation for Wolf Creek Generating Station (TAC No. MD0197)," August 7, 2007.

Table 2-1 NRC Technical Issue Response Road Map

Technical Issue No.	Issue Description	Report Section Addressing Technical Issue
1	Contact pressure between the tube and the tubesheet (Need to define method for computing residual contact pressure from pull out tests)	Section 7.1 <sup>(1)</sup>
2		
3	Allowed degree of slippage at tube pull out loads	Appendix A <sup>(2)</sup>
4	Dimensions and yield strength of test specimens	Appendix A <sup>(2)</sup>
5		
6		
7	Pull out test database adequacy for uncertainties	Section 7.2 <sup>(3)</sup>
8		
9		
10	Thermal expansion coefficient values and variability	Section 3.1 and Appendix B
11	Statistical performance standard for H* adequacy	Section 4.1
12	Propagate input uncertainties to H* uncertainties	Section 7.0 and Section 8.0
13	Accuracy of 2-D Finite Element tubesheet model	Sections 6.1.2
14	Error in the unit load FE analyses for SLB	Section 6.1.2.1.5
15	Input random versus systematic uncertainties	Section 8.1.3 and Section 8.2.2
16	Incremental slippage under normal operation and monitoring	Section 9.8
17	Need to assess accident leakage for feedwater line break (Not Applicable to Model 44F SG)	Section 9.2.3
18	Conservatism of "limiting median crevice pressure approach"	Section 6.4.8 and Section 8.1.1
19	Beta factor adjustment to crevice pressure (tubesheet stiffness)	Section 6.2.4
20	Consider assumptions on divider plate condition	Section 6.2.6
A**	Effects of hole dilation on leakage and contact pressure	Section 6.2.5
B**	Thermal expansion coefficient in the radial direction	Section 3.4 and Appendix B
C**	3D-FEA discrepancies with ANL (gap under DBA)	Section 6.4.6
D**	Accident Leakage Integrity	Section 9.2
** Identified based on Industry activities after February 2008		

<sup>(1)</sup> Residual contact pressure conservatively assumed to be zero in this report.

<sup>(2)</sup> Only previous pull out test program results are included in this report. New pull out test results were not available at the time of printing of this report.

<sup>(3)</sup> Residual contact pressure uncertainties are addressed analytically on this report.

Table 2-2 List of NRC RAI on H\* and Resolution Status

RAI No	Source Document for Initial Response: LTR-CDME-07-72 (Reference 2-2)
1	<p>Enclosure 1 of the application, Sections 6.1 and 6.2 - What were the actual yield strengths and wall thicknesses of the tube specimens used for pull out and leakage testing? How do these values compare to minimum values of these parameters at Wolf Creek? Discuss the effect of tube yield strength and wall thickness on contact pressure between the tube and tubesheet after the tube expansion process (i.e., ignoring pressure and temperature loads). Discuss why the test specimen strengths and wall thicknesses were conservative from the standpoint of minimizing the contact pressures between the tube and tubesheet, or discuss what adjustments need to be made to test results to allow for the variability of yield strength and tube wall thickness.</p> <p><u>Issue Resolution Summary:</u></p> <p>Additional tube pull and leakage data for the original test specimens as requested by the NRC Staff is provided in Appendix A of this report. Other than to provide specific information about the test specimens used in the pull out test, additional test data, together with a new structural analysis which involves a fully probabilistic, whole bundle H* depth calculation for each of the Model 44F H* plants obviate the need to compare the original test data yield strengths and tube wall thicknesses with the tubes at Wolf Creek as requested in this RAI. This RAI has been superseded by Item Numbers 4 and 5 of the list of issues that were outstanding when the Wolf Creek Generating Station amendment was withdrawn. The road map for the resolution of these issues is provided in Section 2.1 of this report.</p>
2	<p>Enclosure 1, Section 6.2.1 - The section states that the leak test program utilized tubesheet simulants (collars) with the nominal tubesheet hole diameter. Was this also the case for the pull out tests? What were the diameters of the tube specimens used in the pull out and leakage tests? Discuss the effect that the field tolerances on these parameters can have on contact pressure between the tube and tubesheet after the tube expansion process (i.e., ignoring pressure and temperature loads). Discuss why the parameter values used for the test specimens were conservative from the standpoint of minimizing the contact pressures between the tube and tubesheet, or discuss what adjustments need to be made to test results to allow for the variability of these parameters.</p> <p><u>Issue Resolution Summary:</u></p> <p>In response to the residual technical issues identified by the Staff, the capability to provide residual contact pressure variability as an input to the H* integration model was developed. The mean value of residual contact pressure is based on test data, and the variability around the mean value is determined for each relevant input variable based on analysis (see Section 7.0 of this report). The individual variability distribution for residual contact pressure are combined in the same manner as discussed above for the probabilistic H* determination (see Section 8.0 of this report). It is noted that the reference H* calculation provided in this report assumes residual contact pressure to be zero. Any positive value of residual contact pressure will decrease the final value of H*.</p>
3	<p>Enclosure 1, Section 6.1, page 27 of 127 - Why was the pull out data evaluated at the lower 95th percentile? Discuss how this supports the ability of tubes to sustain pull out loads, versus using an absolute lower bound value? Given the limited number of tests performed (and the many thousands of tubes in the SGs), should not the lower bound value be evaluated to a high confidence value?</p> <p><u>Issue Resolution Summary:</u></p> <p>See the response to NRC RAI 2 above.</p>

Table 2-2 (Continued) List of NRC RAI on H\* and Resolution Status

RAI No	Source Document for Initial Response: LTR-CDME-07-72 (Reference 2-2)
4	<p>Enclosure 1, Section 6.2.1.2 - The section states that the hydraulic expansion pressure was approximately [proprietary information]. Was hydraulic expansion pressure a measured parameter during SG fabrication that was used for acceptance of each joint? Was the lower limit of the acceptance standard the same as the lower limit of the assumed [proprietary information]? If the answer to either of these questions is no, what is the basis for the assumed [proprietary information]?</p> <p><u>Issue Resolution Summary:</u></p> <p>See the response to NRC RAI 2 above.</p>
5	<p>How does pressure and temperature cycling affect the pull out and leakage resistance of the joints? Cite the available data on this topic, and why it is appropriate that the proposed inspection depths need not specifically account for such cycling.</p> <p><u>Issue Resolution Summary:</u></p> <p>This RAI has been superseded by Item Number 16 of the list of issues that were outstanding when the Wolf Creek Generating Station amendment was withdrawn. The road map for the resolution of these issues is provided in Section 2.1 of this report.</p>
6	<p>Pull out resistance per unit length associated with the tube expansion process (residual pull out resistance) was determined on the basis of pull out tests and on the assumption that pull out resistance is uniform along the length of the joint. The axial force in the tube is maximum at the top of the tubesheet and decreases as joint friction incrementally picks up some of the load with increasing distance into the tubesheet. As axial force in the tube declines, with increasing distance in the tubesheet, the Poisson's contraction of the tube diameter decreases causing contact pressure to increase until it reaches a constant value at the location where axial force in the tube has been reduced to zero. At the pull out load, the pull out resistance per unit length near the bottom of the joint will be higher than the average pull out resistance along the entire joint. The pull out resistance over the upper portion of the joint will be less than the average resistance. Referring to Tables 7-6 to 7-10 in Enclosure 1, would not consideration of the actual distribution of the residual pull out resistance as a function of distance below the top of the tubesheet lead to larger H* values than shown on these tables? If not, explain why not.</p> <p><u>Issue Resolution Summary:</u></p> <p>See the response to NRC RAI 2 above.</p>

Table 2-2 (Continued) List of NRC RAI on H\* and Resolution Status

RAI No	Source Document for Initial Response: LTR-CDME-07-72 (Reference 2-2)
7	<p>The models used to develop the H* lengths are complex. Describe how these models have been verified to yield conservative H* values. Have these models been verified by test? For example, how well do these models predict the actual residual pull out loads for joint test samples with typical H* lengths (i.e., provide comparative data)?</p> <p><u>Issue Resolution Summary:</u></p> <p>This RAI has been superseded by Item Number 12 of the list of issues that were outstanding when the Wolf Creek Generating Station amendment was withdrawn. The road map for the resolution of this issue is provided in Section 2.1 of this report.</p>
8	<p>Enclosure 1, Section 6.2.2 - The section states that room temperature leakage tests were performed on all test specimens at test pressures of 1900, 2650, and 3100 pounds per square inch (psi) (presumably applied on the primary side with nothing more than atmospheric pressure at the top of the joint). However, Table 6-2 only presents room temperature data for a differential pressure of 1000 psi. Where is this latter data discussed? Why aren't the room temperature data for the tests described in Section 6.2.2 included in Table 6-2 and Figure 6-6?</p> <p><u>Issue Resolution Summary:</u></p> <p>The response to this NRC RAI is provided for historical purposes only. The original response to this RAI in LTR-CDME-07-72, "Response to NRC Request for Additional Information Relating to LTR-CDME-05-209-P of the Wolf Creek Generating Station (WCGS) Permanent B* License Amendment Request," still applies.</p>
9	<p>Enclosure 1, Section 6.2.2-1 - The section states that the elevated temperature tests were performed following the room temperature tests. Section 6.2.2.2 states that the room temperature tests were performed following the elevated temperature tests. Please clarify this discrepancy.</p> <p><u>Issue Resolution Summary:</u></p> <p>The response to this NRC RAI is provided for historical purposes only. The original response to this RAI in LTR-CDME-07-72, "Response to NRC Request for Additional Information Relating to LTR-CDME-05-209-P of the Wolf Creek Generating Station (WCGS) Permanent B* License Amendment Request," still applies.</p>

Table 2-2 (Continued) List of NRC RAI on H\* and Resolution Status

RAI No	Source Document for Initial Response: LTR-CDME-07-72 (Reference 2-2)
10	<p>Enclosure 1, Section 6.2.2-2 - The section states that a 1900 psi test pressure was used (simulating normal operating pressure) to keep the pressurizing fluid above saturation pressure. As the Staff understands the report, the pressure at the upper end of the test joint is at atmospheric pressure which is not prototypic for normal operating conditions. As the test leakage goes from the bottom of the joint to the top, pressure at some point drops to less than saturation. Why would the test be expected to show as much leakage through the joint as would be the case under prototypic normal operating conditions?</p> <p><u>Issue Resolution Summary:</u></p> <p>The original response to this RAI in LTR-CDME-07-72, "Response to NRC Request for Additional Information Relating to LTR-CDME-05-209-P of the Wolf Creek Generating Station (WCGS) Permanent B* License Amendment Request," still applies. This RAI has been superseded by Item Number 18 of the list of issues that were outstanding when the Wolf Creek Generating Station amendment was withdrawn. The road map for the resolution of this issue is provided in Section 2.1 of this report.</p>
11	<p>The plot of Model F loss coefficient versus contact pressure in Figure 6-6 of Enclosure 1 exhibits a higher slope than is the case for Model D5. The difference appears attributable to lower loss coefficients at lower contact pressures for Model F than for Model D5. Discuss the differences between the Model F and D5 SG designs that explain their different behaviors. If no significant design differences can be identified, discuss the credibility of the loss coefficient data.</p> <p><u>Issue Resolution Summary:</u></p> <p>This RAI has been superseded by Item Number D** of the list of issues that remain outstanding when the Wolf Creek Generating Station amendment was withdrawn and as a result of industry activities after February 2008. The road map for the resolution of this issue is provided in Section 2.1 of this report.</p>
12	<p>Enclosure 1, Section 6.2.2.1 - The section states that the leak test results averaged 16 drops per minute (dpm) per joint at 1900 psi compared to 59 dpm at higher pressures. This is a factor of 3.7 difference. Discuss why this difference is so high compared to the factor of 2 which, under the bellwether principle, is assumed to bound the increase in leakage going from normal operating to accident conditions.</p> <p><u>Issue Resolution Summary:</u></p> <p>The response to this NRC RAI is provided for historical purposes only. The original response to this RAI in LTR-CDME-07-72, "Response to NRC Request for Additional Information Relating to LTR-CDME-05-209-P of the Wolf Creek Generating Station (WCGS) Permanent B* License Amendment Request," still applies.</p>

Table 2-2 (Continued) List of NRC RAI on H\* and Resolution Status

RAI No	Source Document for Initial Response: LTR-CDME-07-72 (Reference 2-2)
13	<p>Enclosure 1, Section 7.1.2, page 45 of 127: Was the primary pressure unit load applied only to the primary face of the tubesheet, and not to the side of the tubesheet bore holes? Was the secondary pressure unit load applied only to the secondary face of the tubesheet, and not to the side of the tubesheet bore holes? Was the tube end cap pressure load (due to primary and secondary pressures) included in the finite element analyses?</p> <p><u>Issue Resolution Summary:</u></p> <p>The response to this NRC RAI is provided for historical purposes only. The original response to this RAI in LTR-CDME-07-72, "Response to NRC Request for Additional Information Relating to LTR-CDME-05-209-P of the Wolf Creek Generating Station (WCGS) Permanent B* License Amendment Request," still applies. This RAI has been superseded by Item Number 19 of the list of issues that were outstanding when the Wolf Creek Generating Station amendment was withdrawn. The road map for the resolution of this issue is provided in Section 2.1 of this report.</p>
14	<p>Enclosure 1, Section 7.1.2, page 45 of 127: The 500 of unit loads represent which of the following; heating up from 70 to 500 °F, or from 70 to 570 °F? If the former, why isn't 70 °F subtracted from 500 °F in the radial deflection scaling factors in Section 7.1.3 (page 46 of 127)?</p> <p><u>Issue Resolution Summary:</u></p> <p>The response to this NRC RAI is provided for historical purposes only. The original response to this RAI in LTR-CDME-07-72, "Response to NRC Request for Additional Information Relating to LTR-CDME-05-209-P of the Wolf Creek Generating Station (WCGS) Permanent B* License Amendment Request," still applies.</p>
15	<p>Enclosure 1: Regarding the equation for <math>\Delta R_{prTS}</math> top of page 48 of 127, should not <math>P_i</math> be <math>P_o</math> consistent with the last equation appearing on page 48? If not, why not?</p> <p><u>Issue Resolution Summary:</u></p> <p>The response to this NRC RAI is provided for historical purposes only. The original response to this RAI in LTR-CDME-07-72, "Response to NRC Request for Additional Information Relating to LTR-CDME-05-209-P of the Wolf Creek Generating Station (WCGS) Permanent B* License Amendment Request," still applies.</p>

**Table 2-2 (Continued) List of NRC RAI on H\* and Resolution Status**

RAI No	Source Document for Initial Response: LTR-CDME-07-72 (Reference 2-2)
16	<p>Enclosure 1, Section 7.1.3 - The tube inside and outside radii within the tubesheet after expansion shown on page 49 of 127 appear not to be entirely consistent with the numbers on page 44 of 127. Explain this inconsistency or, alternatively, show that this inconsistency does not significantly affect the outcome of the overall analysis.</p> <p><u>Issue Resolution Summary:</u></p> <p>The response to this NRC RAI is provided for historical purposes only. The original response to this RAI in LTR-CDME-07-72, "Response to NRC Request for Additional Information Relating to LTR-CDME-05-209-P of the Wolf Creek Generating Station (WCGS) Permanent B* License Amendment Request," still applies.</p>
17	<p>Enclosure 1, Section 7.1.4 - Near the top of page 50 of 127, it is stated that the secondary pressure is conservatively assumed to act on the outside of the tube and the inside of the tubesheet hole. The Staff agrees that this is conservative from the standpoint of maximizing leakage under normal operating conditions, but is concerned that it may be non-conservative from the standpoint of determining conservative ratios of accident leakage to normal operating leakage. Wouldn't the assumption of no secondary pressure yield a lesser value of normal operating leakage, leading to a higher ratio of accident to normal operating leakage? What is the basis for describing the assumption on secondary pressure as conservative?</p> <p><u>Issue Resolution Summary:</u></p> <p>This RAI has been superseded by Item Numbers 18, 19 and D** of the list of issues that remain outstanding when the Wolf Creek Generating Station amendment was withdrawn and as a result of industry activities after February 2008. The road map for the resolution of these issues is provided in Section 2.1 of this report.</p>
18	<p>Enclosure 1, Section 8.2 - The ligament tearing discussion in Section 8.2 (starting on page 75 of 127) only addresses circumferential cracks. Please provide corresponding discussion for axial cracks.</p> <p><u>Issue Resolution Summary:</u></p> <p>The original response to this RAI in LTR-CDME-07-72, "Response to NRC Request for Additional Information Relating to LTR-CDME-05-209-P of the Wolf Creek Generating Station (WCGS) Permanent B* License Amendment Request," still applies. The original response is also included as Section 9.7.2 of the Final H* Report.</p>

Table 2-2 (Continued) List of NRC RAI on H\* and Resolution Status

RAI No	Source Document for Initial Response: LTR-CDME-07-72 (Reference 2-2)
19	<p>The structural and leakage assessments supporting the proposed technical specification amendment are for tubes with no degradation in the proposed inspection zone. The proposed inspection depths make no allowance for degradation which may occur within this zone prior to the next scheduled inspection. Assess the potential impact of degradation in the inspection zone on (1) contact pressures between the tube and tubesheet, (2) on tube pull out capacity, and (3) on leakage under normal and accident conditions. (Although flaws in this zone will be plugged on detection, this question is relevant to satisfying the tube integrity performance criteria with respect to condition monitoring and operational assessments.) This assessment should address potential axial and circumferential stress corrosion cracks (SCC) and volumetric intergranular attack (IGA) flaws.</p> <p><u>Issue Resolution Summary:</u></p> <p>The original response to this RAI in LTR-CDME-07-72, "Response to NRC Request for Additional Information Relating to LTR-CDME-05-209-P of the Wolf Creek Generating Station (WCGS) Permanent B* License Amendment Request," still applies.</p>
20	<p>Describe the methodology to be employed for performing condition monitoring and operational assessments for the tubesheet inspection zone (for pull out and accident leakage) assuming that SCC and or IGA mechanisms have started to be active.</p> <p><u>Issue Resolution Summary:</u></p> <p>The original response to this RAI in LTR-CDME-07-72, "Response to NRC Request for Additional Information Relating to LTR-CDME-05-209-P of the Wolf Creek Generating Station (WCGS) Permanent B* License Amendment Request," still applies.</p>
21	<p>Enclosure 1: The development of the B* distances assumes that crack leakage resistance is not significant relative to the tube-to-tubesheet joint resistance. Discuss the conservatism of the B* distances given the assumption that crack leakage resistance is the dominant resistance to leakage under normal operating conditions. To the extent this discussion relies on assumptions about contact pressure between the tube and tubesheet local to the crack, justify assumptions relative to the influence of the crack on local contact pressure.</p> <p><u>Issue Resolution Summary:</u></p> <p>The response to this NRC RAI is provided for historical purposes only. The original response to this RAI in LTR-CDME-07-72, "Response to NRC Request for Additional Information Relating to LTR-CDME-05-209-P of the Wolf Creek Generating Station (WCGS) Permanent B* License Amendment Request," still applies.</p>

**Table 2-2 (Continued) List of NRC RAI on H\* and Resolution Status**

RAI No	Source Document for Initial Response: LTR-CDME-07-72 (Reference 2-2)
22	<p>Describe the methodology for performing condition monitoring and operational assessments for accident induced leakage stemming from locations below the specified tubesheet inspection depths.</p> <p><u>Issue Resolution Summary:</u></p> <p>This RAI has been superseded by Item Number D** of the list of issues that remain outstanding when the Wolf Creek Generating Station amendment was withdrawn and as a result of industry activities after February 2008. The road map for the resolution of this issue is provided in Section 2.1 of this report.</p>
23	<p>By letter dated March 28, 2006, you provided revisions to your proposed technical specifications (TS) in accordance with TSTF-449, Rev. 4, to include the following additional sentence into TS 5.5.9 c.1:</p> <p>"All tubes with degradation identified in the portion of the tube within the region from the top of the hot leg tubesheet to 17 inches below the top of the tubesheet shall be removed from service."</p> <p>Describe your plans for revising these words to reflect the February 21, 2006 license amendment and for submitting revisions to this amendment.</p> <p><u>Issue Resolution Summary:</u></p> <p>This RAI does not apply to the Model 44F H* plants going forward.</p>

Table 2-2 (Continued) List of NRC RAI on H\* and Resolution Status

RAI No	Source Document for Initial Response: LTR-CDME-07-72 (Reference 2-2)
24	<p>Discuss your plans to revise TS 5.6.10 to include reporting requirements applicable to the implementation of the tubesheet inspection and alternate repair criteria. For example:</p> <p>*A breakout of indications detected within the tubesheet inspection depths with respect to their location, orientation, and measured size. (The only difference here relative to proposed changes associated with Technical Specification Task Force (TSTF) 449, Revision 4, is that the indications in the tubesheet region would be listed separately from those elsewhere.)</p> <p>*The operational primary to secondary leakage rate observed in each steam generator during the cycle preceding the inspection which is the subject of the report, and (2) the calculated accident leakage rate for each steam generator from the portion of tubing below the tubesheet inspection depths for the most limiting accident. If the calculated accident leakage rate for any steam generator is less than 2 times the total observed operational primary to secondary leakage rate, the 12-month report should describe how it was determined.</p> <p><u>Issue Resolution Summary:</u></p> <p>Proposed changes to the technical specification for the steam generator tube inspection report are provided by the utility as part of the license amendment request.</p>
25	<p>Enclosure 1, Section 7.1.3, page 46 of 127: The tubesheet bow analysis takes credit for resistance against bow provided by the divider plate. Cracks in the welds connecting the tubesheet and divider plate have been found by inspection at certain foreign steam generators. Describe what actions you are taking to ensure that the divider plates can perform their function, including providing the assumed resistance against tubesheet bow.</p> <p><u>Issue Resolution Summary:</u></p> <p>This RAI has been superseded by Item Number 20 of the list of issues that remain outstanding when the Wolf Creek Generating Station amendment was withdrawn and as a result of industry activities after February 2008. The road map for the resolution of this issue is provided in Section 2.1 of this report.</p>

Table 2-2 (Continued) List of NRC RAI on H\* and Resolution Status

RAI No	Source Document for Initial Response: LTR-CDME-07-198 (Reference 2-3)
1	<p>Reference 1, Enclosure I, Table 6-4 - Are the listed F/L, force per length, values correct? If so, please describe in detail how they were calculated. If not correct, please provide all necessary revisions to the H* analysis results. [For Byron 2, Braidwood 2, and Seabrook, F/L is calculated as follows:</p> $F/L = (\text{Pull Force}/\text{specimen length}) \times (\text{net contact pressure}/\text{total contact pressure})$ <p>A consistent approach for Wolf Creek (based on allowing 0.25 inch slip) would yield F/L values on the order of 200 pounds per inch (lb/inch) rather than 563 lb/inch as shown in the Table.]</p> <p><u>Issue Resolution Summary:</u></p> <p>In response to the residual technical issues identified by the Staff, the capability to provide residual contact pressure variability as an input to the H* integration model was developed. The mean value of residual contact pressure is based on test data, and the variability around the mean value is determined for each relevant input variable based on analysis (see Section 7.0 of this report). The individual variability distribution for residual contact pressure are combined in the same manner as discussed above for the probabilistic H* determination (see Section 8.0 of this report). It is noted that the reference H* calculation provided in this report assumes residual contact pressure to be zero. Any positive value of residual contact pressure will decrease the final value of H*.</p> <p>This RAI has been superseded by Item Numbers 1 and 2 of the list of issues that remain outstanding when the Wolf Creek Generating Station amendment was withdrawn and as a result of industry activities after February 2008. The road map for the resolution of these issues is provided in Section 2.1 of this report.</p>

Table 2-2 (Continued) List of NRC RAI on H\* and Resolution Status

RAI No	Source Document for Initial Response: LTR-CDME-07-198 (Reference 2-3)
2	<p>Reference 2, Enclosure I, Response to RAI questions 1 and 2 - provides the sensitivity of contact pressure to many of the material and geometric parameters used in the analyses. The response provides only a qualitative assessment of these sensitivities to support the conclusion that the values assumed in the H* analyses support a conservative calculation of H*. For example, the sensitivity study showed that contact pressure is sensitive to the yield strength of the tubing. The response states that the yield strength of the tubing used in the pull out test specimens was higher than the documented mean yield strength for prototypical tubing material, but did not indicate to what extent the yield strength of the test material bounds the range of prototypic yield strength variability. Thus, the Staff has no basis to agree or disagree with the conclusion that test specimen contact pressures are conservatively low. The steam generators contain up to 5620 tubes, and it needs to be demonstrated that the computed H* distances are conservative for all the tubes, not simply the average tubes or 95% of the tubes. Please provide a quantitative assessment demonstrating that the assumed values of the material and geometric parameters support a conservative H* analysis for all tubes. This assessment should consider thermal expansion coefficient (TEC) for the tube and tubesheet in addition to the parameters included in the Reference 2 response.</p> <p><u>Issue Resolution Summary:</u></p> <p>This RAI has been superseded by Item Number 9 of the list of issues that remain outstanding when the Wolf Creek Generating Station amendment was withdrawn and as a result of industry activities after February 2008. The road map for the resolution of this issue is provided in Section 2.1 of this report.</p>
3	<p>The H* analyses in References 1 and 2 are based, in part, on pull out resistance associated directly with hydraulic expansion process. This pull out resistance was determined by subtracting out the effects of differential thermal expansion between the tube and tubesheet test collar from the measured pull out load. The calculated differential thermal expansion effect was based, in part, on an assumed TEC value of 7.42E-06 in/in/°F for the 1018 steel tubesheet test collar. What is the impact of considering an alternative TEC value of 7E-06 in/in/°F (from Matweb.com for 1018 steel interpolated at 600 degrees Fahrenheit) on the computed pull out force determined from the pull out test and on the computed H* distances?</p> <p><u>Issue Resolution Summary:</u></p> <p>This RAI has been superseded by Item Number 12 of the list of issues that remain outstanding when the Wolf Creek Generating Station amendment was withdrawn and as a result of industry activities after February 2008. The road map for the resolution of this issue is provided in Section 2.1 of this report.</p>

**Table 2-2 (Continued) List of NRC RAI on H\* and Resolution Status**

RAI No	Source Document for Initial Response: LTR-CDME-07-198 (Reference 2-3)
4	<p>Reference 2, Enclosure I, Response to RAI question 7 - The Model D5 steam generator (SG) pull out data in Table 2 indicate that pull out force increases with temperature for the 3-inch long specimens and decreases with temperature for the 6-inch long specimens. For the 4-inch specimens, pull out force increases with temperature to 400°F and decreases with temperature beyond that point. Discuss the reasons for this apparent discrepancy in trends among the data. Discuss whether the reduction in tube yield strength with temperature might be sufficient for some specimens to limit any increase in contact pressure associated with differential thermal expansion between the tube and tubesheet.</p> <p><u>Issue Resolution Summary:</u></p> <p>In response to the residual technical issues identified by the Staff, the capability to provide residual contact pressure variability as an input to the H* integration model was developed. The mean value of residual contact pressure is based on test data, and the variability around the mean value is determined for each relevant input variable based on analysis (see Section 7.0 of this report). The individual variability distribution for residual contact pressure are combined in the same manner as discussed above for the probabilistic H* determination (see Section 8.0 of this report). It is noted that the reference H* calculation provided in this report assumes residual contact pressure to be zero. Any positive value of residual contact pressure will decrease the final value of H*.</p>
5	<p>Following up on question 4 above, is there a possibility that any tubes could be stressed beyond the compressive yield strength (at temperature) of the tube material due to differential thermal expansion, internal pressure, and tubesheet hole dilation for the range of yield strengths in the field? Describe the basis for either yes or no to this question. If yes, how has this been factored into the contact pressures, accumulated pull out resistance load as a function of elevation, and H* in Tables 7-6 through 7-10 and 7-6a through 7-10a of Reference 2, Enclosure I?</p> <p><u>Issue Resolution Summary:</u></p> <p>The original response to this RAI in LTR-CDME-07-198, "Response to NRC Request for Additional Information Relating to LTR-CDME-07-72 P-Attachment and LTR-CDME-05-209-P of the Wolf Creek Generating Station (WCGS) Permanent B* License Amendment Request," still applies.</p>

Table 2-2 (Continued) List of NRC RAI on H\* and Resolution Status

RAI No	Source Document for Initial Response: LTR-CDME-07-198 (Reference 2-3)
6	<p>Reference 2, Enclosure I, Response to RAI question 17 - The response states near the bottom of page 30 of 84 that Case 1 results shown in Table 3.0 are for the limiting cold leg analysis and reflect the following assumption: "Although the pull out test data indicated positive residual mechanical joint strength, the residual joint strength is ignored for SLB [steam line break] accident condition[s] to conservatively account for postulated variability of the coefficient of thermal expansion." The NRC Staff notes, however, that the limiting H* value shown in Table 3.0 for Case 1 is that necessary to resist three times the normal operating pressure end cap load, not that needed to resist 1.4 times SLB. It is the Staff's understanding based on review of Tables 7-6 through 7-10 and 7-6a through 7-10a that the residual mechanical joint strength (522 lb/inch) was reflected in the H* computations for normal operating and accident conditions, including SLB. Discuss and clarify these apparent discrepancies.</p> <p><u>Issue Resolution Summary:</u></p> <p>A new structural analysis which involves a fully probabilistic, whole bundle H* depth calculation for each of the Model 44F H* plants obviates the need to address the sub-parts of this RAI.</p>
7	<p>Reference 2, Enclosure I, Table 7-6 - This table states that the required pull out force is 1680 lb. Table 7-6 indicates that for a tubesheet radius of 12 inches the needed depth of engagement is less than 10.52 (about 10.2 using linear interpolation). However, the table states that an engagement depth slightly greater than 10.52 (i.e., 10.54) is needed. Discuss and explain this apparent (minor) discrepancy.</p> <p><u>Issue Resolution Summary:</u></p> <p>A new structural analysis which involves a fully probabilistic, whole bundle H* depth calculation for each of the Model 44F H* plants obviates the need to address this RAI.</p>

Table 2-2 (Continued) List of NRC RAI on H\* and Resolution Status

RAI No	Source Document for Initial Response: LTR-CDME-07-198 (Reference 2-3)
8	<p>Reference 1, Enclosure I, Table 6-4 - The listed F/L values are based on allowing 0.25 inch slippage. Reference 1 does not address the potential for limited, but progressive incremental slippage under heatup/cooldown and other operational load cycles. Nor does Reference 1 address the effects of slippage on normal operating leakage and on accident-induced leakage or the ratio of normal operating and accident induced leakage. The response to RAI question 5 in Reference 2, Enclosure I, does not provide any further insight into this issue. That response specifically addressed test results for tubes with a hard roll expansion, and the Staff believes that the slippage versus axial load characteristics for such an expansion may be entirely different than for a hydraulic expansion. Discuss and address the potential for progressive incremental slippage under heatup/cooldown and other operational load cycles. In addition, address the potential for slippage under operational and accident conditions to affect the ratio of accident-induced leakage to operational leakage.</p> <p><u>Issue Resolution Summary:</u></p> <p>This RAI has been superseded by Item Number 16 of the list of issues that remain outstanding when the Wolf Creek Generating Station amendment was withdrawn and as a result of industry activities after February 2008. The road map for the resolution of this issue is provided in Section 2.1 of this report.</p>
9	<p>Discuss your plans for revising the proposed technical specification (TS) amendment to monitor the tube expansion transition locations relative to the top of the tubesheet to ensure that the tubes are not undergoing progressive, incremental slippage between inspections.</p> <p><u>Issue Resolution Summary:</u></p> <p>This RAI has been superseded by Item Number 16 of the list of issues that remain outstanding when the Wolf Creek Generating Station amendment was withdrawn and as a result of industry activities after February 2008. The road map for the resolution of this issue is provided in Section 2.1 of this report.</p>

Table 2-2 (Continued) List of NRC RAI on H\* and Resolution Status

RAI No	Source Document for Initial Response: LTR-CDME-07-198 (Reference 2-3)
10	<p>Reference 1, Enclosure I, Section 7.1.4.2 - This section provides a brief discussion of SLB, feed line break (FLB), and loss-of-coolant accident (LOCA) in terms of which is the most limiting accident in terms of tube pull out potential. Expand this discussion to indicate whether SLB and FLB are the most limiting accidents among the universe of design basis accidents (DBA) (or other faulted conditions in the design basis) in terms of both tube pull out, and the margin between the calculated accident-induced tube leakage for each DBA and the assumed accident-induced tube leakage in the safety analysis for that DBA.</p> <p><u>Issue Resolution Summary:</u></p> <p>This RAI has been superseded by Item Numbers 17, A** and D** of the list of issues that remain outstanding when the Wolf Creek Generating Station amendment was withdrawn and as a result of industry activities after February 2008. The road map for the resolution of these issues is provided in Section 2.1 of this report.</p>
11	<p>Figure 11 of Reference 2, Enclosure I contains loss coefficient data for Model F SG tubing that was not included in Figure 6-6 of Reference 1, Enclosure 1. This data was for contact pressures ranging from about 1200 psi to about 2000 psi. Why was this data not included in Figure 6-6? Discuss if this is this because of low expansion pressures and if the data that is not included in Figure 6-6 is room temperature data. [If yes, then the NRC Staff observes that the room temperature loss coefficients for the Model F specimens are relatively invariant with contact pressure above a contact pressure threshold of around 700 psi. The 600 degree F data is also invariant with contact pressure. Thus, loss coefficient may not be a direct function of contact pressure once a threshold degree of contact pressure is established. The difference in loss coefficient data between the 600°F data and the room temperature may be due to parameter(s) other than contact pressure. This other parameter(s) may not be directly considered in the B* analysis.]</p> <p><u>Issue Resolution Summary:</u></p> <p>This RAI has been superseded by Item Numbers 17, A** and D** of the list of issues that remain outstanding when the Wolf Creek Generating Station amendment was withdrawn and as a result of industry activities after February 2008. The road map for the resolution of these issues is provided in Section 2.1 of this report.</p>

Table 2-2 (Continued) List of NRC RAI on H\* and Resolution Status

RAI No	Source Document for Initial Response: LTR-CDME-07-198 (Reference 2-3)
12	<p>Figure 13 of Reference 2, Enclosure I contains additional loss coefficient data taken from the crevice pressure study in the white paper. Provide a figure showing all individual data points from which Figure 13 was developed. Describe the specific applied pressure differentials from the crevice pressure study used to calculate the contact pressure for each data point.</p> <p><u>Issue Resolution Summary:</u></p> <p>This RAI has been superseded by Item Numbers 17, A** and D** of the list of issues that remain outstanding when the Wolf Creek Generating Station amendment was withdrawn and as a result of industry activities after February 2008. The road map for the resolution of these issues is provided in Section 2.1 of this report.</p>
13	<p>Although the means of the regression fits of the loss coefficient data for the Model F and Model D SGs are shown in Figure 13 of Reference 2, Enclosure I, to be within a factor of three of each other, the slope and intercept properties remain highly divergent, seeming to cast further doubt that loss coefficient varies with contact pressure (above some threshold value of contact pressure). Discuss this and describe any statistical tests that have been performed to establish the significance of correlation between loss coefficient and contact pressure. In addition, describe any statistical tests that have been performed to confirm that it is appropriate to combine the data sets to establish the slope and intercept properties of loss coefficient versus contact pressure.</p> <p><u>Issue Resolution Summary:</u></p> <p>This RAI has been superseded by Item Numbers 17, A** and D** of the list of issues that remain outstanding when the Wolf Creek Generating Station amendment was withdrawn and as a result of industry activities after February 2008. The road map for the resolution of these issues is provided in Section 2.1 of this report.</p>

Table 2-2 (Continued) List of NRC RAI on H\* and Resolution Status

RAI No	Source Document for Initial Response: LTR-CDME-07-198 (Reference 2-3)
14	<p>Reference 2, Enclosure I, page 25 of 84 - For the case of assumed zero slope of loss coefficient versus contact pressure, two constant loss coefficient values were compared. Does the first assumed value come from Figure 14? If not, provide additional information on where this assumption comes from. If yes, explain the relationship between the assumed value and Figure 14. Does the second assumed value come from Figure 12? If not, provide additional information on where this assumption comes from. If yes, explain the relationship between the assumed value and Figure 12.</p> <p><u>Issue Resolution Summary:</u></p> <p>The response to this NRC RAI is provided for historical purposes only. The original response to this RAI in LTR-CDME-07-198, "Response to NRC Request for Additional Information Relating to LTR-CDME-07-72 P-Attachment and LTR-CDME-05-209-P of the Wolf Creek Generating Station (WCGS) Permanent B* License Amendment Request," still applies.</p>
15	<p>Reference 2, Enclosure I, Figure 15 - clarify the title of Figure 15 in terms of whether it reflects consideration of residual mechanical strength in the joint during an SLB. Is Figure 15 for the hot or cold leg? Explain the following: (1) why the B* values at small tubesheet radii are less than those listed in Reference 1, Enclosure I, Table 11-1 and (2) why the contact pressures shown in Reference 1, Enclosure I, Figures 9-6 and 9-7 are different from those shown in Tables 7-6 and 7-8 of Reference 1, Enclosure I.</p> <p><u>Issue Resolution Summary:</u></p> <p>A new structural analysis which involves a fully probabilistic, whole bundle H* depth calculation for each of the Model 44F H* plants and a new leakage analysis obviate the need to provide a detailed response to this RAI.</p>
16	<p>Reference 2, Enclosure I - Provide a description of the revised finite element model used to support the revised H* calculations in Tables 6-7 through 6-10 and Tables 6-7a through 6-10a. Compare this revised model to the original model which supported the Reference 1 analysis. Explain why the revised model is more realistic than the original model.</p> <p><u>Issue Resolution Summary:</u></p> <p>A new structural analysis which involves a fully probabilistic, whole bundle H* depth calculation for each of the Model 44F H* plants obviates the need to provide a detailed response to this RAI.</p>

Table 2-2 (Continued) List of NRC RAI on H\* and Resolution Status

RAI No	Source Document for Initial Response: LTR-CDME-07-198 (Reference 2-3)
17	<p>Reference 2, Enclosure 1, Attachment 1 (The Westinghouse Letter Summary of Changes to B* and H*), page 14 - address the status of the divider plate evaluation being performed under EPRI sponsorship, and the schedule for completion of the various topics being addressed in the evaluation. Describe any inspections that have been performed domestically that provide insight on whether the extent and severity of divider plate cracks is bounded by the foreign experience. Discuss the available options for inspecting the divider plates.</p> <p><u>Issue Resolution Summary:</u></p> <p>This RAI has been superseded by Item Number 20 of the list of issues that remain outstanding when the Wolf Creek Generating Station amendment was withdrawn and as a result of industry activities after February 2008. The road map for the resolution of this issue is provided in Section 2.1 of this report.</p>
18	<p>Discuss how the ability of the divider plates at Wolf Creek to resist tubesheet deflection (without failure) under operating and accident loads is assured in the short term, pending completion of the EPRI evaluation. Include in this discussion the actions that are planned in the near term to ensure that the divider plates are capable of resisting tubesheet deflection.</p> <p><u>Issue Resolution Summary:</u></p> <p>This RAI has been superseded by Item Number 20 of the list of issues that remain outstanding when the Wolf Creek Generating Station amendment was withdrawn and as a result of industry activities after February 2008. The road map for the resolution of this issue is provided in Section 2.1 of this report.</p>

**Table 2-2 (Continued) List of NRC RAI on H\* and Resolution Status**

RAI No	Source Document for Initial Response: LTR-CDME-07-198 (Reference 2-3)
19	<p>Reference 2, Enclosure 1, Attachment 1 - Provide a description of the Crevice Pressure Test. This description should address, but not necessarily be limited to the following:</p> <ul style="list-style-type: none"> <li>a. Description of test specimens, including sketches.</li> <li>b. Description of "pre-treatments" of test specimens (hydraulic expansion pressure, heat relief, etc.).</li> <li>c. Description of test setup, including sketches.</li> <li>d. Description of test procedure.</li> <li>e. What were the secondary side temperatures in Tables 1 and 2 corresponding to the listed secondary side pressures and how were the secondary side pressure and temperatures controlled and monitored?</li> <li>f. How long did each test run and how stable were the pressure readings at each of the pressure taps during the course of each test?</li> <li>g. What was the temperature of (1) the coolant in the crevice and (2) the tube and tubesheet collar as a function of elevation?</li> <li>h. How were the temperature distributions for item g determined? Were direct temperature measurements of the tubesheet collar performed as a function of elevation?</li> </ul> <p><u>Issue Resolution Summary:</u></p> <p>The original response to this RAI in LTR-CDME-07-198, "Response to NRC Request for Additional Information Relating to LTR-CDME-07-72 P-Attachment and LTR-CDME-05-209-P of the Wolf Creek Generating Station (WCGS) Permanent B* License Amendment Request," still applies.</p>

**Table 2-2 (Continued) List of NRC RAI on H\* and Resolution Status**

RAI No	Source Document for Initial Response: LTR-CDME-07-198 (Reference 2-3)
20	<p>Reference 2, Enclosure 1, Attachment 1 - The pressure tap locations in Figure 2 are different from those shown in Figure 3. Discuss and explain this difference or provide corrected figures.</p> <p><u>Issue Resolution Summary:</u></p> <p>The original response to this RAI in LTR-CDME-07-198, "Response to NRC Request for Additional Information Relating to LTR-CDME-07-72 P-Attachment and LTR-CDME-05-209-P of the Wolf Creek Generating Station (WCGS) Permanent B* License Amendment Request," still applies.</p>
21	<p>Reference 2, Enclosure 1, Attachment 1 - Figures 2 and 3 assume crevice pressure at the top of tubesheet is at the saturation pressure for the primary system. Discuss and explain the basis for this assumption. Why wouldn't the crevice pressure trend to the secondary side pressure near the top of the tubesheet?</p> <p><u>Issue Resolution Summary:</u></p> <p>The original response to this RAI in LTR-CDME-07-198, "Response to NRC Request for Additional Information Relating to LTR-CDME-07-72 P-Attachment and LTR-CDME-05-209-P of the Wolf Creek Generating Station (WCGS) Permanent B* License Amendment Request," still applies.</p>
22	<p>Reference 2, Enclosure 1, Attachment 1 - Figure 3 refers to tests labeled SLB 9 and SLB 10 which are not listed in Table 2. Discuss and explain this, or provide a revised Table 2 and Figure 3 showing all test results.</p> <p><u>Issue Resolution Summary:</u></p> <p>The original response to this RAI in LTR-CDME-07-198, "Response to NRC Request for Additional Information Relating to LTR-CDME-07-72 P-Attachment and LTR-CDME-05-209-P of the Wolf Creek Generating Station (WCGS) Permanent B* License Amendment Request," still applies.</p>

Table 2-2 (Continued) List of NRC RAI on H\* and Resolution Status

RAI No	Source Document for Initial Response: LTR-CDME-07-198 (Reference 2-3)
23	<p>Reference 2, Enclosure 1, Attachment 1 - Page 6 states in part that the following change should be made to the H*/B* analyses: "The driving head of the leaked fluid has been reduced." Discuss and clarify this sentence. The Staff notes that resistance to leakage occurs from two sources: resistance from the flaw and resistance from the crevice. Because the crevice pressure was assumed to be equal to the secondary pressure, the original analysis assumed the entire pressure drop (the driving head) was across the flaw. The tests described in the white paper eliminate any pressure across the flaw (by using holes rather than cracks) and force the entire pressure drop to occur along the crevice. Thus, there is no net change in the total driving head between the primary and secondary sides. In fact, the driving head from the bottom to the top of the crevice would seem to have been increased.</p> <p><u>Issue Resolution Summary:</u></p> <p>A new structural analysis which involves a fully probabilistic, whole bundle H* depth calculation for each of the Model 44F H* plants which applies a depth-based crevice pressure obviates the need to provide a detailed response to this RAI.</p>
24	<p>Reference 2, Enclosure 1, Attachment 1 - The top paragraph on page 10 states, in part, "the median value of the crevice pressure ratios provides a conservative value that is an average representation of the behavior at the top of the tubesheet. The median is typically a better statistical representation of the data than the mean because the median is not influenced by a smaller data set but by the total range in values in the sample set." The Staff has the following questions regarding these sentences:</p> <ol style="list-style-type: none"> <li>Discuss and clarify what data set "median value" applies to. For example, does the "median value" for the NOP data set in Table 1 mean the median value of the 15 pressure tap data points obtained during three tests, or does it mean a median value of a subset of these 15 data points? If a subset, what subset and why? Alternatively, does it mean the median value at each pressure tap location?</li> <li>Discuss why this median value is a conservative representation of the behavior at the top of the tubesheet.</li> <li>Discuss what is meant by "top of the tubesheet." For 17-inch inspection zone amendments, shouldn't this mean the upper 17-inches to ensure a conservative analysis? If not, why not? To ensure a conservative analysis for H* and B*, should not the objective be to establish crevice pressure as a function of elevation that can be directly applied into the H* and B* computations.</li> <li>Discuss why the median is not influenced by a smaller data set and how the median is influenced by the total range of values in the sample set.</li> </ol> <p><u>Issue Resolution Summary</u></p> <p>A new structural analysis which involves a fully probabilistic, whole bundle H* depth calculation for each of the Model 44F H* plants which applies a depth based crevice pressure obviates the need to provide a detailed response to this RAI (see Sections 6.0 and 8.0).</p>

Table 2-2 (Continued) List of NRC RAI on H\* and Resolution Status

RAI No	Source Document for Initial Response: LTR-CDME-07-198 (Reference 2-3)
25	<p>Reference 2, Enclosure 1, Attachment 1 - Provide a copy of Reference 3. The cited web page appears to be no longer available. Also, provide copy of Reference 4.</p> <p><u>Issue Resolution Summary</u></p> <p>The response to this NRC RAI is provided for historical purposes only. The original response to this RAI in LTR-CDME-07-198, "Response to NRC Request for Additional Information Relating to LTR-CDME-07-72 P-Attachment and LTR-CDME-05-209-P of the Wolf Creek Generating Station (WCGS) Permanent B* License Amendment Request," still applies. A new structural analysis which involves a fully probabilistic, whole bundle H* depth calculation for each of the Model 44F H* plants which applies a depth-based crevice pressure obviates the need to provide a detailed response to this RAI.</p>
26	<p>Reference 2, Enclosure 1, Attachment 1 - What were the specific data sets used to compute the Dixon Ratio values at the top of page 11?</p> <p><u>Issue Resolution Summary</u></p> <p>The response to this NRC RAI is provided for historical purposes only. The original response to this RAI in LTR-CDME-07-198, "Response to NRC Request for Additional Information Relating to LTR-CDME-07-72 P-Attachment and LTR-CDME-05-209-P of the Wolf Creek Generating Station (WCGS) Permanent B* License Amendment Request," still applies. A new structural analysis which involves a fully probabilistic, whole bundle H* depth calculation for each of the Model 44F H* plants which applies a depth-based crevice pressure obviates the need to provide a detailed response to this RAI.</p>
27	<p>Reference 2, Enclosure 1, Attachment 1 - In Table 5 under the heading of outliers, rows 1 and 2 refer to "total set," whereas lines 3 and 4 refer to "included." Does "included" mean the same thing as "total set." If not, how does it differ from "total set," and how does it differ from "excluded?"</p> <p><u>Issue Resolution Summary</u></p> <p>The response to this NRC RAI is provided for historical purposes only. The original response to this RAI in LTR-CDME-07-198, "Response to NRC Request for Additional Information Relating to LTR-CDME-07-72 P-Attachment and LTR-CDME-05-209-P of the Wolf Creek Generating Station (WCGS) Permanent B* License Amendment Request," still applies. A new structural analysis which involves a fully probabilistic, whole bundle H* depth calculation for each of the Model 44F H* plants which applies a depth-based crevice pressure obviates the need to provide a detailed response to this RAI.</p>

Table 2-2 (Continued) List of NRC RAI on H\* and Resolution Status

RAI No	Source Document for Initial Response: LTR-CDME-07-198 (Reference 2-3)
28	<p>Reference 2, Enclosure 1, Attachment 1 - Provide a step-by-step description (including an example) of how the values in Table 5 were obtained.</p> <p><u>Issue Resolution Summary</u></p> <p>The response to this NRC RAI is provided for historical purposes only. The original response to this RAI in LTR-CDME-07-198, "Response to NRC Request for Additional Information Relating to LTR-CDME-07-72 P-Attachment and LTR-CDME-05-209-P of the Wolf Creek Generating Station (WCGS) Permanent B* License Amendment Request," still applies. A new structural analysis which involves a fully probabilistic, whole bundle H* depth calculation for each of the Model 44F H* plants which applies a depth-based crevice pressure obviates the need to provide a detailed response to this RAI.</p>
29	<p>Reference 2, Enclosure 1, Attachment 1 - Confirm that the "unaltered" case in Table 5 reflects the use of the improved tubesheet/divider plate model with a "divider plate factor" of 0.399.</p> <p><u>Issue Resolution Summary</u></p> <p>The response to this NRC RAI is provided for historical purposes only. The original response to this RAI in LTR-CDME-07-198, "Response to NRC Request for Additional Information Relating to LTR-CDME-07-72 P-Attachment and LTR-CDME-05-209-P of the Wolf Creek Generating Station (WCGS) Permanent B* License Amendment Request," still applies. A new structural analysis which involves a fully probabilistic, whole bundle H* depth calculation for each of the Model 44F H* plants which applies a depth-based crevice pressure obviates the need to provide a detailed response to this RAI.</p>

### 3.0 TEST PROGRAM IN SUPPORT OF H\*

Following the withdrawal by Wolf Creek Nuclear Operating Corporation of its License Amendment Request (Reference 3-1), the NRC Staff issued a summary (Reference 3-2) of its technical concerns regarding the technical justification of H\* (References 3-3, 3-4 and 3-5). The issues noted in Reference 3-2 that dealt with coefficient of thermal expansion and residual contact pressure (the interaction between the tubesheet and tube resulting from only the hydraulic expansion) were addressed by test programs during 2008 and 2009. The following sections describe the tests that were performed in support of the H\* technical justification.

#### 3.1 COEFFICIENT OF THERMAL EXPANSION (CTE) OF ALLOY 600 AND SA508 STEEL

The strength of the hydraulically expanded tube-to-tubesheet joint in a steam generator (SG) is due, in large part, to the difference of thermal expansion between the tube and the tubesheet. The tube, which is made of A600, expands more at a given temperature than does the tubesheet, which is made of A508 material, resulting in mechanical interference between the two.

In 2007, the NRC Staff provided data that suggested that there may be cases where the thermal expansion mismatch between the tube and the tubesheet do not follow the expected behavior, i.e., the tubesheet may expand more at a given temperature than the tube, resulting in loss of contact pressure between the tube and the tubesheet at elevated temperature. Because the technical basis of H\* (tube pull out) is significantly dependent on differential thermal expansion between the tube and the tubesheet, the Staff provided the following summary of the outstanding issue (Item No. 10 from Reference 3-2):

– *The [H\* report of record] report considered two different nominal values of thermal expansion coefficient (TEC) for alloy 600 tubing and two different nominal values for the A508 tubesheets. The nominal TEC values are based on (1) nominal ASME Code values for both the tube and tubesheet and (2) data from ANTER Laboratories Inc. for both the tube and tubesheet. TEC variability relative to these nominal values was assumed to have a standard deviation of 1.5% based on reported measurement uncertainty associated with the ANTER data. However, the report provided no evidence that either TEC model (i.e., that based on Code values versus that based on the ANTER data) captures the range of TEC values that may be encountered in the field. In addition, recent TEC data from PMIC indicate smaller TEC differences between the tube and tubesheet materials than is indicated by either of the above TEC models, thus adding to the Staff's concern as whether either TEC model captures the range of TEC values which may exist in the field. A more complete technical justification for the TEC model is needed in terms of its ability to capture the range of TEC differences between the tube and tubesheet that may be encountered in the field. This technical justification should address, but not necessarily be limited to the following:*

- a. *Literature search for relevant TEC data, and evaluation of that data. If the PMIC data is considered not relevant, what is the basis? Apart from the American Society of Mechanical Engineers (ASME) Code vetting process, is there any reason to believe that the pedigree of the PMIC data (or ANTER data) is not as good as the data upon which the Code values are based? What is the feasibility of subjecting the PMIC and ANTER data to a review similar to that performed as part of the Code vetting process?*

- b. *Expert opinion and experience on the variability of TEC that may be exhibited by materials such as alloy 600 and A508 steel that may have fabricated from different heats of material, at different times, and with different processing histories (e.g., mill annealed versus thermally-treated alloy 600, temperatures experienced during post weld heat relief).*
- c. *Expert opinion and experience on potential changes to alloy 600 TEC due to hydraulic expansion process. Data concerning sensitivity of TEC to cold working for metals in general needs to be provided.*

### 3.1.1 Review of Industry Data

In response to the issue summarized in Reference 3-2, industry experts were consulted and a literature search was performed to: (1) identify the sources of coefficient of thermal expansion (CTE) data, and in particular, the sources of the CTE contained in the ASME Code, (2) determine how the Code mean value for CTE was derived and (3) determine what the statistical interpretation of the 10% variability noted on the Code should be. Further, the data provided by the NRC Staff was reviewed to determine the material pedigree, the handling history of the material, the test process and the analysis of the test data. A summary report was prepared which is included in this report as Appendix B. Generally, one of the data points provided by the Staff (referred to as the ANTER data) was found to be reasonably consistent with the available industry data. However, the second data point for SA508 material (referred to as the PMIC data) was found to have deficiencies in the material temperature exposure history and in the test process and was, therefore, not included in the final evaluation for the mean value and variability of CTE. Appendix B of this report provides the details of the data literature search, the results of the analysis, and a rationale for not including the PMIC data. The discussion in Appendix B includes the additional data from a test program discussed in the following section.

## 3.2 CTE TESTS

Because the body of available industry data on CTE of SA508 and A600 was limited, a test program was completed to acquire CTE data for both A508 and A600 material for conditions specifically of interest to H\*. This test program was intended to determine whether the ASME Code reasonably represents the mean CTE values of these materials, and to characterize the statistical variability of CTE for these materials. The ASME Code (Reference 3-6) provides mean values of the CTE and a general statement that the values could vary by +/-10%. Because a probability statement is required for H\*, specification of a broad range of variability without a statistical interpretation was unacceptable.

### 3.2.1 Description of the CTE Tests

#### 3.2.1.1 Materials

##### SA508

Two grades and four heats of A508 pressure vessel steel were tested under this program: SA-508 Grade 3 Class 1 (Heat 03D958-1-6), SA-508 Grade 3 Class 2 (Heats 97D28-1-1, 97B80-1-11, and 97D258-1-1). These materials were provided in block form by Babcock and Wilcox Canada. The chemical

certifications of these materials are contained in Table 3-1, and their mechanical property certifications are contained in Table 3-2.

### Alloy 600

Nine tubes of A600 thermally-treated material, each approximately twelve inches long, were used to perform the CTE measurements on A600 material. Three different heats of material were tested for each of the three sizes of SG tube under consideration (Model F – 0.688 inch dia, Model D5 – 0.750 inch dia., and Model 44F and 51F – 0.875 inch dia.). The Model F SG tubes were represented by Heats NX0419, NX9749, and NX9821, the Model D5 SG tubes were represented by Heats NX1002, NX1019, and NX1145, and the Model 44F/51F SG tubes were represented by Heats NX9180, NX9292, and NX1518. All of these heats of material are from archive samples of tubing heats that were included in production SGs.

The matrix of the tubes with their corresponding heats and nominal outer diameter is contained in Table 3-3, while the chemical and mechanical property certifications are contained in Tables 3-4 and 3-5, respectively.

#### **3.2.1.2 Sample Preparation**

Each block of A508 material was cut into specimens that were 0.25 inch x 0.25 inch x 2 inches long rectangular prisms. The cutting process utilized was a water cooled cut-off wheel to avoid excessive local heating of the material and to provide lubrication.

The tubes of A600 material were first cut in half lengthwise; one half was used for the non-strain hardened CTE measurements, and the other half was saved for the strain hardened part of the test program. The first half of each of the tubes was subsequently cut into strips whose chord length was 0.25 inch and whose length was 2 inch. The length dimension was parallel to the axis of the original tube.

In order to strain harden the tube, the tubes were hydraulically expanded at a nominal pressure of 31,000 psi into split collars made of 1018 carbon steel, which were designed to simulate the stiffness of the tubesheet based on the results of Middlebrooks et al. (Reference 3-7). Specifically, the collars were manufactured so that a ratio between the outer diameter of the tubesheet and the outer diameter of the tube were kept to 2.42 as closely as possible. Drawings of the split collars for each of the SG models used in the current test program are shown in Figures 3-1 through 3-3. The dimensions are such that the ratio of 2.42 was maintained between the center hole and the upper/lower surface of the block, between the center hole and the bolt hole (horizontally), and between the center hole and the counter bore of the bolt hole. The resulting radial strain on the material was approximately 3%. These tubes were then cut in the same manner as the non-strain hardened tube with the exception that care was taken to make sure that all of the strips were removed from the expanded section only.

### 3.2.2 CTE Tests

Table 3-6 shows the complete test matrix for the CTE tests performed. A total of 132 individual CTE tests were performed. All CTE testing was performed in air in a Unitherm™<sup>1</sup> 1091 unit according to ASTM E228-06 (Reference 3-8). The tests ran from room temperature to 700°F and were heated at a rate of approximately 3.6°F/min. (2°C/min. specified). All tests were performed by ANTER Laboratories.

Four types of tests were performed:

The first test was a determination of the CTE under heat-up conditions, consistent with the accepted test practice. In addition, industry experts recommended that using heat-up only data would avoid hysteresis effects upon cooling. Ten specimens from each of the four heats of A508 material were tested. Similarly, all of the A600 heats were tested. The ten specimens were on a tube diameter basis instead of a heat basis. Thus, for the Model F steam generator tube (0.688 inch dia.), 4 specimens from Heat NX0419 were tested and 3 specimens from each of Heat NX9749 and Heat NX9821 were tested. For the Model D5 steam generator tube (0.750 inch dia.), 4 specimens from Heat NX1002 were tested and 3 specimens from each of Heat NX1019 and Heat NX 1145 were tested. Likewise, for the Model 44F/51F steam generator tube (0.875 inch dia.), 4 specimens from Heat NX9180 were tested and 3 specimens from each of Heat NX9292 and Heat NX1518 were tested.

The second test was the determination of repeatability of results. Ten heat-up tests of A508 material (Heat 97D258-1-1, Sample #8) and ten heat-up tests of A600 material (Heat NX1019, Sample #3) were performed. These two specific samples were chosen because they most closely exhibited the mean behavior of their respective materials from Test 1.

The third test was the heat-up of the strain hardened A600 material. Just like the non-strain hardened A600 CTE tests, the three heats of material for each SG model were tested in the ratio of 4:3:3. That is, for the Model F SG tube, 4 specimens were tested from Heat NX0419 and 3 specimens from each of Heat NX9749 and Heat NX9821 were tested. For the Model D5 SG tube, 4 specimens were tested from Heat NX1002 and 3 specimens from each of Heat NX1019 and Heat NX 1145 were tested. Likewise, for the Model 44F SG, 4 specimens were tested from Heat NX9180 and 3 specimens from each of Heat NX9292 and Heat NX1518 were tested.

Anomalous behavior in some of the individual specimens was observed in this test. Specifically, some specimens exhibited decreasing CTE with increasing temperature, reaching a minimum CTE value at approximately 200°F to 300°F, and then showing increasing CTE values with increasing temperature from approximately 300°F to 700°F. The anomalous behavior of some of the test specimens was addressed in the subsequent test.

The fourth test was a diagnostic test to explain some anomalous behavior observed in the prior (third) test. It was postulated by Begley (Reference 3-9) that if strain hardened A600 was subjected to temperatures above approximately 600°F, it should revert to its non-strain hardened behavior. Thus, three samples that exhibited anomalous behavior were retested 3 times each, and 1 sample that initially exhibited “normal” behavior was retested 3 times. The anomalous samples chosen for retest were from Model F, Heat

---

<sup>1</sup> Unitherm™ is a registered trademark of Anter Corporation

NX0419, Sample 3; Model D5, Heat NX1019, Sample 2; and Model 44F, Heat NX9180, Sample 4. One sample that initially exhibited “normal” behavior was Model D5, Heat NX1145, Sample 3.

### 3.3 CTE TEST RESULTS

The complete data package for the CTE tests is documented in Reference 3-11. Due to the extensive list of figures to describe the results of the testing, a summary table, Table 3-7, lists the tests, materials, and figure numbers. Briefly, Figures 3-4 through 3-24 show the results of the heat-up testing on the A508 and non-strain hardened A600 material; Figures 3-25 and 3-26 show the results of the multiple tests on one sample each of A508 material and A600 material, Figures 3-27 through 3-35 show the results of the tests on strain hardened A600 material, and Figures 3-36 through 3-39 show the results of the 3 repeat tests on A600 strain hardened material that initially exhibited anomalous behavior and the 1 repeat test on A600 strain hardened material that initially exhibited “normal” behavior.

### 3.4 DISCUSSION

#### SA508 Material

The heat-up tests on A508 material all exhibit a trend of increasing CTE value with increasing temperature, and the shape is consistently non-linear. The scatter is divided into two regions; the scatter below approximately 350°F is more significant than the scatter in the region above approximately 350°F, but still well within 10% of the individual mean curves. The data in the higher temperature region are quite close to the individual mean curves. The scatter in the lower temperature region is believed to be due to (1) thermal inertia and (2) measurement inaccuracy due to very small thermal expansions in that temperature range (fractions of microns) (Reference 3-10). Expansions below 200°F were typically less than 0.1%. This translates into less than 2 mils of growth, which is approximately the same as the measurement tolerance of the dilatometer used to measure CTE.

A plot of the mean curves of the individual heats of A508 material versus the ASME Code data shows that the current test data diverge from the mean ASME Code curve below approximately 350°F and align very well with the ASME Code data above approximately 350°F (see Figure 3-8). A few CTE measurements lie slightly outside the uncertainty associated with the ASME Code curve ( $\pm 10\%$ ) at 100°F, but this is not a concern because of the reasons outlined above. Thus, use of the ASME Code curve in steam generator tube-to-tubesheet joint thermal calculations is generally conservative as discussed in Appendix B.

#### Non-Strain Hardened A600 Material

The curves of CTE versus temperature for the non-strain hardened A600 material also exhibit increasing CTE values with increasing temperature, and most are non-linear. Unlike the A508 material, however, a few of the CTE versus temperature curves for non-strain hardened A600 material show an almost linear behavior. The data scatter is also more pronounced in the lower temperature region and small in the upper temperature region.

Comparing these data to the ASME Code curve (see Figures 3-13, 3-18, 3-23, and 3-24), the mean curves for the individual heats of material generally lie above the mean of the ASME Code curve. This would

imply that, in a SG tube-to-tubesheet joint thermal calculation, use of the ASME Code curve would be conservative (the tube is predicted to expand less than the test data show). Taken together with the data for the A508 material, the ASME Code curves would predict that the tubesheet will expand more and the tube will expand less than the current data show. Thus, use of the ASME Code curves will predict less contact pressure due to thermal growth and mismatch than the data indicate, and is therefore conservative.

#### Repeat Tests

One sample from the A508 material (Heat 97D258-1-1, Sample #8) and one sample from the A600 material (Heat NX1019, Sample #3) were tested multiple times in an effort to determine the repeatability of the data. In both cases, the means of the repeat test data are slightly higher than their respective original tests at 100°F, but otherwise, they are nearly identical to the original curves. The scatter on these curves is again similar to the other plots, i.e., there is more scatter in the lower temperature regime than in the upper temperature regime. Therefore, there is ample evidence that the tests are repeatable.

#### Strain Hardened A600 Material

The results of the CTE measurements made on strain hardened A600 material lend themselves to three noteworthy observations: (1) there is more scatter in the lower temperature regime than in the upper temperature regime, (2) some curves exhibit “normal” behavior defined as increasing CTE values with increasing temperature while other curves contain data that initially show a decrease of CTE value with increasing temperature followed by expected behavior, and (3) the mean curves of the strain hardened data are rotated clockwise from their non-strain hardened counterparts, i.e., the mean CTE values are higher in the low temperature regime and lower in the high temperature regime than CTE values of the non-strain hardened data. One may expect a differing behavior in CTE measurements between the strain hardened and non-strain hardened material due to the increase in the number of vacancies as well as the increasing number of, and entangling of, dislocations during plastic deformation. The tests performed immediately after cold working show this. However, this effect is not present after cold working and subsequent exposure of the specimens to temperatures above 600°F.

The hypothesis that this effect can be alleviated by thermal treatment above 600°F (Reference 3-9) led to the decision to perform repeat tests on a number of previously tested strain hardened specimens. Three samples were chosen because of the originally anomalous behavior of their data (Model F tube, Heat NX0419; Model D5 tube, Heat NX1019; and Model 44F tube, Heat NX9180), and one was chosen because it initially exhibited “normal” behavior (Model D5 tube, Heat NX1145). These are shown in Figures 3-36 through 3-39, respectively. In all cases initially exhibiting anomalous behavior, the effect did not recur, and the mean of the retest data CTE curves align much more closely with the non-strain hardened curves. Recall that the initial CTE tests on the strain hardened material were taken to 700°F. This is beyond the postulated 600°F and indicates that the strain hardened material has experienced some elastic recovery. Further, since the strain hardening only worked the material to approximately 3% strain, there is little plastic deformation incurred.

### **3.5 CONCLUSIONS**

1. The data indicate that use of the ASME Code curves for A508 and A600 material would be conservative for a SG tube-to-tubesheet joint calculation. That is, the tubesheet is predicted by

the ASME Code curve to expand more than the data show, and the tubes are predicted by the ASME Code curve to expand less than the data show. This would have the effect of lessening the thermal mismatch between the tube and the tubesheet, and it would then decrease the thermal component of the contact pressure between them.

2. The mean curves of CTE versus temperature for the A508 material all lay within the uncertainty associated with the ASME Code curves. Some individual data lay outside the lower bound on the curve at 100°F, but this is of no concern since the expansion of the material at these temperatures is well within the measurement tolerance of the instrumentation. The mean curves of CTE versus temperature for the A600 material and all of the individual data lay within the uncertainty associated with the ASME Code curves.
3. All samples show a general curve of increasing CTE with increasing temperature. All of the A508 material show non-linear behavior, while some of the A600 material shows nearly linear behavior.
4. The data scatter is more pronounced in the temperature regime below approximately 350°F than in the regime above approximately 350°F. This is due to thermal inertia and measurement uncertainty due to very small thermal expansions in that temperature range (fractions of microns).
5. Performing multiple tests on a single specimen results in a similar data scatter pattern as that on data from individual heats of material. This suggests that the variability is inherent to the test apparatus and does not reflect actual variability of CTE. It is concluded that within the accuracy of the test method, the CTE values are repeatable and consistent.
6. Strain hardening does not affect the CTE of A600 material after exposure of the strain hardened material to temperatures of 600 degrees or greater. While initial tests of strain hardened samples of A600 material show a mean CTE versus temperature curve that has been rotated relative to the original, non-strain hardened mean CTE versus temperature curve, re-testing of these specimens returns the CTE behavior to its original, non-strain hardened behavior. Some individual curves exhibit anomalous behavior at low temperature increase, i.e., an initially decreasing CTE value with increasing temperature. The tests showed that this behavior is eliminated upon retesting, due to the fact that temperatures above approximately 600°F provide enough thermal energy to induce elastic recovery. In addition, the plastic strain introduced by the strain hardening was small.
7. A detailed analysis of the CTE data was performed to determine the mean value and variability of the CTE of SA508 and A600 material. This analysis is included in Appendix B of this report and shows that the use of the ASME Code CTE mean properties is conservative for H\* calculations. Statistical variability parameters are also provided for both materials.

### 3.6 REFERENCES

- 3-1 WCNOC Letter ET 08-0010, "Withdrawal of License Amendment Request for a Permanent Alternate Repair Criteria in Technical Specification (TS) 5.5.9, Steam Generator (SG) Program," February 14, 2008.

- 3-2 NRC Letter, "Wolf Creek Generating Station – Withdrawal of License Amendment Request on Steam Generator Tube Inspections (TAC No. MD1097)," February 28, 2008."
- 3-3 Wolf Creek Letter ET 06-0004, "Revision to Technical Specification 5.5.9, Steam Generator Tube Surveillance Program," February 21, 2006.
- 3-4 Wolf Creek Letter WO 07-0012, "Response to Request for Additional Information Related to License Amendment Request to Revise the Steam Generator Program," May 3, 2007.
- 3-5 Wolf Creek Letter ET 07-0043, "Response to Request for Additional Information Related to License Amendment Request to Revise the Steam Generator Program," September 27, 2007.
- 3-6 ASME Boiler and Pressure Vessel Code, Section II, New York: ASME International, 2007.
- 3-7 W. B. Middlebrooks, D. L. Harrod, and R. E. Gold, *Nuclear Engineering and Design* 143, 1993, pp. 159-169.
- 3-8 ASTM E228-06, "Standard Test Method for Linear Thermal Expansion of Solid Materials with a Push-Pull Rod Dilatometer," West Conshohocken: ASTM International, 2006.
- 3-9 J. Begley, private communication.
- 3-10 D. Gaal, Laboratory Director, ANTER Corporation, private communication.
- 3-11 Westinghouse CN-SGMP-09-2, "Analysis of the Coefficients of Thermal Expansion of A600 and A508 Material."

**Table 3-1<sup>1</sup> Chemical Certifications (in Weight Percent) for A508 Pressure Vessel Steel Used in the CTE Test Program**

Heat	C	Si	Mn	P	S	Ni	Cr	Mo	V	Cu	Al
03D958-1-6	0.24 max.	0.15/ 0.40	1.14/ 1.56	0.010 max.	0.010 max.	0.37/ 1.03	0.15/ 0.25	0.42/ 0.53	0.010 max.	0.10 max.	0.040 max.
97D28-1-1	0.22	0.23	1.41	0.005	0.001	0.94	0.20	0.52	<0.003	0.03	0.018
97B80-1-11	0.21	0.23	1.49	0.007	0.001	0.93	0.19	0.51	<0.003	0.05	0.019
97D258-1-1	0.20	0.23	1.47	0.005	0.001	0.93	0.18	0.51	<0.003	0.03	0.022

**Table 3-2<sup>2</sup> Mechanical Certifications for A508 Pressure Vessel Steel in the CTE Test Program**

Heat	Yield Strength (ksi)	Tensile Strength (ksi)	Elongation (%)	Reduction of Area (%)
03D958-1-6	68.8	90.3	29.2	74.6
97D28-1-1 <sup>3</sup>	73.9	96	28	73
	75.5	97.4	28.4	73.4
97B80-1-11	74	96.7	28	71.7
97D258-1-1	70.3	92.0	29.2	71.7
	71.4	93.8	28	70.4

<sup>1</sup> Chemical certifications provided courtesy of the Muroran Plant of the Japan Steel Works, Ltd.

<sup>2</sup> Mechanical certifications provided courtesy of B&W Canada.

Table 3-3<sup>3</sup> Summary of the A600 Tubes Used in the CTE Test Program

Steam Generator Model	Heat	Condition	Nominal Outer Diameter (in.)
F	NX0419	Thermally-Treated	0.688
F	NX9749	Thermally-Treated	0.688
F	NX9821	Thermally-Treated	0.688
D5	NX1002	Thermally-Treated	0.750
D5	NX1019	Thermally-Treated	0.750
D5	NX1145	Thermally-Treated	0.750
44F	NX9180	Thermally-Treated	0.875
44F	NX9292	Thermally-Treated	0.875
44F	NX1518	Thermally-Treated	0.875

Table 3-4<sup>4</sup> Chemical Certifications (in Weight Percent) of the A600 Tubes Used in the CTE Test Program

Heat	C	Mn	Fe	S	Si	Cu	Ni	Cr	Al	Ti	Co	P	B
NX0419	0.029	0.13	9.16	0.001	0.20	0.28	74.26	15.94	0.30	0.26	0.03	0.012	0.004
NX9749	0.040	0.23	8.14	0.001	0.29	0.22	74.99	16.09	0.21	0.24	0.04	0.010	0.005
NX9821	0.028	0.16	7.47	0.001	0.22	0.42	75.76	15.94	0.31	0.22	0.02	0.008	0.005
NX1002	0.027	0.29	9.67	0.003	0.12	0.28	73.83	15.78	0.13	0.13	0.04	0.010	0.004
NX1019	0.047	0.26	9.00	0.001	0.18	0.28	74.49	15.74	0.24	0.23	0.04	0.008	0.005
NX1145	0.037	0.29	9.39	0.001	0.15	0.30	73.64	16.19	0.30	0.23	0.05	0.009	0.004
NX9180	0.030	0.19	9.77	0.003	0.12	0.41	73.48	16.00	0.33	0.25	0.02	0.009	0.005
NX9292	0.020	0.23	8.99	0.002	0.10	0.38	75.15	15.13	0.25	0.22	0.04	0.010	0.004
NX1518	0.030	0.34	8.82	0.001	0.28	0.20	74.46	15.87	0.19	0.23	0.05	0.008	0.004

<sup>3</sup> Two values were reported for this heat of material.<sup>4</sup> All values provided courtesy of Westinghouse STD.

Table 3-5<sup>4</sup> Mechanical Certifications of the A600 Tubes Used in the CTE Test Program

Heat	Yield Strength (ksi)	Tensile Strength (ksi)	Elongation (%)	Hardness (R <sub>B</sub> )
NX0419	51	106	37.5	84
NX9749	49	106	38.5	85
NX9821	53	106	38.0	84
NX1002	44	100	40.5	79
NX1019	52	111	36.5	85
NX1145	55	111	35.5	86
NX9180	51	101	41.5	85
NX9292	47	98	45.5	83
NX1518	51.5	107.4	38.5	87

<sup>4</sup> All values provided courtesy of Westinghouse STD.

Table 3-6 Matrix for Coefficient of Thermal Expansion Tests

Material	Heat No.	Tube Dia. (in.)	Heat-Up CTE	Repeatability	Strain Hardened	Retest of Strain Hardened
A508	03D958-1-6	na	10 <sup>(1)</sup>	na	na	na
	97D28-1-1	na	10 <sup>(1)</sup>	na	na	na
	97B80-1-11	na	10 <sup>(1)</sup>	na	na	na
	97D258-1-1	na	10 <sup>(1)</sup>	10 (sample 8) <sup>(2)</sup>	na	na
A600	NX0419	0.688	3 <sup>(1)</sup>	na	3 <sup>(1)</sup>	3(sample 3) <sup>(2)</sup>
	NX9749		4 <sup>(1)</sup>	na	4 <sup>(1)</sup>	na
	NX9821		3 <sup>(1)</sup>	na	3 <sup>(1)</sup>	na
	NX1002	0.750	4 <sup>(1)</sup>	na	4 <sup>(1)</sup>	na
	NX1019		3 <sup>(1)</sup>	10 (sample 3) <sup>(2)</sup>	3 <sup>(1)</sup>	3 (sample 2) <sup>(2)</sup>
	NX1145		3 <sup>(1)</sup>	na	3 <sup>(1)</sup>	3 (sample 3) <sup>(2)</sup>
	NX9180	0.875	4 <sup>(1)</sup>	na	4 <sup>(1)</sup>	3 (sample 4) <sup>(2)</sup>
	NX9292		3 <sup>(1)</sup>	na	3 <sup>(1)</sup>	na
	NX1518		3 <sup>(1)</sup>	na	3 <sup>(1)</sup>	na
<b>Total Tests</b>			<b>70</b>	<b>20</b>	<b>30</b>	<b>12</b>
Notes:						
1. Different specimens						
2. Same specimen; retested						

Table 3-7 Listing of the Test Results and Their Corresponding Figure Numbers

Material	Heat	Test Description	Figure No.
A508 Gr. 3 Cl. 1	03D958-1-6	Heat-up	4
A508 Gr. 3 Cl. 2	97D28-1-1	Heat-up	5
A508 Gr. 3 Cl. 2	97B80-1-11	Heat-up	6
A508 Gr. 3 Cl. 2	97D258-1-1	Heat-up	7
A508	All	Mean curves versus ASME Code	8
A600 (0.688 inch dia.)	NX9749	Heat-up	9
A600 (0.688 inch dia.)	NX0419	Heat-up	10
A600 (0.688 inch dia.)	NX9821	Heat-up	11
A600 (0.688 inch dia.)	All	Heat-up	12
A600 (0.688 inch dia.)	All	Mean curves versus ASME Code	13
A600 (0.750 inch dia.)	NX1002	Heat-up	14
A600 (0.750 inch dia.)	NX1019	Heat-up	15
A600 (0.750 inch dia.)	NX1145	Heat-up	16
A600 (0.750 inch dia.)	All	Heat-up	17
A600 (0.750 inch dia.)	All	Mean curves versus ASME Code	18
A600 (0.875 inch dia.)	NX9180	Heat-up	19
A600 (0.875 inch dia.)	NX9292	Heat-up	20
A600 (0.875 inch dia.)	NX1518	Heat-up	21
A600 (0.875 inch dia.)	All	Heat-up	22
A600 (0.875 inch dia.)	All	Mean curves versus ASME Code	23
A600	All	Mean curves versus ASME Code	24
A508 Gr. 3 Cl. 2	97D258-1-1	Multiple tests on Sample 8	25
A600 (0.750 inch dia.)	NX1019	Multiple tests on Sample 3	26
A600 (0.688 inch dia.)	NX9749	Strain hardened, heat-up	27
A600 (0.688 inch dia.)	NX0419	Strain hardened, heat-up	28
A600 (0.688 inch dia.)	NX9821	Strain hardened, heat-up	29
A600 (0.750 inch dia.)	NX1002	Strain hardened, heat-up	30
A600 (0.750 inch dia.)	NX1019	Strain hardened, heat-up	31
A600 (0.750 inch dia.)	NX1145	Strain hardened, heat-up	32
A600 (0.875 inch dia.)	NX9180	Strain hardened, heat-up	33
A600 (0.875 inch dia.)	NX9292	Strain hardened, heat-up	34
A600 (0.875 inch dia.)	NX1518	Strain hardened, heat-up	35
A600 (0.688 inch dia.)	NX0419	Strain hardened, repeat testing on Sample 3	36
A600 (0.750 inch dia.)	NX1019	Strain hardened, repeat testing on Sample 2	37
A600 (0.875 inch dia.)	NX9180	Strain hardened, repeat testing on Sample 4	38
A600 (0.750 inch dia.)	NX1145	Strain hardened, repeat testing on Sample 3	39



**Figure 3-1 Model F Steam Generator Split Collar Used to Strain Harden A600 Tubing**

a,c,e



**Figure 3-2 Model D5 Steam Generator Split Collar Used to Strain Harden A600 Tubing**



**Figure 3-3 Model 44F Steam Generator Split Collar Used to Strain Harden A600 Tubing**

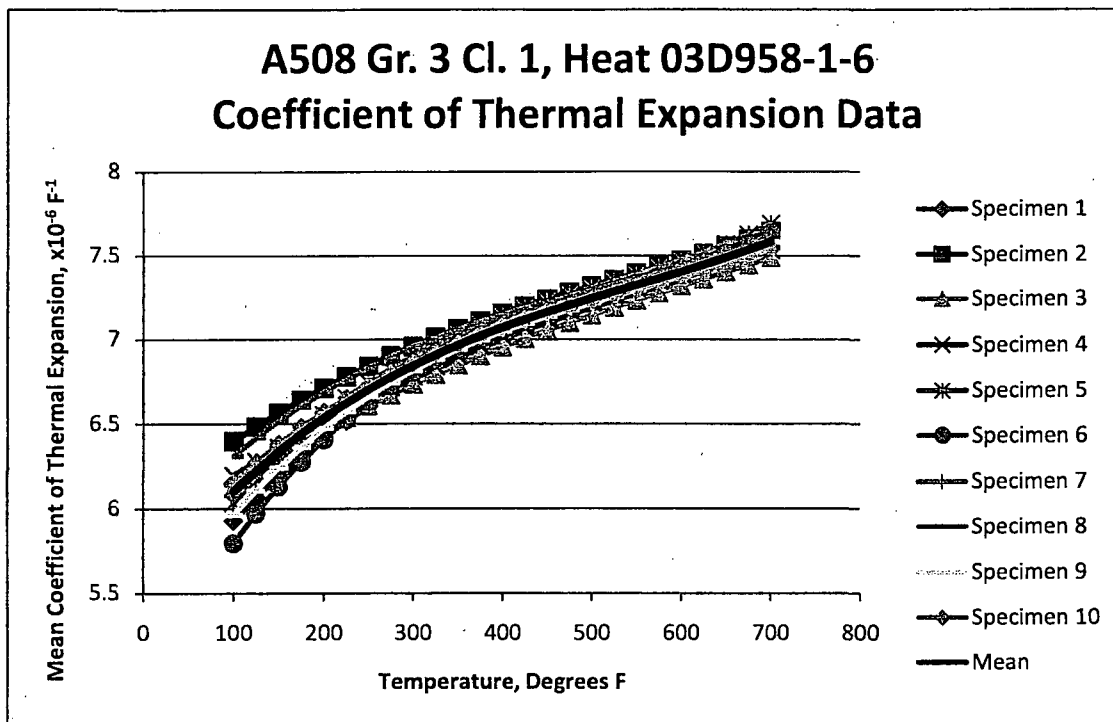


Figure 3-4 Heat-Up Test on A508 Gr. 3 Cl. 1 Material

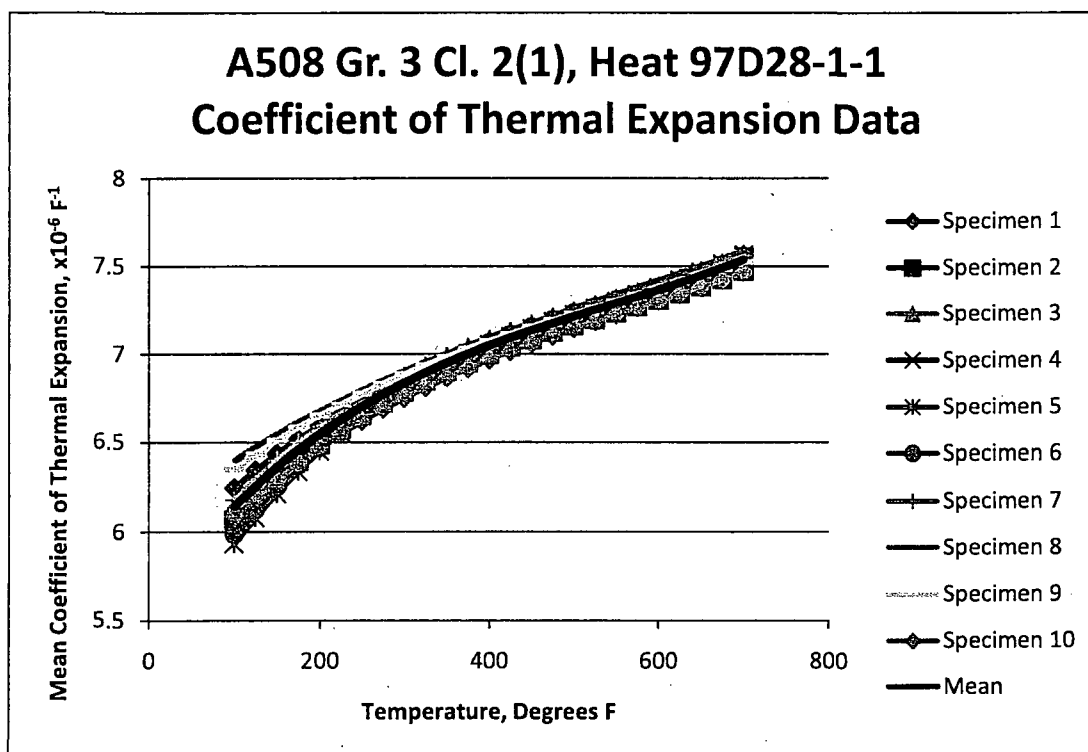


Figure 3-5 Heat-Up Test on A508 Gr. 3 Cl. 2 Material

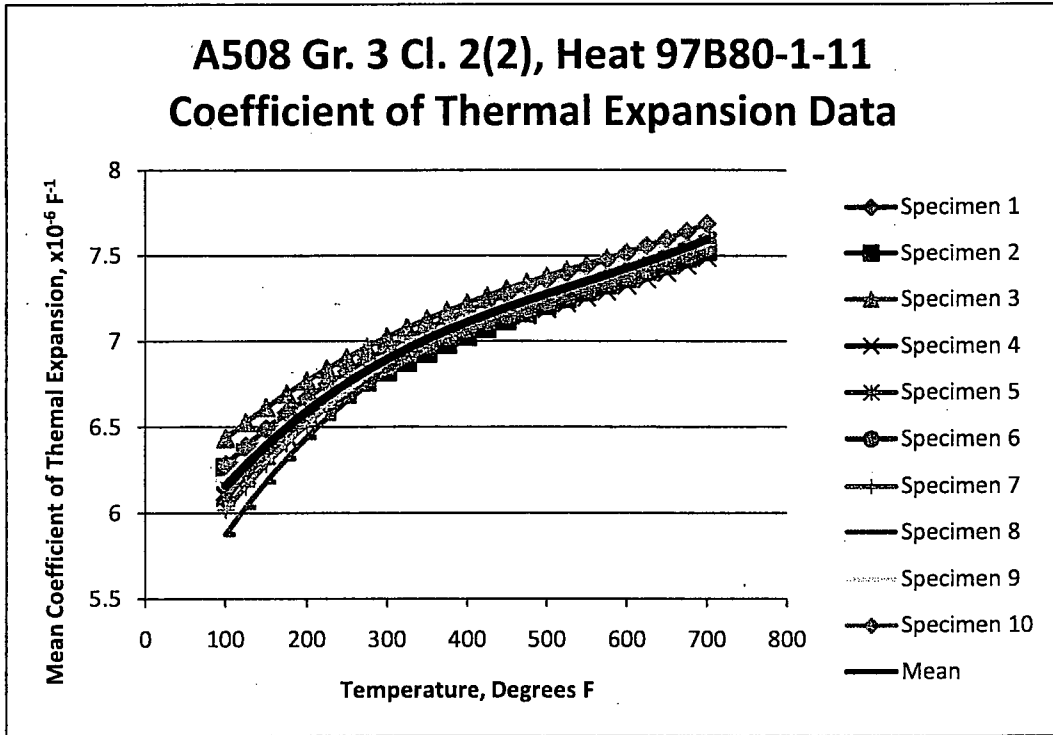


Figure 3-6 Heat-Up Test on A508 Gr. 3 Cl. 2 Material

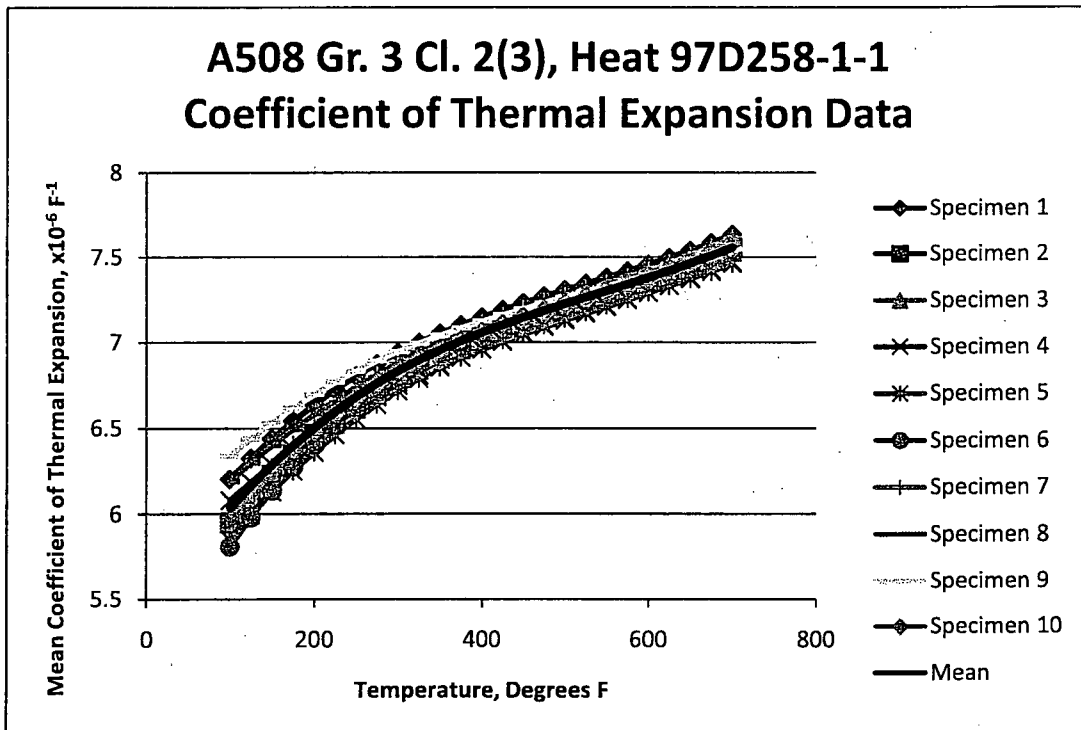


Figure 3-7 Heat-Up Test on A508 Gr. 3 Cl. 2 Material

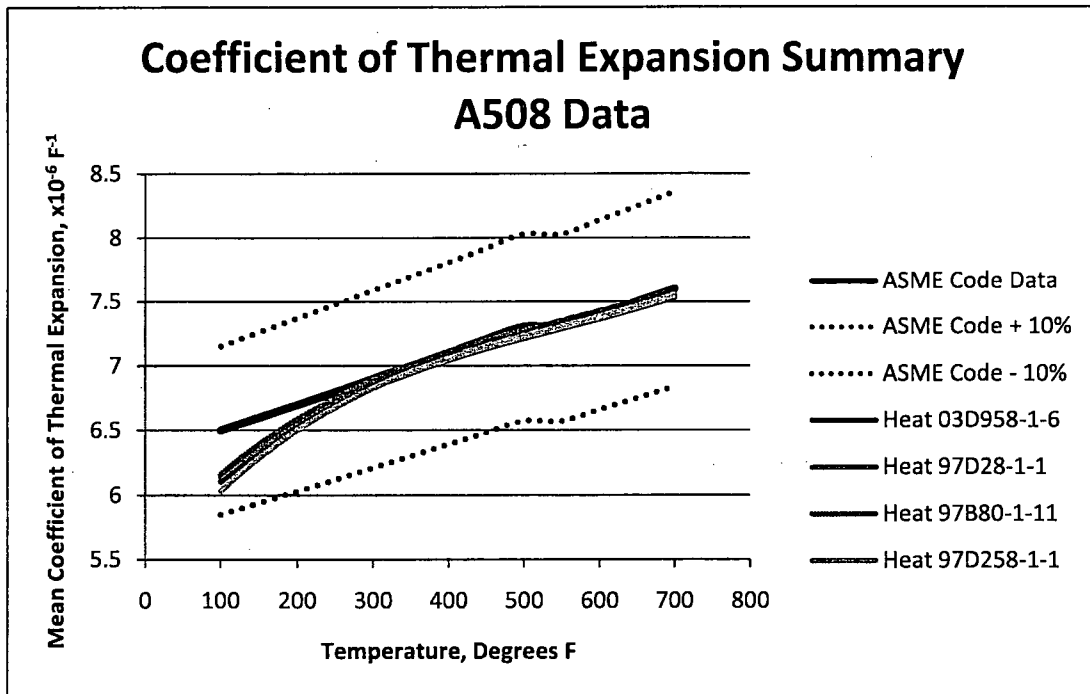


Figure 3-8 A508 Mean Curves Versus the ASME Code Curves

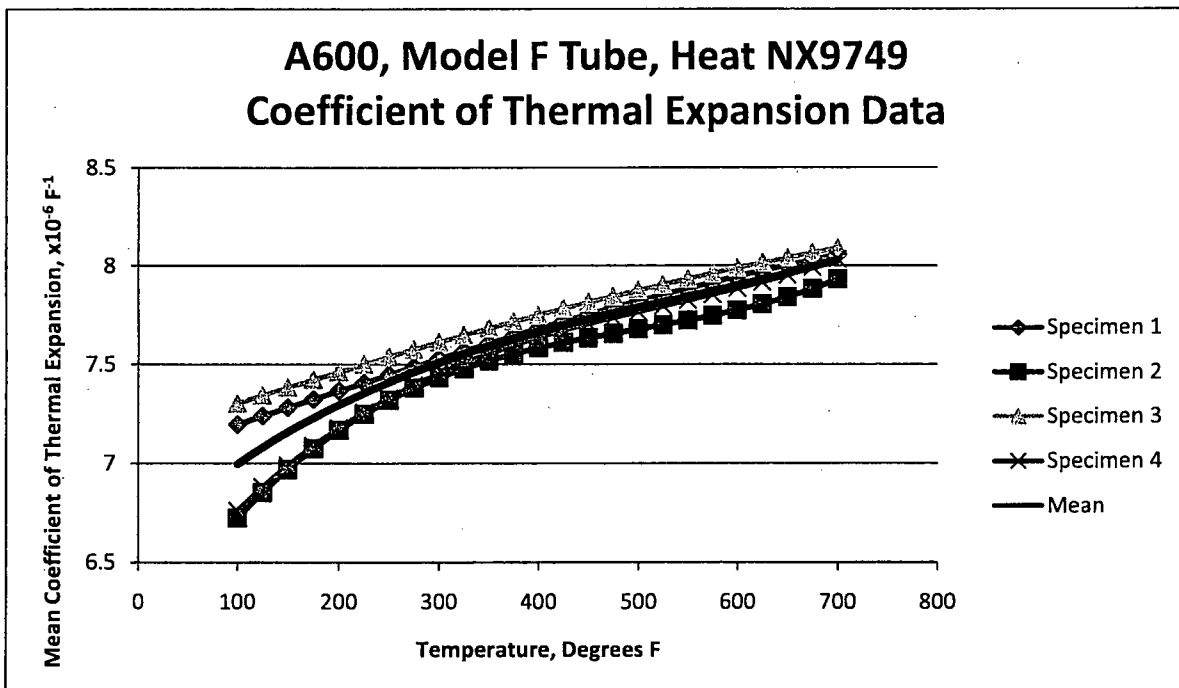


Figure 3-9 Heat-Up Test on A600, Model F Tube, Heat NX9749

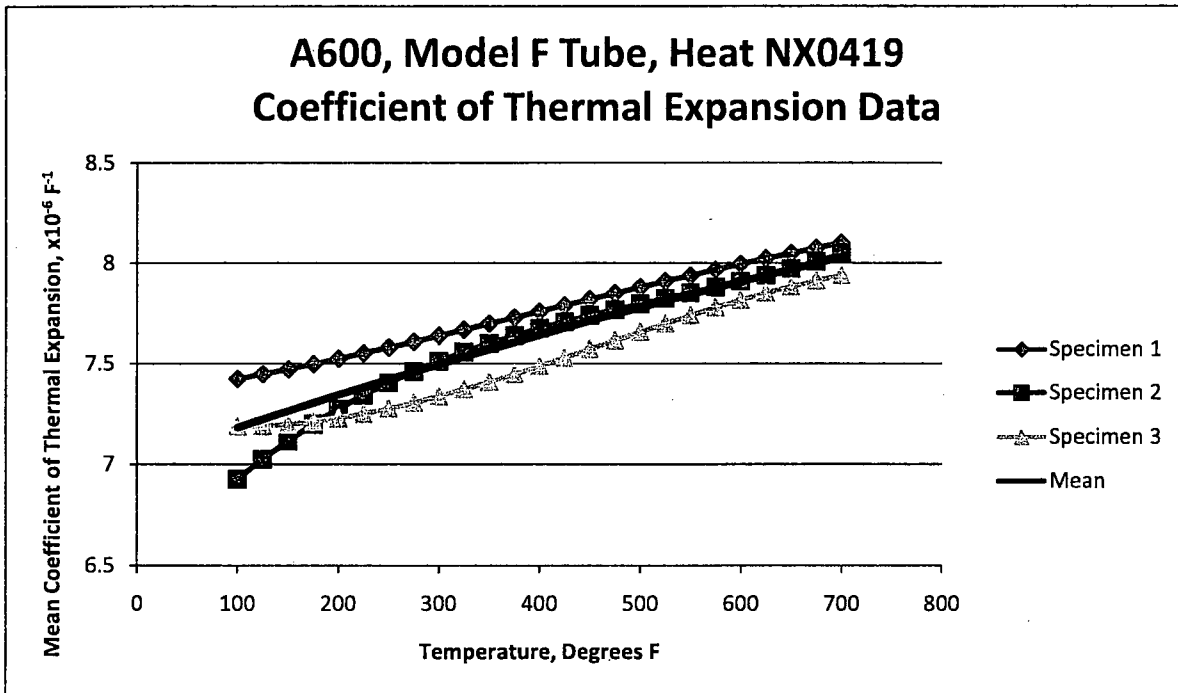


Figure 3-10 Heat-Up Test on A600, Model F Tube, Heat NX0419

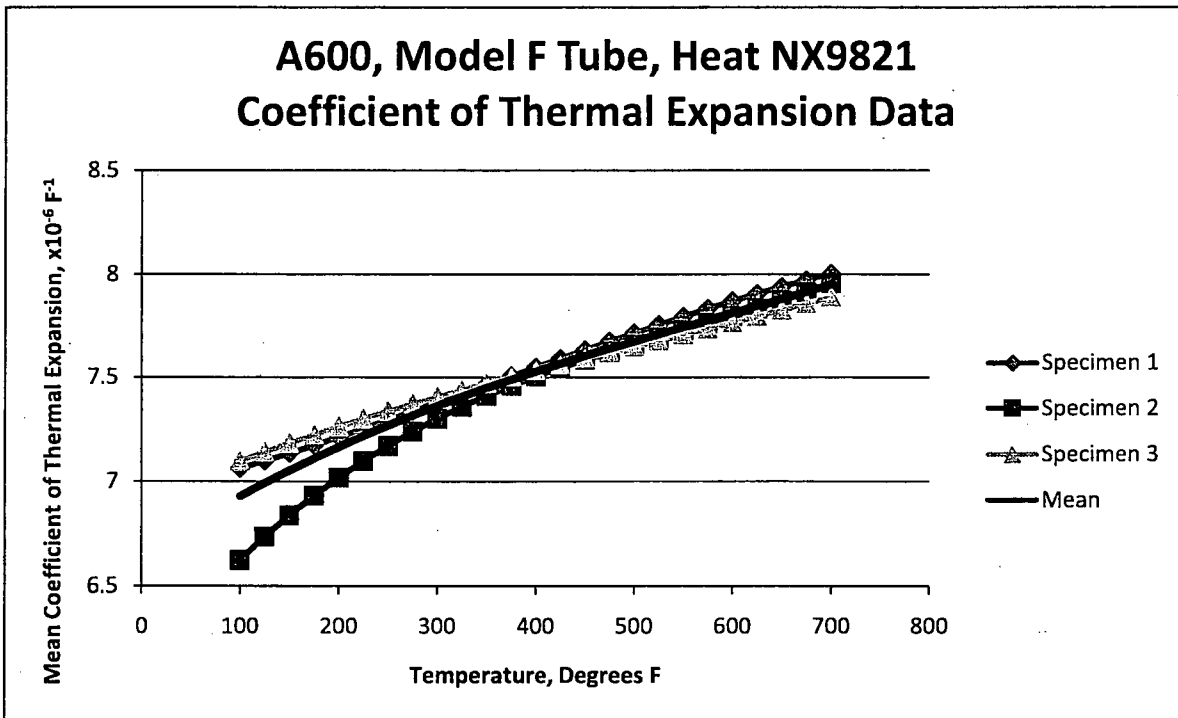


Figure 3-11 Heat-Up Test on A600, Model F Tube, Heat NX9821

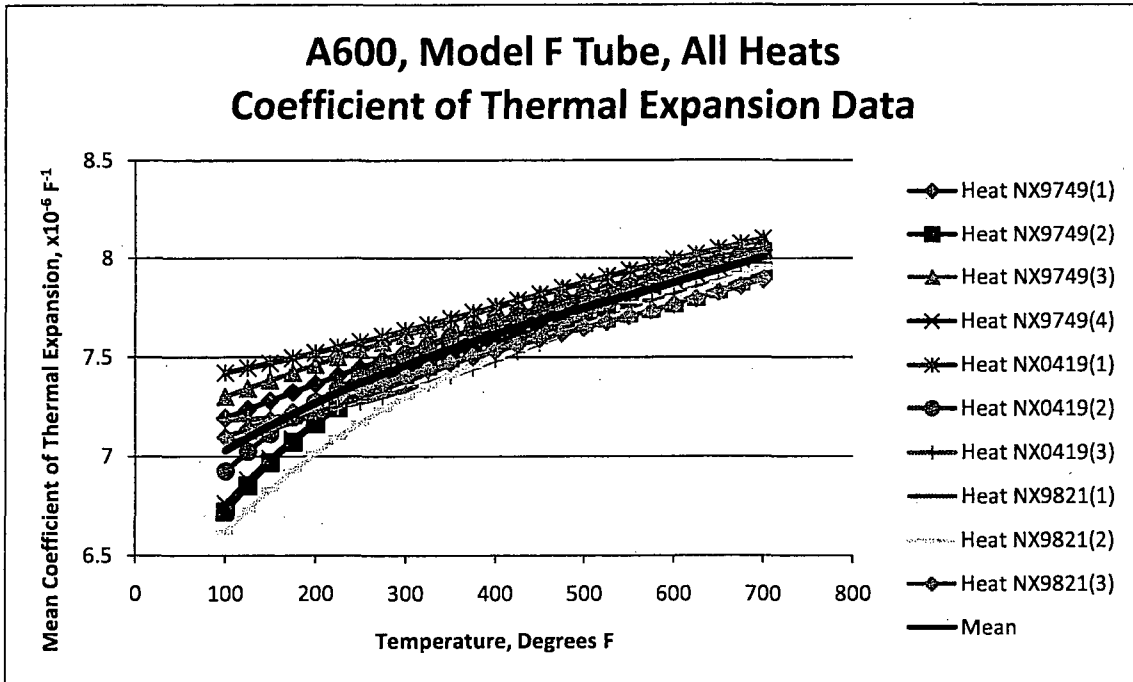


Figure 3-12 Summary of Heat-Up Testing of All Heats of A600 Model F Tube

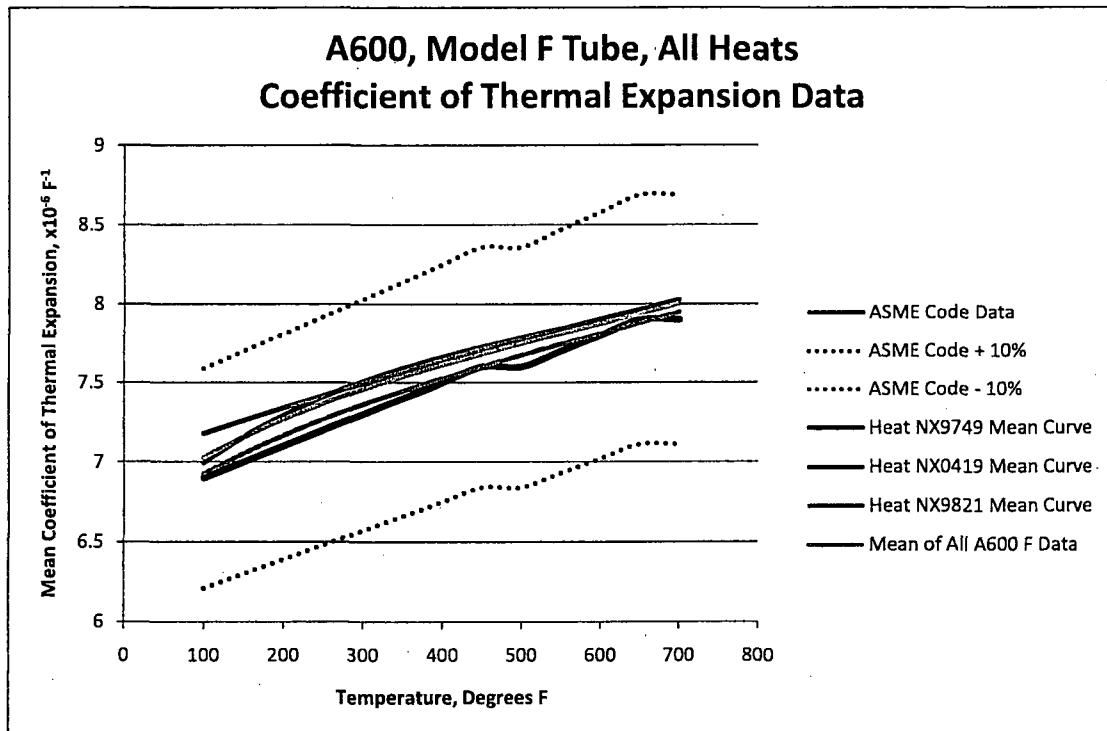


Figure 3-13 Mean Curves of Heats of A600 Model F Tube Versus the ASME Code Curve

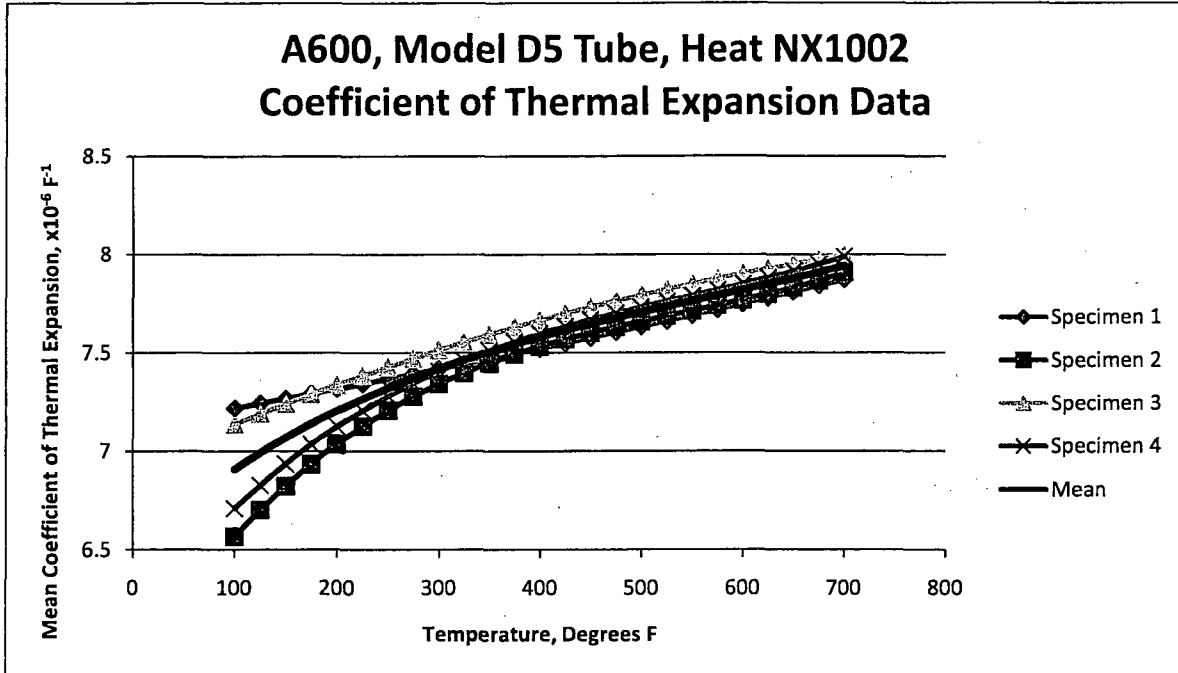


Figure 3-14 Heat-Up Test of A600, Model D5 Tube, Heat NX1002

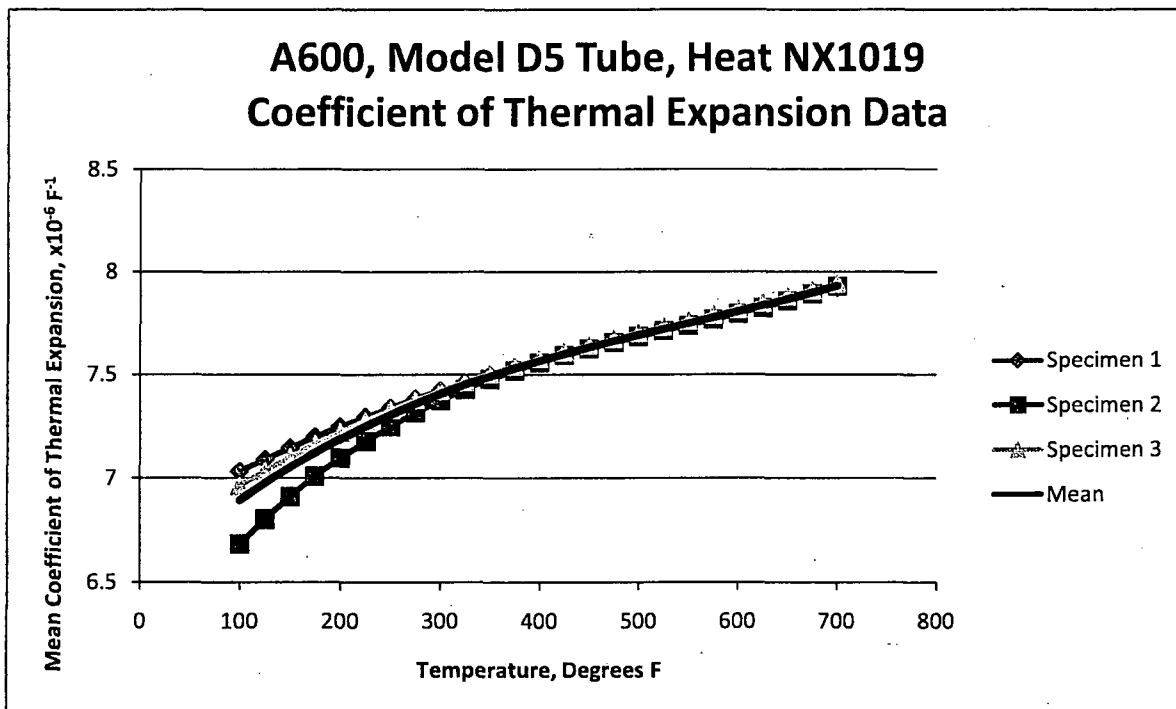


Figure 3-15 Heat-Up Test of A600, Model D5 Tube, Heat NX1019

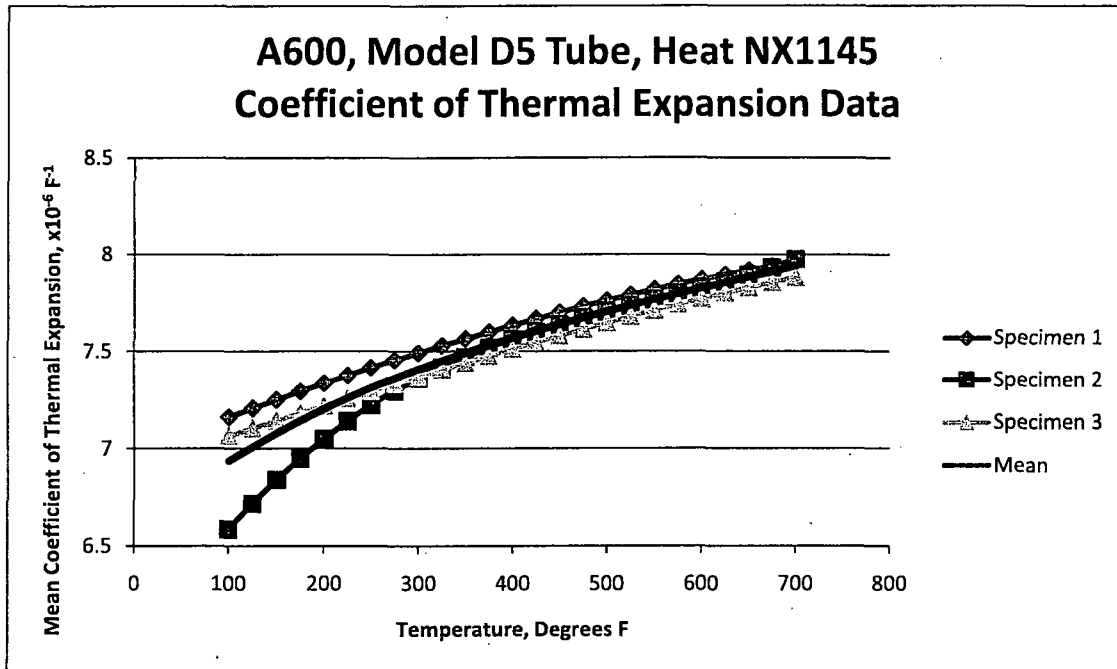


Figure 3-16 Heat-Up Test of A600, Model D5 Tube, Heat NX1145

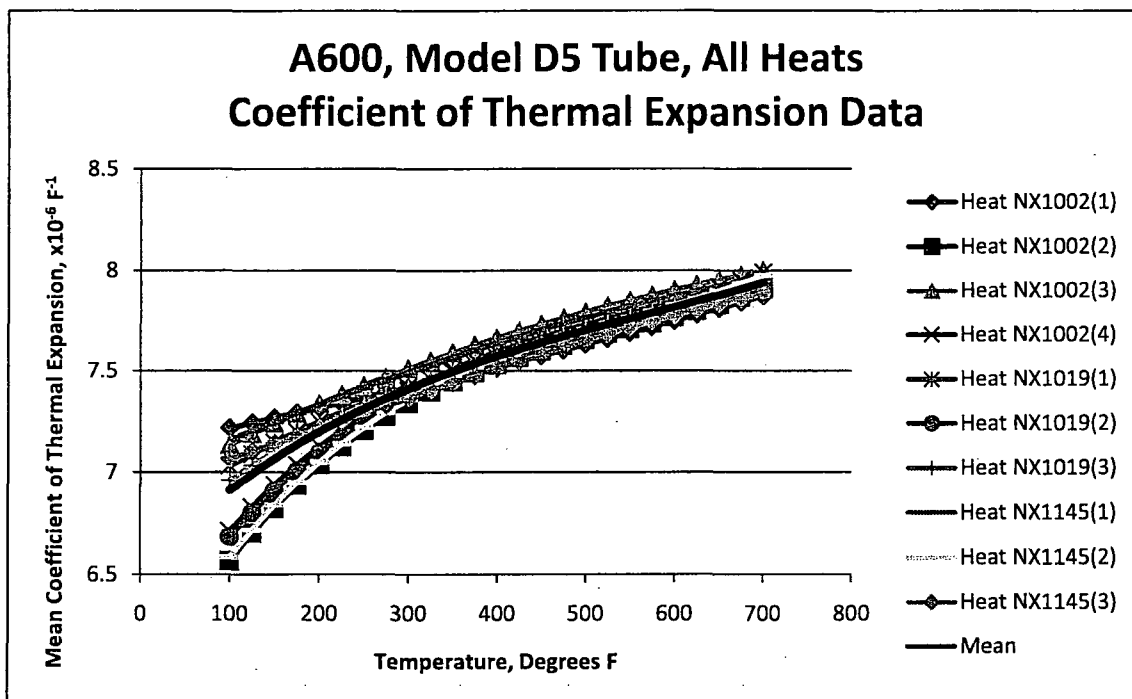


Figure 3-17 Summary of Heat-Up Testing of All Heats of A600 Model D5 Tube

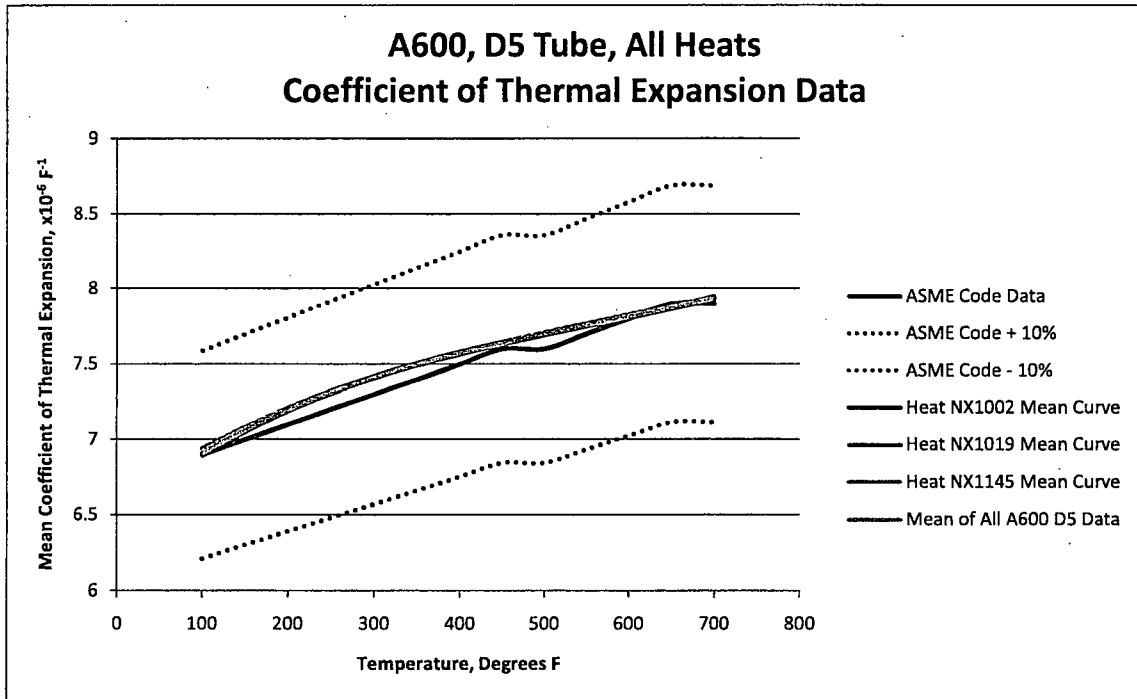


Figure 3-18 Mean Curves of Heats of A600 Model D5 Tube Versus the ASME Code Curve

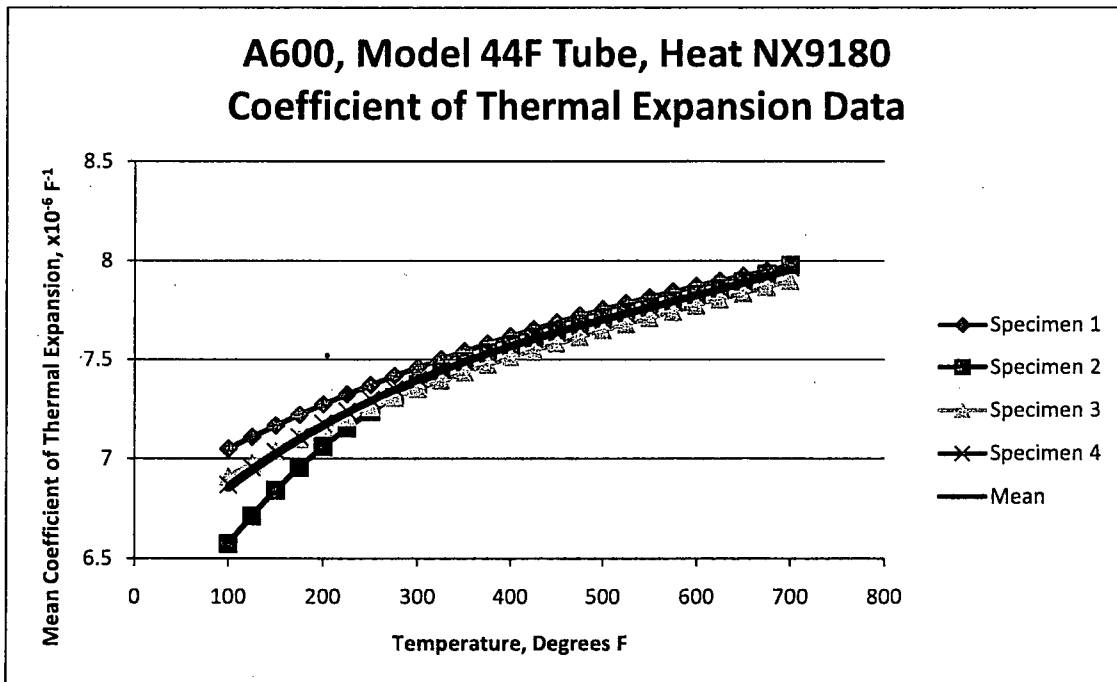


Figure 3-19 Heat-Up Tests of A600, Model 44F Tube, Heat NX9180

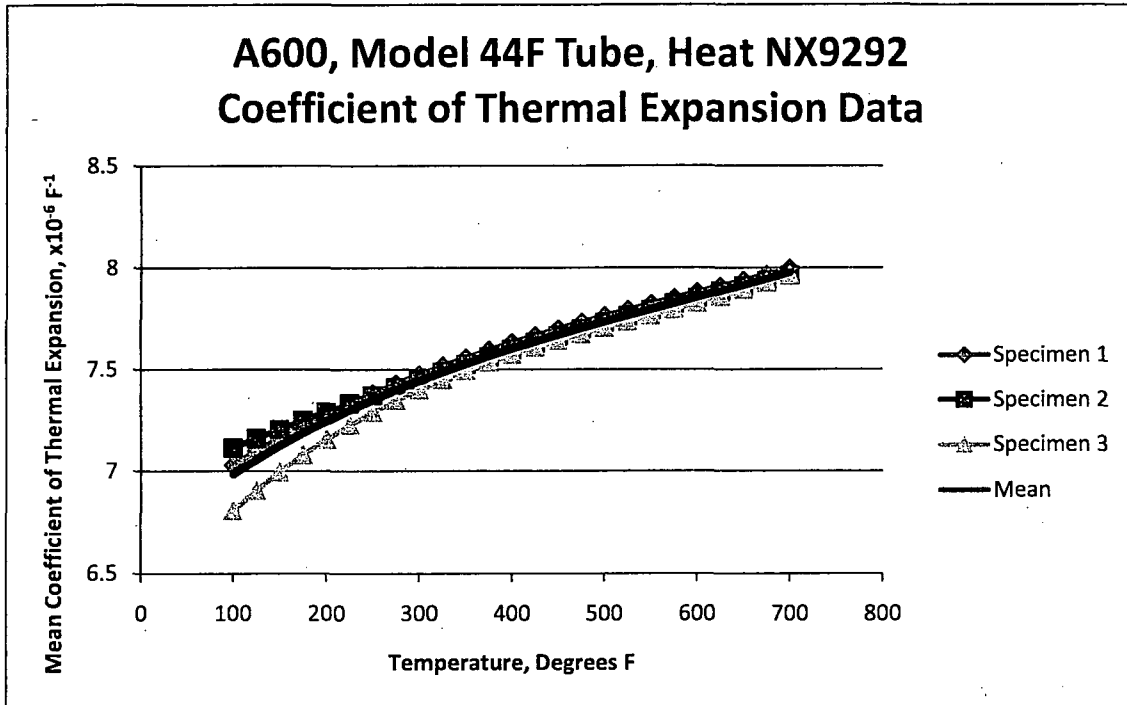


Figure 3-20 Heat-Up Tests of A600, Model 44F Tube, Heat NX9292

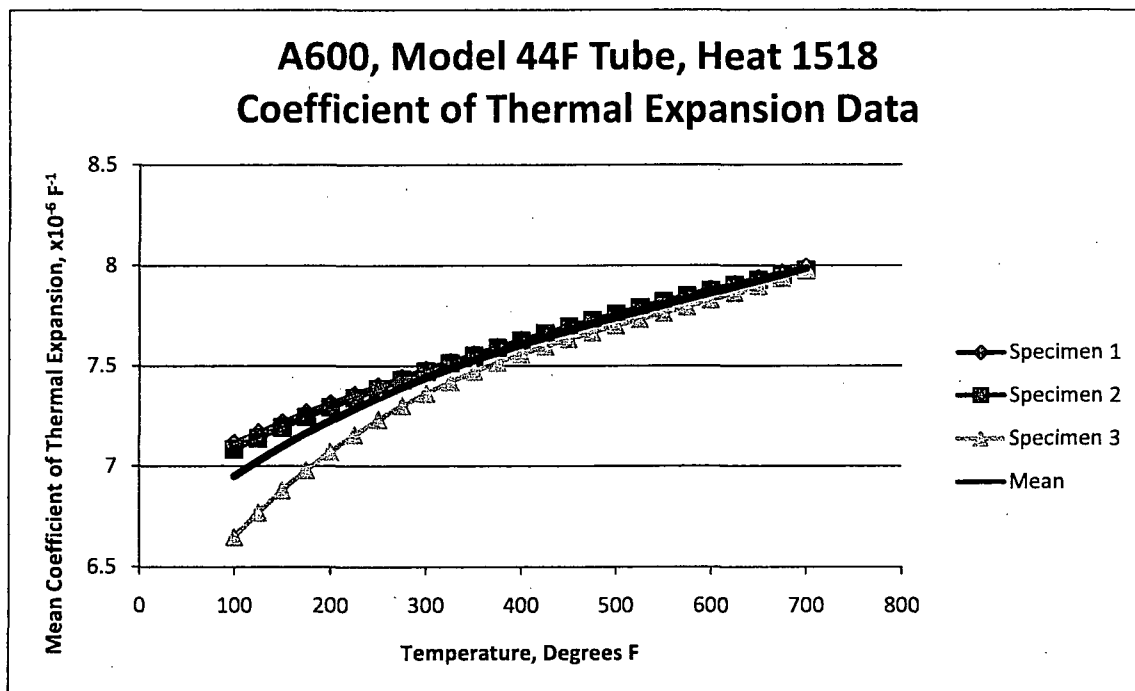


Figure 3-21 Heat-Up Tests of A600, Model 44F Tube, Heat NX1518

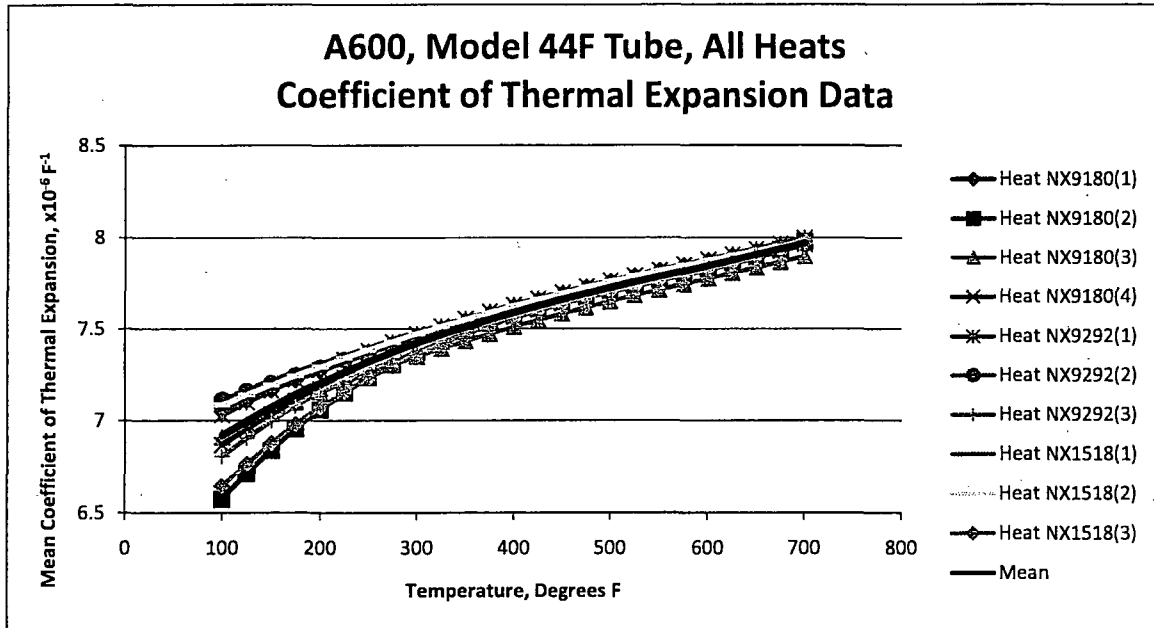


Figure 3-22 Summary of Heat-Up Testing of All Heats of A600 Model 44F Tube

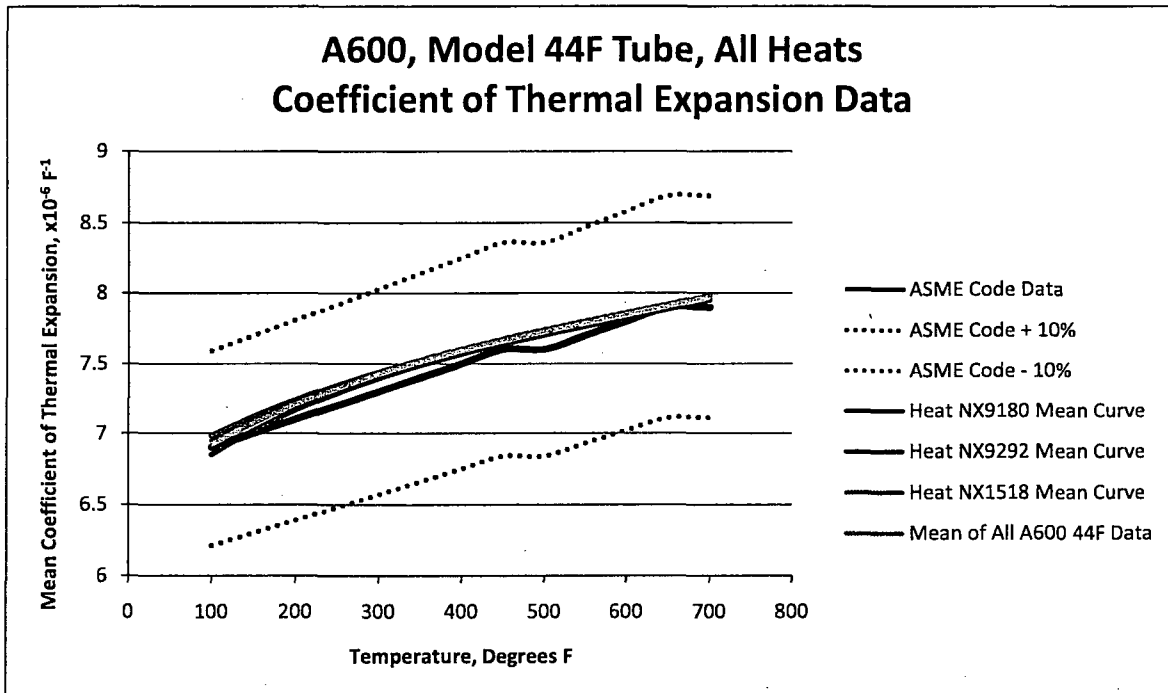


Figure 3-23 Mean Curves of Heats of A600 Model 44F Tube Versus the ASME Code Curve

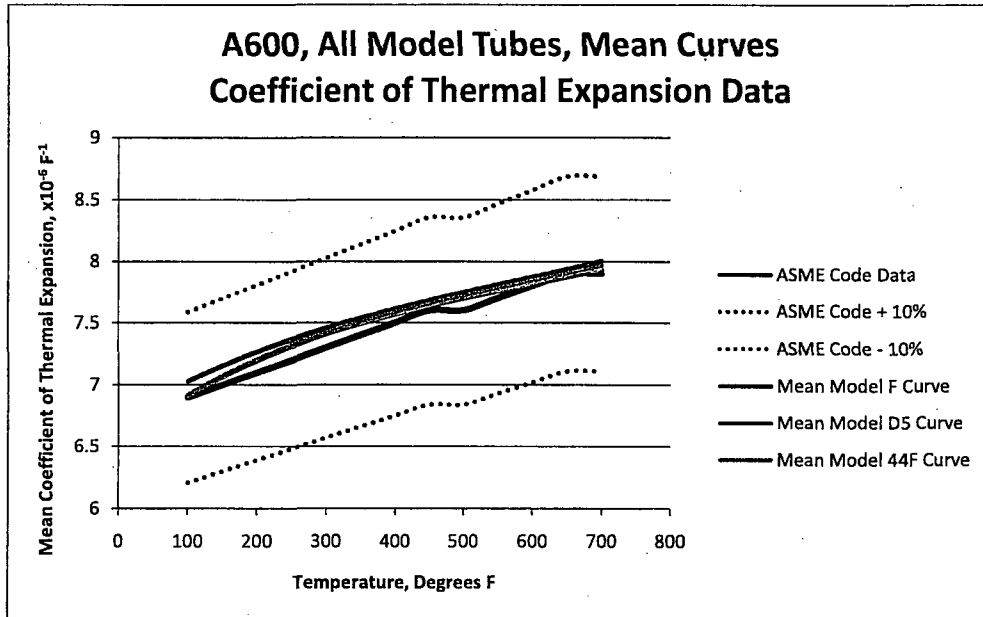


Figure 3-24 Mean Curves of All A600 Steam Generator Model Data Versus the ASME Code Curve

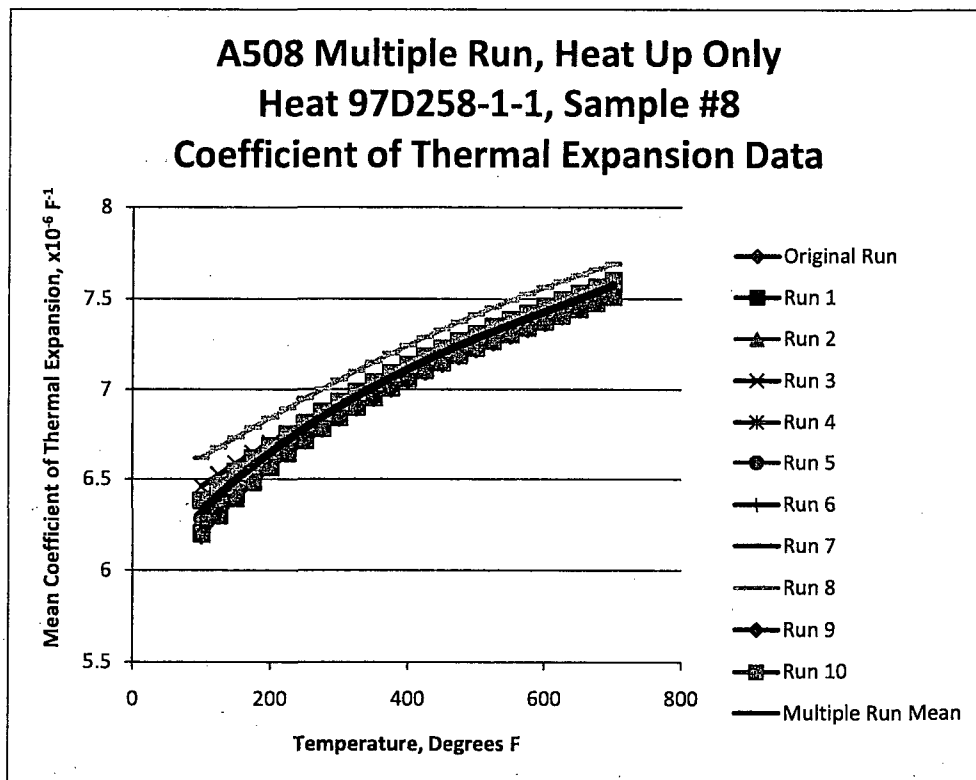


Figure 3-25 A508, Heat 97D258-1-1, Sample 8 Multiple Testing

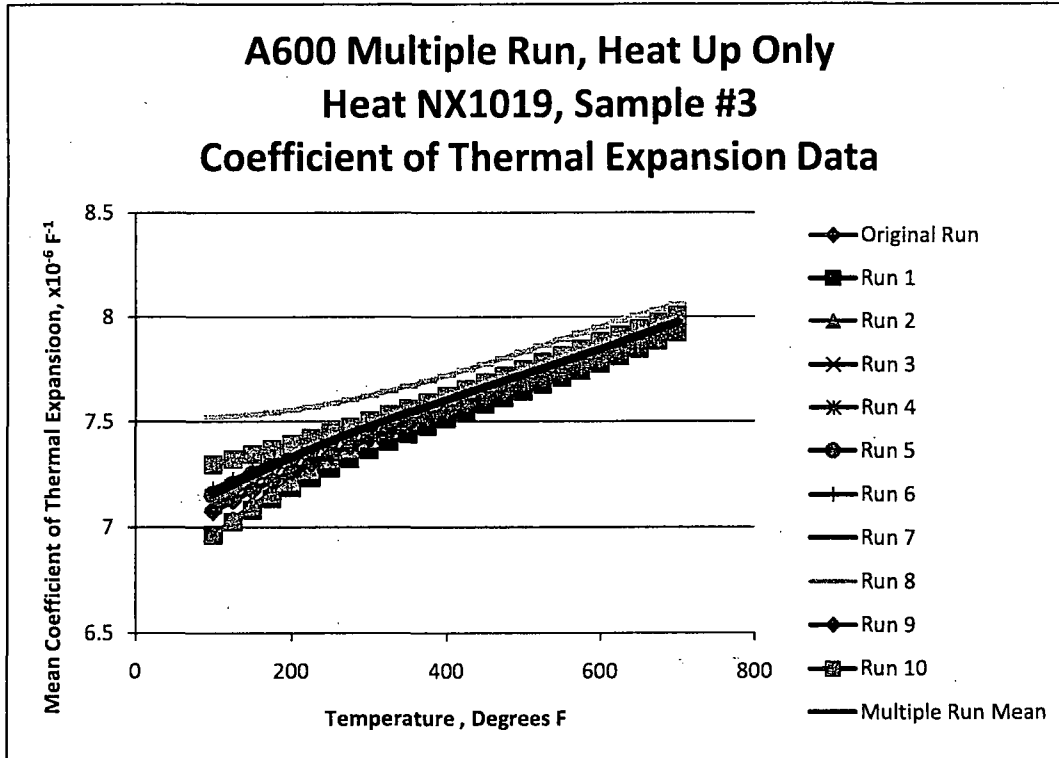


Figure 3-26 A600, Heat NX1019, Sample 3 Multiple Testing

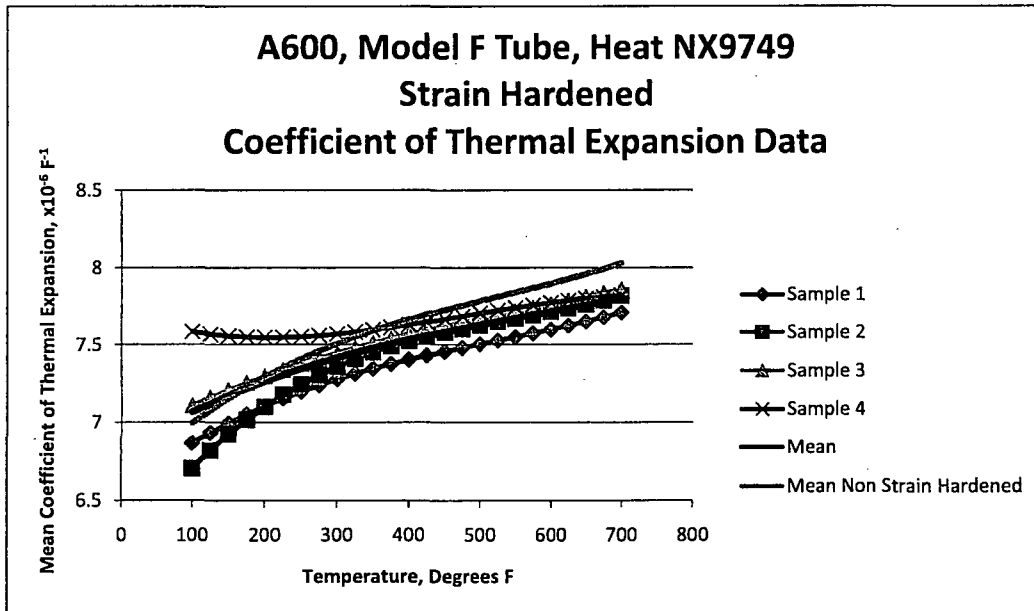


Figure 3-27 Heat-Up Tests of Strain Hardened A600 Model F Tubing, Heat NX9749

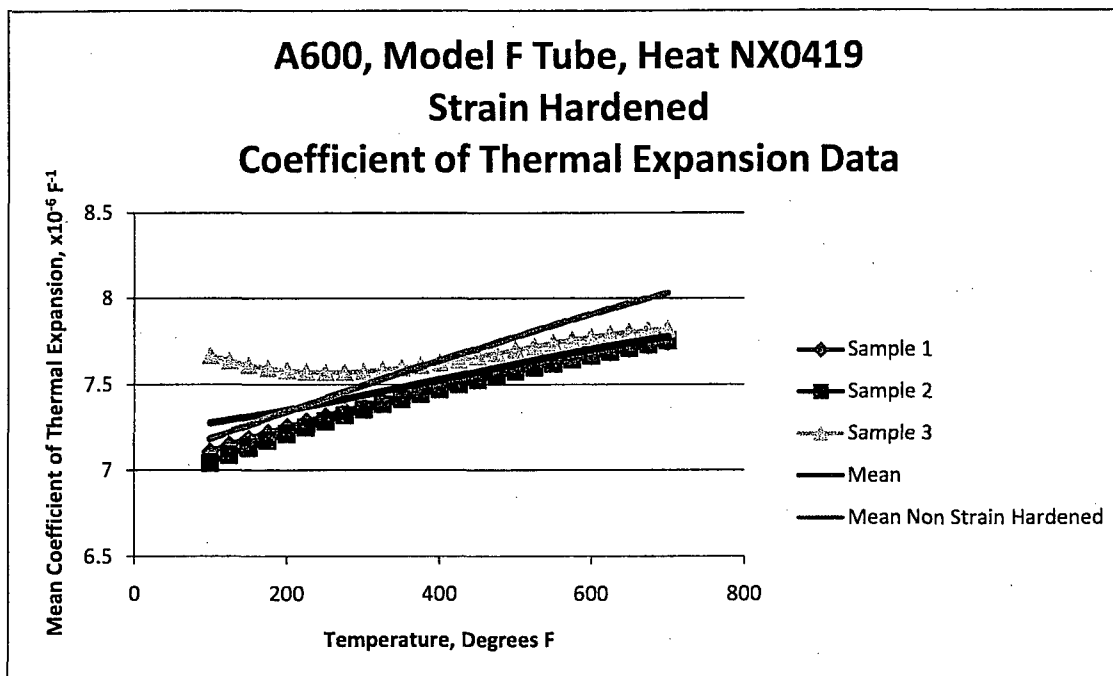


Figure 3-28 Heat-Up Tests of Strain Hardened A600 Model F Tubing, Heat NX0419

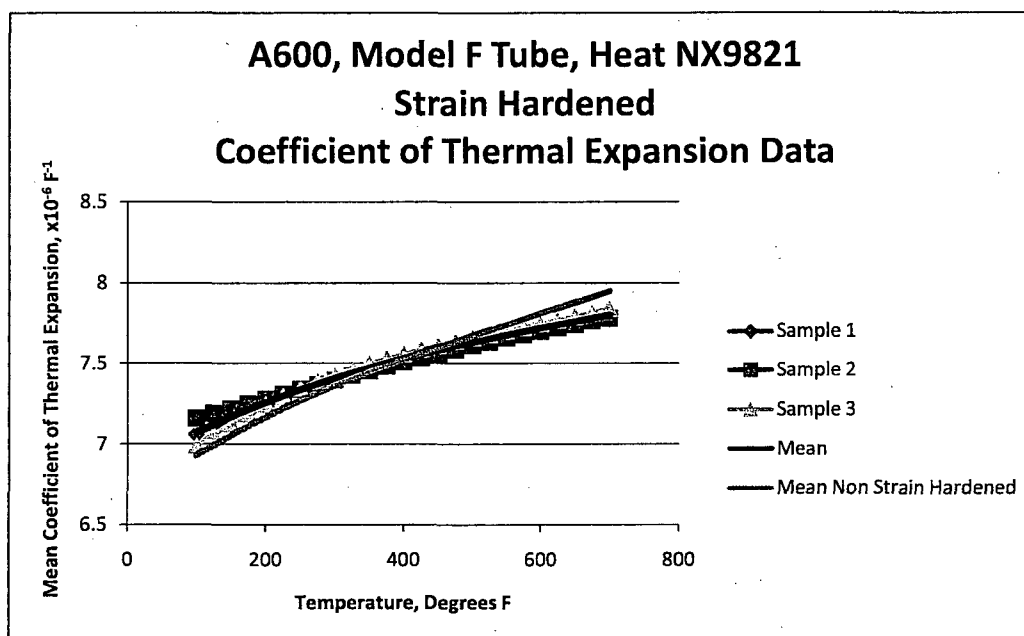


Figure 3-29 Heat-Up Tests of Strain Hardened A600 Model F Tubing, Heat NX9821

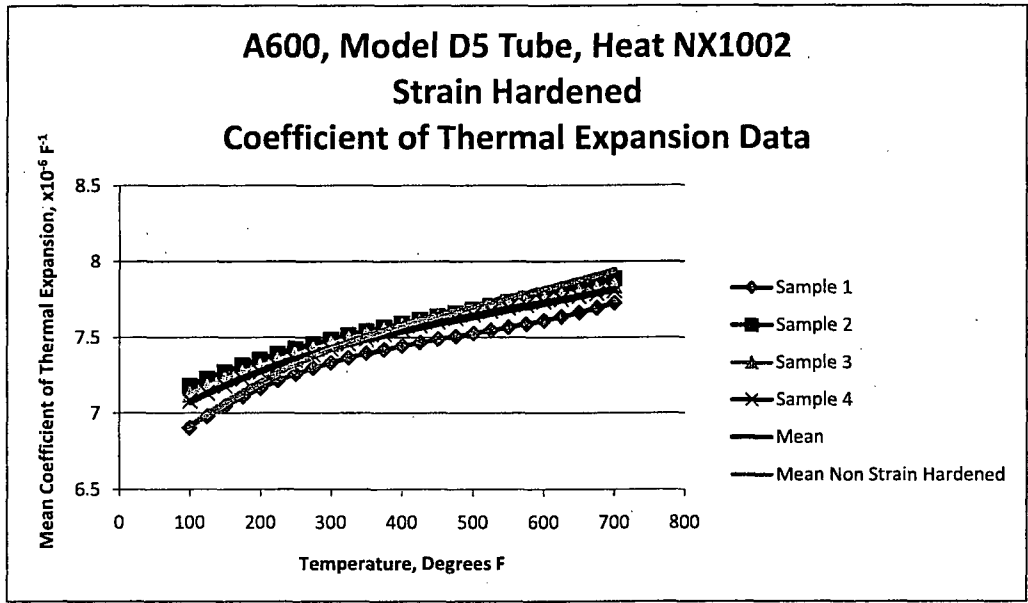


Figure 3-30 Heat-Up Tests of Strain Hardened A600 Model D5 Tubing, Heat NX1002

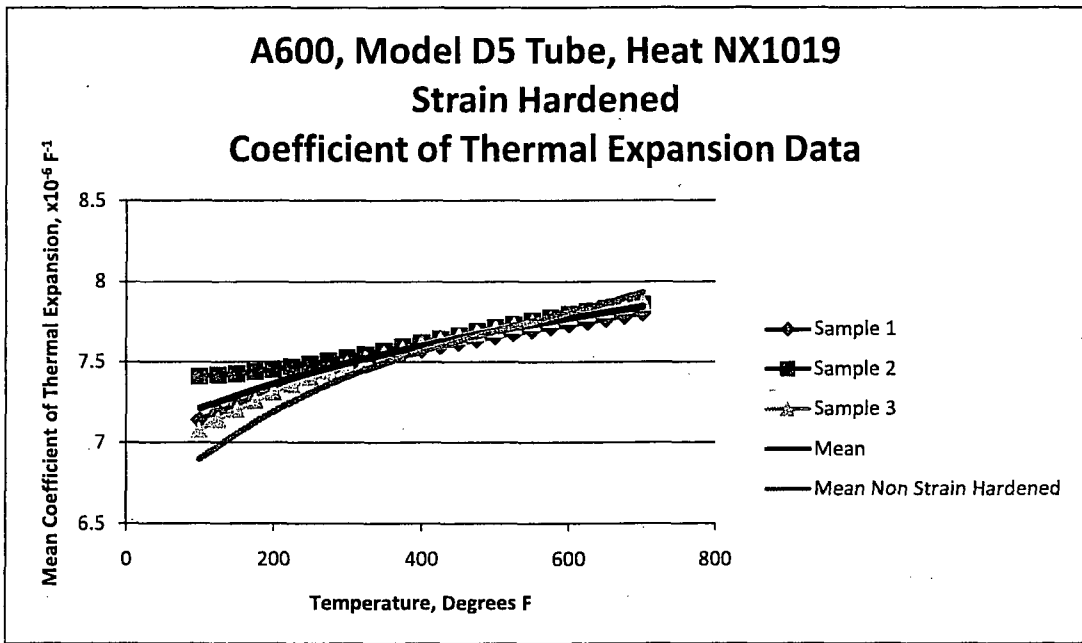


Figure 3-31 Heat-Up Tests of Strain Hardened A600 Model D5 Tubing, Heat NX1019

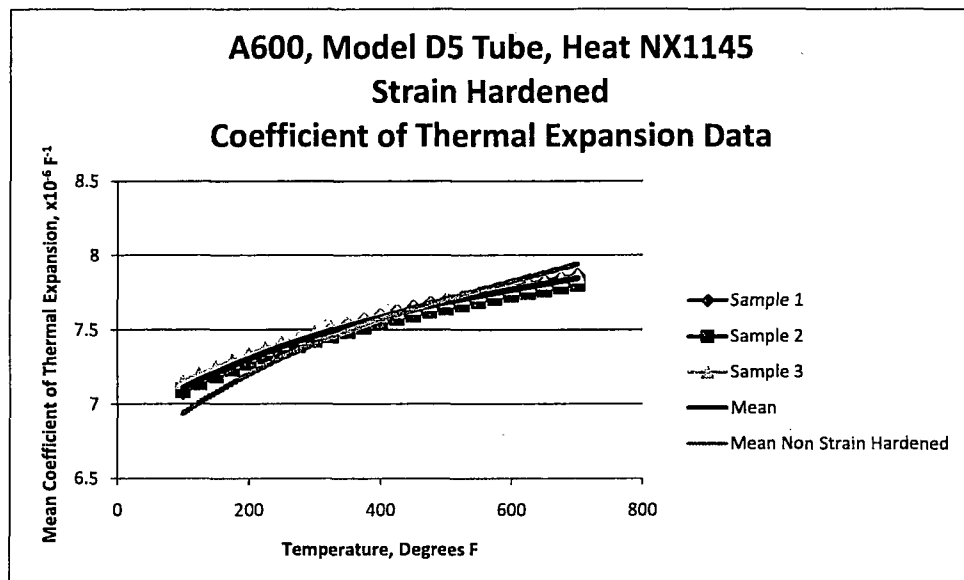


Figure 3-32 Heat-Up Tests of Strain Hardened A600 Model D5 Tubing, Heat NX1145

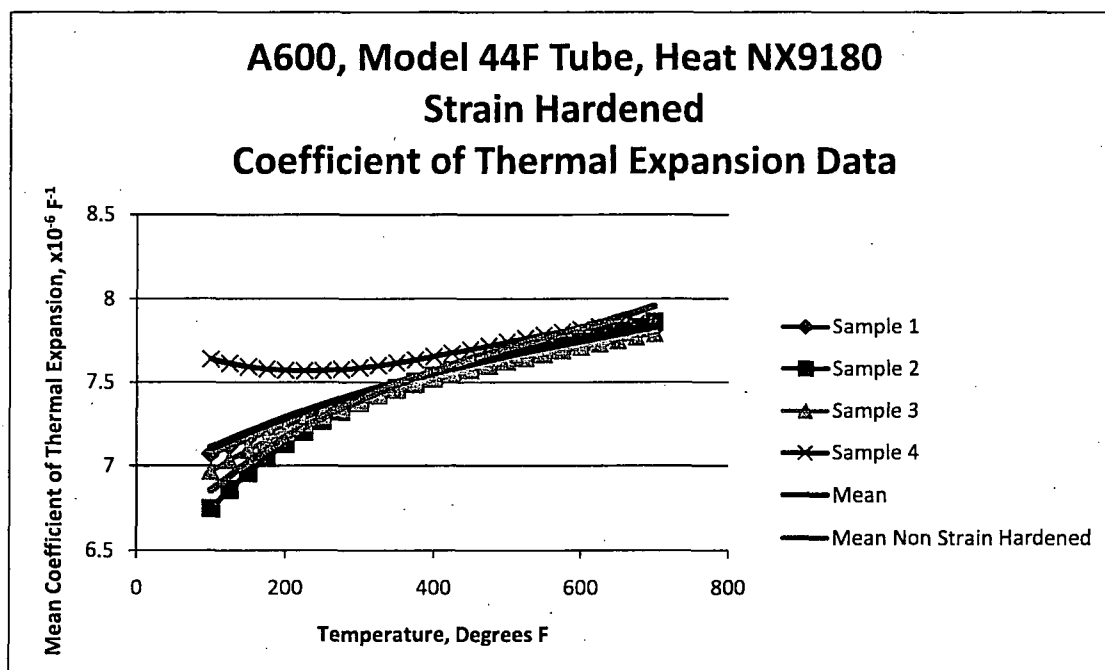


Figure 3-33 Heat-Up Tests of Strain Hardened A600 Model 44F Tubing, Heat NX9180

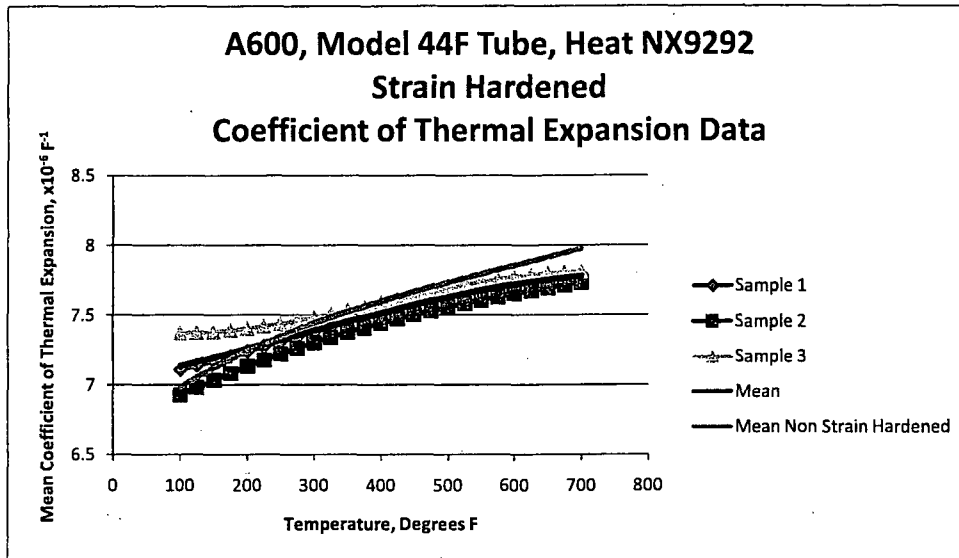


Figure 3-34 Heat-Up Tests of Strain Hardened A600 Model 44F Tubing, Heat NX9292

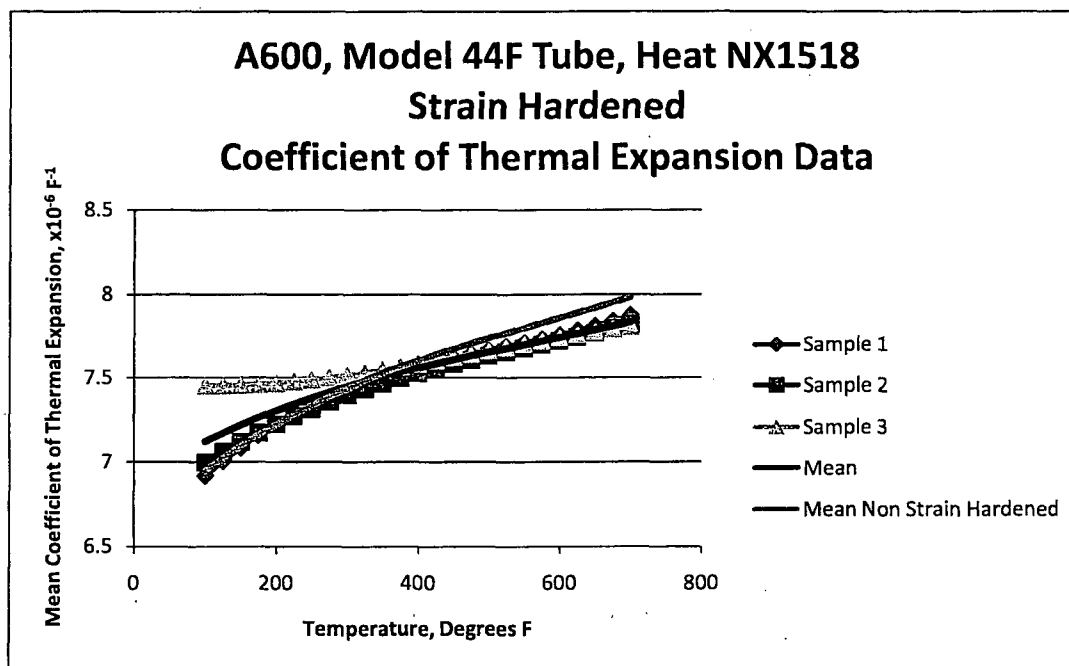


Figure 3-35 Heat-Up Tests of Strain Hardened A600 Model 44F Tubing, Heat NX1518

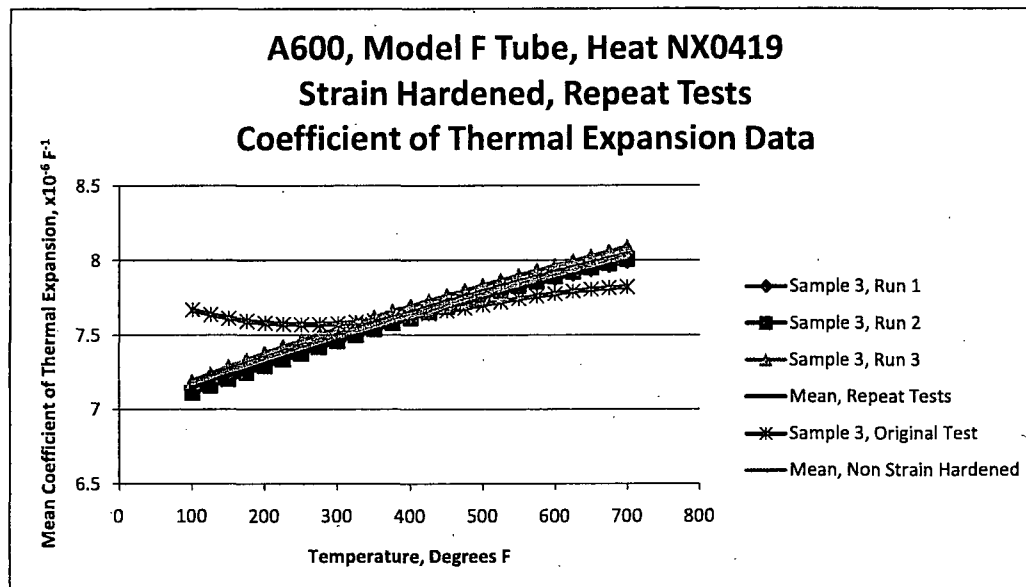


Figure 3-36 A600 Model F Tube, Heat NX0419, Repeat Test

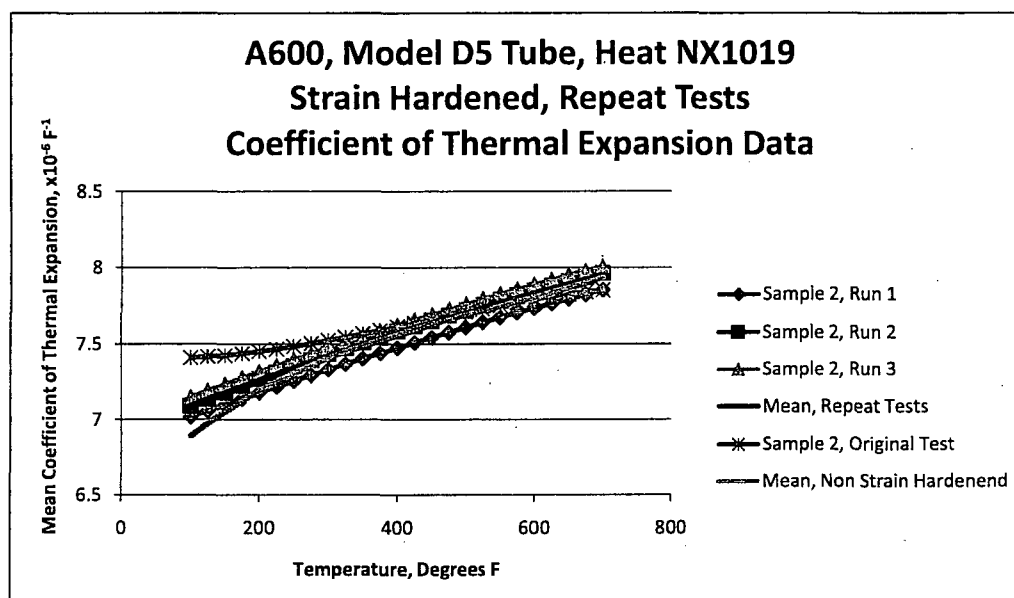


Figure 3-37 A600 Model D5 Tube, Heat NX1019, Repeat Test

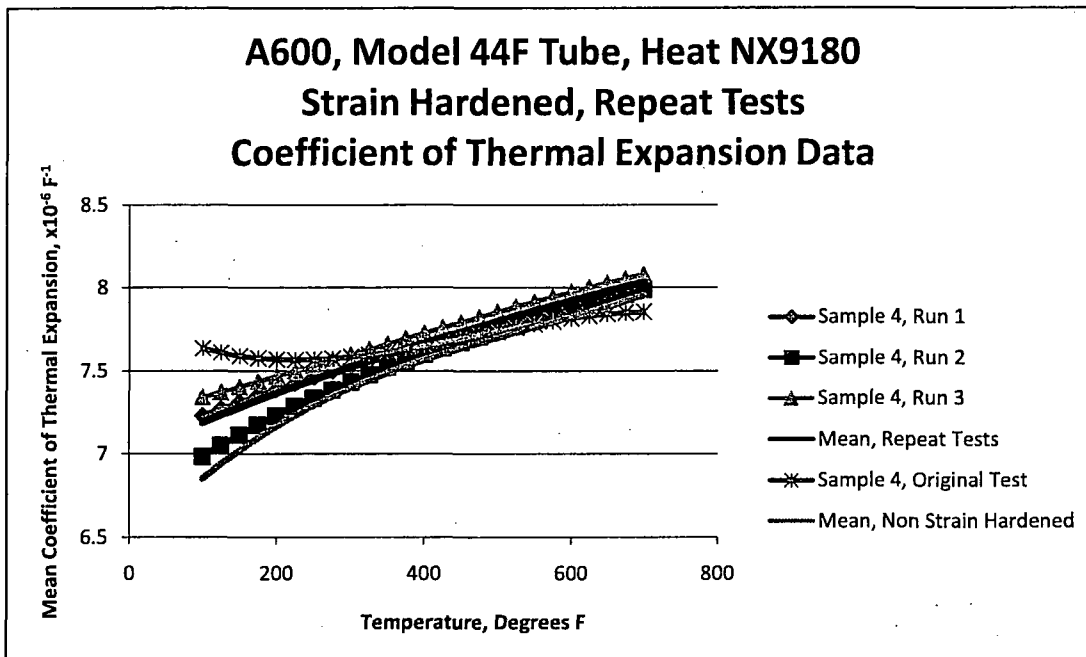


Figure 3-38 A600 Model 44F Tube, Heat NX9180, Repeat Test

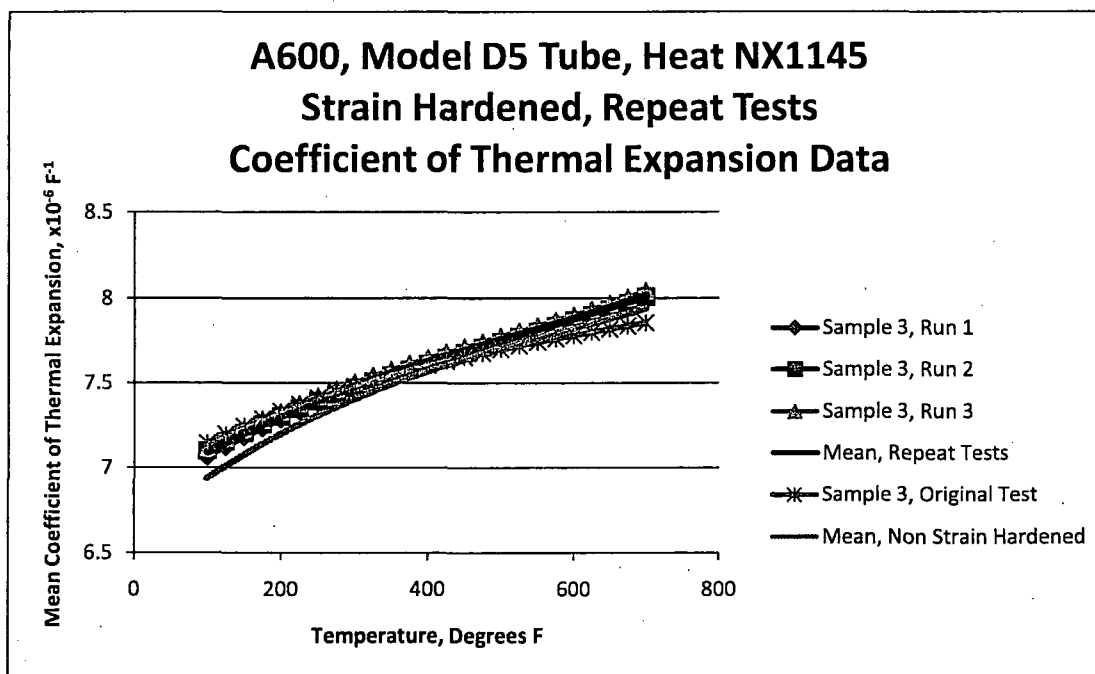


Figure 3-39 A600 Model D5 Tube, Heat NX1145, Repeat Test

## 4.0 STRUCTURAL AND LEAKAGE INTEGRITY ACCEPTANCE CRITERIA

As noted in NEI 97-06, Rev. 2 (Reference 4-1), the steam generator (SG) performance criteria identify the standards against which tube integrity is to be measured. Meeting the three performance criteria – structural integrity, accident-induced leakage and operational leakage – provides reasonable assurance that the SG tubing will remain capable of fulfilling the specific function of maintaining reactor coolant pressure boundary integrity throughout each operating cycle.

The structural integrity performance criterion from Reference 4-1 is:

*“All in-service steam generator tubes shall retain structural integrity over the full range of normal operating conditions (including startup, operation in the power range, hot standby, and cooldown and all anticipated transients included in the design specification) and design basis accidents. This includes retaining a safety factor of 3.0 against burst under normal steady-state full power operation primary-to-secondary pressure differential and a safety factor of 1.4 against burst applied to the design basis accident primary-to-secondary pressure differentials. Apart from the above requirements, additional loading conditions associated with the design basis accidents, or combination of accidents in accordance with the design and licensing basis, shall be evaluated to determine if the associated loads contribute significantly to burst or collapse. In the assessment of tube integrity, those loads that do significantly affect burst or collapse shall be determined and assessed in combination with the loads due to pressure with a safety factor of 1.2 on combined primary loads and 1.0 on axial secondary loads.”*

The accident-induced leakage performance criterion from Reference 4-1 is:

*“The primary-to-secondary accident-induced leakage rate for all design basis accidents, other than the steam generator tube rupture, shall not exceed the leakage rate assumed in the accident analysis in terms of total leakage rate for all steam generators and leakage rate for the individual steam generator. Leakage is not to exceed 1.0 gpm per SG, except for specific types of degradation at specific locations as documented in the Steam Generator Program technical specifications.”*

The operational leakage performance criterion from Reference 4-1 is:

*“The reactor coolant system (RCS) operational primary-to-secondary leakage through any one steam generator shall be limited to 150 gallons per day.”*

Reference 4-2 provides guidance for implementing NEI 97-06 and, thus, meeting the integrity assessment performance criteria described in NEI 97-06. This document reflects current industry practices and represents an acceptable method for integrity assessment.

Since 2003, an alternate repair criterion (ARC) titled H\* has been under development and Nuclear Regulatory Commission (NRC) review. The key technical issues have been: 1) the acceptance criterion for H\*, 2) the methodology for demonstrating an acceptable probability of meeting the acceptance criterion, and 3) the methodology for addressing primary-to-secondary leakage during postulated design

basis accident (DBA) conditions. The acceptance criteria for the alternate repair criteria for hydraulically expanded tube joints are based on current industry SG guidelines and are discussed in detail below.

The program elements described in Reference 4-1 provide guidance on structuring steam generator programs to meet the challenges posed by SG tube degradation. The EPRI Guidelines that form the basis of the SG program requirements are:

- PWR Steam Generator Examination Guidelines
- PWR Primary-to Secondary Leak Guidelines
- PWR Secondary Water Chemistry Guidelines
- PWR Primary Water Guidelines
- Steam Generator Integrity Assessment Guidelines
- Steam Generator In-situ Pressure Testing Guidelines

The Steam Generator Integrity Assessment Guideline document is used to develop the requirements and methodology used to meet the performance criteria defined in NEI 97-06, Rev. 2.

The availability of TSTF-449, Rev. 4, "Steam Generator Tube Integrity," was announced in the Federal Register on May 6, 2005 as part of the NRC Staff consolidated line item improvement process (CLIP). By letter dated September 3, 2005, the NRC Staff agreed with the observation that NEI 97-06, Rev. 2, "Steam Generator Program Guidelines," is consistent with Technical Specification Task Force Traveler (TSTF 449, Rev. 4) and that the adoption of TSTF-449 by all pressurized water reactors (PWRs) will result in an improved regulatory framework.

Based on the above, it is concluded that compliance with the requirements and methodologies described in NEI 97-06, Rev. 2 and the EPRI guideline documents represents the best path for regulatory approval of the proposed alternate repair criterion, H\*.

#### **4.1 STRUCTURAL INTEGRITY ACCEPTANCE CRITERIA**

The primary justification of H\* is the completion of a semiprobabilistic, whole bundle H\* depth calculation using a three-dimensional finite element analysis (3D FEA) structural model for calculating tubesheet displacement. A mean H\* value is calculated for selected radii throughout the tube bundle to represent the tube structural limit along with the consideration of appropriate uncertainties in the input parameters and material properties that affect tubesheet displacements and, therefore, the H\* pull out length. The uncertainties considered in the analysis include residual contact pressure and material properties such as Young's Modulus and the coefficient of thermal expansion of the tube and the tubesheet. Residual contact pressure (the contact pressure resulting from only the hydraulic expansion process) is assumed to be zero for this analysis, although tests show that there is a positive value of residual contact pressure. An uncertainty assessment for residual contact pressure is provided that includes the effects of variation in material yield strength, initial gap between the tube and the tubesheet before hydraulic expansion, hydraulic expansion pressure variation, and strain hardening (see Section 7.0 of this report for more detail). It is noted that assuming the residual contact pressure to be zero is a

significant conservatism in this analysis; any positive value of residual contact pressure will reduce the value of  $H^*$ .

All tubes in the SG tube bundle are shown to have an  $H^*$  value from the top of the tubesheet with a 0.95 probability with 50 percent confidence (see Section 8.0) of meeting the structural integrity performance criteria (SIPC) margin requirements as defined in NEI 97-06, Rev. 2.  $H^*$  values are calculated for normal operating and postulated steam line break conditions. Section 5.0 of this report provides the rationale for not considering the locked rotor and control rod ejection events in the calculation of the  $H^*$  value.

Tube burst cannot occur within the thickness of the tubesheet. Therefore, tube pull out is the structural failure mode of interest in the development of the  $H^*$  criterion since the tubes are radially constrained against axial fish-mouth rupture by the presence of the tubesheet. Because burst cannot occur in the tubesheet region, the structural criteria from Reference 4-2 do not directly address tube degradation in the tubesheet expansion region. However, absent other directly applicable criteria, the NRC Staff has, in prior reviews of  $H^*$  justification submittals, treated failure to meet  $H^*$  equivalent to burst.

The axial force that could produce pull out derives from the tube end cap loads due to primary-to-secondary pressure differentials associated with normal operating and design basis accident conditions. The NRC Staff, in its approval of a 17 inch non-permanent  $H^*$  (Reference 4-4), has accepted that it is adequate to determine the required engagement distance on the basis of maintaining a factor of three (3) against tube pull out under normal operating conditions and a factor of 1.4 against pull out under accident conditions. Given that the  $H^*$  distance of each individual tube has a certain probability of not meeting the performance criteria, it must be verified that the probability of any tube in the bundle in the faulted loop failing to meet the performance criteria is less than 0.05 with 50 percent confidence.

Because failure to meet  $H^*$  is interpreted as being equivalent to burst, the criteria applied for  $H^*$  justification are extremely conservative. The probability of a single tube failing to meet the  $H^*$  distance is extremely small because, for a Model 44F SG, each bundle contains 3214 tubes and the entire bundle is shown to meet  $H^*$  at the 0.95 probability. Failure to meet  $H^*$  (pull out) is defined as small incremental motion, such that a postulated tube severance may be slightly above the defined  $H^*$  distance, and not complete separation of the tube from the tubesheet. Because there is no possibility of burst of the tube within the tubesheet, and because the factors of safety of three (3) on the normal operating loads and 1.4 on design basis accident loads are already included in the justification of  $H^*$ , failure to meet  $H^*$  has negligible impact on the primary pressure boundary. Indeed, the  $H^*$  justification is based on meeting the probabilistic criteria above without any slippage.

## **4.2 PRIMARY-TO-SECONDARY LEAKAGE ACCEPTANCE CRITERIA**

Industry guidelines (Reference 4-2) permit application of either a deterministic approach or a probabilistic approach that satisfies the limit requirements for the accident-induced limiting performance criterion (AILPC) of at least 0.95 at 50 percent confidence.

Upon implementation of the  $H^*$  criterion, the existence of 100 percent through-wall cracks will be assumed below the  $H^*$  depth because no inspections of the tube below  $H^*$  will be required. Therefore, the potential for leakage of primary coolant through the crack and through the hydraulically expanded joint between the tubes and tubesheet to the secondary system must be evaluated. A detailed leakage

prediction model has been developed in support of the  $H^*$  criterion that considers the resistance to leakage within the thickness of the tubesheet. The model is based on the Darcy flow equation, which is described in detail in Section 9.0 of this report. The NRC Staff has noted that the use of the Darcy equation, which states that leakage is proportional to the applied pressure differential, is conservative relative to other alternative models such as the Bernoulli or orifice models, which assume leak rate to be proportional to the square root of the differential pressure.

The original manifestation of the leakage analysis (Reference 4-3) was known as  $B^*$ . In lieu of the original  $B^*$  approach, which required the definition of a leak loss coefficient, the margin against leakage during an accident event is now defined by developing the ratio of accident-induced leakage to normal operating leakage by the following process (see Section 9.0 for a detailed discussion):

1. Based on test data, show that the loss coefficient is constant under normal operating and design basis accident conditions.
2. Determine the ratio of design basis accident pressure differential to normal operating pressure differential.
3. Multiply the pressure differential ratio by the ratio of the dynamic viscosity ( $\mu_{NOP}$ ) during normal operating conditions to dynamic viscosity during accident conditions ( $\mu_{DBA}$ ).
4. Multiply the result of Item 3 by the ratio of effective flow path length ( $l_{NOP}$ ) under normal operating conditions to effective flow path length under steam line break conditions ( $l_{DBA}$ ).

The effective flow path length is the crevice length, above the  $H^*$  distance, over which there is contact between the tube and the tubesheet. It has been shown by the 3D FEA for the Model 44F SGs (Section 6.0) that contact between the tubes and the tubesheet is assured during all plant conditions for each tube through the entire length of the tubesheet thickness. Therefore, the effective flow path length ratio,  $l_{NOP}/l_{DBA}$ , above the  $H^*$  length for each transient condition that models primary-to-secondary leakage is 1.0.

For a postulated design basis accident, the expected increase in leakage is a function of only the increase in pressure differential that occurs across the tubesheet during the plant transient and the change in dynamic viscosity. Plant-specific leak rate factors have been developed for each of the  $H^*$  plants and are included within this report in Section 9.0.

For the condition monitoring assessment, the component of leakage from below the  $H^*$  distance observed during the prior cycle will be added to that from all other sources and compared to the allowable leakage limit for each design basis accident that models primary-to-secondary leakage. For the operational assessment, the difference in leakage from each design basis accident analysis assumption used in the plant's Final Safety Analysis Report (FSAR) and the accident leakage from all other sources will be divided by the leakage factor for the appropriate design basis accident and compared to the observed operational leakage and, if the result is less than the observed leakage, an administrative limit (for operational leakage) will be established not to exceed the calculated value.

---

### 4.3 REFERENCES

- 4-1 NEI 97-06, Rev. 2, "Steam Generator Program Guidelines," Nuclear Energy Institute, Washington, DC, May 2005.
- 4-2 Steam Generator Integrity Assessment Guidelines: Revision 2, EPRI, Palo Alto, CA, 1012987, July 2006.
- 4-3 WCAP-15932-P (Proprietary), Revision 1, "Improved Justification of Partial-Length RPC Inspection of the Tube Joints of Model F Steam Generators of Ameren-UE Callaway Plant," Westinghouse Electric Company LLC, Pittsburgh, PA, May 2003.
- 4-4 USNRC; Safety Evaluation by the Office of Nuclear Regulation Related to Amendment No. 150 to Facility Operating License No. NPF-37, Amendment No. 150 to Facility Operating License No. NPF-66---IARC SER, Amendment No. 144 to Facility Operating License No. NPF-72, and Amendment No. 144 to Facility Operating License No. NPF-77; Exelon Generating Company, LLC, Byron Station, Unit Nos. 1 and 2, Braidwood Station Units 1 and 2; Docket Nos. STN 50-455, STN 50-456 and STN 50-457; April 2007.

---

## **5.0 PLANT OPERATING CONDITIONS AND LOADINGS (MODEL 44F)**

### **5.1 NORMAL OPERATING CONDITIONS AND LOADINGS**

Table 5-1 provides values for the current steam generator (SG) thermal-hydraulic parameters during normal operating conditions for each of the H\* plants with Model 44F SGs. These conditions are used to establish the H\* distances and to determine overall leakage factors identified in this report for each plant.

### **5.2 FAULTED CONDITIONS**

Each of the faulted events are considered in this section and are described below. These include: steam line break (SLB), locked rotor (LR) and control rod ejection (CRE). The transient response curves for these events are included in Section 9.0 of this report.

Previous analyses have shown that SLB is the limiting faulted condition, with tube lengths required to resist push out during a postulated loss-of-coolant accident (LOCA) typically less than one-fourth of the tube lengths required to resist pull out during SLB (References 5-1 and 5-2). Therefore, LOCA was not considered in the H\* analysis.

#### **5.2.1 Steam Line Break**

In accordance with plant emergency operating procedures, it is expected that the operator would take action following a high energy secondary line break to stabilize the reactor coolant system conditions. The expectation for a SLB with credited operator action is to stop the system cooldown through isolation of the faulted SG and control temperature by the auxiliary feedwater system. Steam pressure control would be established by either the SG safety valves or control systems via steam dump or the atmospheric relief valves. For any of the steam pressure control options, the maximum temperature would be approximately the no-load temperature and would be well below the normal operating temperature for the plant. Subsequently, the operator would initiate a cooldown and depressurization of the reactor coolant. The peak pressure differential and asymptotic temperatures from the design specification transients are used in the structural analysis. The pertinent parameters for these transients are described in Table 5-2.

#### **5.2.2 Locked Rotor**

This accident is based on the instantaneous seizure of the reactor coolant pump with the plant operating at full power. The locked rotor can occur in any loop. Reactor trip occurs almost immediately, as a result of low coolant flow in the affected loop. Conservatively, the transient is based on a locked rotor pump for a two-loop plant. Because of the short duration of the transient, the temperatures in the hot and cold leg of the SG and secondary side that correspond to the maximum pressure differential during the locked rotor event design basis accident are used in the structural and leakage analysis. The pertinent parameters of this transient are listed in Table 5-3.

### 5.2.3 Control Rod Ejection

This accident is based on the single-most reactive control rod being instantaneously ejected from the core. This reactivity insertion in a particular region of the core causes a severe pressure increase in the reactor coolant system such that the pressurizer safety valves will lift and also causes a more severe temperature transient in the loop associated with the affected region than in the other loops. For conservatism, the analysis is based on the reactivity insertion and does not include the mitigating effects (on the pressure transient) of coolant blowdown through the hole in the vessel head vacated by the ejected rod. Like the locked rotor transient, because of the short duration of the transient, the temperatures in the hot and cold legs of the SG and secondary side that correspond to the maximum pressure differential during the design basis accident are used in the structural and leakage analysis. The pertinent parameters of this transient are listed in Table 5-4.

### 5.3 CALCULATION OF APPLIED END CAP LOADS

The tube pull out loads<sup>1</sup> (also called end cap loads) to be resisted during normal operating (NOP) and faulted conditions for a representative Model 44F plant (Turkey Point Units 3 and 4) for the hot leg are shown below. End cap load is calculated by multiplying the required factor of safety times the cross-sectional area of the tubesheet bore hole times the primary side to secondary side pressure difference across the tube for each plant condition.

Operating Condition	$\Delta P$ (psi) ( $P_{pri}-P_{sec}$ )	Area (in <sup>2</sup> ) (See Note 1)	End Cap Load (lbs.)	Factor of Safety	H* Design End Cap Load (lbs.)
a,c,e					

The above calculation of end cap loads is consistent with the calculations of end cap loads in prior H\* justifications and in accordance with the applicable industry guidelines (Reference 5-3). This approach results in conservatively high end cap loads to be resisted during NOP and faulted conditions because a cross-sectional area larger than that defined by the tubesheet bore mean diameter is assumed.

The end cap loads noted above include a safety factor of 3 applied to the normal operating end cap load and a safety factor of 1.4 applied to the faulted condition end cap loads to meet the associated structural performance criteria consistent with NEI 97-06, Rev. 2 (Reference 5-3).

Seismic loads have also been considered, but they are not significant in the tube joint region of the tubes (Reference 5-1).

H\* values are not calculated for the locked rotor and control rod ejection transients because the pressure differential across the tubesheet is essentially bounded by the SLB transient for the 3-loop Model 44F plant. For the 2-loop Model 44F plants, an H\* value is not calculated for the locked rotor event because the pressure differential across the tubesheet is bounded by the SLB event. Also, an H\* value is not calculated for the control rod ejection event because of the short duration of the pressure spike (< 5 seconds), the magnitude of the pressure increase is not significantly greater than a SLB event, (2372 psi versus 2240 psi) as well as the existence of elevated temperature in the tubesheet relative to a

<sup>1</sup> The values for end cap loads in this subsection of the report are calculated using an outside diameter of the tube equal to the mean diameter of the tubesheet bore plus 2 standard deviations.

postulated SLB event which provides greater resistance to pull out due to the greater differential thermal expansion of the tubing relative to the tubesheet.

In support of the leakage analysis provided in Section 9.0, the parameters included in Tables 5-1 through 5-5 are used to compare contact pressures during normal operating plant conditions and all design basis accident conditions for all radial locations throughout the thickness of the tubesheet.

#### **5.4 REFERENCES**

- 5-1 CN-SGDA-02-152, Rev. 1 (Proprietary), "Evaluation of the Tube/Tubesheet Contact Pressures for Callaway Model F Steam Generators," Westinghouse Electric, Pittsburgh, PA, March 2003.
- 5-2 CN-SGDA-03-133 (Proprietary), Rev. 0, "Evaluation of the H\* Zone Boundaries for Specific Model D-5 and Model F Steam Generators," Westinghouse Electric, Pittsburgh, PA, October 2003.
- 5-3 NEI 97-06, Rev. 2, "Steam Generator Program Guidelines," Nuclear Energy Institute, Washington, DC, May 2005.

**Table 5-1 Operating Conditions – Model 44F/51F Plants**

Parameter and Units		Plant				
		Turkey Point Units 3 and 4 <sup>(1)</sup>	Surry Units 1 and 2 <sup>(2)</sup>	H.B. Robinson Unit 2 <sup>(3)</sup>	Point Beach Unit 1 <sup>(4)</sup>	Indian Point Unit 2 <sup>(5)</sup>

a,c,e

**Table 5-2 Steam Line Break Conditions**

Parameters and Units	Turkey Point Units 3 and 4	Surry Units 1 and 2	H. B. Robinson Unit 2	Point Beach Unit 1	Indian Point Unit 2

a,c,e

**Table 5-3 Locked Rotor Event Conditions**

Parameters and Units	Turkey Point Units 3 and 4	Surry Units 1 and 2	H. B. Robinson Unit 2	Point Beach Unit 1	Indian Point Unit 2

a,c,e

**Table 5-4 Control Rod Ejection Event Conditions**

Parameters and Units	Turkey Point Units 3 and 4	Surry Units 1 and 2	H. B. Robinson Unit 2	Point Beach Unit 1	Indian Point Unit 2

a,c,e

**Table 5-5 H\* Design End Cap Loads for Normal Operating Plant Conditions, Locked Rotor and Control Rod Ejection for Model 44F Plants**

Plant	Low $T_{avg}$ End Cap Load w/Safety Factor (lbf)	High $T_{avg}$ End Cap Load w/Safety Factor (lbf)	Locked Rotor End Cap Load (lbf)	Control Rod Ejection End Cap Load (lbf)

a,c,e

## 6.0 STRUCTURAL ANALYSIS OF THE TUBE-TO-TUBESHEET JOINT

The H\* structural analysis consists of four separate models as shown in the process description in Section 1.0. Tubesheet deflections are calculated using a three-dimensional finite element analysis (3D FEA) model. The tubesheet displacements are input to a Microsoft Excel® spreadsheet model (Figure 1-1, H\* Analysis Process for H\*). The spreadsheet model calculates the contact pressure between the tubes and the tubesheet as a function of radial and axial position in the tubesheet. The contact pressure is transformed into an axial pull out resistance through friction and shear between the tube outside diameter (OD) surface and the tubesheet tube bore inside diameter (ID) surface. The pull out resistance is integrated as a function of axial position and compared to the applied end cap loads and axial forces. The axial distance below the top of the tubesheet (TTS) where the axial pull out resistance is equal to or greater than applied pull out forces is the calculated H\* depth. In the following discussions, the structural analysis will commonly be referred to as the contact pressure analysis.

The third model is an Microsoft Excel® spreadsheet model that calculates the residual contact pressures (RCP) from the available pull out test data and provides the RCP as input to the H\* Integrator model. In the current application, RCP is assumed to be zero (0 psi) and the RCP model is not utilized. A fourth finite element model is utilized to calculate the variability influence factors for residual contact pressure. Additional finite element models and results are used to support the H\* analysis. Supporting analyses were performed to address specific issues such as definition of the “worst tube” in the bundle, tubesheet bore dilation effects on contact pressure, etc., that validate the use of the 3D FEA model.

The structural analysis for H\* has evolved since the Wolf Creek License Amendment request in 2006 (see References 6-16 and 6-20). This evolution resulted from a number of studies that utilized the state-of-the-art structural analysis methods to benchmark the methods utilized in the Wolf Creek request. This report section describes the technical basis of these models and the benchmarking analyses performed to test and validate the model results.

### 6.1 RESULTS SUMMARY

The H\* structural analysis conservatively calculates the tubesheet deflections as input to the analysis of the contact pressure distribution between the tube and the tubesheet for an assumed length of tube in the limiting region of the steam generator (SG) bundle to resist the applied pull out forces. The limiting region of the tubesheet is defined as that region of the tubesheet in which the deflections are calculated to be maximized, resulting in the largest value of H\*. The length of tubing considered is the predicted length required to equilibrate the design basis pull out forces. The results of the structural analysis, for the bounding Model 44F SG in the fleet, show that a length of [ ]<sup>a,c</sup> inches provides sufficient engagement length into the tubesheet to resist the applied pull out loads during normal operations and limiting faulted conditions, assuming that all input variables are at their mean value and the crevice pressure adjustment to the final tube length is excluded. Figure 6-1 shows the distribution of the mean H\* values as a function of tubesheet radius in the limiting sector of the tubesheet. The applied pull out loads include the required safety margins prescribed in NEI-97-06, Rev. 2 (Reference 6-2) and the analysis of the operating conditions and design transients meets the requirements defined in the ASME Code (Reference 6-3). The mean analysis results for H\* are references in (Reference 6-39).



**Figure 6-1 Mean H\* Values for the Limiting Model 44F Plant (w/o crevice pressure adjustment)**

### 6.1.1 Introduction

The H\* analysis determines the required engagement length of an SG tube into the tubesheet necessary to resist pull out forces. Pull out forces develop from the temperatures and pressures that occur during normal, upset and accident operating conditions in the SG (see Section 5.3 for the calculation of the applicable pull out forces). The pull out load on a tube is resisted by local tube thermal and pressure-induced deformations and contact that transfer the load on a tube to the surrounding tubesheet material in shear via friction forces. The ability of a tube to transfer the pull out loads to the tubesheet through friction is directly related to the magnitude of the contact pressure between the inner diameter of the tubesheet bore and the outer diameter surface of the tube.

The temperatures and pressures that develop the pull out forces on the tube also act to deform the SG tubesheet such that it will both expand in the radial direction and deflect in the transverse (thickness) direction. The deformations in the perforated region of the tubesheet affect the resistance of the SG tubes to the applied pull out loads because a deformation that acts to increase the tube-hole size relative to the initial undeformed tube-hole configuration will decrease the contact pressure between the tube and the tubesheet. The reverse is also true; a decrease in the tube hole size relative to the initial undeformed tube hole configuration will increase the contact pressure between the tube and the tubesheet. Other factors, such as Poisson contraction of the tube cross section and the potential for fluid to be present between the tube outer diameter and the tubesheet inner diameter, also affect the contact pressure. The distribution of the contact pressure between the tube and the tubesheet varies as a function of radial position in the tubesheet and elevation within the tubesheet.

The H\* structural analysis that provides the tubesheet radial and axial deflections utilizes a 3D finite element model that is described in Section 6.2. Section 6.2.2 discusses the analysis input. Section 6.2.3

discusses the determination of the limiting region of the tubesheet with respect to the tube pull out resistance. Section 6.2.4 discusses the radius specific treatment of the local tubesheet stiffness in the H\* structural model. Section 6.2.5 discusses the effects of tubesheet hole dilation on the leakage and structural aspects of the H\* analysis. Section 6.2.6 discusses the modeling of the SG divider plate and how the potential for degradation of the divider welds is accounted for in the analysis. Section 6.3 discusses the effects of tubesheet rotation and deformation and Section 6.4 discusses how the previous results are used to calculate the tube-to-tubesheet contact pressure. Section 6.4 also discusses the benchmark models used to validate the 3D finite element model.

The contact pressure results presented in this section include detailed sensitivity studies on the effect of material variability, SG design variability, variability in SG tube installation, operating condition variability and the effect of SG structures, such as the divider plate, that can alter the deflection of the tubesheet and tube bore. The finite element models that support the contact pressure analysis were compared to an independent analysis created by Argonne National Laboratories (ANL) using a different FEA code (ABAQUS). The ANL ABAQUS models produced essentially the same results when similar input conditions were used. The results described in this report conservatively bound the requirements for both the hot leg and the cold leg in any Model 44F SG.

The contact pressure results in this report are based on a proven theory of elasticity model (Reference 6-18) that uses results from the supporting finite element analyses as input. The results of the theory of elasticity model were benchmarked using alternative finite element models and shown to be conservative (see Section 6.4.5).

### 6.1.2 Evolution and Development of the H\* Structural Model

Prior analyses for H\* (Reference 6-24) utilized a two-dimensional (2D) axisymmetric structural model to calculate tubesheet displacements. The 2D model results came from a linear superposition of unit loads. In the linear superposition method, unit loads, both thermal and pressure, were applied to obtain deflections that were then scaled with a ratio according to the applicable pressure and temperature conditions to obtain the results for specific conditions such as normal operating conditions (NOP) or accident loading conditions. Due to temperature differences between different structures in the lower SG complex on the order of [ ]<sup>a,c</sup> °F or more, different deflection results are obtained when the reference case for the model is changed. For example, when the model is loaded with pressures and temperatures similar to NOP conditions and those results are then scaled to represent steam line break (SLB) conditions, the results are different than when the model is directly loaded with pressures and temperatures similar to SLB. The discovery of this difference between the scaled results and the results of directly applying condition specific loads meant that new models were necessary to benchmark the 2D structural modeling approach. Further, although the 2D model was an axisymmetric model, this use of axisymmetry was questioned because of the presence of the uni-directional divider plate and tube lane. Questions were also raised about the effectiveness of the divider plate as a structural member. A three-dimensional (3D), non-axisymmetric, finite element analysis (FEA) model was created to benchmark the 2D model results. The initial goal of the 3D finite element model was to provide a comparison to the previously established 2D axisymmetric finite element model of the tubesheet, channelhead and stub barrel. The development of 3D FEA models to benchmark the 2D axisymmetric model led to the decision to replace the 2D model with the 3D FEA model.

The 3D FEA model was not initially considered as the reference analysis basis for H\* because of a difficulty in obtaining the nodal outputs at the exact locations required by the H\* integration routine. Therefore, the initial function of the 3D FEA model was to perform benchmark analyses to verify the results of the 2D axisymmetric model. However, processes were developed to overcome the node-matching issue with the H\* integration routine during the continued evolution of the 3D FEA model. Because of this, and because the 2D axisymmetric model utilized the code WECAN (a finite element program that is no longer supported by Westinghouse or any other organization) a decision was made to adopt the state-of-the-art 3D FEA analysis model as the reference model for H\* calculations.

The 3D finite element model allows for more detailed modeling of the lower SG complex than an axisymmetric finite element model. Some of the details that cannot be included in an axisymmetric finite element model are:

1. Tubesheet Tube Lane
2. Bearing/Support Pads
3. Divider Plate
4. Simultaneously Applied Hot Leg and Cold Leg Conditions

These non-axisymmetric features in the SG have a significant effect on the radial displacement of the tubesheet during all modeled plant operating conditions.

The force integration spreadsheet that is used to determine the H\* distance was developed by assuming a radially and axially fixed nodal map of the tubesheet to provide a structured force integration and H\* tubesheet mapping capability. The mesh for the perforated tubesheet region (the region of interest in the model) is seeded in a very specific fashion with [ ]<sup>a,c,e</sup> divisions over the radius of the tubesheet and [ ]<sup>a,c,e</sup> nodes through the thickness of the tubesheet. For example, Figure 6-5 shows a plot of the elements (also known as a screen shot) of a typical 2D axisymmetric finite element mesh of the lower SG complex without a tubesheet (TS) support ring.

The 3D model also has [ ]<sup>a,c,e</sup> horizontal divisions over the radial dimension and it also has [ ]<sup>a,c,e</sup> nodes through the thickness of the tubesheet in the region of interest. The 3D mesh is seeded without a bias at the top of the tubesheet (TTS) and the bottom of the tubesheet (BTS) but additional nodes are included in the model. The choice of higher order tetrahedral elements in the 3D perforated tubesheet region allows for interpolation of the tubesheet displacements at any elevation or radial location required.

The mesh density in both the 3D and the axisymmetric model was selected to produce a spatially converged result that gives a smooth radial displacement output in the perforated region of the tubesheet. Further refinement in the 3D finite element mesh did not yield a significant difference [ ]<sup>a,c,e</sup>% in tubesheet displacement for the perforated region. [ ]

[ ]<sup>a,c,e</sup>. Figure 6-6 shows a picture of a typical 3D finite element mesh of the lower SG complex without a tubesheet support ring.

The 3D finite element mesh was also defined azimuthally, with the mesh seeding at the 45° and 90° planes being equal to the mesh seeding and divisions at the 0° plane. See Figure 6-7 for a top plane view of the tubesheet mesh that shows the divisions at the 0°, 45° and 90° planes. See Figure 6-7 and Figure 6-8 for pictures of the rear of the 3D mesh.

There are a total of [ ]<sup>a,c,e</sup> solid higher order (10-node) tetrahedral and higher order quadrilateral elements in a typical 3D finite element model of the Model 44F SG. There are [ ]<sup>a,c,e</sup> nodes in the 3D model for a total of [ ]<sup>a,c,e</sup> degrees of freedom. Plant-specific finite element models may have more or less nodes than a typical Model 44F, but, that does not affect the final results of the analysis.

### 6.1.2.1 Comparison of 2D and 3D Model Boundary Conditions

It is expected that the results from a 3D finite element analysis of the lower SG complex and those from a 2D axisymmetric analysis will yield different results. The 3D analysis is capable of responding more realistically to variations in the operating conditions and material properties. The tubesheet displacements calculated from the 3D analysis accurately reflect the applied loading conditions for the material properties used in the analysis.

The results in Sections 6.2.1 through 6.2.3 were not considered in the tube-to-tubesheet contact pressure analyses prior to 2008. This is because the effect of the non-axisymmetric structures and boundary conditions could not be included in the axisymmetric model used to analyze the tubesheet displacements due to thermal and pressure load effects. Similarly, the effect of the non-axisymmetric structures on the deformations of the tube bore could not be included in the analysis of the contact pressure. The prior axisymmetric finite element analysis used displacement, pressure and temperature boundary conditions that are different from the ones discussed in Sections 6.2.2.2 through 6.2.2.5. The following sections summarize the boundary condition differences between a 3D analysis and a 2D axisymmetric analysis of the lower SG complex.

#### 6.1.2.1.1 Displacement Boundary Conditions

An axisymmetric model is “pinned” with respect to the radial direction along the central axis of the model. This means that all vertical and radial displacements are calculated with respect to a fixed central axis that cannot translate or deflect in any direction. In the case of a SG with a tubesheet support ring, this requirement will alter the displaced shape of the tubesheet due to thermal and pressure loads. This condition also increases the tubesheet bow in the case of a tubesheet without a tubesheet support ring. However, the contact pressure results generated from the 2D axisymmetric tubesheet model displacements have been shown to be conservative when compared to the results of a contact pressure analysis using 3D tubesheet model displacements.

#### 6.1.2.1.2 Applied Pressure Loads

The axisymmetric model cannot calculate the azimuthal variation of the tubesheet displacement due to pressure loads. The axisymmetric model also cannot calculate the deflection of the tubesheet for different simultaneously applied hot leg and cold leg primary fluid pressures.

### 6.1.2.1.3 Applied Thermal Loads

The axisymmetric model cannot calculate the deflection of the tubesheet for different simultaneously applied hot leg and cold primary fluid temperatures. The axisymmetric model over-estimates the tubesheet deflections due to thermal loads because the non-axisymmetric structures in the model influence how the tubesheet can deflect and rotate. Eliminating the non-axisymmetric structures from the analysis means that the stiffness of the tubesheet in those regions will be significantly reduced at operating conditions and, therefore, the estimated thermal displacements will be greater.

### 6.1.2.1.4 Applied Boundary Conditions for the Linear Superposition Approach for Combining Tubesheet Axisymmetric Displacements

The tubesheet displacement calculations for the tube-to-tubesheet contact pressure prior to 2008 were based on unit load combinations, not the actual applied pressures and temperatures. The radial tubesheet displacement was recorded during each unit load case as a function of tubesheet radius and elevation. The unit load approach consisted of the following pressure cases:

- 1000 psia pressure on all primary faces at room temperature ( $\Delta R_{PRI}$ )
- 1000 psia pressure on all secondary faces at room temperature ( $\Delta R_{SEC}$ )

The unit load approach consisted of the following temperature cases:

- 500°F temperature difference on the stub barrel ( $\Delta R_{SB}$ )
- 500°F temperature difference on the channelhead ( $\Delta R_{CH}$ )
- 500°F temperature difference on the tubesheet ( $\Delta R_{TS}$ )

with all other structures held at room temperature during each applied unit temperature load case. The stress free reference, or ambient room temperature, is assumed to be 70°F for each material in the analysis. The tubesheet displacement for a specific operating condition was then calculated using the equation:

a,c,e

The values for  $\Delta T_{CH}$ ,  $\Delta T_{SB}$  and  $\Delta T_{TS}$  were taken from the change in the fluid temperatures during each operating condition (relative to room temperature). The maximum radial tubesheet deflection predicted using this method for a Model 44F SG was approximately [ ]<sup>a,c,e</sup> inch. The minimum radial tubesheet deflection predicted using this method for a Model 44F SG was approximately [ ]<sup>a,c,e</sup> inches. In comparison, the maximum tubesheet deflection for a Model 44F SG using the 3D finite element analysis is approximately [ ]<sup>a,c,e</sup> inch or less. The minimum tubesheet deflection for a Model 44F SG using the 3D finite element analysis is approximately [ ]<sup>a,c,e</sup> inch.

#### **6.1.2.1.5 Limits of the Linear Superposition Approach for Calculating Tubesheet Displacement**

The purpose of the linear superposition method was to reduce the number of FEA models necessary to calculate the contact pressure. In theory, it also allowed for the simple calculation of a number of different effects on the contact pressure by simply changing the operating temperatures and pressures when post-processing the displacement results. However, there are three fundamental rules of a linear superposition analysis that must be considered when using the method for an analysis of the lower SG complex. The three fundamental rules of the linear superposition analysis are:

1. All connected structures should be at similar temperatures.
2. All connected structures should respond to changes in the environment in a linear fashion.
3. All connected structures should respond to changes in the applied load in a linear fashion.

The secondary face of the tubesheet and the stub barrel are at significantly different temperatures during all operating conditions. The smallest temperature difference between the primary fluid and the secondary fluid is more than 100°F. The thermal expansion coefficient and modulus of elasticity for the tubesheet, stub barrel and channelhead change at different rates with respect to temperature. This means that the way that each structure responds to changes in temperature is not necessarily linear with respect to changes in another structure's material property. Also, the stiffness of the connection between the tubesheet and the channelhead, or the tubesheet and the stub barrel, is very different when the two structures are at operating temperatures versus one or the other being at a room temperature. The tubesheet displacements cannot be accurately predicted based on linear scaling of the unit load results for the stub barrel and channelhead. This is especially true for different operating conditions with a large difference in primary and secondary fluid temperatures. For example, calculating the tubesheet displacements from a 500°F applied temperature difference and then scaling those results to represent a SLB condition ( $\Delta T = 350^\circ\text{F}$ , or more) will give dramatically larger displacement results compared to calculating the tubesheet displacements from a 350°F temperature difference. This difference is exacerbated when variations in material properties are considered because the material stiffness of the connections between the tubesheet and the attached structures change at different rates with respect to temperature. The end result is that the calculated tubesheet displacements from a linear superposition of axisymmetric finite element results will have a very different distribution and magnitude compared to the applied conditions on a 3D finite element model.

The 3D finite element analysis results are the preferred analysis basis for the tube-to-tubesheet contact pressure analyses. This is because the 3D finite element analysis more correctly captures the SG operating conditions and accurately includes the significant structures in an operating SG. The 3D finite element analysis also responds to variations in input parameters in a more realistic fashion.

## **6.2 3D FINITE ELEMENT TUBESHEET DISPLACEMENT ANALYSIS**

### **6.2.1 Description of the Tubesheet Complex Model**

The channelhead, tubesheet, divider plate and lower shell (i.e., stub barrel) are typically referred to as the lower steam generator (SG) complex. See Figure 6-9 for a picture of the important structures in the lower SG complex model. The modeling of the tubesheet itself is broken up into two different material models

in a non-axisymmetric fashion. There are four linear elastic material models in the analysis and one orthotropic elastic material model in the finite element analysis.

The tubesheet in a typical Model 44F SG consists of a large perforated region where the tube bundle is expanded into the tubesheet, a solid (non-perforated) lane of tubesheet material between the cold leg and hot leg sides of the bundle, and a ring of solid material on the periphery of the interior of the SG. In the Model 44F SG without tubesheet support rings, the lower SG complex is supported by four bearing pad connections on the channel at roughly 45° to either side of the tube lane. See Figure 6-10 for details of the different regions of the tubesheet.

The displacement inputs to the H\* integration model are generated by a 3D finite element model created in ANSYS WorkBench, Versions 10 and 11. ANSYS WorkBench is a computer aided engineering (CAE) and modeling tool designed as a front end and interactive graphic user interface for the finite element code ANSYS. Although created initially to benchmark the 2D axisymmetric model (Reference 6-20), the 3D FEA models were modified to represent plant-specific geometry and design conditions to determine the limiting plant among the Model 44F population.

Each plant or SG design-specific model includes the appropriate solid representations for the stub barrel (or lower shell), the perforated region of the tubesheet, the solid portion of the tubesheet and the support ring (if it is present in the specific plant of interest), the divider lane, the divider plate, and the channelhead. The combination of these structures is referred to as the lower SG complex. An undegraded divider plate is included in the model. Tubesheet displacements are scaled to account for potential divider plate degradation in post-processing. The perforated region of the tubesheet is modeled using effective orthotropic properties to account for the square pitch tube bore perforations. All other solid structures are modeled using linear, temperature dependent, material properties. The material input properties are taken from the 1989 edition of the ASME Boiler and Pressure Vessel Code.

The perforated region of the tubesheet is modeled using effective orthotropic elastic material properties according to Slot (Reference 6-5). The tube lane (also referred to as the divider lane) and the divider plate (also referred to as the partition plate) represent significant structures in the tubesheet complex and both affect the radial displacements of the tubesheet. The radial displacement of the tubesheet with a divider lane and an intact divider plate during NOP is typically on the order of [ ]<sup>a,c,e</sup> inch, or less. The vertical displacement of the tubesheet with a divider lane and an intact divider plate during NOP is typically on the order of [ ]<sup>a,c,e</sup> inch, or less. The original analysis for the Model 44F and Model 51-type SGs noted that including the tube lane reduces the vertical displacements at the centerline of the tubesheet by more than [ ]<sup>a,c,e</sup>% (Reference 6-6), relative to a tubesheet with no divider lane. The original analysis for the Model 44F and Model 51-type SGs noted that including a divider plate without fully considering the channelhead-to-divider plate welds reduces the vertical displacements at the centerline of the tubesheet by at least [ ]<sup>a,c,e</sup>% (Reference 6-28), relative to a tubesheet without a divider plate. The divider plate reduces both the radial and vertical displacements of the tubesheet because it restricts the rotation of the tubesheet and vertical displacement of the tubesheet. In fact, if the vertical connection of the divider plate to the primary face of the tubesheet is assumed to be severed, the net reduction in displacement is still at least [ ]<sup>a,c,e</sup> % (Reference 6-7) due to the remaining welded connections between the divider plate and the channelhead reducing the rotation of the tubesheet. If all of the divider plate connections are considered intact, the tubesheet displacements are reduced by

approximately [ ]<sup>a,c,e</sup> % (Reference 6-7). See Section 6.2.6 for a detailed discussion of divider plate modeling.

The tubesheet support ring is another significant structure to consider when estimating tubesheet displacements. The tubesheet support ring acts to “girdle” the perforated region of the tubesheet and is the structure where a SG is typically supported and connected to the containment structure. None of the H\* plants with Model 44F SG have a support ring. If a SG does not have a support ring, the boundary conditions that apply to the SG change to reflect the required bearing support pad structures. The bearing support pad structures reduce the displacement of the channelhead structure and have less of an effect on the tubesheet displacements. See Table 6-7 for a list of the plants in the H\* fleet with and without tubesheet support rings. The operating parameters and conditions for all of the Model 44F plants in the H\* fleet are listed in Table 5-1. The applied operating pressures and temperatures for each analysis condition, and for each operating SG in the H\* fleet, are listed in Section 5.0 of this report.

The tubesheet is a thick plate and the application of the pressure load results in a generalized plane strain condition. The pitch of the square, perforated hole pattern is [ ]<sup>a,c,e</sup> inch and the tubesheet hole diameter is conservatively assumed to be [ ]<sup>a,c,e</sup> inch, noting that the nominal bore diameter is approximately [ ]<sup>a,c,e</sup> inch. The inside diameter (ID) of the tube after expansion into the tubesheet is taken to be about [ ]<sup>a,c,e</sup> inch based on an approximation of [ ]<sup>a,c,e</sup> % thinning during installation associated with constant material volume. Equivalent properties of the tubesheet are calculated without taking credit for the stiffening effect of the tubes, which results in a conservatively calculated tubesheet deflection.

The tubesheet ligament efficiency,  $\eta$ , is defined as:

$$\eta = \frac{h_{\text{nominal}}}{P_{\text{nominal}}}$$

$$\begin{aligned} h_{\text{nominal}} &= P_{\text{nominal}} - d_{\text{maximum}} \text{ (ligament thickness)} \\ P_{\text{nominal}} &= [ ]^{\text{a,c,e}} \text{ inch, the pitch of the square hole pattern} \\ d_{\text{maximum}} &= [ ]^{\text{a,c,e}} \text{ inch, the tube hole diameter} \end{aligned}$$

Therefore,  $h_{nominal} = [ \quad ]^{a,c,e}$  inch (i.e.,  $[ \quad ]^{a,c,e}$  inch and  $\eta = [ \quad ]^{a,c,e}$  when the tubes are not included. From Slot (Reference 6-5) the in-plane mechanical properties for Poisson's ratio of 0.3 are:

		Value
=	=	
=	=	
=	=	
=	=	
=	=	
=	=	

where the subscripts  $P$ ,  $d$  and  $y$  refer to the pitch, diagonal and thickness directions, respectively. These values are substituted into the expressions for the anisotropic elasticity coefficients given previously. The coordinate system used in the analysis and derivation of the tubesheet equations is given in Reference 6-4. Using the equivalent property ratios calculated above in the equations presented at the beginning of this section yields the elasticity coefficients for the equivalent solid plate in the perforated region of the tubesheet for the finite element model.

The three-dimensional structural model is used in two different analyses: 1) a static structural analysis with applied pressure loads at a uniform temperature and 2) a steady-state thermal analysis with applied surface loads. The solid model and mesh is the same in the structural and thermal analyses but the element types are changed to accommodate the required degrees of freedom (e.g., displacement for structural, temperature for thermal) for each analysis. The tubesheet displacements for the perforated region of the tubesheet in each analysis are recorded for further use in post-processing. Figure 6-2 is screen shots of the three-dimensional solid model of the Model 44F SG. Figure 6-3 shows the entire 3D model mesh.

Figure 6-3 3D Model Mesh Screen Shot



Figure 6-2 Solid 3D Model of a Typical 44F SG

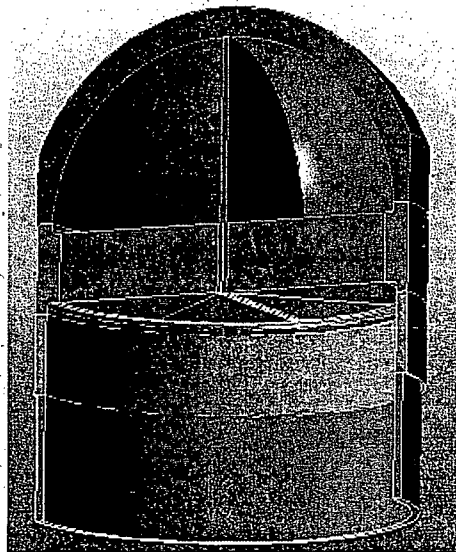
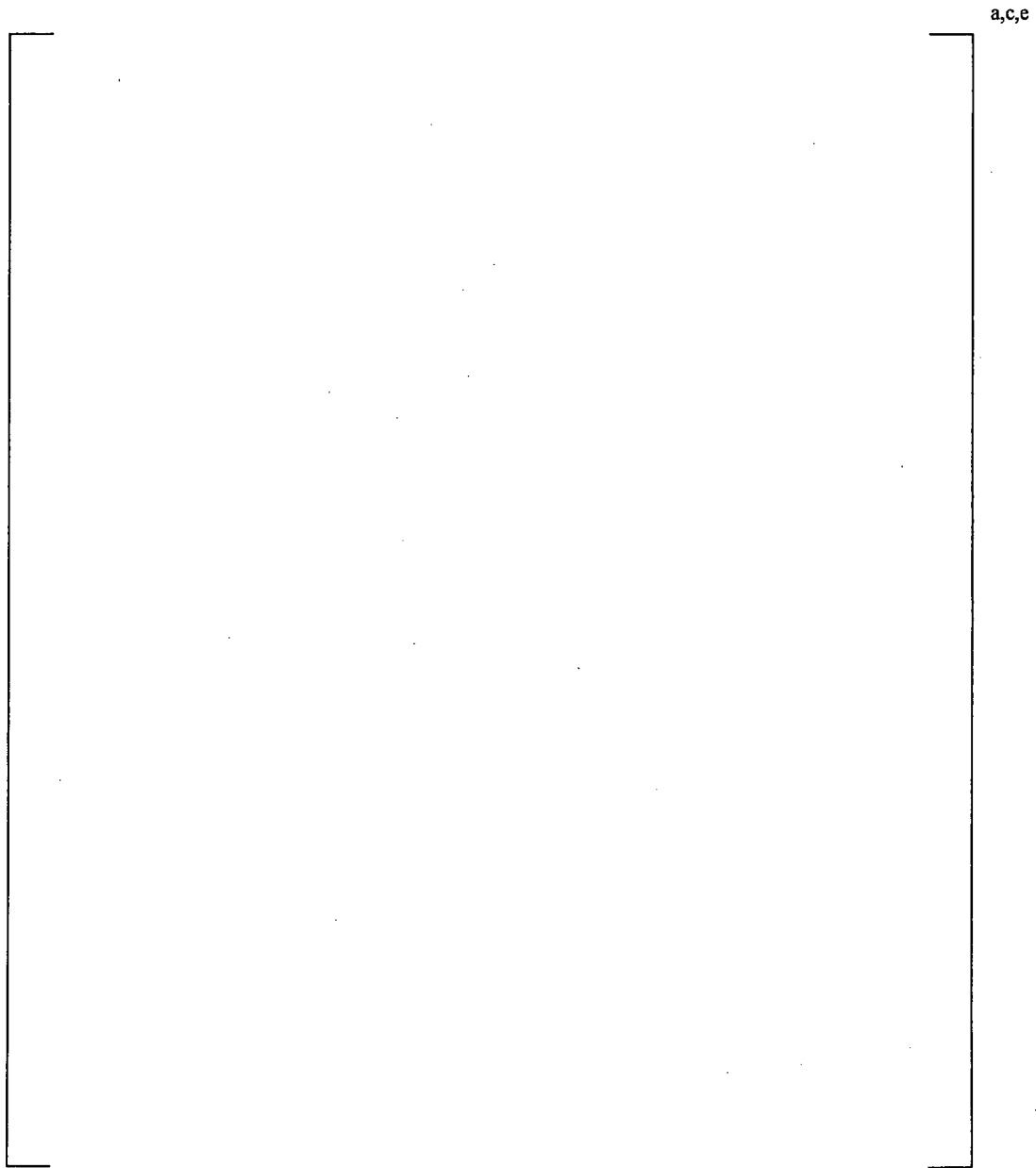
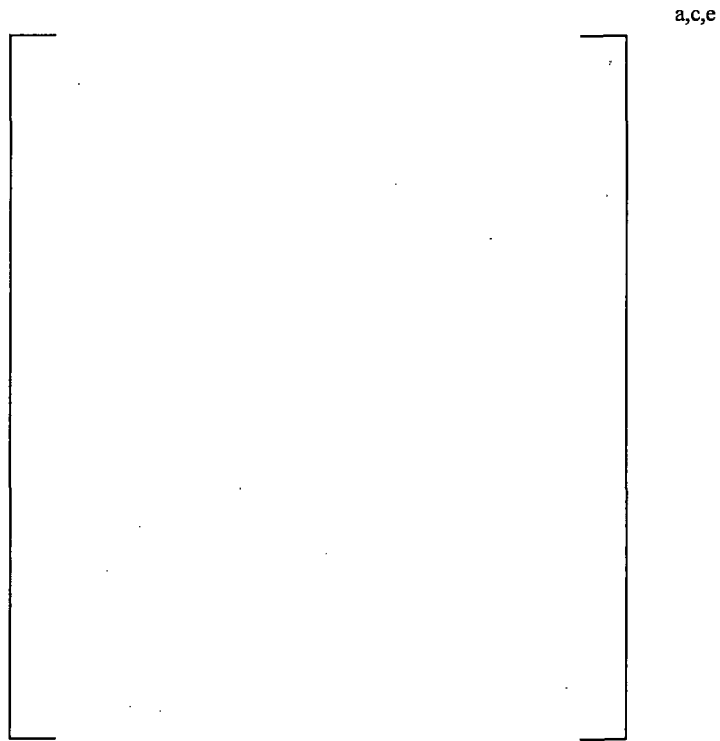


Figure 6-4 Close-Up of Tubesheet Junction Mesh





**Figure 6-5 Typical Finite Element Mesh for a Prior Axisymmetric Tubesheet-Channelhead-Stub Barrel Model**



**Figure 6-6 3D Tubesheet Mesh Close-Up Screen Shot**

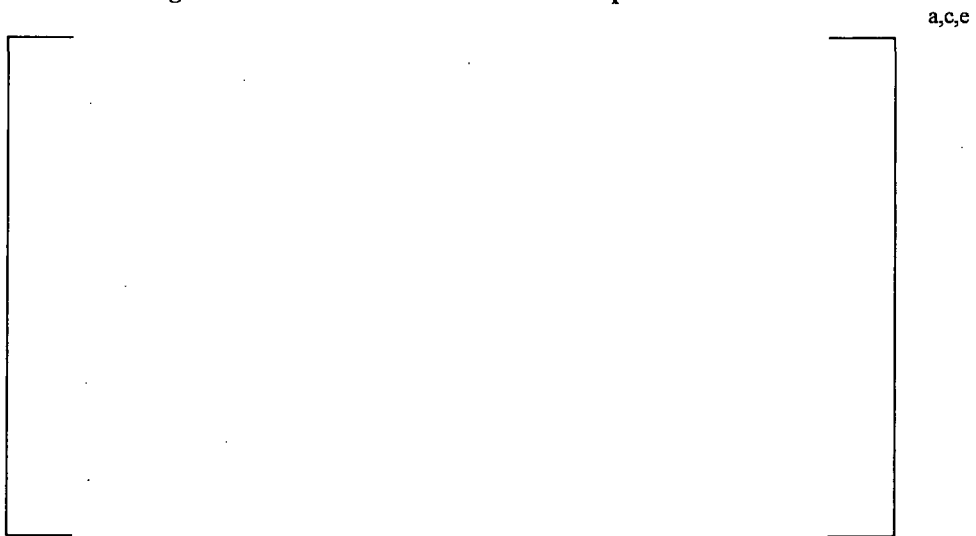


**Figure 6-7 Top Plane View of Perforated Tubesheet Mesh**

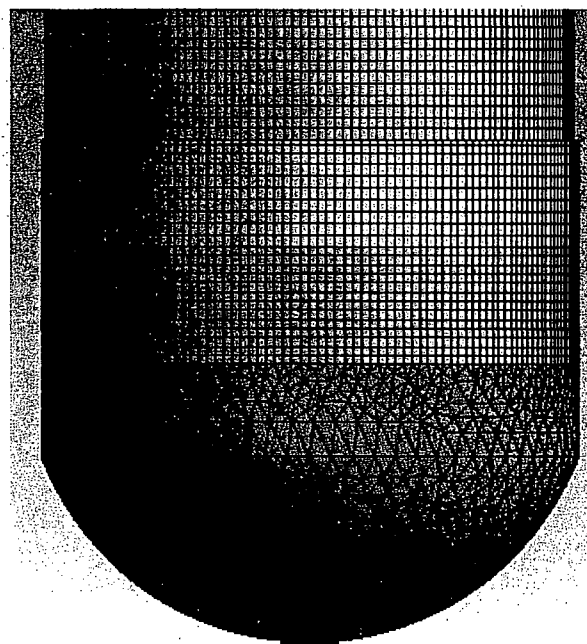


**Figure 6-8 Rear View of 3D Model Mesh**

## 6.2.2 Inputs to the Model and Their Variability

### 6.2.2.1 3D FEA Model Materials and Material Properties

The materials used in modeling the 3D Model 44F SG are the same as those noted in the engineering and design specification of the Model 44F SG. See Reference 6-16 for a description of the typical material properties used in a contact pressure analysis. See Reference 6-4 for a discussion of the reference design specification data and material properties in the 3D finite element model. The material properties for each material in the analysis are the mean material properties taken from the 1989 American Society of Mechanical Engineers Boiler and Pressure Vessel (ASME B&PV) Code unless otherwise noted.

**Table 6-1 List of Lower SG Complex Materials**

Component	ASME Code Specification
Tubesheet	SA-508 Class 2a
Lower Shell	SA-533 Grade A Class 2
Channelhead	SA-216 Grade WCC
Divider Plate	Alloy 600

The tubes in the Model 44F SGs are fabricated from Alloy 600 thermally-treated (A600TT) material. Summaries of the applicable mechanical and thermal properties for the tube material are provided in Table 6-2. Table 6-3 summarizes the material of fabrication for the tubesheet (SA-508, Class 2a). The shell material is SA-533, Grade A, Class 2, and its properties are in Table 6-4. Finally, the channelhead material is SA-216, Grade WCC, and its properties are in Table 6-5. The divider plates are fabricated from A600 material (see Reference 6-7). The material properties were all obtained from the ASME B&PV Code (Reference 6-3). See Table 6-6 for a list of representative mean operating input properties used in the Model 44F H\* contact pressure analysis.

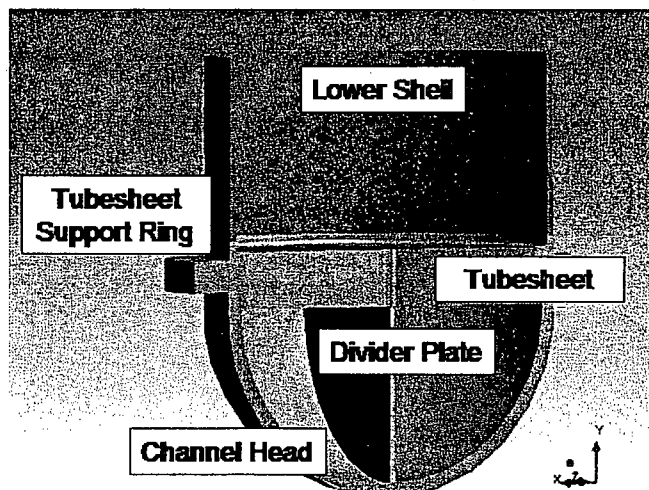


Figure 6-9 Important Structures in the Lower SG Complex

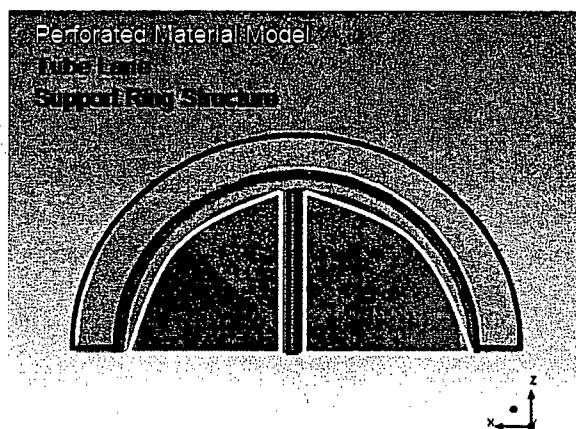


Figure 6-10 Top View of Tubesheet Showing Different Tubesheet Structures

**Note that Model 44F SGs do not have a tubesheet support ring.**

The effective orthotropic material properties of the tubesheet were calculated using the method described by Slot (Reference 6-5).

The perforated tubesheet in the Model 44F channelhead assembly is treated as an equivalent solid plate in the finite element analysis. An accurate model of the overall plate behavior was achieved by using the concept of an equivalent elastic material with anisotropic properties. For square pitch tubesheet hole patterns, the equivalent material properties depend on the orientation of loading with respect to the symmetry axes of the pattern. The stress-strain relations for the axisymmetric perforated part of the tubesheet are given by:

$$\left[ \begin{array}{c} \phantom{\sigma} \\ \phantom{\sigma} \\ \phantom{\sigma} \end{array} \right] \quad \text{a,c,e}$$

with the elasticity coefficients calculated as:

$$\left[ \begin{array}{c} \phantom{\sigma} \\ \phantom{\sigma} \\ \phantom{\sigma} \end{array} \right] \quad \text{a,c,e}$$

$$\left[ \begin{array}{c} \phantom{\sigma} \\ \phantom{\sigma} \\ \phantom{\sigma} \end{array} \right] \quad \text{a,c,e}$$

$$\left[ \begin{array}{c} \phantom{\sigma} \\ \phantom{\sigma} \end{array} \right] \quad \text{a,c,e}$$

$$\left[ \begin{array}{c} \phantom{\sigma} \\ \phantom{\sigma} \end{array} \right] \quad \text{a,c,e} \quad \text{and} \quad \left[ \begin{array}{c} \phantom{\sigma} \\ \phantom{\sigma} \end{array} \right] \quad \text{a,c,e}$$

$$\left[ \begin{array}{c} \phantom{\sigma} \\ \phantom{\sigma} \end{array} \right] \quad \text{a,c,e} \quad \text{and} \quad \left[ \begin{array}{c} \phantom{\sigma} \\ \phantom{\sigma} \end{array} \right] \quad \text{a,c,e}$$

where

The variables in the equation are:

- $\bar{E}_p^*$  = Effective elastic modulus for in-plane loading in the pitch direction,
- $\bar{E}_z^*$  = Effective elastic modulus for loading in the thickness direction,
- $\bar{\nu}_p^*$  = Effective Poisson's ratio for in-plane loading in the thickness direction,
- $\bar{G}_p^*$  = Effective shear modulus for in-plane loading in the pitch direction,
- $\bar{G}_z^*$  = Effective shear modulus for transverse shear loading,
- $\bar{E}_d^*$  = Effective shear modulus for in-plane loading in the diagonal direction,
- $\bar{\nu}_d^*$  = Effective Poisson's ratio for in-plane loading in the diagonal direction, and,
- $\nu$  = Poisson's ratio for the solid material,
- $E$  = Elastic modulus of solid material,
- $\gamma_{RZ}$  = Transverse shear strain,
- $\tau_{RZ}$  = Transverse shear stress,
- $[D]$  = Elasticity coefficient matrix required to define the anisotropy of the material.

**Table 6-2 Summary of Material Properties for Alloy 600 Tube and Divider Plate Material**

Property	Temperature (°F)						
	70	200	300	400	500	600	700
Young's Modulus (psi·10 <sup>6</sup> )	31.00	30.20	29.90	29.50	29.00	28.70	28.20
Thermal Expansion (in/in/°F·10 <sup>-6</sup> )	6.90	7.20	7.40	7.57	7.70	7.82	7.94
Density (lb-sec <sup>2</sup> /in <sup>4</sup> ·10 <sup>-4</sup> )	7.94	7.92	7.90	7.89	7.87	7.85	7.83
Thermal Conductivity (Btu/sec-in·°F·10 <sup>-4</sup> )	2.01	2.11	2.22	2.34	2.45	2.57	2.68
Specific Heat (Btu-in/lb-sec <sup>2</sup> ·°F)	41.2	42.6	43.9	44.9	45.6	47.0	47.9

**Table 6-3 Summary of Material Properties for SA-508 Class 2a Tubesheet Material**

Property	Temperature (°F)						
	70	200	300	400	500	600	700
Young's Modulus (psi·10 <sup>6</sup> )	29.20	28.50	28.00	27.40	27.00	26.40	25.30
Thermal Expansion (in/in/°F·10 <sup>-6</sup> )	6.50	6.67	6.87	7.07	7.25	7.42	7.59
Density (lb-sec <sup>2</sup> /in <sup>4</sup> ·10 <sup>-4</sup> )	7.32	7.30	7.29	7.27	7.26	7.24	7.22
Thermal Conductivity (Btu/sec-in·°F·10 <sup>-4</sup> )	5.49	5.56	5.53	5.46	5.35	5.19	5.02
Specific Heat (Btu-in/lb-sec <sup>2</sup> ·°F)	41.9	44.5	46.8	48.8	50.8	52.8	55.1

**Table 6-4 Summary of Material Properties for SA-533 Grade A Class 2 Shell Material**

Property	Temperature (°F)						
	70	200	300	400	500	600	700
Young's Modulus (psi·10 <sup>6</sup> )	29.20	28.50	28.00	27.40	27.00	26.40	25.30
Thermal Expansion (in/in/°F·10 <sup>-6</sup> )	7.06	7.25	7.43	7.58	7.70	7.83	7.94
Density (lb-sec <sup>2</sup> /in <sup>4</sup> ·10 <sup>-4</sup> )	7.32	7.30	7.283	7.265	7.248	7.23	7.211

**Table 6-5 Summary of Material Properties for SA-216 Grade WCC Channelhead Material**

Property	Temperature (°F)						
	70	200	300	400	500	600	700
Young's Modulus (psi·10 <sup>6</sup> )	29.50	28.80	28.30	27.70	27.30	26.70	25.50
Thermal Expansion (in/in/°F·10 <sup>-6</sup> )	5.53	5.89	6.26	6.61	6.91	7.17	7.41
Density (lb-sec <sup>2</sup> /in <sup>4</sup> ·10 <sup>-4</sup> )	7.32	7.30	7.29	7.27	7.26	7.24	7.22

Table 6-6 Summary of H\* Point Beach Unit 1 Analysis Mean Input Properties

<b>Plant Name</b>	Point Beach 1		
<b>Plant Alpha</b>	WEP		
<b>Plant Analysis Type</b>	Hot Leg		
<b>SG Type</b>	44F		
<b>Input</b>	<b>Value</b>	<b>Unit</b>	<b>Reference</b>
<b>Accident and Normal Temperature Inputs</b>			
NOP T <sub>hot</sub>	611.1	°F	PCWG-07-49
NOP T <sub>low</sub>	592.9	°F	PCWG-07-49
SLB TS ΔT	142.0	°F	See Reference 9-12
SLB CH ΔT	142.0	°F	See Reference 9-12
Shell DT	142.0	°F	See Reference 9-12
SLB Primary ΔT	-142.0	°F	See Reference 9-12
SLB Secondary ΔT	-307.0	°F	See Reference 9-12
Secondary Shell ΔT Hi	492.6	°F	PCWG-07-49
Secondary Shell ΔT Low	481.6	°F	PCWG-07-49
Cold Leg ΔT	32.6	°F	PCWG-07-49
Hot Standby Temperature	547.0	°F	PCWG-07-49
<b>Operating Pressure Input</b>			
Faulted SLB Primary Pressure	2235.0	psig	See Reference 9-12
Normal Primary Pressure	2235.0	psig	Other
Cold Leg ΔP	35.0	psig	PCWG-07-49
NOP Secondary Pressure – Low	586.0	psig	PCWG-07-49
NOP Secondary Pressure – Hi	712.0	psig	PCWG-07-49
Faulted SLB Secondary Pressure	0.0	psig	See Reference 9-12



### 6.2.2.2 Applied 3D Boundary Conditions

The calculated radial tubesheet deflection is the starting point for determining the effect of tubesheet bending and tube bore distortion on the contact pressure. The boundary conditions in the finite element model reflect the applied loading conditions in an operating SG as well as conservatively calculating the radial tubesheet deflection. The H\* analysis is a static, steady-state, analysis by definition because the maximum pressures and temperatures are applied as if they were constant during SG operation. Applying the maximum temperatures and pressures in this fashion maximizes the radial deflection of the tubesheet due to thermal growth and pressure differential and also maximizes the applied end cap load on the tubes. Time varying, or transient, analyses of the operating pressures and temperatures reduce the thermal and pressure loads on the tube and tubesheet.

There are three categories of applied boundary conditions in the 3D finite element model:

1. Displacements
2. Pressures
3. Temperatures

The applied displacement boundary conditions in the model are required to prevent rigid body translation of the model. The displacement boundary conditions were also selected to conservatively account for deflection modes of the tubesheet. The applied pressures represent the primary and secondary conditions in the SG and are based on the most recent bounding plant operating conditions and parameters available. The applied temperatures are selected based on the secondary and primary fluid operating temperatures. Each of the boundary conditions used in the finite element analysis and a comparison to the previous axisymmetric model boundary conditions are provided in the following sections.

#### 6.2.2.2.1 Applying Boundary Conditions in the 3D Finite Element Model

There are five possible surface groups to apply pressure and temperature loads in the 3D finite element model of the lower SG complex. These surface groups are:

1. Hot Leg/Cold Leg Primary Surfaces
2. Secondary Surfaces
3. Lower Shell Cut Face
4. Exterior Surfaces
5. Lower SG Complex Symmetry Plane

See Figure 6-11 for an illustration of the surface groups in the model.

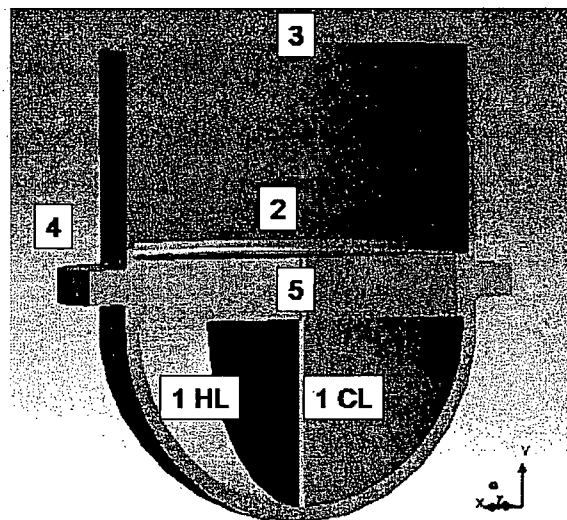


**Figure 6-11 Surface Groups for a Typical SG FEM**

There are also three edges in the model that are used to apply displacement boundary conditions. These edges are:

1. Lower edge of the tubesheet solid/tubesheet support ring
2. Centerline of the divider lane
3. Lower edge of the divider plate solid

Figure 6-12 and Figure 6-13 illustrate the edges in the model.

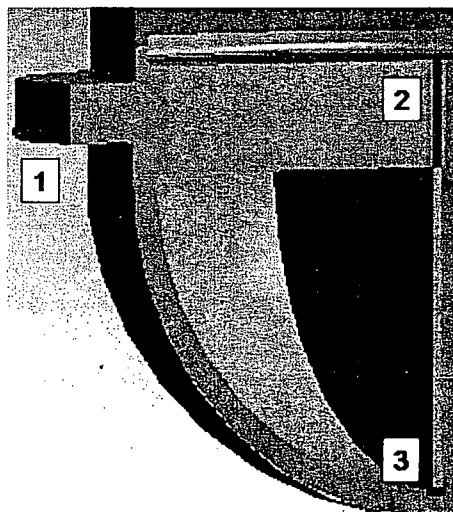


**Figure 6-12 Important Edges in a Typical SG FEM With a Tubesheet Support Ring**

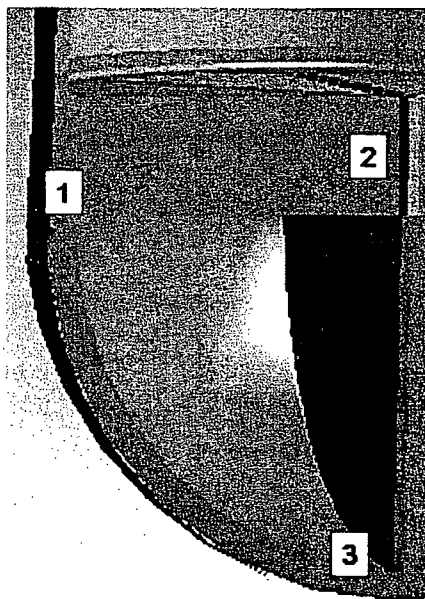


**Figure 6-13 Important Edges in a Typical SG FEM Without a Tubesheet Support Ring**

#### **6.2.2.2.2 Discussion of Displacement and Pressure Boundary Conditions**

The choice of boundary conditions is the most important factor in determining the tubesheet displacement output. The support structures and bearing pads for an SG typically restrain the structure in the vertical and horizontal directions and connect it to the floor of the containment building. All operating Model 44F SGs have bearing pads to connect the SG to the containment structure. A tubesheet support ring acts to restrain the motion of the SG in the vertical and horizontal directions. See Figure 6-13 for an illustration of how the boundary conditions for a non-support ring model are applied. The boundary conditions in the structural model reflect the appropriate constraints for 44F SGs without tubesheet support rings and are consistent with the as-built conditions. However, the SG is freely allowed to expand in a stress free fashion during heat-up. The boundary conditions in the thermal model reflect the ability of the SGs to expand radially without restraint. Figure 6-14 and Figure 6-15 are illustrations of the typical applied load conditions in the structural model and the thermal model. Figure 6-16 and Figure 6-17 are illustrations of the boundary conditions typically applied to the tubesheet to prevent rigid body translation.

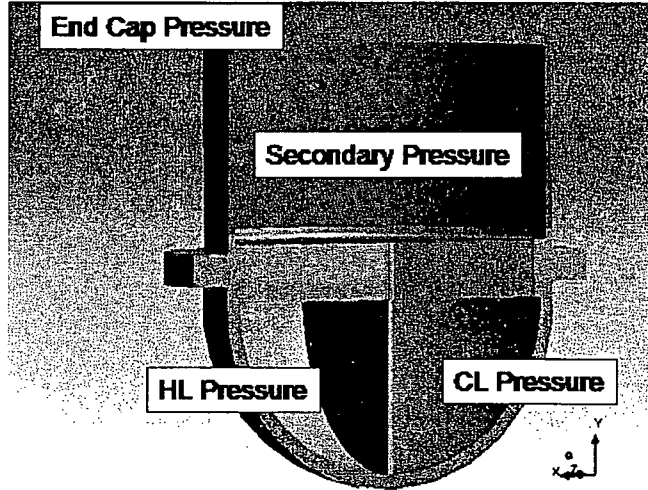


Figure 6-14 Typical Structural Model Applied Loads

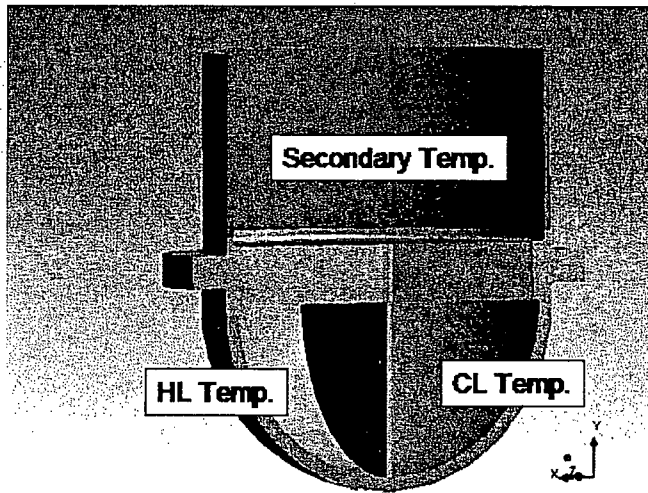


Figure 6-15 Typical Thermal Model Applied Loads

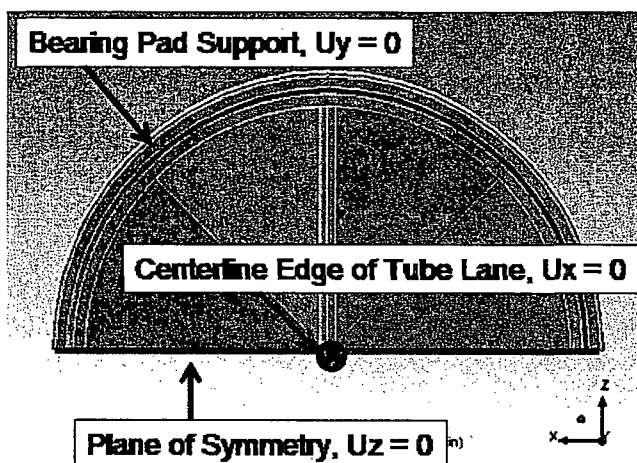


Figure 6-16 Typical Thermal Model Tubesheet Boundary Conditions Shown on Top View SG

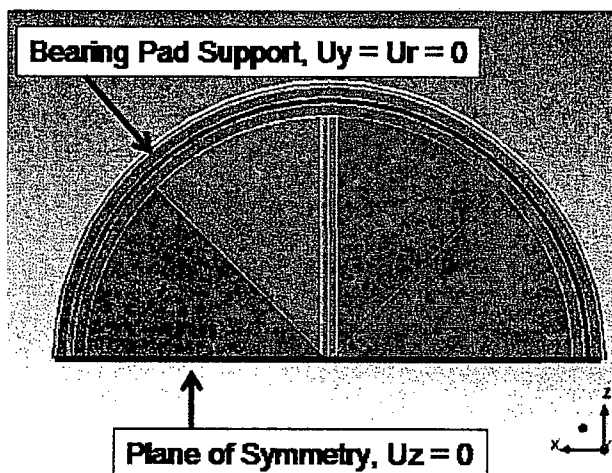


Figure 6-17 Typical Structural Model Tubesheet Boundary Conditions Shown on Top View of Typical SG

In Figure 6-14 and Figure 6-15, displacement in the Z-direction (perpendicular to the page) is fixed at the half-symmetry plane that bisects the lower shell, tubesheet, channelhead and divider plate. The displacements in the vertical (Y-axis) and horizontal (X-axis) directions are fixed at zero on the outer-most, lower edge, of the support ring. The primary and secondary pressure loads are applied to the primary and secondary surfaces. The vessel end cap pressure load is calculated using the thin shell relationship ( $\sigma = p_{sec}r_m/2t$ ) and applied along the top surface of the lower shell. The lower shell dimensions typically place it in the thin shell regime. The ratio of the lower shell radius to its wall thickness does not exceed the criteria for a thin shell analysis. The primary pressure in the hot and cold leg chambers in the channelhead are modeled separately based on the system curves and the appropriate transient analysis details. The height of the lower shell included in the model is equal to at least  $4.6\sqrt{R_m t}$ , per ASME Code requirements, unless a drawing reference dimension specifies a lower height, to attenuate any effects from the cut edge of the vessel and the applied end cap load so that loads are

transmitted to the tubesheet region in a correct fashion. A portion of the transition shell is included in the model if the height of the lower shell is less than the ASME Code limit.

[

]a.c°. The reference temperature for the structural model is also set to the hot leg primary fluid temperature so that no temperature differential is considered in the structural pressure load model. This is conservative because it uniformly reduces the stiffness of the solid and perforated regions of the tubesheet to the lowest level for each operating condition. The reference temperature in the thermal load model is set to 70 °F so that all displacements and strains are measured with respect to ambient room temperature. The typical thermal analysis boundary conditions are shown in Figure 6-16. The typical structural analysis boundary conditions are shown in Figure 6-17. Notice that the horizontal displacements are fixed at the centerline of the tubesheet instead of at the bearing pads in the thermal analysis. The temperature conditions are applied as surface loads and then the analysis determines what the final steady-state temperature distribution is due to conduction. The surfaces of the model are considered to be perfectly insulated and neither radiation nor convection losses are permitted. This is a conservative assumption that is consistent with the steady-state, static, nature of the analysis that considers only the maximum or minimum applied temperatures and pressures rather than the more realistic conditions taken from the system operating curves or the transient definitions in the SG design specification.

The current operating parameters in the Model 44F H\* fleet are listed in Table 5-1. The generic parameters for a Model F 4-loop H\* plant are listed in Table 6-8 through Table 6-13. These parameters are not used in the Model 44F analysis in any way, but are provided so that the general trends and conditions discussed in Section 6.4.7 can be clearly understood. The parameters in Table 6-8 through Table 6-13 are based on conservative assumptions drawn from Table 5-1 in WCAP 17071-P. Please refer to Table 6-8 through Table 6-13 for the pressures and temperatures in each operating condition. The details in the operating condition tables come from the System Curve reference for a Model F operating plant (SSDC-1.3F) and the latest, approved and published PCWG conditions for Millstone Unit 3 (PCWG-06-9). The Millstone Unit 3 conditions were used as a comparison because they represent the highest operating temperatures in the domestic H\* SG fleet. These selected conditions cannot actually occur in an operating SG but are used in a comparative analysis described in Section 6.4.7 to determine the effect on H\* for postulated normal operating conditions. For example, it is not possible to have both a low secondary side pressure and a high secondary side fluid temperature, but using the maximum and minimum conditions from Table 5-1 assumes those conditions can exist simultaneously. The determination of the limiting plant in the Model 44F fleet is made using the actual specified plant operating conditions and not the generic conditions from Table 6-8 through Table 6-13.

**Table 6-8 Conservative Generic NOP Pressures and Temperatures for 4-Loop Model F**  
 (These values do not exist in operating SG and are produced by examining worst-case comparisons.)

		a,c,e

**Table 6-9 Generic NOP Low  $T_{avg}$  Pressures and Temperatures for 4-Loop Model F**

		a,c,e

**Table 6-10 Generic NOP High  $T_{avg}$  Pressures and Temperatures for 4-Loop Model F**

		a,c,e

**Table 6-11 Generic SLB Pressures and Temperatures for 4-Loop Model F**


a,c,e

**Table 6-12 Generic FLB Pressures and Temperatures for 4-Loop Model F**


a,c,e

**Table 6-13 Conservative Generic SLB Pressures and Temperatures for 4-Loop Model F**  
 (These values do not exist in operating SG and are produced by examining worst-case comparisons.)


a,c,e

### 6.2.2.2.3 Effect of Tubesheet Support Ring on Displacement Boundary Conditions

The Model 44F lower SG complex does not include a tubesheet support ring structure. Therefore, the tubesheet support ring has no effect on the displacements and boundary conditions of the tubesheet.

### 6.2.2.2.4 Applied Pressures

The primary fluid pressure is applied to the interior primary surface of the channelhead, the primary face of the tubesheet, and the surface of the divider plate. The hot leg pressure is applied to the inlet chamber of the channelhead plenum, the hot leg primary face of the tubesheet, and the hot leg surface of the divider plate. The cold leg pressure is applied to the outlet chamber of the channelhead plenum, the cold leg primary face of the tubesheet, and the cold leg surface of the divider plate. The secondary fluid pressure is applied to the interior secondary face of the tubesheet and the lower shell. The lower shell cut face is the surface where the vessel end cap load is applied to the model. The vessel end cap load is calculated using the thin shell pressure vessel calculations unless the ratio of the lower shell wall thickness to the inner radius of the lower shell dictates that the thick shell end cap load equations should be used instead (Reference 6-8). The exterior surface of the SG includes the exterior surface of the channelhead, the exterior surface of the tubesheet, and the exterior surface of the lower shell. The pressures applied to each of the surfaces is the absolute pressure, not the gauge pressure; therefore the exterior surface of the SG can be pressurized to 15 psi (atmospheric pressure). [

]<sup>a,c,e</sup>. The effect of atmospheric pressure on the exterior surfaces is conservatively ignored in the  $H^*$  analysis and the finite element analysis.

### 6.2.2.2.5 Applied Temperatures

Each of the transient analysis conditions applied to the finite element model are considered to be static and steady-state. In the context of the thermal analysis, the static assumption means that there is zero heat transfer from radiation and convection mechanisms in the SG. The static condition assumption also means that there is no primary fluid flow through the SG tubes. The static assumption in the SG means that the temperature profile through the tubesheet will develop based on the conduction properties of the tubesheet material. Pure conduction through the tubesheet will result in a linear distribution of temperature ranging from the primary fluid temperature at the primary face of the tubesheet to the secondary fluid temperature at the secondary face of the tubesheet. The linear temperature distribution is reasonable during steam line break (SLB) conditions due to the assumed static analysis conditions. The linear temperature distribution is also reasonable during the faulted conditions because the tubesheet rapidly approaches equilibrium with the primary and secondary fluids during SLB due to the low thermal mass of the perforated tubesheet and the large difference in primary and secondary fluid temperatures.

The normal operating conditions (NOP) are analyzed using different assumptions. During NOP, it is reasonable to assume that primary fluid is flowing in the tubes. Therefore, heat transfer across the tube wall from the primary fluid is the main heat source within the tubesheet during NOP. Previous analysis (Reference 6-9) suggests that the temperature throughout the thickness of the tubesheet during NOP is nearly uniform at the primary side temperature until the upper 2 inches of the tubesheet. The tubesheet displacements due to pressure already assume that the tubesheet is uniformly at the highest primary fluid temperature, so this assumption does not affect the pressure related displacement results. The effect of

the different temperature distribution during NOP was studied using two different sets of boundary conditions and meshing schemes in the finite element analysis. All methods assumed a primary fluid temperature equal to the highest normal operating temperature (NOP Hi- $T_{avg}$ ) in the Model 44F fleet (616.8 °F). The secondary fluid temperature in both methods assumed that the secondary fluid was at a constant value equal to the average of the feedwater temperature and the steam outlet temperature for Point Beach Unit 1 (483 °F). A higher secondary fluid temperature in this context is conservative because it means that both surfaces of the tubesheet are at high temperatures and will radially expand more. The difference between the two methods lies in how the heat is distributed through the thickness of the tubesheet. The linear temperature distribution assumes that the tubes contribute no heat to the tubesheet and that the final thermal distribution is determined by pure conduction. [

.]<sup>a,c,e</sup> See Figure 6-18 for a graph comparing the linear temperature distribution to the modified temperature distribution used in the study.



**Figure 6-18 Comparison of Different Temperature Distributions Through the Tubesheet due to Varying Boundary Conditions**

The resulting thermal displacements from the modified and linear temperature distribution analysis were then used as inputs to an  $H^*$  analysis. The use of the actual tubesheet displacements from each thermal distribution condition is an improvement over the method described in the  $H^*$  analysis of the Model F SG. Specifically, in the prior  $H^*$  analyses the thermal offset came from a comparison of the different tubesheet displacements because the actual tubesheet displacements from the modified thermal distribution could not be used in the analysis.

The Model 44F  $H^*$  analysis results showed a slight decrease of 0.50 inch in the  $H^*$  value with the modified temperature distribution compared to the  $H^*$  value with the linear temperature distribution. This is a logical outcome from the analysis because even though the two types of thermal distributions are different, the net effect on the thermal tubesheet deformation over the depth of the tubesheet is minimal

and the difference in the contact pressure distributions is small. It is also important to note that the Model 44F tubesheet-to-channelhead and tubesheet-to-lower shell connections were not optimized to reduce the amount of metal in the forgings and that the 44F channelhead and tubesheet are thicker than the other model SG. For example, the typical channelhead wall thickness in the Model 44F is approximately 9.7 inches, where as in the Model D5 SG it is approximately 7.5 inches and in the Model F SG it is approximately 5 inches. The Model 44F tubesheet is also 21.81 inches thick, compare to 21.03 inches for the Model F and Model D5. This means that the amount of material to resist tubesheet deformation in the lower SG complex of the Model 44F SG is significantly increased relative to the Model D5 and Model F SG designs. Therefore, it is conservative to ignore the thermal distribution offset for the Model 44F SG because of the above reasons and because including it in the  $H^*$  analysis would lead to a reduction in the calculated  $H^*$  value.

### 6.2.2.3 Variability in Material Properties and Input Conditions

#### 6.2.2.3.1 Material Property Variability

The materials properties of the tube and the tubesheet affect the distribution of contact pressure between the tube and the tubesheet. The material inputs and related inputs in the contact pressure analysis are:

1. Young's Modulus ( $E$ )
2. Coefficient of Thermal Expansion ( $\alpha$ )
3. Poisson's Ratio ( $\nu$ )

The effect of varying the material properties in either the tube or the tubesheet develops from the related stiffness coefficients in finite element analysis of the tubesheet deflections and the theory of elasticity analysis which determines how the tube and the representative tubesheet structure respond to the applied loads and deformations.

The linear material and orthotropic material models used in the analysis follow from a direct application of Hooke's Law; therefore,  $E$  and  $\nu$  are inter-related. Either  $E$  or  $\nu$  can vary with respect to temperature or material effects, but not both. The values for  $E$  vary according to temperature and material structure and the values for  $\nu$  are held constant at 0.3 in the analysis. The mean values for  $E$  for each material, with respect to temperature, in the contact pressure analysis are taken from the ASME Code. The one sigma ( $1\sigma$ ) variability of  $E$  at any given temperature is defined as [ ]<sup>a,c,e</sup>% (Reference 6-13). The mean values of coefficient of thermal expansion ( $\alpha$ ) are taken from the ASME Code for each material in the analysis. The one sigma ( $1\sigma$ ) variability of  $\alpha$  is defined for both the tube and the tubesheet material as [ ]<sup>a,c,e</sup>% and [ ]<sup>a,c,e</sup>%, respectively (Reference 6-14)<sup>1</sup>.

The yield strength of the tube material ( $Y$ ) and the tangent modulus ( $E_T$ ) of the tube material are not required in the contact pressure analysis. Instead, the effect of varying both parameters separately is included in the residual contact pressure analysis described in Section 7.0 of this report.

<sup>1</sup> : The  $1\sigma$  value of  $\alpha_{TS}$  used in structural analysis is conservatively greater than the value cited in Reference 6-14.

### 6.2.2.3.2 Design and Process Related Input Variability

The geometric and design/process tolerances for the SG tubes and tubesheet tube bore can influence the contact pressure distribution. These variables include:

1. Tube Outer Diameter (OD)
2. Tube Wall Thickness
3. Tubesheet Tube Bore Inner Diameter (ID)
4. Tubesheet Collar OD
5. Hydraulic Expansion Pressure

The tube ID and tube OD, as well as the tubesheet ID, are varied according to the reported tolerances described in Section 7.0. Most of these sources of variability affect the calculation of residual contact pressure (RCP) variability only. The variability in these parameters has negligible effect on  $H^*$  if the RCP is assumed to be zero. The variables that affect RCP variability are:

- Initial gap between the tube OD and the tubesheet tube bore ID
- Variability in the hydraulic expansion pressure

The RCP variability with respect to each parameter is discussed in Section 7.0. The current  $H^*$  analysis assumes zero (0 psi) residual contact pressure in the contact pressure analysis. The tube OD and tube ID are explicitly used in the contact pressure analysis to determine the stiffness coefficients. The tubesheet collar OD and tube bore ID are also explicitly used in the contact pressure analysis to determine the stiffness coefficients of the representative tubesheet collar in the theory of elasticity analysis. A value of the maximum tubesheet bore ID plus two standard deviations ( $+2\sigma$ ) is conservatively used to maximize the tube end cap load. In the Model 44F  $H^*$  analysis, a tubesheet bore ID of  $\sim 0.896$  inch is assumed for the calculation of end cap loads and for all structural calculations between the tube and the tubesheet.

### 6.2.2.3.3 Coefficient of Friction Variability

The coefficient of friction between two materials is a property of the surface characteristics and loading method leading to different cases of friction (e.g., static, sliding, stiction, etc.). A value of [ ]<sup>a,c,e</sup> is the lowest estimate from prior test data (Reference 6-12) and is more conservative than the published coefficient for greased nickel sliding over a steel surface of 0.3 (Reference 6-11). Other test and analysis data suggest that the coefficient of friction between the tube and the tubesheet could be as high as [ ]<sup>a,c,e</sup> (Reference 6-12). A coefficient of friction of [ ]<sup>a,c,e</sup> is recommended for the  $H^*$  contact pressure analysis. For simplicity and conservatism, the coefficient of friction is conservatively assumed to be [ ]<sup>a,c,e</sup> in the integration of contact pressure to determine the pull out resistance.

## 6.2.3 Bounding Sector Analysis

A 3D FEA model was developed to determine the limiting region of the tubesheet to be considered for the  $H^*$  calculations. This model was originally intended to benchmark the earlier 2D axisymmetric model. The perforated tubesheet region of the three-dimensional finite element model was partitioned into sectors

to study the asymmetric tubesheet displacements. Figure 6-19 is an illustration of the tubesheet sectors used in the finite element study.

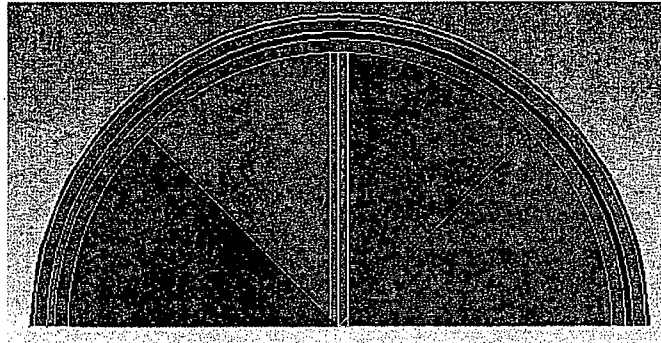


**Figure 6-19 Top View of Model 44F Tubesheet Showing Sector Regions for Displacement Analysis**

The finite element analysis used the Model F FLB, SLB and NOP conditions in Table 6-8, Table 6-12 and Table 6-13. These values are bounding and produce larger displacements in the tubesheet compared to the actual Model 44F tubesheet displacements. Therefore, the Model F results are conservative and bounding when applied to the Model 44F. A summary of the condition-specific temperatures and pressures for those conditions is provided in Section 5.0. The displacement results for the 0°, 45° and 90° sector boundaries were obtained using a macro code written in the native ANSYS Program Development Language (APDL). The 0° sector boundary is the edge of the tubesheet perpendicular to the face of the divider plate (i.e., along the symmetry plane of the tubesheet). The 45° sector boundary is the edge 45° clockwise from the symmetry plane of the SG tubesheet. The 90° sector boundary is the edge of the tubesheet perpendicular to the tubesheet symmetry plane, parallel to the divider plate face, along the edge of the tube lane. The results at each sector boundary face were obtained as a function of both elevation and radius for comparison and use in contact pressure calculations.

The results of the study showed that the maximum radial tubesheet displacement for the applied pressure loading occurred perpendicular to the face of the divider plate. The radial displacement for the applied thermal loading does not vary azimuthally during NOP or SLB because the thermal properties of the tubesheet and the resulting thermal gradients do not vary as a function of sector angle. See Figure 6-20 for representative curves of the radial tubesheet displacements during NOP in the Model 44F SG. It should be noted that the azimuthal radial displacements due to pressure during NOP bound the azimuthal radial displacement due to pressure during SLB and FLB. Note that the difference in the perforated region in the tubesheet leads to a different shape in the displacement curves at the maximum perforated radius. It is also significant that the Model 44F tubesheet displacements due to pressure at the maximum perforated TS radius are approximately 70% of the Model F tubesheet displacements at the maximum perforated radius. Therefore, the Model F results for the contact pressure variation are a function of azimuthal position in the tubesheet are conservative when applied to the Model 44F because the actual Model 44F displacements would yield much higher contact pressures as a function of changing angular position in the tubesheet.



**Figure 6-20 Radial TS Displacement due to Pressure at TTS and BTS for  
TS Radius ~ 55 Inches During NOP**

Similar to the Model F TS, the zero degree ( $0^\circ$ ) face of the Model 44F tubesheet in the finite element model has the largest values of deformation due to an applied pressure differential. It is logical for the  $0^\circ$  sector boundary face to be the limiting face for radial displacement because it is furthest away from the constraints of the divider plate and tube lane. The results of the azimuthally varying radial tubesheet displacements in the analysis of the tube-to-tubesheet contact pressures show that the lowest contact pressure occurs on the  $0^\circ$  face. [

] <sup>a,c,e</sup> The radial displacements due to the pressure differential were linearly scaled by the difference in the azimuthal radial displacement to study the effect of the change in contact pressure as a function of TS angle. [

] <sup>a,c,e</sup> See Figure 6-21 for a typical graph showing the effect of decreasing radial tubesheet displacement as a function of sector angle and the related increase in tube pull out resistance during NOP conditions.



**Figure 6-21 Relative Change in Tubesheet Displacement as a Function of Sector Angle During NOP for a Model F SG**  
 (The effect of the decreasing radial tubesheet displacements on tube pull out resistance is noted in 5% increments.)

Figure 6-21 shows that the pull out resistance of a tube increases the closer that tube is to the tube lane. The pull out resistance of a tube increases by roughly [ ]<sup>a,c,e</sup>% for every [ ]<sup>a,c,e</sup>% decrease in the radial tubesheet displacement. Therefore, the 0° sector face, normal to the tube lane, is the limiting sector in the tube bundle and all of the tubes outside of the [ ]<sup>a,c,e</sup> degree sector can be shown to have greater pull out resistance to applied end cap loads. The azimuthal variation of the radial tubesheet displacement is conservatively ignored during both NOP and SLB conditions in the contact pressure analysis in favor of using the results for the limiting sector. Only the most limiting tubes in the bundle at the 0° face of the tubesheet, for both the hot leg and cold leg sides of the tubesheet, are considered in the H\* contact pressure analysis.

## 6.2.4 Radius Dependent Tubesheet Stiffness Analysis

### 6.2.4.1 Summary

The Goodier model (Reference 6-18) for calculating the tube-to-tubesheet contact pressure assumes that a representative collar of tubesheet (TS) material can be removed from the tubesheet and still provide the same constraint as if the tube and tubesheet structure were still in the tubesheet. The expansion of the pressurized tube bore, local to a tube of interest, can change the predicted values of the tube bore dilation due to internal pressure. In other words, the deflections of a single tubesheet cell are not independent from the deflections of other tubesheet cells. A combined planar, tube and tubesheet model is studied so that this effect can be included in the effective tubesheet collar approach used in the Goodier model. Two finite element models were used to examine the character of the local deformations of a tubesheet hole ID surface for the case where the tube location in the bundle varies and the tubes in the vicinity of the tube of interest may or may not be pressurized. Different values of primary pressure are used to envelope both the high and low values of applied pressure in the problem and possible combinations of pressurized and un-pressurized tubes surrounding a tube of interest. The end result of this study is a ratio that can be used to modify the tubesheet collar thickness, as a function of position, to approximate the constraint that a pressurized tubesheet would provide on a single tube. This study used the geometry of the Model F tubesheet. However, the increased tubesheet bore diameter and pitch in a Model 44F SG means that the results presented below are conservative when applied to a Model 44F SG. The effect of using a Model 44F specific geometry would be to further increase tube to tubesheet contact pressure due to the local stiffness interaction between the tube and the tubesheet which would produce a non-conservative value of  $H^*$  relative to using the current Model F results.

### 6.2.4.2 Introduction

The radial expansion of the inner surface of an open thick shell, or collar, due to internal pressure, is given by the equation:

$$\left[ \frac{P_{crev}}{E_{TS}} \left( \frac{d^2}{c^2} - 1 \right) \right]^{a,c,e} \quad (6-1)$$

Where

- $P_{crev}$  = The crevice pressure acting on the ID surface of the tubesheet collar and the OD surface of the tube,
- $E_{TS}$  = The elastic modulus of the tubesheet material,
- $c$  = The inner radius (IR) of the tubesheet collar,
- $d$  = The outer radius (OR) of the tubesheet collar and,
- $\nu$  = The Poisson's ratio of the collar material

The thickness of the representative tubesheet collar wall was determined by 2D finite element analysis in 1993 (Reference 6-23). The collar thickness was calculated so that the tubesheet cylinder wall thickness

would provide the same radial stiffness as the surrounding tubesheet material for the case of a single pressurized tube in a bundle of non-pressurized tubes. The original analysis (Reference 6-23) considered only the effective stiffness of a collar necessary to account for the material around a single pressurized tube within a tubesheet. This was a conservative approach to approximate the behavior of a single TS collar for most thermal and pressure related deformations because it maximized the tubesheet deflection. However, there is pressure acting on all of the non-plugged TS cells simultaneously during operating conditions. The effect of all of the tubes in a bundle acting to simultaneously pressurize the perforated region of the tubesheet is not captured when a single removed TS collar is analyzed. The compatibility condition for the analysis of the tubesheet to tube friction interface does account for the tubesheet collar expanding due to an applied pressure on the ID surface of the tubesheet, but the amount of expansion is calculated assuming that the collar acts as a single thick walled cylinder, not a cellular unit within a tubesheet that has a number of ID surfaces that are also pressurized.

The approximate perforated plate material model accurately captures the total radial and axial deformations of the perforated tubesheet but the deformations and stresses at the local tube-to-tubesheet surface level are not calculated in the analysis. Analysis of the deformations and stresses in the vicinity of a single tube hole due to pressure and temperature requires a model detailed of a perforated tubesheet with the correct operating conditions applied to each tube bore. The deformation of a single tubesheet perforation will be affected by the primary side pressure transmitted through the tube wall, the temperature of the tubesheet, the distribution of any crevice pressure due to a tube with a 100% through-wall flaw, the presence of other structures that can limit local deformations in the tube hole and the deformation of the tube holes nearest the tubesheet cell of interest. The possibility exists that tubes in the vicinity may be plugged which would negate any effect due to the pressure deformation of that specific hole. However, in the limit, for a tube in the middle of the bundle with no other pressurized tubes around it, the original analysis accurately describes the behavior of a tubesheet cell. For tubes in the near radius (close to the divider lane) or the periphery, the presence of other structures such as the tube lane and the tubesheet annulus act to reduce tubesheet deflections and radial expansions. A change in the predicted amount of tube bore dilation due to internal pressure directly affects the tube-to-tubesheet contact pressure calculated by the Goodier model (Reference 6-18). The deformations of a tube surrounded by pressurized tubes will be different from that of a lone pressurized tube in the center of a bundle. This study quantifies the difference in stiffness between the case of a single pressurized tube in a tubesheet and the case of a pressurized tube in a tubesheet surrounded by other pressurized tubes.

#### **6.2.4.3 Background**

An important concern relating to the structural model was raised at the December 13, 2007 meeting with the NRC Staff at Waltz Mill (Reference 6-25). The concern was that current thick shell equations that model the contact pressure between the tube and the tubesheet do not include any restoring forces for the tubesheet. These restoring forces are generated by the elastic resistance to deformation of the tubesheet material surrounding a tube and also by the simultaneous inflation of adjacent tubes in contact with the tubesheet. The current tube-to-tubesheet contact model is based on the theory of elasticity and the work of Goodier and Schoessow (Reference 6-18). The model considers the relative elastic flexibility between a single tube that has been expanded to contact with an equivalent collar that simulates the constraint of the surrounding tubesheet material. The results are combined using the principle of linear superposition to describe the resulting net effect on radial displacement in order to calculate the net contact pressure between the tube and the tubesheet. No additional forces or stiffness are added to the

tubesheet model; therefore it is theoretically possible for the tubesheet material to expand proportionally to the increase in crevice pressure without limit.

In prior submittals of H\* (Reference 6-20), the pressure in the crevice between the tube and the tubesheet was assumed to be at the secondary side saturation pressure. The crevice pressure acted on the ID of the tubesheet material and the OD of the tube material. The results of the crevice pressure testing that disproved that fundamental model assumption were summarized in a White Paper provided to the NRC Staff (Reference 6-28). The result of test data was to increase the crevice pressure for the purposes of calculating the contact pressure between the tube and the tubesheet because the data showed that leakage from the primary side remains in the liquid phase for most of the length of the crevice. The crevice prevents the fluid from rapidly expanding or moving through the crevice medium (thereby keeping the static portion of the fluid energy large). Therefore, the component of radial displacement that is caused by the tubesheet collar ID deflecting away from the OD of the tube increased. The amount that the tube OD expanded into contact with the ID of the tubesheet was reduced due to a reduction of the pressure differential across the tube wall. The net effect of both of these changes on the tube-to-tubesheet contact pressure model is to reduce the contact pressure and increase the required H\* inspection distance.

The impact of the crevice pressure test data led to two additional important realizations regarding the analysis model for contact pressure:

1. The contact pressure analysis model did not properly apply the increased crevice pressure to the ID of the tubesheet collar. Instead, the secondary side pressure was still being applied to the tubesheet ID.
2. A built-in factor in the H\* analysis model, known as the beta, or  $\beta$ , factor, intended to correct for the crevice pressure issue, was not being properly applied by the model.

The required changes to the spreadsheet model for the increased crevice pressure condition and the prior reduced secondary side pressure in the crevice pressure model were compared. The details of the comparison revealed that the tube-to-tubesheet contact pressure reduction when the tubesheet bore ID expansion was increased by the increased crevice pressure. When Items 1 and 2 above were addressed, the applied crevice pressure was reduced on the tubesheet bore ID and the tube-to-tubesheet contact pressure increased. Using the secondary side pressure as the crevice pressure reduced the crevice pressure applied to the tubesheet tube bore ID by roughly [ ]<sup>a,c,e</sup> % compared to the crevice pressure model based on the test data.

The current H\* modeling approach does not use a  $\beta$  factor, nor does it reduce the applied crevice pressure when calculating the tube bore expansion due to internal pressure. The test data is applied to the OD of the tube wall and the ID of the tubesheet tube bore as a function of elevation for each operating condition.

During the continuing development of the H\* methodology, the model was modified to exclude application of the  $\beta$  factor, but to represent the same effect through a modification of the collar thickness of the surrounding effective tubesheet material in the Goodier analysis to account for the difference in stiffness due to a pressurized tubesheet. This approach was reviewed by a panel of industry experts in structural analysis and is included in the current analysis for H\*.

#### 6.2.4.4 Finite Element Model Details and Results

The TS ID study used two different 2D plane stress models. The first model (Model 1) represents the tubes along the plane of half symmetry in the SG. The second model (Model 2) represents the tubes perpendicular to the plane of symmetry and parallel to the tube lane. The calculated tubesheet deformation changes as a function of tubesheet radius, elevation and azimuthal angle with respect to the divider lane. See Section 6.2.3 for a discussion of the azimuthal change in the tubesheet displacements, and the related azimuthal dependence of the tube pull out resistance. Both models neglect the tube lane and solid rim material (tubesheet annulus) which includes the lower shell, divider plate and channelhead connections. The presence of the tube lane is represented by the applied boundary conditions. Additional material is modeled in each finite element analysis to prevent artificially induced deflections due to the boundary conditions and reduce the effect of a stiff boundary by representing the additional tubesheet material that would be present in a real SG. In prior analyses (Reference 6-23), a radius equal to  $[ ]^{a,c}$  tube pitches was determined to be adequate. A  $[ ]^{a,c}$  pitch boundary of additional tubesheet material was added in Model 1 and Model 2 based on the prior analysis results. It is important to note that these models do not represent symmetry planes or symmetric sections of the tubesheet but are instead isolated sections of the perforated tubesheet region that are defined by the similarity in radial displacement among the tubes represented in the model. Figure 6-22 shows the arrangement of the finite element models used to study the problem. See Figure 6-23 for an illustration of the Model 1 geometry and Figure 6-24 for an illustration of the Model 2 geometry.

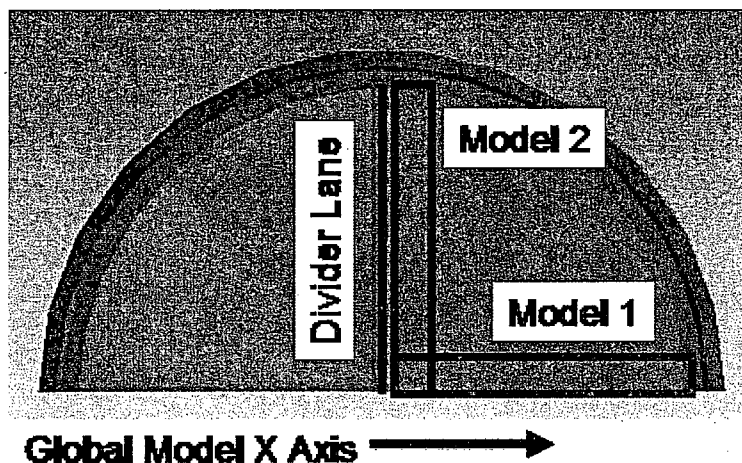
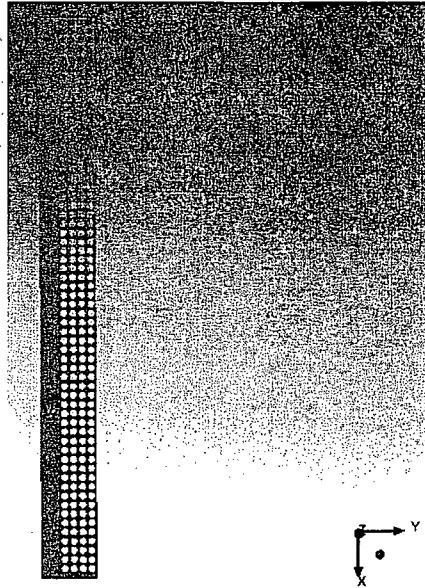
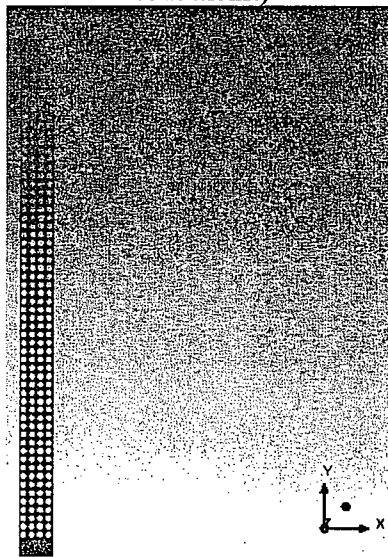


Figure 6-22 FEA Model Orientations as Shown From a Top View of a Typical Tubesheet



**Figure 6-23 Model 1 Geometry, Region of Tubesheet Perpendicular to Tube Lane**  
(The material to the left of the perforations is added to soften the applied displacement boundary conditions.)



**Figure 6-24 Model 2 Geometry, Region of Tubesheet Parallel to Tube Lane**  
(The material on the bottom of the model is added to soften the applied displacement boundary conditions.)

The focus of the study was purely on the effect that the perforated portion of the tubesheet structure has on the local displacement of the tubesheet hole ID surface. The lower shell, associated component welds and junctions and the tubelane act as girdles which reduce the TS displacement and therefore also limit the local deformation of the tubesheet hole ID. Including the structures attached to the tubesheet further decreases the pressure expansion of the perforated region of the tubesheet, which would act to increase

the restoring forces on the tube bore resisting the pressure expansion. Therefore, it is conservative to ignore these structures in the model and they are not required in the planar analysis. See Figure 6-25 and Figure 6-26 for pictures of the applied boundary conditions in each model.

Each individual TS hole was pressurized with either the NOP primary side pressure (2250 psig) or the SLB primary side pressure (2560 psig) as the bounding upper limit for the internal pressure acting on the face of the tubesheet tube bore. The TS holes were also pressurized with the primary side condition saturation pressures. The NOP saturation pressure was [ ]<sup>a,c,e</sup> psia and the SLB saturation pressure was [ ]<sup>a,c,e</sup> psia. The saturation pressures represent the lower bounding limits for the tubesheet tube bore. The upper bounding limit on tube bore pressure occurs near the bottom of the tubesheet for the case when the tubesheet surface is directly exposed to the primary fluid, such as in the case of a through-wall crack. The lower bounding limit on the tube bore pressure occurs when the tubesheet surface is in contact with pressurized crevice fluid that is near to, or has already, flashed to steam at the top of the tubesheet crevice (Reference 6-24). Three holes were chosen in each model to illustrate the different effects that TS constraint and tube pressurization have on the local deformation of a tube hole surface. In addition to the other pressurized conditions, several cases were run so that the three tubes of interest were the only tubes in the bundle that were pressurized. The hole locations in Model 1 are shown in Figure 6-27 through Figure 6-30. The tubes of interest correspond to a radius of roughly 2 inches ("inside" tube bore), 30 inches ("middle" tube bore) and 59 inches ("outside" tube bore).

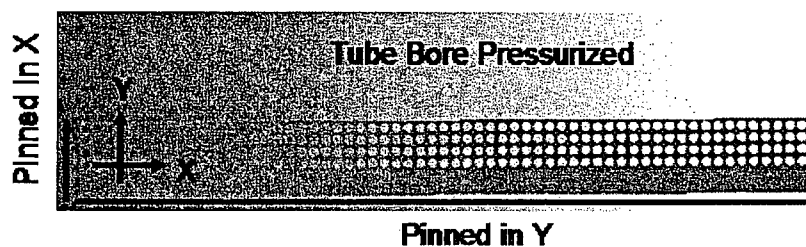


Figure 6-25 Model 1 Applied Boundary Conditions - Perpendicular to Divider Lane

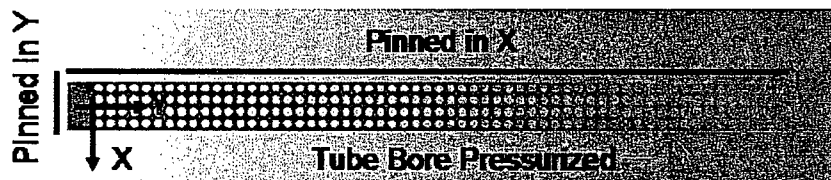


Figure 6-26 Model 2 Applied Boundary Conditions - Parallel to Divider Lane



**Figure 6-27 Relative Location of the Three Tube Holes of Interest in Model 1 and Model 2**  
**(The tubes of interest correspond to a radius of roughly 2 inches (“inside” tube bore), 30 inches (“middle” tube bore) and 59 inches (“outside” tube bore).)**



**Figure 6-28 Close-Up of Inside Hole Location**  
**(Red circles added for clarity)**



**Figure 6-29 Close-Up of Middle Hole Location**  
**(Red circles added for clarity)**



**Figure 6-30 Close-Up of Outside Hole Location**  
**(Red circles added for clarity)**

The hole locations in Model 2 are achieved by rotating the holes in Model 1 through 90° counter clockwise. The boundary conditions for each 2D model were compared to the displacements of the perforated region of the tubesheet from the 3D finite element model in order to benchmark the 2D results. The same temperature difference and primary side pressure load was applied from the 3D model. In both Model 1 and Model 2, the difference in the radial displacement at the mid-plane of the tubesheet between the 2D perforated region and the 3D perforated region with the approximate material properties was on the order of [ ]<sup>a,c,e</sup>% or less. The results of the 2D planar analysis are not dependent on tubesheet thickness and can be assumed to be constant throughout the thickness of the tubesheet. The final analysis of the tube hole deformation at each location used only an [

]<sup>a,c,e</sup>. The body temperature for NOP and FLB was 620°F (~622.6°F at Millstone Unit 3) and the body temperature for SLB was 450°F. Both temperatures are representative of the highest operating primary fluid temperatures in the H\* fleet and result in the TS being evaluated when the ligaments have the least resistance (i.e., lowest Young's Modulus) to expansion. This is a conservative assumption because [

]<sup>a,c,e</sup>.

#### 6.2.4.5 Calculation Method and Results

The displacements in the  $X$  and  $Y$  directions around each of the three tube bores of interest were calculated as a function of angular position relative to the center of each hole. The coordinates of each hole in the deformed configuration were shifted so that only tube hole deformation was considered and no tube hole translation was retained. The deformation of the tube hole for NOP and SLB conditions is then calculated as a function of circumferential angle for each tube location. The net deflection of a tube hole, at a given point around the circumference, is defined as:

$$\left[ \right] \quad \text{a,c,e} \quad (6-2)$$

where the values of  $U_x$  and  $U_y$  represent the translation of the hole center, relative to the global finite element model reference coordinate system from the initial undeformed configuration to the final deformed state. In this analysis, only the deformation of the circumference of the tube hole (or the deflection of the tube hole OD) is examined.<sup>2</sup> The results for the Net FEA deflection are plotted as a function of circumferential angle to compare against the unit deflection predicted by the thick shell equations (see Figure 6-32 through Figure 6-37). The result from the TS hole ID expansion calculated using thick shell equations is subtracted from the net total displacement so that equivalent measures are compared to calculate the total difference between the thick shell equation result and the finite element results (see Equation 6-3). A value greater than zero for the total difference indicates that the effective stiffness of the tubesheet collar can be reduced, by changing the thickness of the collar, when calculating the expansion of the tubesheet ID due to internal pressure. A value less than zero indicates that the tubesheet collar thickness should be increased when calculating the expansion of the tubesheet ID due to internal pressure.

$$\left[ \text{Net FEA Deflection} - \text{Thick Shell Equation Result} \right]_{a,c,e} \quad (6-3)$$

The average value of the FEA result is obtained by calculating the area under the curve for the Net FEA Deflection as a function of tube hole angle and dividing that result by 360°. The end result of this comparison is a relationship that estimates the limiting tubesheet collar thickness as a function of TS radius.

The total radial deformation for each tube of interest in Model 1 is shown in Figure 6-32 through Figure 6-37. The results plotted include only the direct dilation or deformation of the tube hole and not the translation of the tube hole due to expansion of the entire tubesheet. The tube hole deformation plotted in Figure 6-32 through Figure 6-37 directly compares to the predicted displacement from the thick shell calculation (see Equation 6-1). In several cases during SLB conditions, the net displacement of the TS hole ID surface around the circumference of the hole is negative, which means that the deflection of the other pressurized holes in the tubesheet acts to compressively deform the tube hole into greater contact with the tube. This result means that regardless of the location of the tube in the bundle, in the presence of other pressurized tubes the effective thickness of the TS collar is greater than the TS collar thickness for a pressurized tube that is not surrounded by pressurized tubes. The results in Figure 6-32 through Figure 6-37 show that the calculated tube bore dilation using the thick shell equations included in the H\* integration model is greater than the predicted tube bore dilation using the finite element analysis for most, or all, of the tube bore circumference. The tube hole deformation results are referenced to the convention shown in Figure 6-31.

<sup>2</sup> The terms dilation, deformation and deflection are used throughout Section 6.0. In general, deformation is the change in a material relative to an unloaded initial configuration. Dilation is the growth or expansion of a surface due to some pressure. Deflection is the change in a surface relative to an unloaded initial configuration.

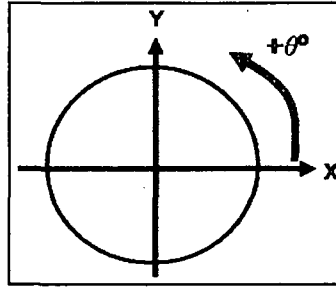


Figure 6-31 Reference Configuration for Tube Bore Deflection Plots



Figure 6-32 Inside Hole Results for NOP Conditions,  $P_{pri} = 2250$  psi, for Model 1



**Figure 6-33 Middle Hole Results for NOP Conditions,  $P_{pri} = 2250$  psi, for Model 1**



**Figure 6-34 Outside Hole Results for NOP Conditions,  $P_{pri} = 2250$  psi, for Model 1**



**Figure 6-35 Inside Hole Results for SLB Conditions,  $P_{pri} = 2560$  psi, for Model 1**



**Figure 6-36 Middle Hole Results for SLB Conditions,  $P_{pri} = 2560$  psi, for Model 1**



**Figure 6-37 Outside Hole Results for SLB Conditions,  $P_{pri} = 2560$  psi, for Model 1**

The results in Figure 6-32 through Figure 6-37 for Model 1 bound the results for tube hole deformation in Model 2, with the exception of the inside hole, which is the same in both models and has the same deformation in both orientations. The results of Equations (6-1) and (6-2) are shown in Figure 6-38. These results do not significantly change when the tube material is introduced to the tubesheet. The tube material conforms to the deformation of the tubesheet material with no gaps forming between the OD of the tube and the ID of the tubesheet tube bore in all cases. It is important to note that the results discussed in Section 6.2.4 pertain to applied pressure loads acting on a material at operating temperature, but without any applied temperature differentials. Therefore, these results ignore [

] <sup>a,c,e</sup>. Refer to Section 6.2.5 for a discussion of tube dilation within a tubesheet cell due to both temperature and pressure effects and Section 6.4.5 for a discussion of the combined effect of pressure and temperature differentials on tube-to-tubesheet contact pressure.

a,c,e



**Figure 6-38 Comparison of FEA Results and Thick Shell Equations for NOP and SLB Using Equations (6-1) and (6-2)**

a,c,e



**Figure 6-39 Typical Result for Including the Tube Cross Section Within the Tube Bore, for the Outside Hole, When All of the Tube Bores are Pressurized  
(The displacement results in the figure are magnified 500x)**

The effect of nearby plugged tubes, leaking tubes, and the practical bounds of variability on the radial dilation of the tube bore due to changing crevice pressure was also examined. The study of the different pressure combinations focused on the inside tube bore because the results in Figure 6-32 through Figure 6-38 show that the inside tube bore had the greatest magnitude of radial deflection. The result of the different pressurized tube bore study showed that varying combinations of pressure in the tube bore at different locations in the bundle do not result in a tube deformation that exceeds the case when all of the tube bores are pressurized to the full primary side pressure. This result is true for the SLB case and the NOP case. This result is also true for the case when the primary side saturation pressure is applied to the inside tube bore at varying locations. The calculated thick shell tube bore dilation due to internal pressure exceeded the average total deflection for all cases and combinations of pressure loading.

The internal pressure in the combination study was applied separately to four different regions: the internal pressure in the tube bore of interest, the tube bore local to the inside tube bore (local), the tube bore radii that bound the effective collar thickness determined by Reference 6-23 (mid-range), and the tube bore more than three times the effective collar thickness determined in Reference 6-23 (far field) (see Figure 6-40). The results of comparing different combinations of pressure in the four different tube bore regions are given in Table 6-14. The SLB tube deflections are bounded by the NOP tube bore deflections because the tubesheet Young's modulus during NOP (620°F) is less than the tubesheet Young's modulus at SLB (450°F). The results in Table 6-14 show that the thick shell calculation for the dilation of the inner surface of the tubesheet collar bound the deflection of all possible combinations of pressure, in and around, the tube of interest. The average total deformation results (without subtracting the translation of the tube hole)<sup>3</sup> of the FEA solution when all of the tube bores are pressurized to the full NOP primary side pressure for the interior dilation of the inside inner tube bore surface [ ]<sup>a,c,e</sup> inch is [ ]<sup>a,c,e</sup> % less than the predicted thick shell results [ ]<sup>a,c,e</sup> inch. If only the tube bore deflection is considered, by subtracting the effect of tube bore translation, the FEA solution for the inside tube bore dilation [ ]<sup>a,c,e</sup> inch is [ ]<sup>a,c,e</sup> % less than the predicted thick shell results [ ]<sup>a,c,e</sup> inch. Therefore, the thick shell calculations on an effective tubesheet collar for the assumed case of a tube bundle pressurized to the full primary side pressure conservatively bound the results of any FEA result for tube bore dilation due to any applied internal pressure or combination of pressurized tubes. It is important to note that the results for the planar model assume that both the pressure and temperature remain at the worst-case conditions throughout the tubesheet crevice without changing. Any reduction in temperature or pressure, relative to the primary fluid pressure and temperature used in the model, would act to reduce the predicted tube bore dilation.

<sup>3</sup> The translation of the center of the tube hole of interest changes with each combination of applied pressure in Table 6-14. Because the tube of interest in the cases shown in Table 6-14 is the inside hole, and the magnitude of the tube bore translation is small for the inside hole, it is acceptable to consider all of the results in Table 6-14 as comparable.

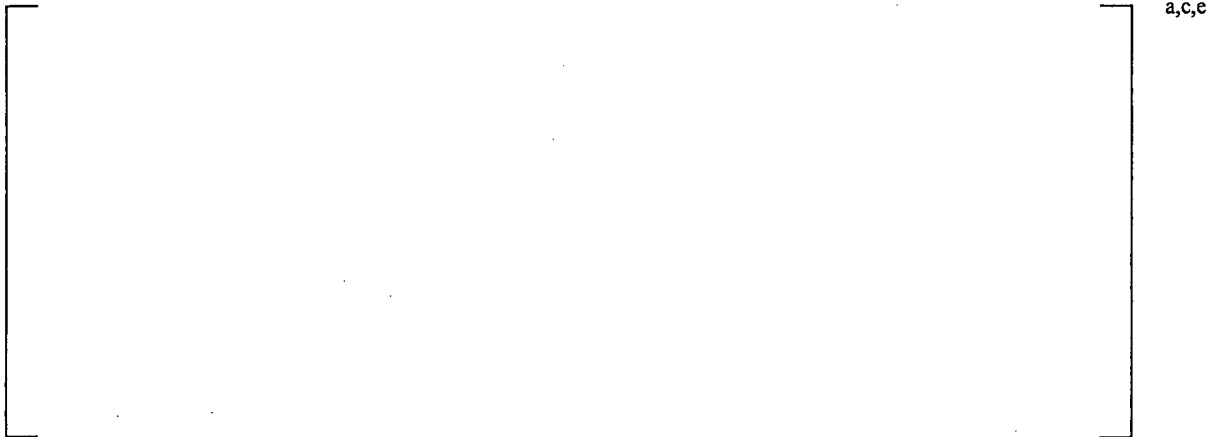


**Figure 6-40 Graphic of Applied Pressure Regions in Separate Pressure Combination Study**

The results in the Table 6-14 Cases 5 through 12 are provided to illustrate possible combinations of pressures in the vicinity of the tube of interest. These cases are not intended to reflect actual plant operating conditions. They are provided as evidence that regardless what combination of plugged, leaking, or fully pressurized tube bore surround a given tube, the greatest deflection of the tube bore is obtained when the entire perforated region is fully pressurized to the primary fluid pressure. This result makes intuitive sense because reducing the number of pressurized tube bores in the tubesheet directly reduces the strain in the tubesheet, which will directly decrease the deflections of the tube bore.



The FEA results pose a difficulty in modeling the predicted dilation of the tube bore ID. All of the FEA results predict non-uniform dilation which at some points in a tube bore becomes negative. It is not logical, or feasible, to use Equation (6-1) to predict a negative dilation from a positive pressure applied to the tube bore ID. Further, the range of deformations predicted by the FEA results cannot be calculated using Equation (6-1). The tubesheet expansion equation is asymptotic with respect to  $d$  for values much greater than the initial  $d$ . See Figure 6-41 for a graph of the calculated TS deflection during NOP as a function of  $d$ .

a,c,e

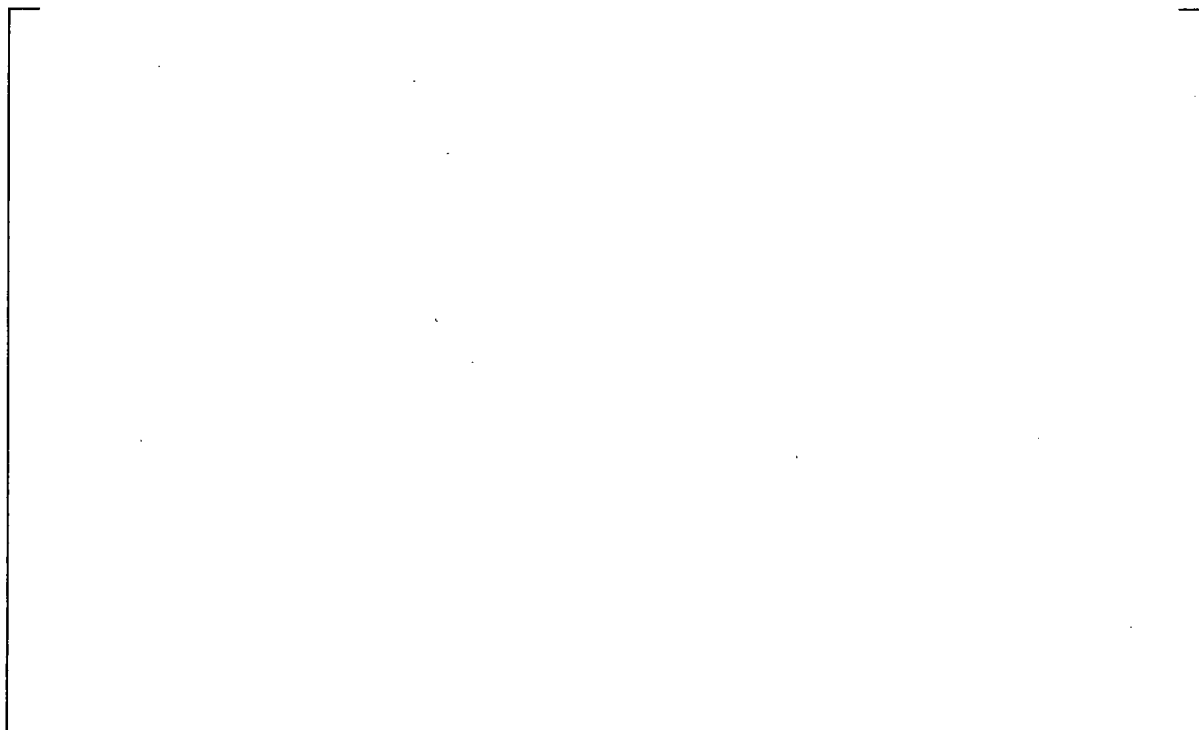


**Figure 6-41 Tube Bore ID Deflection due to a Constant Applied Internal Pressure as a Function of Outer Collar Radius**

The relationship between  $d$  and the tubesheet collar inside radius (IR) deflection in Figure 6-41 shows that the effect of  $d$  on the stiffness of a [ ]<sup>a,c,e</sup> inch (or greater) collar wall is the same as that of a [ ]<sup>a,c,e</sup> inch thick collar wall. This is because the tubesheet material, from the perspective of Poisson effects due to axial loads on the tube and the corresponding deformations of the tubesheet collar, only “sees” a limited radius of the effective tubesheet collar. Beyond a certain radius, the interaction of the additional tubesheet material collar stiffness to the tube deflections, or the tube bore dilation, is irrelevant.

The relationship between  $d$  and the TS ID surface expansion means that calculating the equivalent tubesheet expansion based upon the exact FEA results could yield a tubesheet collar thickness much larger than the original  $d$ . Very large values of  $d$ , more than [ ]<sup>a,c,e</sup> times the original thickness, begin to call into question the basis for the Goodier model and the compatibility relationship used to solve for the tube bore dilation. Very large values of  $d$  are also not conservative because the parameter  $d$  appears in both the numerator and denominator of the equation used to evaluate the contact pressure between the tube and the tubesheet in the Goodier model (Reference 6-18). Therefore, it is appropriate to consider the

results from the FEA as a general trend that describes the effective behavior of the tubesheet collar at different locations in a tubesheet.

The following approach accommodates the Goodier model framework in a conservative and appropriate manner while also taking into consideration the FEA results:

a,c,e



The FEA results are compared to results of the thick shell equations in Table 6-15. The calculation of the adjusted  $d$  values is shown in Table 6-16. The comparison of the tube bore ID dilation for the initial  $d$  value and the adjusted  $d$  value is given in Table 6-17. The calculated tube bore ID dilation results using this procedure are slightly reduced from the initial results and also accommodate the trend from the finite element analysis (see Figure 6-32 through Figure 6-37). The original goal of this process was to approximate the trend from the FEA because the actual values from the FEA cannot be obtained using the thick shell relationships. The trend from the FEA results is that there is a marked difference between the FEA and the thick cylinder results as the position in the TS changes. In order to capture that trend, it is necessary to define the difference between the two analyses. The inner diameter ( $c$ ) cannot change in either analysis. Further, it is required that the internal pressure, Young's modulus ( $E$ ) and Poisson's ratio ( $\nu$ ) are the same in both analyses. Therefore, the only parameter that can reasonably be changed to accommodate this trend, is the  $d$  value.

The limiting case for both the NOP and SLB operating conditions occurs when all tubes are pressurized at the full primary side pressure. The limiting case is defined as the greatest positive net deflection of the tube bore ID in the finite element analysis for the three tubes of interest. This result bounds the case when no tubes are pressurized in the vicinity of the tube of interest and when select tube bores are either pressurized or unpressurized based on the assumption of locally plugged tube holes adjacent to the tube bore of interest. The calculated deflection using the thick shell results is always greater than the average predicted deflection of the tubesheet hole ID surface using FEA.

Using the inside collar deflection as the reference case means that the middle and outside collar locations should have a thickness between [ ]<sup>a,c,e</sup> times the initial *d* value that would be calculated assuming no other tubes in the bundle are pressurized (see Table 6-16). The ratio approach is used in order to maintain compatibility in the H\* calculation method. The use of the limiting pressure and temperature results for the Model F SG means that these results may be considered generally applicable regardless of the plant-specific operating conditions. This approach also considers the results in Reference 6-12 and Reference 6-24 which show that the lower tubesheet radius tubes (i.e., TS radius less than 30 inches) have the limiting (i.e., lowest value) tube-to-tubesheet contact pressures. Therefore, maximizing the tube bore dilation due to internal pressure and minimizing the tubesheet collar stiffness in the lower tubesheet radius tubes when calculating contact pressures is conservative. The relationship between TS radius and the *d* parameter for SLB and NOP conditions is shown in Figure 6-42.

**Table 6-15 Comparison of FEA Results and Thick Shell Results**

Location	Condition	(1)	(2)	(3)	(4)	(3) - (4)
		FEA Deflection Results			Thick Shell Results	Total Difference
		Max	Min	Avg		
-	-	in	in	in	in	in

a,c,e

**Table 6-16 Calculation of Adjusted *d***

Location	Condition	(1)	(2)	(3)	(2) x (3)
		Total Difference	Deflection Difference Ratio	Initial <i>d</i>	Adjusted <i>d</i>
-	-	in	in/in	in	in

a,c,e

**Table 6-17 Comparison of Thick Shell Results for Initial *d* and Adjusted *d* Values**

Location	Condition	Thick Shell Results		
		Avg. FEA in	Initial in/in	Adjusted in

a,c,e

a,c,e

**Figure 6-42 Linear Relationships Between Applied Effective Outer Radius (*d*) and TS Radius for the NOP and SLB Conditions**

The results in Figure 6-42 are conservative because they are based on the calculated deflections from the case of the entire tubesheet being fully pressurized to the primary side pressure throughout the entire tubesheet depth. The amount of the dilation in the contact pressure analysis will use the depth based crevice pressure distribution based on Specimen 8 data (Reference 6-28) to determine the applied crevice pressure in the probabilistic analysis of the contact pressure distribution. The relationship for the *d* parameter as a function of tubesheet radius is based on the adjusted *d* values in Table 6-16 using the Case 1 and Case 3 results in Table 6-14.

The final effect on the tube-to-tubesheet contact pressure, and therefore, the value of *H\**, calculated by using the Goodier analysis approach with the tubesheet radius dependent collar stiffness applied to the result of a three-dimensional finite element analysis of tubesheet displacements is small,

increasing by [ ]<sup>a,c,e</sup>%. The final effect on the tube-to-tubesheet contact pressure calculated by reducing the interior dilation of the tube bore to the values predicted by the finite element study is an increase of approximately [ ]<sup>a,c,e</sup>%. Therefore, using the calculated thick shell results for the tube bore dilation of an effective tubesheet collar due to internal pressure is conservative.

A significant result is that the varying collar stiffness reduces the sensitivity of the H\* model to material data input variations. Constant tubesheet collar stiffness for each operating condition produces an unrealistic profile in the contact pressure distribution as a function of tubesheet radius that exaggerates the effect of tubesheet deflection when the coefficient of thermal expansion or the Young's modulus of the tubesheet are varied in the worst-case direction. Adjusting the tubesheet collar stiffness as a function of the tubesheet radius for each operating condition produces a smooth contact pressure relationship. The FEA results reinforce the conservatism used in the representative TS collar thickness analysis approach and in the pull out study tests.

#### 6.2.4.6 Conclusions and Discussion

A series of finite element models explored the interaction between tubes and tubesheet bore in a fully pressurized bundle. Several combinations of internal pressure were applied so that the possibility of a tube surrounded by cracked tubes, or a cracked tube surrounded by uncracked tubes, or a cracked/un-cracked tube surrounded by plugged tubes, are all accounted for in the analysis. The results of the analyses are two equations that can be used to modify the tubesheet collar thickness as a function of tubesheet radius. The most limiting relationship comes from a linear fit of the model results during NOP and SLB, for the case of all tubes in the bundle being cracked and fully pressurized. See Figure 6-42 for a graph of the two linear relationships.

The relationship for the NOP case is:

$$\left[ \begin{array}{l} \text{---} \\ \text{---} \\ \text{---} \end{array} \right] \text{ a,c,e}$$

The relationship for the SLB case is:

$$\left[ \begin{array}{l} \text{---} \\ \text{---} \\ \text{---} \end{array} \right] \text{ a,c,e}$$

The NOP relationship is applied to the FLB operating condition, but the FLB pressures are used to calculate the tube bore dilation. This is conservative because a hotter tubesheet, with reduced elastic modulus, is used to calculate the adjusted  $d$  values, and because the NOP relationship predicts a smaller value of  $d$  as a function of tubesheet radius than the SLB relationship.

### 6.2.5 Tubesheet Tube Bore Dilation

#### 6.2.5.1 Background

Section 6.2.4 discussed the results of the radius dependent tubesheet stiffness analysis. The results of that analysis showed that tubesheet bore ovalization caused a variable deflection profile around the tubes (see Figure 6-32 through Figure 6-37). The variable profiles led to questions regarding the tube conformity to

the tubesheet bore holes. The analysis discussed in this section addresses this issue to show that the tubes conform to the shape of the tubesheet bore in all cases.

The purpose of this analysis is to determine the effect of local tubesheet distortion on the contact pressure distribution between the surface of the outer tube diameter and the inner surface of the tubesheet tube bore. This analysis also provides an alternative way to verify the range of contact pressure calculated by the H\* analysis due to pressure effects.

#### 6.2.5.2 Analysis

The source of local tubesheet bore distortion is the deflection of the tubesheet due to pressure and thermal loads. The pressure loads acting on the tubesheet and the tubesheet bore distort the tube bore material in two different ways. The pressure difference between the primary and secondary faces of the tubesheet acts to deflect, or “bow”, the tubesheet in the direction of the greatest pressure differential. The primary fluid pressure acting on the internal surface of the tubes in the bundle also acts on the pressurized tube bore. The internal pressure distorts the tube bore differently depending on the location of the tube bore relative to other pressurized tubes and the non-perforated regions of the tubesheet structure such as the divider lane and the solid peripheral rim (Reference 6-29).

The contact pressure studied in this analysis is generated, in general, by the residual installation effects from hydraulic tube expansion and the applied pressure differential acting on the inner surface of the tube. The contact pressure generated by the installation and expansion process is referred to as the residual contact pressure. The starting point for this analysis is the mean residual contact pressure calculated in Reference 6-30. Although Reference 6-30 includes calculations of residual contact pressure for Model F, Model D5 and Model 44F SGs under various conditions of dimensional tolerances and material properties, this analysis will only use the nominal dimensions and material properties for the Model F. The Model F has the lowest residual contact stress for nominal conditions in Reference 6-30; therefore, this analysis conservatively bounds the conditions for the Model D5 and Model 44F.

A 2D plane strain ANSYS finite element model (FEA) is used to explore the effects of tube bore distortion. The model is shown in Figure 6-43. This model is similar to the models in Reference 6-30 except that the model in this analysis is square and represents a single tube/tubesheet unit cell of the Model F SG. The X-Y coordinate system for this model is shown on Figure 6-31. The dimensions of the model are:

- Outside dimension of tubesheet square = [     ]<sup>a,c,e</sup> inch (equal to the tube center to center distance of the Model F SG)
- Inside diameter of tubesheet hole = [     ]<sup>a,c,e</sup> inch
- Unexpanded tube outside diameter = [     ]<sup>a,c,e</sup> inch
- Tube wall thickness = [     ]<sup>a,c,e</sup> inch

This model simulates the tube expansion during the manufacturing process, distortion of the tubesheet during operation, and tube pressurization during operation. The model is run in seven loading steps. These are, in order of application in the model:

1. Initialize the Model: No loads, zero stress.
2. Initial Expansion Pressure Step (Pressurize the tube to [ ]<sup>a,c,e</sup> psi). The tube expansion pressure is broken into two steps so that the FEA does not overcompensate for the stiffening effect of the tube and predict a greater residual contact pressure than would actually develop during tube installation.
3. Increase pressure on the tube to [ ]<sup>a,c,e</sup> psi. This is a conservatively low estimate of the actual manufacturing expansion pressure range of [ ]<sup>a,c,e</sup> ksi to [ ]<sup>a,c,e</sup> ksi.
4. Release pressure on tube. This step locks in the tube with strain hardening effects and initializes the model for the application of operating pressure loads.
5. Displace the tubesheet cell. The applied range of displacement includes both the thermal loads and the pressure loads acting to deflect the tubesheet, but both the tube and the tubesheet are considered to be at ambient conditions (70°F).
6. Pressurize tube to [ ]<sup>a,c,e</sup> psi (equal to primary side pressure minus secondary side pressure at no load; [ ]<sup>a,c,e</sup> psi). The presence of secondary fluid (at the top of the tubesheet) or primary fluid (from a leak within the tubesheet portion of the tube) in the crevice between the tube and the tubesheet would reduce the pressure differential across the tube wall. Reducing the pressure differential across the tube wall means that less contact pressure will develop between the tube and the tubesheet.
7. Increase internal pressure on the tube to 2250 psi (equal to primary side pressure under no load and operating conditions). Note that this pressure is conservatively lower than the operating primary pressure during feedwater line break (FLB) and steam line break (SLB) conditions.

Thermal expansions under operating conditions were not included in this model.

Steps 1 through 4 simulate the tube expansion process during manufacturing. During this process, the tube will exceed the yield stress and will act in a plastic manner. When the expansion pressure is released in Step 4, there will be a residual stress between the tube and tubesheet and the tube will be strain hardened. The maximum expansion pressure in this analysis was selected to give the same residual contact pressure at the end of Step 4 as the Model F nominal condition in Reference 6-30 [ ]<sup>a,c,e</sup> psi). (Although the H\* analysis assumes zero residual contact pressure for conservatism of the pull out calculations, the value of residual contact pressure used for this study is a reasonable estimate of the actual expected residual contact pressure.) The application of the full expansion pressure would result in a greater magnitude of residual contact pressure and strain hardening. Therefore, the results presented in this analysis should be considered conservative lower estimates of the contact pressure between the tube and the tubesheet. Step 5 applies tubesheet distortion under operating conditions to determine the effects on contact stresses between the tube and tubesheet. The source of the distortion is a combination of the tubesheet bow due to pressure loads, thermal expansion distortions and the potential for distortion of the tube bore and ligaments due to local effects from neighboring tubes. There are several different postulated types and amounts of tubesheet distortion. Steps 6 and 7 add in the pressure that the tube would see under operating conditions.

During Steps 1 through 4, the boundary conditions are the same for all of the computer runs. The outside edges of the tubesheet are constrained from moving. The tube is constrained to stay centered in the hole in the tubesheet to prevent free body movement of the tube. This is shown in Figure 6-44. The outside of the tube and the inside of the hole in the tubesheet have contact elements to allow separation between the tube and tubesheet but allow transfer of load when contact is made.

Several different configurations of tubesheet distortion were analyzed. Each represents the bounding assumptions on the potential cause of the tubesheet bore distortion and the possible location of the unit tube/tubesheet bore cell in the tube bundle.

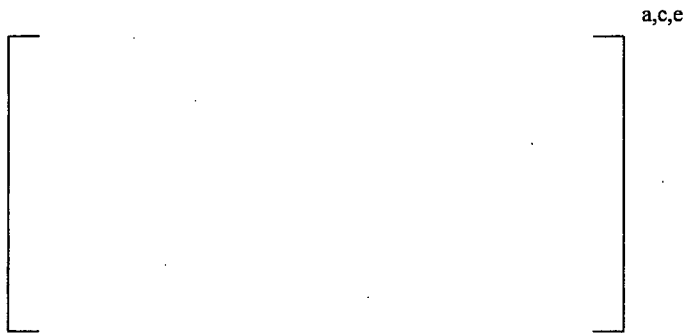
The first type of tubesheet distortion simulated is stretching of the tubesheet in the direction parallel to the Y axis (called square displacement) of the model with the model fixed to allow no movement at the edges in the X direction. This type of idealized distortion is similar to the deflection in the tube bore directly perpendicular to the face of the divider plate in the middle of the bundle. The distortion generated by these boundary conditions represents a worst-case condition with respect to contact pressure because the tube bore material can only distend and is not allowed to redistribute the strain around the tube bore. Redistributing the strain around the tube bore due to Poisson effects would act to pinch the tube and increase contact pressure. These boundary conditions are applied by displacing the "top" edge of the model by half the stretching amount in the +Y direction, displacing the "bottom" edge of the model by half the stretching amount in the -Y direction and fixing the "sides" of the model in the X direction. Note that the use of the terms "top", "bottom" and "sides" refer only to the orientation as shown in Figure 6-44 and other figures in this analysis and not to the orientation of the actual SG tubesheet. Figure 6-45 shows the displaced shape in solid lines and shaded elements (with displacements exaggerated) and the undisplaced shape in dashed lines without shaded elements. Note the top and bottom edges of the model are displaced but the sides are not displaced. Six different displacements are investigated and these computer runs are labeled as follows.



The maximum value of the predicted tubesheet tube bore distortion from the  $H^*$  calculation is typically on the order of [ ]<sup>a,c,e</sup> inch or less (see Section 6.3 for a discussion of the equations used to calculate those distortions and dilations due to pressure and thermal effects). The maximum value of the tubesheet tube bore distortion predicted by FEA is [ ]<sup>a,c,e</sup> inch or less. Therefore, these applied displacements are conservative and bound the predicted range of distortion from both FEA and classical thick shell equations.

The second type of tubesheet distortion simulated allows the tubesheet cell material to redistribute the strain according to Poisson effects. The distortion is same as the first type in the Y direction but with the sides of the tubesheet portion of the model free to move in the X direction but constrained to stay in a

straight line. This is achieved by node coupling in the X direction on the side edges of the model. The displaced and undisplaced shapes for this condition are shown in Figure 6-46. Note here that the top and bottom edges of the model are displaced similar to Figure 6-45, but the sides of the model have displaced inward from the undisplaced sides. The computer run labels are as follows.



The next type of tubesheet distortion simulated is displacement in a tube pattern diagonal direction. This type of distortion is similar to the tube bore deflections experienced by the tube bore at some angle to the face of the divider plate in the bundle. The upper right corner of the model is displaced in the upper right diagonal direction by half the total displacement and the lower left corner is displaced in the lower left diagonal direction by half the total displacement. The other two corners are fixed and the edges of the tubesheet portion of the model are constrained to be straight lines between the corners using linear constraint equations. The node constraints for this model are shown in Figure 6-47. The expansion pressure in Step 3 was changed to [ ]<sup>a,c,e</sup> psi in order to achieve a residual contact pressure of [ ]<sup>a,c,e</sup> psi at the end of Step 5 due to the diagonal model orientation to make the initial conditions from the RCP variability study as similar as possible to the initial conditions in the tubesheet dilation study. The displaced and undisplaced shapes for this model are shown in Figure 6-48. Note that the upper right and lower left corners of the model are displaced, but the other two corners are not displaced. Again, six different displacements were investigated and the computer run labels are as follows:



The total displacement is the vector sum of the X and Y displacement. Note that these displacements are the S.1.X model displacements from above times the square root of two. Since the square model displacements are measured from one side to the opposite side of the model, and the diagonal model displacements are measured for one corner to the opposite corner, the diagonal model displacements have the same displacement per inch as the square model displacements.

The last type of tubesheet distortion simulated is same as the previous type in displacement in the diagonal direction of the upper right and lower left corners but the other two corners are free to move. The displaced and undisplaced shapes for this condition are shown in Figure 6-49. Note that the upper

right and lower left corners are displaced similar to Figure 6-48, but the other two corners are allowed to displace inward from the undisplaced corners. The computer run labels are as follows.



Tables 1 and 2 show the contact pressure results between the tube and the tubesheet for all the steps for all the computer runs.

Figure 6-50 through Figure 6-62 show the stress intensity and contact pressure for each step in a typical computer run – in this case Run S.1.5. The S.x.5 cases are the most representative of the tube bore dilations that result from the applied pressures and temperatures acting on the tubesheet. The figures are shown to assist in visualizing what is happening during a run. On all of these figures the stress intensity and contact pressures are in psi. Displacements shown are in true scale, with no magnification of the results (i.e., 1 to 1).

Figure 6-50 shows the stress intensity for Step 1. Since there is no displacement or pressure in Step 1, the stress intensity is zero everywhere. Figure 6-50 shows that there is an initial gap between the tube and the tubesheet. Since there is no contact between the tube and the tubesheet there is no contact pressure between the tube and the tubesheet.

In Step 2 of the computer run, the inside of the tube is pressurized to [ ]<sup>a,c,e</sup> psi. The resulting stress intensity is shown in Figure 6-51. Note that the stress intensity in the tube is in the range of [ ]<sup>a,c,e</sup> to [ ]<sup>a,c,e</sup> psi which is above the yield stress of [ ]<sup>a,c,e</sup> psi. The tube has plastically deformed and the gap between the tube and tubesheet has closed. The maximum stress in the tubesheet is less than [ ]<sup>a,c,e</sup> psi. Figure 6-52 shows the contact pressure at the end of Step 2. The contact pressure is very close to uniform at about [ ]<sup>a,c,e</sup> psi. Note that the tube expansion during manufacturing is done in a single step to maximum pressure. Step 2 is in the analysis to make it easier to see the stresses, displacement and contact stresses about half way through the expansion process.

In Step 3 of the computer run, the inside of the tube is pressurized to about [ ]<sup>a,c,e</sup> psi. The resulting stress intensity is shown in Figure 6-53. Note that the maximum stress in the tube has only increased from about [ ]<sup>a,c,e</sup> psi in Step 2 to [ ]<sup>a,c,e</sup> psi in Step 3 even though the tube internal pressure has almost doubled. This is because the tube is in the plastic region of the stress strain curve where the tangent modulus is much less than the elastic modulus of the tubesheet. The stress in the tubesheet has increased significantly, but is still below about [ ]<sup>a,c,e</sup> psi. The contact pressure at the end of Step 3 is shown in Figure 6-54. This contact pressure is close to [ ]<sup>a,c,e</sup> psi and is very uniform around the circumference of the tube.

In Step 4 of the computer run, the pressure inside the tube is reduced to zero. This corresponds to the end of the tube expansion manufacturing process.

Figure 6-55 shows the stress intensity at the end of Step 4. The residual stress in the tube is less than [ ]<sup>a,c,e</sup> psi and the residual stress in the tubesheet is less than [ ]<sup>a,c,e</sup> psi. The loading at the end of Step 4 is the same as in Step 1, that is, no displacement or pressure load applied to the model. The reason that the tube does not return to the condition of Step 1 (Figure 6-50) is that the tube has been plastically deformed during Steps 2 and 3. Figure 6-56 shows the residual contact pressure between the tube and tubesheet. The residual contact pressure varies between 316 and 421 psi with an average of 372 psi.

In Step 5 the tubesheet is stretched, the upper edge by [ ]<sup>a,c,e</sup> inch in the upper direction and the lower edge by [ ]<sup>a,c,e</sup> inch in the lower direction. The side edges of the tubesheet are fixed in the X direction. Figure 3 shows the displacement greatly magnified. Figure 6-57 shows the stress intensity in the tube and tubesheet at the end of Step 5. The maximum stress in the tube has decreased slightly, and the maximum stress in the tubesheet is less than [ ]<sup>a,c,e</sup> psi. The maximum stress in the tubesheet occurs at the side edges of the tube hole which is to be expected given the tubesheet stretching in the vertical direction. Figure 6-58 shows the contact pressure between the tube and tubesheet at the end of Step 5. This contact stress is less than in Step 4 but it is always positive and no gaps have opened between the tube and tubesheet.

Steps 6 and 7 pressurize the inside of the tube with pressure seen at the hot standby condition in operation. At hot standby, the primary pressure is 2250 psi and the secondary pressure is 1020 psi. Step 6 uses a tube pressure of 1230 psi which is equal to the difference between the primary side pressure and the secondary side pressure. This would be the net pressure on the tube if there was a gap between the tube and tubesheet. Step 7 uses a tube pressure of 2250 psi. This is the pressure on the tube if there is no gap between the tube and the tubesheet. Figure 6-59 shows the stress intensity and Figure 18 shows the contact pressure at the end of Step 6. Figure 6-61 shows the stress intensity and Figure 6-62 shows the contact pressure at the end of Step 7. Since there are no gaps at the end of Step 6 (the contact pressure is positive all the way around in Figure 6-60), then Step 7 is valid for this tubesheet displacement condition. The final contact pressure varies from [ ]<sup>a,c,e</sup> to [ ]<sup>a,c,e</sup> psi. The magnitude of the final contact pressure would be different if a smaller or zero value of residual contact pressure were assumed. The value of contact pressure assumed in this analysis is solely for the purposes of matching the initial conditions from the RCP variability study and it is impossible to obtain the same level of strain hardening in a tube approximately [ ]<sup>a,c,e</sup> % and not have some calculated value of residual contact pressure. However, the trend in the results would be the same and the final effect (i.e., the variation of the contact pressure around the circumference of the tube is small) is also expected to be the same.

The idealized distortion cases from the S.1.x runs had the limiting contact pressure distributions and values for all conditions. The contact pressure was always greater than zero for the entire circumference of the tube at the expected level of distortion during operating conditions. The variation in the contact pressure distributions for the expected maximum distortion was on the order of [ ]<sup>a,c,e</sup> psi for Step 6 and Step 7. A variation of [ ]<sup>a,c,e</sup> psi in the contact pressure represents a [ ]<sup>a,c,e</sup> % difference, or less, compared to the average contact pressure value around the circumference of the tube. Refer to Section 7.0 for a discussion on the average contact pressure for the mean Model F material and geometric properties. Therefore, it can be concluded that the contact pressure does not significantly vary around the circumference of the tube during operating conditions and that no gaps between the outer tube surface and the inner tubesheet tube bore surface develop due to pressure effects or tubesheet distortion.

### 6.2.5.3 Summary of Results

The tubesheet tube bore dilation study results show that tubesheet deformations in the range predicted for the plants in the H\* fleet does not create a gap between the tube OD and the tubesheet tube bore ID. Two models were used to study this effect: a square unit cell model and a diagonal, or "diamond", unit cell model. Each model represented the potential direction of the applied loads on a tube within a tubesheet tube bore. The square unit cell model predicted more uniform contact pressure results due to the applied dilation and the diamond model tended to predict contact pressures that were skewed to the maximum value in the distribution. The absolute maximum tube bore dilation predicted in Reference 6-29 is less than [ ]<sup>a,c,e</sup> inch. The average predicted tube bore dilation in the H\* contact pressure analysis is approximately [ ]<sup>a,c,e</sup> inch. The average predicted tube bore dilation from the tubesheet stiffness study is on the order of [ ]<sup>a,c,e</sup> inch (see Section 6.2.4). The variation in the residual contact pressure around the circumference of the tube, due to a tube bore dilation of [ ]<sup>a,c,e</sup> inch an unpressurized tube at room temperature, for the square tubesheet cell boundary conditions in Table 6-18 is less than [ ]<sup>a,c,e</sup> psi. The variation in the residual contact pressure around the circumference of the tube, due to a tube bore dilation of [ ]<sup>a,c,e</sup> inch in an unpressurized tube at room temperature, for the diagonal tubesheet cell boundary conditions in Table 6-19 is less than [ ]<sup>a,c,e</sup> psi. There was residual contact pressure present for all applied boundary conditions, regardless of the tubesheet cell model used in the analysis, for the bounding tube bore dilation of [ ]<sup>a,c,e</sup> inch. In the case of a pressurized tube in the square tubesheet cell, the variation around the circumference of the tube was also less than [ ]<sup>a,c,e</sup> psi. In the case of a pressurized tube in the diagonal tubesheet cell, the variation around the circumference of the tube was less than [ ]<sup>a,c,e</sup> psi. A variation of less than [ ]<sup>a,c,e</sup> psi for a tube at room temperature with an internal primary fluid pressure of 2250 psi and an applied tube bore dilation of [ ]<sup>a,c,e</sup> inch is equal to a [ ]<sup>a,c,e</sup>% variation, or less, in the contact pressure around the circumference of the tube. The variation in the contact pressure around the circumference of the tube decreases to [ ]<sup>a,c,e</sup>%, or less, for the maximum calculated tube bore dilation from Reference 6-29. Therefore, it is not necessary to consider the circumferential variation in the contact pressure distribution between a tube and the tubesheet. It is also concluded that the tube OD and tubesheet tube bore ID always maintain contact in the predicted range of tubesheet displacements.

**Table 6-18 Contact Pressure for Square Displacement Model <sup>(1)</sup>**

a,c,e


- (1) All contact pressures in psi.
- (2) Each displaced side of square displaced to half this distance.
- (3) For run names S.1.X, the non-displaced sides of the square are fixed in the X direction. For run names S.2.X, the non-displaced sides of the square are free to move in the X direction but constrained to be a straight line.

**Table 6-19 Contact Pressure for Diagonal Displacement Model <sup>(1)</sup>**

a,c,e


- (1) All contact pressures in psi.
- (2) Each displaced corner of square displaced to half this distance.
- (3) For Run Names D.1.X, non-displaced corners are fixed. For Run Names D.2.X, non-displaced corners are free.

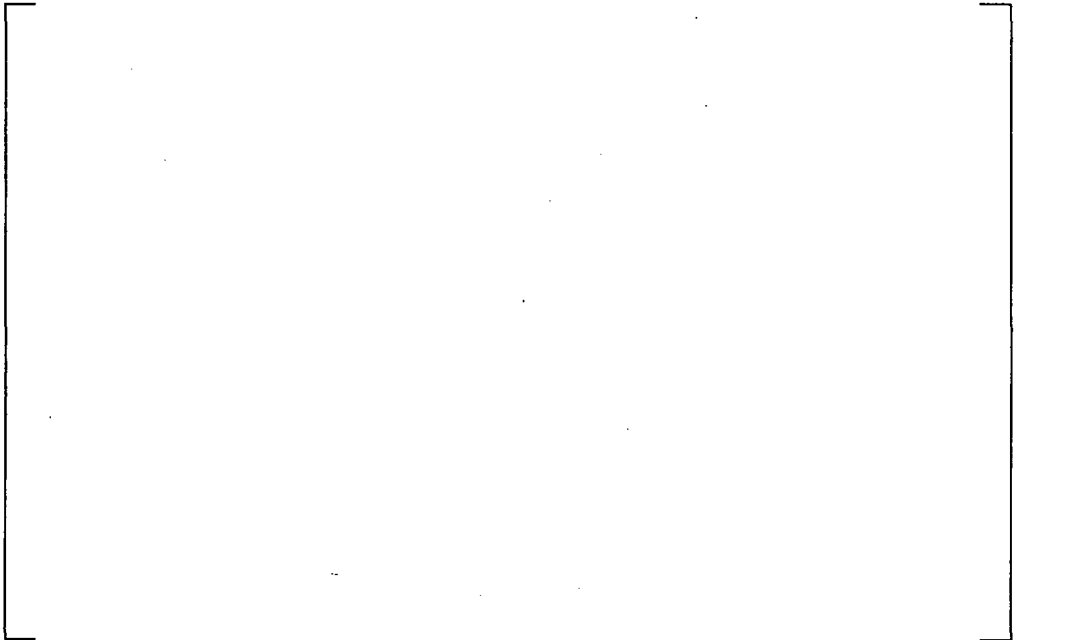


**Figure 6-43 Finite Element Model**

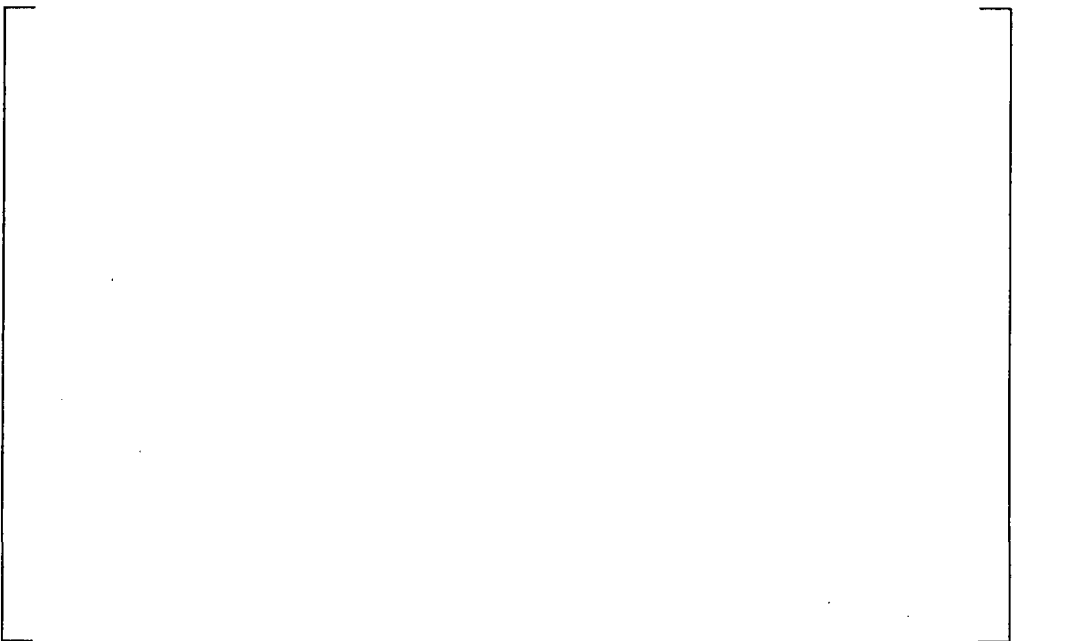


**Figure 6-44 Boundary Conditions for Square Displacement Model**



**Figure 6-45 Displaced Shape for S.1.1 Through S.1.6 Computer Runs**



**Figure 6-46 Displaced Shape for S.2.1 Through S.2.6 Computer Runs**



**Figure 6-47 Boundary Conditions for Diagonal Displacement Model**

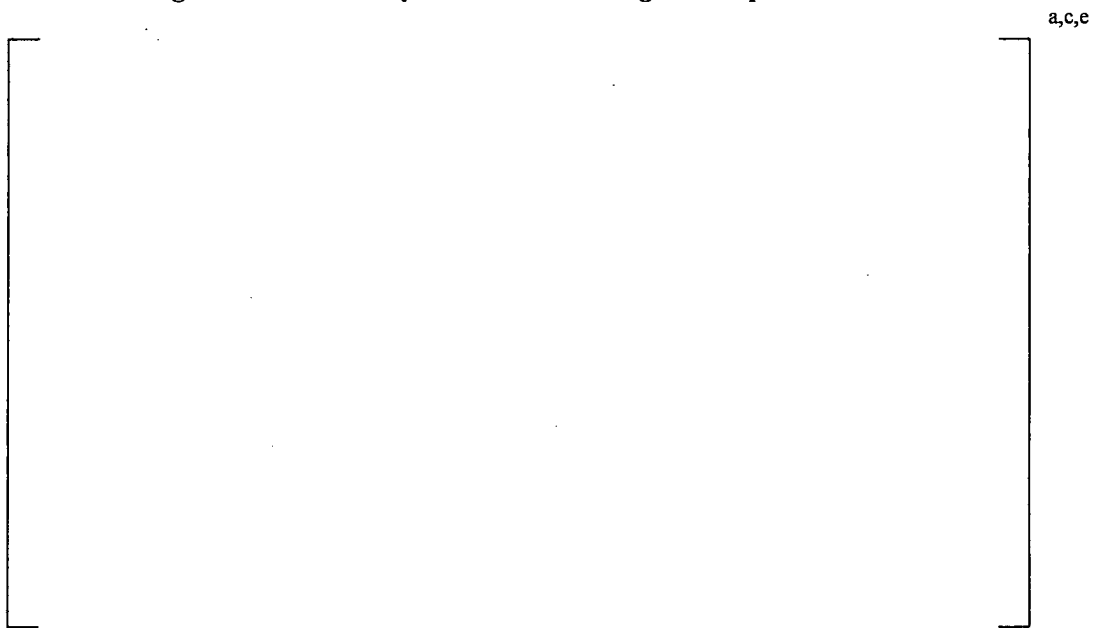


**Figure 6-48 Displaced Shape for D.1.1 Through D.1.6 Computer Runs**



**Figure 6-49 Displaced Shape for D.2.1 Through D.2.6 Computer Runs**

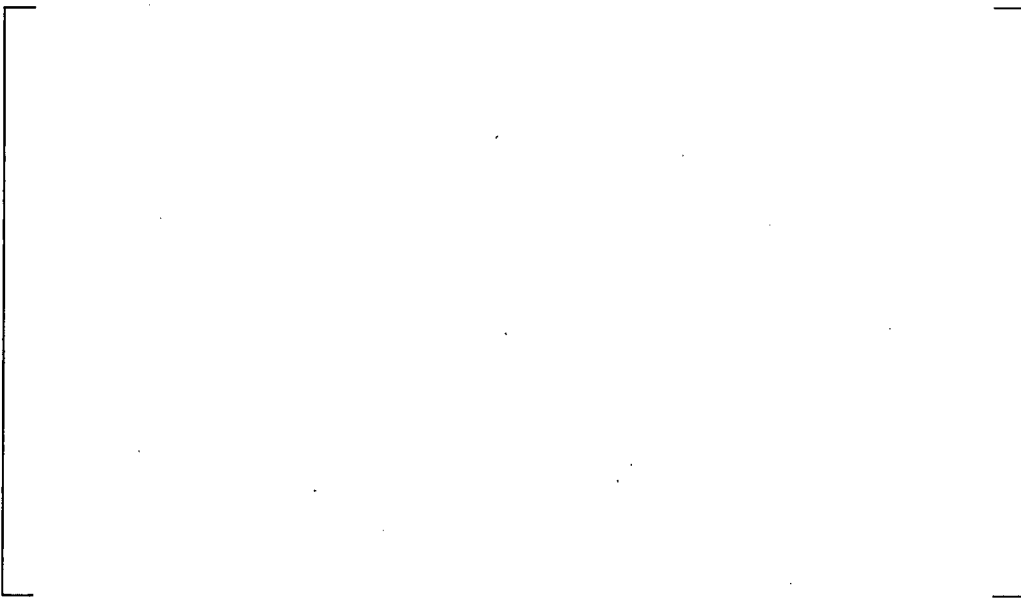


**Figure 6-50 Computer Run S.1.5, Step 1, Stress Intensity**



a,c,e

**Figure 6-51 Computer Run S.1.5, Step 2, Stress Intensity**



a,c,e

**Figure 6-52 Computer Run S.1.5, Step 2, Contact Pressure**



**Figure 6-53 Computer Run S.1.5, Step 3, Stress Intensity**

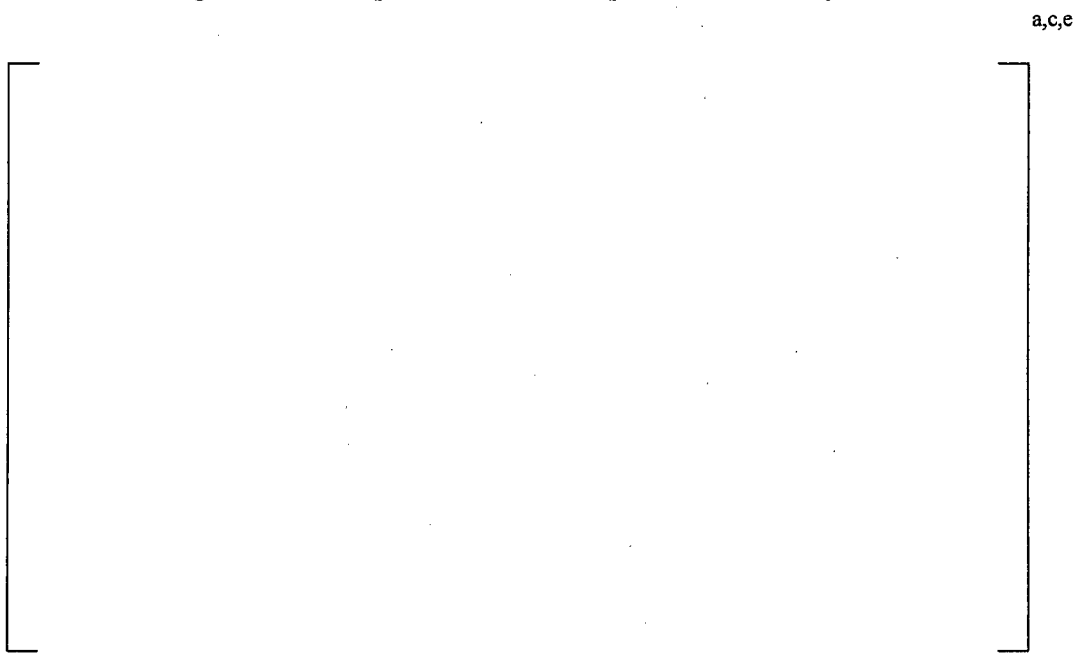


**Figure 6-54 Computer Run S.1.5, Step 3, Contact Pressure**

a,c,e



**Figure 6-55 Computer Run S.1.5, Step 4, Stress Intensity**

a,c,e



**Figure 6-56 Computer Run S.1.5, Step 4, Contact Pressure**



**Figure 6-57 Computer Run S.1.5, Step 5, Stress Intensity**



**Figure 6-58 Computer Run S.1.5, Step 5, Contact Pressure**



a,c,e

**Figure 6-59 Computer Run S.1.5, Step 6, Stress Intensity**



a,c,e

**Figure 6-60 Computer Run S.1.5, Step 6, Contact Pressure**



**Figure 6-61 Computer Run S.1.5, Step 7, Stress Intensity**



**Figure 6-62 Computer Run S.1.5, Step 7, Contact Pressure**

## 6.2.6 Divider Plate Modeling

The effect of the divider plate is modeled in the H\* Integration model (Excel® spreadsheet model) through an adjustment factor to account for the presence or absence of the divider plate. The results in this section are based on the worst case model SG in the domestic fleet and conservatively applied to the Model 44F SG to maximize the calculated H\* values. The divider plate factor is normalized to the condition represented in the ASME Code Stress Report that assumes a non-functional, (or missing) divider plate to maximize the design stresses on the tubesheet. The tubesheet deflection corresponding to the ASME Code stress analysis of the tubesheet without the divider plate, therefore, results in a divider plate factor of [ ]<sup>a,c,e</sup>. Based on the use of the original structural model for the divider plate, the divider plate factor for the case of a fully functional divider plate is [ ]<sup>a,c,e</sup> because the tubesheet deflection would be decreased relative to the reference case.

During the development, the structural model of the tubesheet complex was significantly improved by including structural features such as the solid tubesheet rim and solid, non-perforated section in the tubelane, divider plate structural support of the channelhead, as well as other features that more correctly represented the tubesheet complex structure. Analysis of the tubesheet deflection using the improved model results in reduced predicted tubesheet deflection. For the case of a fully functional divider plate, the predicted deflection normalized to the original tubesheet deflection yields a divider plate factor of [ ]<sup>a,c,e</sup>. For the case of a non-functional divider plate, represented by eliminating the upper [ ]<sup>a,c,e</sup> inches of the divider plate where it attached to the tubesheet, but retaining the divider plate in the channelhead, results in a divider plate factor of [ ]<sup>a,c,e</sup>.

Cracking has been observed in the heat affected zone of the stub runner to divider plate welds in foreign SGs (Reference 6-7). The cracks appear to be the result of combined primary water stress corrosion cracking (PWSCC) and mechanical fatigue. Degradation of the divider plate to stub runner connections can affect the deflection of the tubesheet due to pressure loads. This degradation could affect an analysis that depends upon the divider plate to limit the vertical displacement of the tubesheet as well as analyses that take credit for a divider plate factor (DPF).

As noted above, the H\* analysis bounds the effect of a severely degraded divider plate by increasing the tubesheet deflections by the ratio of the DPF for a degraded divider plate [ ]<sup>a,c,e</sup> to the DPF for an intact divider plate [ ]<sup>a,c,e</sup>, or [ ]<sup>a,c,e</sup>. In the context of the lower SG complex model and the H\* contact pressure analysis, a degraded divider plate is considered a divider plate with the upper [ ]<sup>a,c,e</sup> inches of the weld, stub runner, and heat affected zone of the divider plate removed. This level of degradation has never been observed in any foreign SG and is extremely conservative compared to the reported levels of degradation over the prior 15 years of inspections in the foreign fleet (References 6-33, 6-34, and 6-35). See Reference 6-7 for a description of the divider plate factor for different levels of weld degradation and how the divider plate factor is calculated. Refer to Section 6.2.1 for a description of how the divider plate is included in the lower SG complex model.

Degradation of the divider plate does not significantly affect the pressures or temperatures of the primary fluid during any operating condition (Reference 6-36). The limiting sector of the tubesheet is perpendicular to the face of the divider plate. Refer to Section 6.2.3 for a discussion of the tubesheet displacements as a function of azimuthal position. The combined radial tubesheet displacements at the 90° plane of the perforated tubesheet region (parallel to the face of the divider plate along the edge of the

divider lane) are typically [ ]<sup>a,c,e</sup> % less than the tubesheet displacements perpendicular to the face of the divider plate. Reducing the tubesheet displacements increases the contact pressure between the tube and the tubesheet. See Figure 6-21 for a graph showing the increase in pull out resistance as a function of azimuthal angle in the tubesheet. Increasing the contact pressure between the tube and the tubesheet reduces the calculated H\* value. See Figure 6-63 for a comparison of the mean H\* values for a degraded divider plate and an intact divider plate. Note that the tubesheet displacements with a degraded divider plate predict a larger value of H\* than the tubesheet displacements with an intact divider plate.



**Figure 6-63 Comparison Between H\* Values for a Degraded Divider Plate (DPF = [ ]<sup>a,c,e</sup>) and an Intact Divider Plate (DPF = [ ]<sup>a,c,e</sup>).**

### 6.3 TUBESHEET ROTATION EFFECTS

The H\* integrator model includes a calculation for tubesheet hole dilation due to tubesheet rotations. A study was performed to evaluate if the tube bore dilation model from the reference case (Reference 6-15) in the H\* integration is appropriate when the 3D FEA displacements are used. The study compared the results for tubesheet bore dilation from the original 2D axisymmetric model and those from the 3D FEA model. This section summarizes the results of this study.

Loads are imposed on the tube OD as a result of tubesheet deflections. The interaction between the tubesheet and the other structures in the lower SG complex results in the tubesheet rotating due to the deflections under the applied pressure and temperature conditions. The radial displacements produced by the thermal loads are unaffected by the divider plate. The analysis results in this report conservatively assume (see Section 6.2.6) that the stub-runner-to divider plate weld is non-functional (i.e., there is no restraint provided to the vertical displacement of the tubesheet by the divider plate). The radial deflection,  $U_R$ , at any point within the tubesheet is found by combining the radial tubesheet deflections at that location according to:

$$\left[ \quad \quad \quad \right]^{a,c,e} \quad (6-4)$$

where

$DPF$  = The divider plate factor,

$U_{AP}$  = The radial tubesheet deflections at the  $0^\circ$  face of the tubesheet (see Section 6.2.3) due to the applied pressure loads on the lower SG complex for the specific operating condition and

$U_{AT}$  = The radial tubesheet deflections due to the applied temperature loads on the lower SG complex for the specific operating condition.

This expression is used to determine the radial deflections along a line of nodes at a constant axial elevation (e.g., top of the tubesheet, mid-plane, etc.) within the perforated area of the tubesheet. The expansion of a hole of diameter  $D$  in the tubesheet at a radius  $R$  is given by:

$$\text{Radial:} \quad \Delta D = D \{dU_R(R)/dR\} \quad (6-5)$$

$$\text{Circumferential:} \quad \Delta D = D \{U_R(R)/R\} \quad (6-6)$$

$U_R$  is available directly from the finite element results. The value for  $dU_R(R)/dR$  is obtained by numerical differentiation of the combined displacement field. The maximum expansion of a hole in the tubesheet is in either the radial or circumferential direction. Typically, these two values are within [ ]<sup>a,c,e</sup>% of each other. Since the analysis for calculating contact pressures is based on the assumption of axisymmetric deformations with respect to the centerline of the hole, a representative value for the hole expansion must be used that is consistent with the assumption of axisymmetric behavior. A two-dimensional finite element study (Reference 6-15) was performed to determine the effect of hole "out-of-roundness" on the contact pressures between a sleeve and a tube, and between the tube and tubesheet. The equation used for the hole  $\Delta D$ ,  $D_{max} - D_{min}$ , is:

$$\left[ \quad \quad \quad \right]^{a,c,e} \quad (6-7)$$

where SF is a scale factor between [ ]<sup>a,c,e</sup> and [ ]<sup>a,c,e</sup>. For the eccentricities typically encountered during tubesheet rotations, SF varies between approximately [ ]<sup>a,c,e</sup> and [ ]<sup>a,c,e</sup>. The eccentricities on the tube bore are due to combined pressure and temperature effects (e.g., tubesheet bow, thermal expansion, etc.). Eccentricity in this context is taken to mean the difference between the maximum hole diameter and the minimum hole diameter ( $\Delta D$ ). These values are listed in the following table:

**Table 6-20 Scale Factor as a Function of Initial Eccentricity**

		a,c,e

The data for initial eccentricities were fit to the following polynomial equation (Reference 6-15):

$$\left[ \begin{array}{l} \\ \\ \\ \\ \\ \end{array} \right] \quad \begin{array}{l} a,c,e \\ \\ \\ \\ \\ (6-8) \end{array}$$

The hole expansion calculation as determined from the 3D finite element results includes the effects of tubesheet rotations and deformations caused by the system pressures and temperatures. It does not include the local effects produced by the interactions between the tube and tubesheet hole. The hole expansion equation was compared against the range of calculated displacements from the 3D finite element analysis. Both the previously calculated scale factors and  $\Delta D$  factors were applicable when the displacements from the 3D finite element analysis were used. The results of the 2D hole expansion calculation were shown to be conservative and both increased hole growth and reduced contact pressure compared to the 3D results. Refer to Section 6.2.5 for a discussion of contact pressure variation due to tubesheet tube bore dilation. Therefore, the 2D hole expansion calculation is reasonable when the 3D FEA displacement results are used and the  $\Delta D$  and SF equations can be used in the  $H^*$  contact pressure analysis.

### 6.3.1 Topical White Paper: Relationship Between Tubesheet Tube Bore Eccentricity and Contact Pressure at Lower Temperatures and Pressures

#### Introduction

Report WCAP-17071-P was issued to the  $H^*$  participants as the report of record for the Model F steam generators. During the continuing development of  $H^*$  for the Model 44F steam generators, some questions were encountered that require resolution to facilitate the review of the reference report. This White Paper is an adjunct to WCAP-17071-P; however, the information in this paper is included in the Model 44F report. This is because Point Beach Unit 1 has a cold temperature SLB condition. Therefore, the methodology for calculating the contact pressure described in the White Paper was used to calculate SLB contact pressures for the Model 44F SG. Liberal reference is made to WCAP-17071-P; " $H^*$ : Alternate Repair Criteria for the Tubesheet Expansion Region in Steam Generators with Hydraulically Expanded Tube (Model F)."

---

## Issue Summary

1. The Model D5 main steam line break (SLB) transient defined in the E-spec describes primary fluid temperatures in the steam generator (SG) that are 100°F, or more, colder than the Model F SG SLB transient specification.
2. Preliminary analysis of the tube-to-tubesheet (T/TS) contact pressure when a conservative static, steady-state, application of the as-specified Model D5 SLB transient conditions were used resulted in a case where the design basis accident (DBA) T/TS contact pressures apparently did not exceed the T/TS contact pressures at normal operating condition (NOP) for all depths in the tubesheet (TS).
3. The NRC had requested to be informed if a condition was found under which the DBA T/TS contact pressure did not exceed the NOP T/TS contact pressure at all depths through the TS. The NRC Technical Staff was informed of the situation on April 24, 2009.
4. Westinghouse has reviewed the contact pressure analysis and the preliminary Model D5 results. The T/TS contact pressure during DBA conditions does exceed the T/TS contact pressure during NOP when the appropriate relationship between T/TS contact pressure and tube bore eccentricity is used for the Model D5 SLB condition.

## Background

This White Paper discusses an original fit and a new fit for the relationship between the tubesheet bore eccentricity and contact pressure. Both data fits are derived from a two-dimensional structural model and both data fits are applied for the current H\* analysis in the three-dimensional finite element model. For the original fit, tubesheet bore eccentricity was derived from a two-dimensional structural analysis based on higher temperature input and a 4<sup>th</sup> order polynomial fit was developed for the relationship between tubesheet bore eccentricity and contact pressure. During the continued development of H\*, a separate two-dimensional finite element model was developed for the express purpose of evaluating contact pressure as a function of tubesheet bore eccentricity. This model used assumed tubesheet bore eccentricities as input, independent of how the values of eccentricity are generated in the H\* analysis. The range of the tubesheet tube bore eccentricities considered in the model was based on detailed finite element studies of tubesheet designs with perforations specifically modeled into the structure of the thick plate. The original fit is not appropriate for use at lower temperatures because the 4<sup>th</sup> order polynomial produces physically impossible results at those temperatures. The original fit, when applied within its supporting database, is conservative relative to the new fit at higher temperatures because it produces lower values of the integrated contact pressure.

## Discussion

The analysis process for H\* for the Model D5 steam generators was reviewed to determine the reason for the observations noted above in items 1 and 2. Two key details were observed during the tubesheet bore deformation (eccentricity) calculations in the H\* spreadsheet discussed in WCAP-17071-P:

- The original calculated hole deformations during SLB were much less than the calculated hole deformations during NOP and FLB. The hole deformations are based on fundamental axisymmetric deformation relationships and were not derived as part of the H\* program. These relationships are noted as the second and third equations in Section 6.3 of WCAP-17071-P.
- Despite the fact that the tube hole deformation during SLB was less than the tube hole deformation during NOP/FLB, the T/TS contact pressure was less for SLB than for NOP. This was an inconsistent result because the decrease in tube bore deformation is expected to result in greater T/TS contact. Further, the difference between the tube (T) and tubesheet (TS) coefficients of thermal expansion ( $\Delta CTE$ ) increases at lower temperatures (i.e.,  $CTE_{TUBE} > CTE_{TS}$ ) and this should also result in greater T/TS contact pressure.

Review of Reference 6-15 in WCAP 17071-P, which defines the relationship between tube bore eccentricity and contact pressure, showed that colder primary fluid conditions (less than  $[ ]^{a,c,e} - [ ]^{a,c,e} \text{ } ^\circ\text{F}$ ) and lower pressure conditions (less than 2250 psi) were not considered in prior analyses (dating back to 2003). The relationship between tube bore eccentricity and contact pressure is described in Section 6.3 of the WCAP-17071-P. The data in Section 6.2.5 of the WCAP-17071-P proved that the relationship between tube bore eccentricity and contact pressure was conservative for all of the Model F operating conditions. The fit of the relationship between tubesheet bore eccentricity and contact pressure that is described in Section 6.3 on page 6-85 relies on data from finite element models that used boundary conditions representative of NOP conditions. The eccentricity and contact pressure analysis described in Section 6.3 produced a 4<sup>th</sup> order polynomial fit that was specific to a range of temperature and pressure conditions that are different from the Model D5 SLB conditions. Prior Model D5 analyses included the B\* approach, which, in all cases, was bounded by H\*; therefore, the relative arrangement of the SLB vs. NOP contact pressures was not identified as a concern. Prior analyses were based on the use of ratios to determine the applicable tubesheet deformations from the results of 2D axisymmetric unit load cases. Evolution of the H\* calculation process to the use of a 3D FEA approach now requires that a specific relationship between contact pressure and input temperatures be used when evaluating operating conditions outside of those on which the original fit was based.

Because of the observations noted above, it is not appropriate to apply the same relationship in Section 6.3 of WCAP-17071 to the analysis of the T/TS contact pressure during the Model D5 SLB condition. Therefore, it was required to develop a new relationship between tube bore eccentricity and contact pressure for the different Model D5 SLB condition. An analysis, documented in WCAP-17071, Section 7.2.2, performed to determine the variability of contact residual pressure for varying parameter inputs, showed that the Model F tubesheet properties represented the bounding case among the population of H\* candidate plants with respect to reduction of contact pressure due to tubesheet bore eccentricity. A separate planar model was constructed, based on the Model F geometry, to evaluate the contact pressure for a range of tubesheet bore deformation (eccentricity). This analysis is documented in WCAP -17071, Section 6.2.5. This model was driven by assumed hole displacements to bound the actual displacement

calculated in the  $H^*$  analysis that result from applied pressure and thermal loads. In this manner, it was possible to construct a relationship between tubesheet bore eccentricity and tube to tubesheet contact pressure.

Figure 1 [Figure 6-64 in this report] shows the bounding fit of the T/TS contact pressure described in Section 6.2.5 from the data from Table 6-18 of WCAP 17071-P. The tube bore eccentricity in this analysis is assumed but represents the tubesheet bore eccentricity resulting from applied pressures to the diameter of the tubesheet bore, thermal growth of the tubesheet and local effects acting to further deform the tubesheet bore. The tubesheet bore eccentricity ( $e$ ), or differential tubesheet cell displacement, is the maximum distance that the major axis of the diameter of the tubesheet bore is displaced relative to the minor axis of the tubesheet bore.

Section 6.4.1 of WCAP-17071 summarizes the equations for calculating the contact pressures used to determine the value of  $H^*$ . With reference to the final equation in Section 6.4.1, the final term in the numerator,  $\Delta R_{ROT}$ , represents the effect of tubesheet bore eccentricity, as shown in Figure 1 [Figure 6-64 in this report], on the T/TS contact pressure,  $P_2$ . A maximum value of  $\Delta R_{ROT}$  results in a minimum value of  $P_2$ . Therefore, the fit in Figure 1 [Figure 6-64 in this report] is bounding because it results in the least amount of contact pressure ( $P_2$ ) at smaller tubesheet bore deformations (which corresponds to a longer value of  $H^*$ ) and zero contact pressure at the smallest tubesheet bore deformations.

The data used for the fit in Figure 1 [Figure 6-64 in this report] is valid regardless of the applied temperature or pressure because the data in the finite element analysis used to develop the new relationship is based on an assumed range of worst case tube bore eccentricity values at room temperature together with a reduction in NOP primary pressure of 45% (i.e., the analysis assumes a hot tubesheet during normal operating conditions with cold tubes at low pressures). Two data points are provided on Figure 1 [Figure 6-64 in this report] which demonstrates that increasing the temperature of the tube in the finite element analysis increases the T/TS contact pressure. The data from those two points show a significant increase in the T/TS contact pressure relative to the cold tube conditions for the same value of tube bore eccentricity. Similarly, an increase in the internal tube pressure would also act to increase the T/TS contact pressure. Because both the internal tube pressure and the tube temperature used in the analysis bound the lowest operating pressures and temperatures, the fit described in Figure 1 [Figure 6-64 in this report] is a conservative representation of the reduction of T/TS contact pressure with respect to tube bore eccentricity. The slope of the fit is significant because the bounding fit should represent the most rapid decrease in contact pressure as a function of tubesheet bore eccentricity. Thus, the linear fit shown on Figure 1 [Figure 6-64 in this report] represents the most rapid reduction in contact pressure due to tubesheet bore eccentricity as well as the lowest contact pressure as a function of tubesheet bore eccentricity.

Figure 2 [Figure 6-65 in this report] shows how the bounding fit relationship is implemented in the  $H^*$  contact pressure analysis discussed in Section 6.4.1 of WCAP 17071-P. Figure 2 [Figure 6-65 in this report] is derived by taking the fit in Figure 1 [Figure 6-64 in this report] and inverting the relationship such that the decrease in T/TS contact pressure from the maximum value at 0 inch tube bore eccentricity is predicted. Note that because the new fit relationship is linear it is valid at a wide range of temperatures and pressures. The prior data fit was a 4th order polynomial fit, which, if extrapolated significantly outside its supported data range, provided physically unrealistic results. The linear relationship is an

excellent fit to the data, with an  $R^2$  value of 0.9998, which accurately predicts the maximum reduction in contact pressure at the minimum value of tube bore eccentricity. The equation of the fit from this plot is:

$$T/TS \text{ Contact Pressure} = -2005.9e + 0.015$$

This relationship should be used whenever a transient condition is defined with the primary fluid at temperatures less than [ ]<sup>a,c,e</sup> °F, such as the Model D5 SLB condition. The original fit that is described in the WCAP-17071-P is conservative for all other operating conditions at higher temperatures because it predicts lower T/TS contact pressure than the new linear fit described in Figure 2 [Figure 6-65 in this report]. Applying the new relationship to NOP or FLB conditions in the Model F or Model D5 SG would increase the T/TS contact pressure during the NOP and FLB conditions. Thus it is conservative to apply the original contact pressure and tubesheet bore eccentricity relationship for the Model F SGs and for the current NOP and FLB evaluation of the Model D5 SGs.

A comparison of the new data fit to the old data fit shown on page 6-85 of WCAP-17071-P reveals that in the range where the tube bore eccentricities are common the new data fit predicts greater contact pressure than the original data fit. Therefore, it is not necessary to apply this relationship to the Model F H\* analysis; however, the new relationship should be applied in T/TS contact pressure analyses that involve primary fluid temperatures equal to, or less than [ ]<sup>a,c,e</sup> °F. The only region in the Model F TS that this new data fit could apply is in the cold leg, and the H\* results in the Model F cold leg are bounded by the Model F H\* results in the hot leg. A review of the Model F cold leg contact pressure data shows that with the new data fit the cold leg contact pressures would increase compared to those predicted by the original data fit. Therefore, it is not necessary to apply the new data fit for the Model F cold leg and hot leg contact pressures used in the H\* analysis.

The radius dependent tubesheet stiffness adjustment is not required at internal tube pressures less than [ ]<sup>a,c,e</sup> psi or primary fluid temperatures less than [ ]<sup>a,c,e</sup> °F because the difference between the standard thick shell equation for the tubesheet bore and the adjusted relationship is insignificant under those conditions. No changes to the H\* calculation methodology are required to accommodate the difference in eccentricity relationship.

Figure 6-74 shows the Model D5 tube-to-tubesheet contact pressure at the limiting tubesheet radius with the appropriate tubesheet bore eccentricity relationship. The original relationship is conservatively used for the NOP condition and the new relationship between tubesheet bore eccentricity and contact pressure is used for the SLB condition to accurately address the lower temperature conditions. The SLB tube to tubesheet contact pressures are determined to bound the NOP contact pressures at all elevations. Application of the resulting contact pressure distributions shows that for the limiting structural condition for H\* (NOP, Low  $T_{avg}$ ) the worst case mean H\* is [ ]<sup>a,c,e</sup> inches. This is similar to the Model F H\* results; the small difference reflects the differences in the Model D5 and Model F SG tubesheet complex (i.e., tube pitch, tube diameter, support ring).

## Conclusions

1. The applicable design transient conditions for the Model F SG and the Model D5 SG during SLB are significantly different with respect to their maximum temperatures. The Model D5 SLB design transient is specified as having a maximum temperature of approximately 300°F, whereas,

---

the limiting design transient for the Model F has a maximum temperature of approximately 420°F.

2. The existing relationship between tubesheet bore deformation and contact pressure was defined based on high temperature, high pressure conditions and is inappropriate for use at lower temperatures because it requires extrapolation far outside its supporting database. This had not been discovered previously because prior analyses were based on the use of ratios to determine the applicable tubesheet deformations from the results of 2D axisymmetric unit load cases. The original approach provided conservative values of  $H^*$  but was not constrained by a desire to show that contact pressure at DBA conditions exceed the contact pressure at NOP conditions.
3. Data developed during the evolution of the  $H^*$  calculation process using new finite element models, which is included in the reference report, WCAP-17071-P, was used to define a new relationship between contact pressure and tubesheet bore eccentricity which adequately bounds the range of eccentricities that would be expected under any temperature and pressure conditions. Therefore, this relationship is appropriate for low temperatures under either high pressure or low pressure conditions.
4. When the appropriate relationship between tubesheet tube bore eccentricity and contact pressure is used, the DBA tube-to-tubesheet contact pressures exceed the NOP contact pressure at all elevations in the tubesheet at the limiting tubesheet radius and at all other tubesheet locations for the Model D5 SGs.
5. No change to WCAP-17071-P for the Model F SG is required because the original contact pressure relationship used is appropriate for the Model F conditions and provides conservative results with respect to contact pressures at the applicable temperature conditions.



**Figure 6-64 Calculated T/TS Contact Pressure as a Function of Tube Bore Eccentricity  
Based on FEA in Section 6.2.5 of WCAP-17071-P**

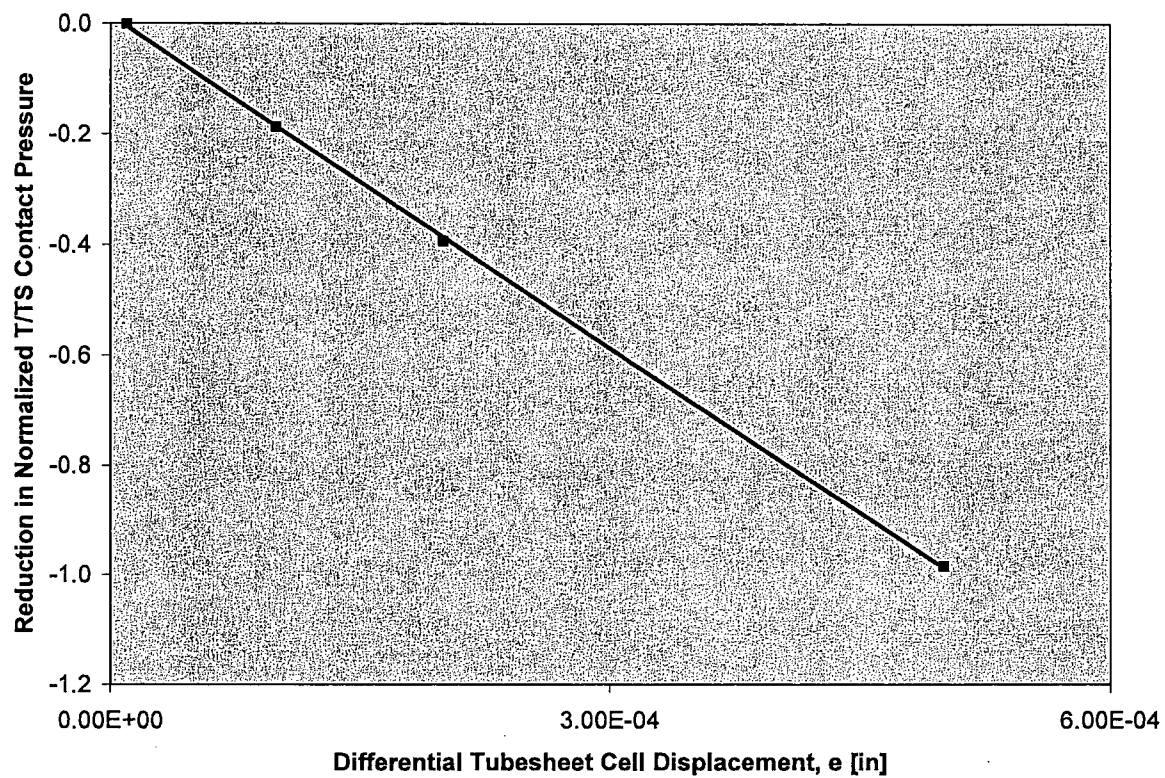


Figure 6-65 Reduction in T/TS Contact Pressure Based on Limiting Fit from Figure 1

## 6.4 CALCULATION OF TUBE-TO-TUBESHEET CONTACT PRESSURE

### 6.4.1 Calculation of Local Effects Due to Interaction of the Tube and Tubesheet Hole

Standard thick shell equations, including accountability for the end cap axial loads in the tube (Reference 6-17), in combination with the hole expansions results from Section 6.3, are used to calculate the contact pressures between the tube and the tubesheet. The thick shell equations are assembled using the model provided by Goodier (Reference 6-18). The unrestrained radial expansion of the tube OD due to thermal expansion is calculated as:

$$\left[ \dots \right]^{a,c,e}$$

and, from pressure acting on the inside and outside of the tube as,

$$\left[ \dots \right]^{a,c,e}$$

where:

- $P_i$  = Internal primary side pressure,  $P_{pri}$  psi
- $P_o$  = Crevice pressure,  $P_{cp}$  psi
- $b$  = Inside radius of tube = [ ]<sup>a,c,e</sup> inch
- $c$  = Outside radius of tube = [ ]<sup>a,c,e</sup> inch
- $\alpha_t$  = Coefficient of thermal expansion of tube, in/in/°F
- $E_t$  = Modulus of Elasticity of tube, psi
- $T_t$  = Temperature of tube, °F, and,
- $\nu$  = Poisson's Ratio of the material

The thermal expansion of the hole ID is included in the finite element results and does not have to be expressly considered in the algebra; however, the expansion of the hole ID produced by pressure is given by:

$$\left[ \dots \right]^{a,c,e}$$

where:

- $E_{TS}$  = Modulus of Elasticity of tubesheet, psi
- $d$  = Outside radius of cylinder which provides the same radial stiffness as the tubesheet

Note that the outside radius of the representative tubesheet cylinder,  $d$ , is modified using the results described in Section 6.2.4. If the unrestrained expansion of the tube OD is greater than the expansion of the tubesheet hole, then the tube and the tubesheet are in contact. The inward radial displacement of the outside surface of the tube produced by the contact pressure is given by (Note: the use of the term  $\delta$  in this section is unrelated to its potential use elsewhere in this report):

$$\left[ \dots \right] \quad a,c,e$$

The radial displacement of the inside surface of the tubesheet hole produced by the contact pressure between the tube and hole is given by:

$$\left[ \dots \right] \quad a,c,e$$

The equation for the contact pressure ( $P_2$ ) is obtained from:

$$\left[ \dots \right] \quad a,c,e$$

where  $\Delta R_{ROT}$  is the hole expansion produced by tubesheet rotations obtained from finite element results. The  $\Delta R$ 's are:

$$\left[ \dots \right] \quad a,c,e$$

The resulting equation is:

$$\left[ \dots \right] \quad a,c,e$$

where:

- $P_i$  = Internal primary side pressure,  $P_{pri}$  psi
- $P_{cp}$  = Crevice pressure, psi
- $b$  = Inside radius of tube, in

- $c$  = Outside radius of tube, in  
 $\alpha_t$  = Coefficient of thermal expansion of tube, in/in/°F  
 $E_t$  = Modulus of Elasticity of tube, psi  
 $T_t$  = Temperature of tube, °F, and,  
 $\nu$  = Poisson's Ratio of the material.  
 $P_2$  = Contact Pressure

For a given set of primary and secondary side pressures and temperatures, the above equation is solved for selected elevations in the tubesheet to obtain the contact pressures between the tube and tubesheet as a function of radius. The elevations selected ranged from the top to the bottom of the tubesheet. The contact pressure calculation results are limited to a minimum value of zero (0 psi) because it is not possible to have less than zero contact pressure between two objects. The OD of the tubesheet cylinder in the analysis is initially equal to that of the cylindrical (simulate) collars ([ ]<sup>a,c,e</sup> inches) designed to provide the same radial stiffness as the tubesheet, which was determined from a finite element analysis of a section of the tubesheet (References 6-19 and 6-20). See Section 6.2.4 for a discussion of how the tubesheet cylinder OD is modified in the contact pressure analysis as a function of tubesheet radius. The tube inside and outside radii within the tubesheet are obtained by assuming a nominal plus 2 sigma diameter for the hole in the tubesheet ([ ]<sup>a,c,e</sup> inch) and wall thinning in the tube equal to the average of that measured during hydraulic expansion tests. That thickness is [ ]<sup>a,c,e</sup> inch for the tube (Model 44F tube wall thickness after hydraulic expansion).

#### 6.4.1.1 Changes in the Contact Pressure Calculation and H\* Calculation Methodology

The contact pressure analysis methodology has not changed since 2007 (Reference 6-21). However, the inputs to the contact pressure analysis and how H\* is calculated have changed in that period of time. For example, the effective stiffness of the simulated tubesheet collar can now vary as a function of tubesheet radius in the contact pressure analysis (see Section 6.2.4). The details describing the inputs to the contact pressure analysis are discussed in Section 6.0.

The calculation for H\* includes the summation of axial pull out resistance due to local interactions between the tube bore and the tube. The calculation for H\* conservatively ignores any additional pull out resistance due to tube bending within the tubesheet or Poisson expansion effects acting on the severed tube end. In previous submittals, the force resisting pull out acting on a length of a tube between any two elevations  $h_1$  and  $h_2$  was defined in Equation (6-9):

$$\left[ \begin{array}{c} \text{---} \\ \text{---} \\ \text{---} \end{array} \right]^{a,c,e} \quad (6-9)$$

where:

- $F_{HE}$  = Resistance per length to pull out due to the installation hydraulic expansion,  
 $d$  = Expanded tube outer diameter (not related to the tubesheet collar outer diameter),

- $P$  = Contact pressure acting over the incremental length segment  $dh$ , and,
- $\mu$  = Coefficient of friction between the tube and tubesheet, conservatively assumed to be [ ]<sup>a,c,e</sup> for the pull out analysis to determine  $H^*$ .

The current  $H^*$  analysis generally uses the following equation to determine the axial pull out resistance of a tube between any two elevations  $h_1$  and  $h_2$ :

$$\left[ \dots \right]^{a,c,e} \quad (6-10)$$

where the other parameters in Equation (6-10) are the same as in Equation (6-9), and  $\mu_E$  and  $F_{HE}^{APP}$  are new parameters that account for the differences in modeling the effect of the installation hydraulic expansion. The  $\mu_E$  parameter is the effective coefficient of friction evaluated for the final length of the tube portion within the tubesheet. The effective coefficient of friction can be calculated using Soler's method (Reference 6-37) or it can be an assumed value. The  $F_{HE}^{APP}$  is the applied effective resistance per length to pull out due to the installation hydraulic expansion, based on the work of Goodier (Reference 6-18). The combination of Soler's method with Goodier's analysis provides two equations to solve for the two unknowns in the residual contact pressure analysis: the distribution of the residual contact pressure for a given tube length, and the coefficient of friction between the tube and the tubesheet (Reference 6-38). The  $H^*$  analysis has the option of calculating the residual resistance to pull out for any given tube length based on test data alone, calculations involving the test data, or some other user-defined distribution of residual effects. This means that if an  $H^*$  analysis uses any value of residual contact pressure, the distribution of residual contact pressure is also adjusted in the final calculation of the  $H^*$  value during the adjustment for the crevice pressure distribution. Refer to the  $H^*$  analysis process diagram, Figure 2-1, for an illustration of the analysis sequence. However, the reference basis for the  $H^*$  analysis is the assumption that residual installation pressure contributes zero (0) additional resistance to tube pull out. Therefore, the equation to calculate the pull out resistance in the  $H^*$  analysis is:

$$\left[ \dots \right]^{a,c,e} \quad (6-11)$$

The contact pressure is assumed to vary linearly between adjacent elevations in the top part of Table 6-25 and Table 6-26. Substitution of a linear distribution of contact pressure into Equation (6-11) gives the following result between any two elevations in the tubesheet ( $L_1$  and  $L_2$ )

$$\left[ \dots \right]^{a,c,e}$$



6-66 and Figure 6-67 for graphs of the typical tubesheet deformations in the 3D finite element model for Point Beach Unit 1. The results for Point Beach Unit 1 are bounding for all domestic 3-loop Model 44F SG plant. See Figure 6-68 through Figure 6-70 for graphs of the combined radial tubesheet displacement for Point Beach Unit 1. The results shown in Figure 6-68, Figure 6-69 and Figure 6-70 are the sum of the scaled pressure displacements (i.e., multiplied by the divider plate factor ratio of 1.60) and the thermal displacements for different tubesheet elevations. As expected, the bottom of the tubesheet is "tighter" than the top of the tubesheet and there is no bending at the neutral axis of the tubesheet. The resulting contact pressure distribution for Point Beach Unit 1, at the limiting tubesheet radius of [ ]<sup>a,c</sup> inches, is shown in Figure 6-71. The mean H\* distribution for Point Beach Unit 1, as a function of tubesheet radius is shown in Figure 6-1.

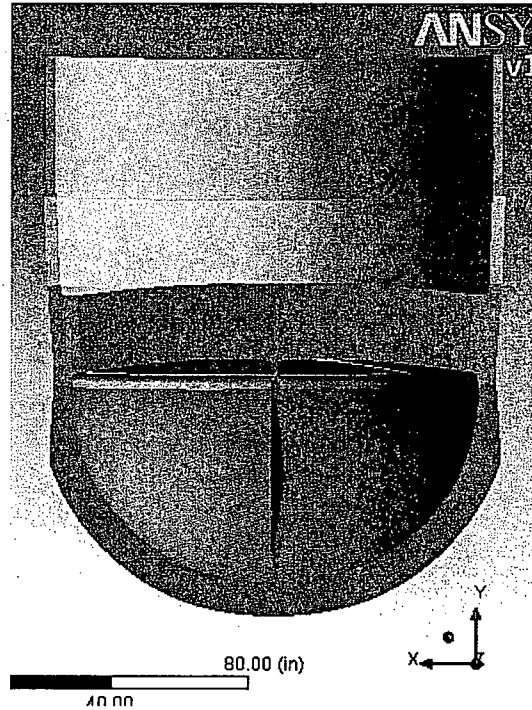


**Figure 6-66 Typical Model 44F Pressure Displacement Results for 3D Model  
(Plotted on deflected mode shape, with a displacement magnification of 100x.)**

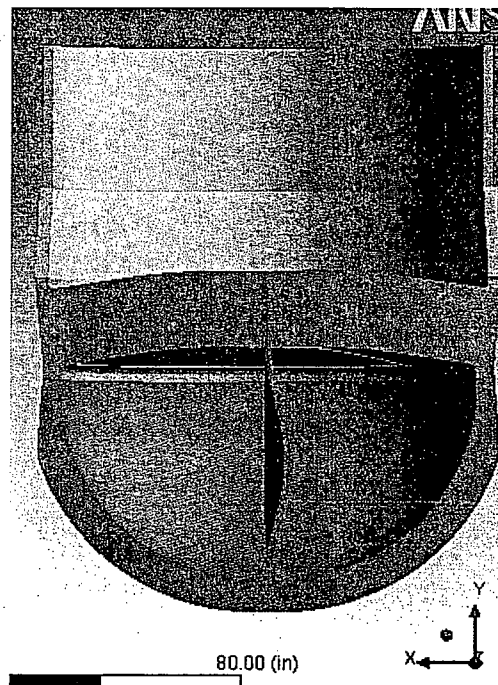


**Figure 6-67 Typical Model 44F Pressure Displacement Results for 3D Model During SLB  
(Plotted on deflected mode shape, with a displacement magnification of 100x.)**



**Figure 6-68 Combined Thermal and Pressure Tubesheet Radial Displacement for Point Beach Unit 1 at the Bottom of the Tubesheet, DPF = [ ]<sup>a,c,e</sup>**

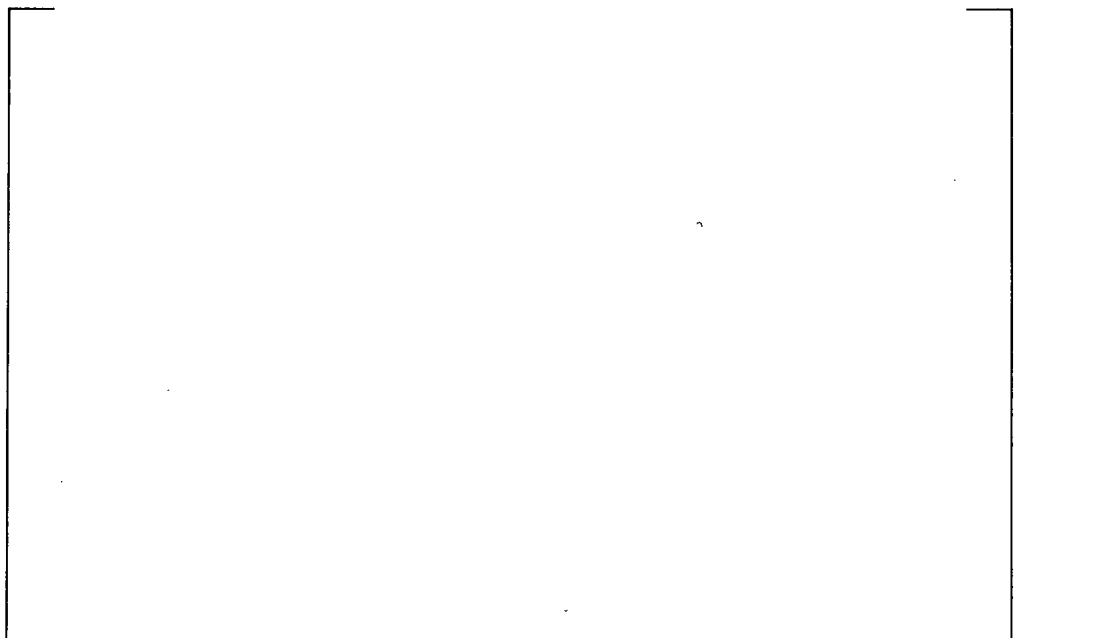


**Figure 6-69 Combined Thermal and Pressure Tubesheet Radial Displacement for Point Beach Unit 1 at the Neutral Axis of the Tubesheet, DPF = [ ]<sup>a,c,e</sup>**

a,c,e

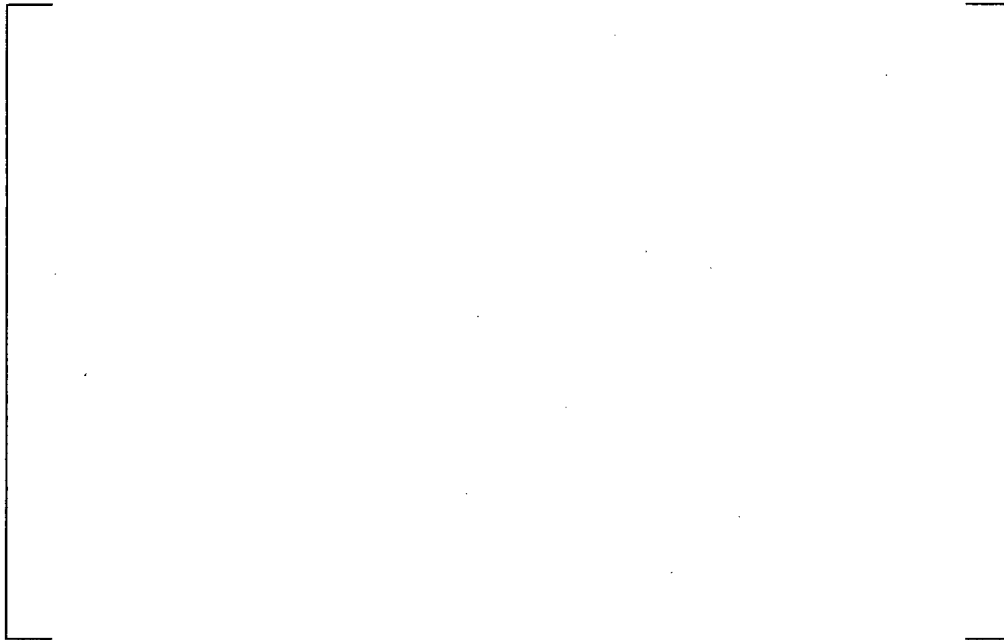


**Figure 6-70 Combined Thermal and Pressure Tubesheet Radial Displacement for Point Beach Unit 1 at the Top of the Tubesheet, DPF = [ ]<sup>a,c,e</sup>**

a,c,e



**Figure 6-71 Comparison of Tube-to-Tubesheet Contact Pressure for Point Beach Unit 1 at the Limiting Tubesheet Radius of [ ]<sup>a,c,e</sup> inches**

(Results include all crevice pressure specimen data.)

### 6.4.3 General Description of 3D FEA Post-Processing

The structural analysis of the tubesheet complex provides the input displacement to the H\* Integrator Excel® model (see Figure 2-1). In prior analyses for H\*, the nodal arrangement in the 2D axisymmetric model was matched to the axial and radial nodes in the Excel® model so that the output matrix of tubesheet deflections could be used directly in the H\* integration model. The 3D FEA model has a slightly different arrangement of nodes in the perforated tubesheet region due to the different plant-specific geometries and the higher order nodes. Therefore, it was necessary to “post-process” the deflection outputs from the 3D FEA model for use in the H\* Integrator.

The result of the finite element analysis in ANSYS WorkBench is a binary data file that contains information about all of the requested displacements in the model at every node in the model. An ANSYS APDL macro routine is used to post-process the binary data file to obtain the necessary tubesheet displacement data. The output of the APDL macro is a 4 column by 1171 row vector that contains the ANSYS node number, radial coordinate, vertical elevation coordinate and the radial tubesheet displacement for each node on the 0° face of the tubesheet. The output from the APDL macro is the input for a spreadsheet that interpolates the tubesheet displacement data. The output from the spreadsheet is the input for the H\* contact pressure analysis. This process is repeated for the thermal and pressure related displacements for each of the limiting operating conditions. The APDL macro and interpolation spreadsheet are capable of obtaining data from any azimuthal slice in the tubesheet. Only the results on the 0° tubesheet face are specified in this analysis because it has been shown to be the limiting region in the tubesheet (see Section 6.2.3).

### 6.4.4 Determination of Limiting Model 44F SG Plant in the H\* Fleet

The limiting Model 44F H\* plant was determined by a contact pressure analysis of each specific plant in the Model 44F fleet. The choice of the limiting Model 44F plant was based on three criteria:

1. The lowest calculated contact pressure at the bottom of the tubesheet.
2. The smallest rate of increase of the contact pressure from the top of the tubesheet to the mid-plane.
3. The greatest degree of sensitivity to variations in material properties due to plant operating conditions.

The comparison of the tube-to-tubesheet contact pressures was done on the zero degree (0°) face of the tubesheet at all tubesheet radii. See Figure 6-72 for a comparison of the mean tube-to-tubesheet contact pressure results at the limiting TS radius [ ]<sup>a,c,e</sup> inch) for all plants in the Model 44F fleet.

Criterion 1 is important because it describes how much potential margin is available for the contact pressure results. For example, if an analysis predicts lower contact pressures at the top of the tubesheet but greater contact pressures in the identified region of interest in a SG tube (due to potential flaws) that tube is at a lower risk of pull out.

Criterion 2 is also important because a greater rate of contact pressure increase indicates that less axial tube length is required to meet the pull out load.

Criterion 3 is the most significant because the final  $H^*$  and contact pressure analysis is a full bundle analysis that primarily depends upon a statistical variation in the ( $E$ ) Young's Modulus and Coefficient of Thermal Expansion ( $\alpha$ ) of the tube and tubesheet.



**Figure 6-72 Comparison of Contact Pressures for Model 44F Fleet Including Specimen 8 Crevice Pressure Data At Limiting TS Radius [  $^{a,c,e}$  BTS = 21.81 inches, TTS = 0.0 inches**



**Figure 6-73 Tube-to-Tubesheet Contact Pressure for the Limiting Model 44F Plant (Point Beach Unit 1) at the Limiting TS Radius Using Only the Specimen 8 Crevice Pressure Data**

The Model 44F plant that satisfies all three criteria is Point Beach Unit 1, for the post-uprating condition. All of the Model 44F plants are similar with respect to Criteria 1 and 2, although the Point Beach Unit 1 results indicate lower contact pressures at the bottom of the tubesheet and a smaller contact pressure gradient at the limiting radius. However, Point Beach Unit 1 has the highest specified operating pressure differential (see Table 5-1). This is important because the end cap load on the tube for Point Beach is significantly higher than the other Model 44F SGs. The primary fluid operating temperature is also important because the coefficient of thermal expansion for the tube and the tubesheet decreases with increasing temperature. The hotter that a plant operates, the more sensitive it is to variations in the thermal expansion coefficient. The difference in the coefficient of thermal expansion for the tube and the tubesheet between 600°F and 700°F is 4.00E-7 or less. Point Beach Unit 1 operates at a relatively high normal operating fluid temperatures (NOP Low Tavg = 592.9 °F, NOP High Tavg = 611.1 °F) and also much colder steam line break conditions (SLB = 212°F) than the other Model 44F plants. It is likely that the thermal component of the contact pressure calculation will be minimized during normal conditions because at NOP Low Tavg the thermal expansion of the tube is reduced and at NOP High Tavg the differential thermal expansion between the tube and the tubesheet is reduced while increasing the thermal expansion of the tubesheet. Therefore, the results from a Model 44F contact pressure analysis using the geometry and operating conditions from Point Beach Unit 1 are the conservative bounding results for the Model 44F fleet.

#### 6.4.5 Sample Mean H\* and Contact Pressure Calculation

The calculation of H\* relies upon the input for the finite element models discussed in Section 6.2, the operating parameters for a specific plant, and material properties. The initial value of H\*, and the contact pressure, are modified by allowances for inspection uncertainty, temperature distribution and crevice

pressure. The initial H\* results come from a comparison of the pull out resistance at a given radius to the uniformly applied pull out loads. The calculated tube engagement length required to equilibrate the loads on the tube for each operating condition in the analysis is calculated and the maximum engagement length at any given radius is used as the initial H\* value for that radius. It is typical for one operating condition to produce the lowest tube-to-tubesheet contact pressures at all radii which generates the largest (bounding) H\* values for the plant. If a value of less than one inch is predicted at any given radius the final H\* value at that radius is adjusted to a minimum value of one inch. See Table 6-21 for a summary of the initial mean H\* values using the mean material inputs and operating parameters for Point Beach Unit 1 based on the tubesheet displacements at the zero degree (0°) face of the tubesheet.

**Table 6-21 Initial Mean H\* Values**


a,c,e

The maximum H\* values occur during the NOP Low-T<sub>avg</sub> condition and those values bound the H\* results at all other tube radii. The limiting H\* result, or the worst-case tube, is at the [ ]<sup>a,c,e</sup> inch radius. The maximum H\* values occur during the NOP condition. The Model 44F H\* results do not need to be adjusted to account for the difference in the thermal distributions. See Section 6.2.2.2.5 for the effect of assuming different tubesheet displacements due to different thermal distributions. See Table 6-22 for a summary of the mean H\* values with the thermal distribution adjustment.

**Table 6-22 Mean H\* Values Adjusted for Thermal Distribution Effect**


a,c,e

The mean H\* values are further adjusted to include the offset for the uncertainty in the location of the bottom of the expansion transition (BET). The BET offset for a Model 44F SG is 0.30 inch. This offset was developed from an uncertainty analysis of the location of the BET documented in Reference 6-22 provides a summary of the adjusted mean H\* values including the BET offset. The results in are shown in Figure 6-1.

**Table 6-23 Mean H\* Values Including BET Offset**

a,c,e


The adjusted H\* values with the BET offset represent the first estimate of the final tube engagement length based on the assumption that the tube is severed at the bottom of the tubesheet. The definition of H\* is that the tube below the specified H\* depth is assumed to be nonexistent. Therefore, the initial estimate for H\* must be adjusted so that the final tube length accommodates the crevice pressure distribution referenced to the calculated H\* value. Changing the length in the analysis of the tube portion within the tubesheet redistributes the crevice pressure and changes the resulting contact pressure distribution. The result of shortening the tube length within the tubesheet (i.e., the difference between the initial assumption of the location of the severance and the initial prediction of H\*) is to increase the calculated H\* distance, typically increasing H\* between [ ]<sup>a,c,e</sup> inch and [ ]<sup>a,c,e</sup> inches depending on the initial predicted value of H\*. The adjustment required is proportional to the predicted initial H\*. The result of including the thermal distribution adjustment, the BET offset and the crevice pressure adjustment is the final H\* value. Table 6-24 summarizes the final mean H\* values. The contact pressures related to the results in Table 6-21 are given in Table 6-25 and Table 6-26.

**Table 6-24 Final Mean H\* Values**

a,c,e


The variations in H\* for a probabilistic study do not include the BET offset or the crevice pressure adjustment. The recommended input deck from a Monte Carlo analysis is used to determine the final H\* values at a probabilistic confidence level and the resulting tube length that gives the crevice pressure adjustment. A final H\* value calculated using the square root sum of the squares (SRSS) approach includes the thermal distribution effect and the BET and a conservative estimate of the crevice pressure adjustment. See Figure 1-1 for a graphical representation of the multiple passes required to generate the Final H\* value with the crevice pressure adjustment.

**6.4.6 Validation of Calculated Contact Pressures and Supporting Models**

The discussion in this section is based on the results for a Model F SG. The Model F SG geometry and design was the basis of the independent review and the alternate calculation method. The Model F results for the alternate calculation method bound all other contact pressure results in the domestic fleet. Therefore, the results discussed below are conservative when applied to a Model 44F SG.

The results of the contact pressure and lower SG complex models were verified using two different means:

- Independent peer review using alternate models
- Alternate calculation method using Finite Element Analysis

Comparing the H\* analysis results to these alternate analyses showed that the H\* contact pressure analysis, and the related analysis models, are reasonable.

A comparison of the tubesheet complex structural model with a similar structural model prepared by Argonne National Laboratory (ANL) was performed during the development of the H\* analysis, thus providing an independent assessment of the model ANL created a similar finite element model, with some geometry differences, of the lower SG complex using ABAQUS. The tubesheet model included a single tube bore with a contact law to approximate the contact pressure distribution between a tube and the tubesheet at the limiting radius.

The comparison with the ANL model included a comparison of the maximum vertical (transverse) displacement of the tubesheet during NOP and SLB conditions for essentially the same input conditions. The ANL review also included a comparison of the calculated contact pressure at the limiting tubesheet radius as a function of the elevation within the tubesheet. The maximum vertical tubesheet deflections calculated in the H\* lower SG complex model and the ANL finite element model were within [ ]<sup>a,c,e</sup>% of each other when the same material properties, pressure loads and temperatures were used. Therefore, the deflections in the H\* lower SG model are reasonable and agree with the results from a different and independent finite element analysis.

The contact pressure results of the ANL model closely agreed with the contact pressure results from the H\* analysis. The characteristic of the contact pressure distributions in the H\* analysis and the ANL analysis were within [ ]<sup>a,c,e</sup>% of each other when the same material properties and boundary conditions were used. The same trend in the contact pressure distributions (minimum tube-to-tubesheet contact pressure at the top of the tubesheet, maximum tubesheet contact pressure at the bottom) was also observed. Both the ANL model and the H\* model showed that the SLB contact pressure increased relative to the NOP contact pressure when the model boundary conditions changed from NOP to SLB. It is significant to note that the ANL model relied on a contact law with a different meshing scheme to achieve these results. Based on this comparison, it is concluded that the H\* contact pressure analysis is reasonable and validated by a completely different model and analysis approach.

Because the H\* contact pressure analysis is a complex process, a separate analysis was performed to verify the contact pressure analysis. The tubesheet deformations, tube bore deformations due to pressure and temperature, tube deformations due to pressure and temperature, strain hardening effects from installation, effects due to thermal lock-up between the tube and the tubesheet, etc., are all combined to calculate the contact pressure distribution between the tube OD and the tube bore ID. To verify the accuracy of the H\* contact pressure analysis, a separate 2D planar finite element model of a tube within a single tubesheet cell was created. The tube and tubesheet cell model boundary conditions allowed the model to simulate separately each effect that the H\* contact pressure model used in the calculation. The boundary conditions on the 2D planar tubesheet/tube cell model included:

1. Tube expansion
2. Permanent strain hardening of the tube
3. Installation pressure release
4. Tube bore dilation due to pressure and temperature loads on the tubesheet
5. Heat-up of the tube and tubesheet
6. Pressurization of the tube to an internal pressure of 1220 psi
7. Pressurization of the tube to an internal pressure of 2250 psi

Items 6 and 7 in the applied boundary conditions allow the 2D planar model to compare contact pressure results at different tubesheet elevations. The case of the reduced pressure (1220 psi) in Item 6 represents the upper 6 inches of the tube bore (close to the top of the tubesheet) when the crevice pressure acting on the tube is reduced but still affecting the total pressure differential across the tube wall. The case of the increased internal pressure (2250 psi) in Item 7 models the condition of no crevice pressure acting on the tube. The mean material properties were used for both the tube and the tubesheet in the 2D planar model and the H\* contact pressure analysis. The maximum tube bore dilation for the NOP case, as calculated using the results from Section 6.2.4, were used for the 2D planar model, were applied so that the tubesheet bore could only extend along a major axis without acting to “pinch” the tube in the orthogonal axis (i.e., zero Poisson contraction). The tube bore dilations in the H\* contact pressure analysis were calculated using the tubesheet deflections and the eccentricity relationship described in Section 6.3. The contact pressure result, at an elevation that had approximately the same tube bore dilation as the input to the 2D planar model, was used to compare the two different methods. Both the tube and the tubesheet were heated to 600°F in the 2D planar model. The H\* contact pressure analysis used the boundary conditions for a typical Model F SG in the domestic fleet. The 2D finite element analysis showed that the tube and the tubesheet always maintain contact throughout Steps 1 through 7. Further, the 2D planar analysis showed that the variation in contact pressure around the circumference of a tube and tubesheet cell with applied deformations, pressures and temperatures was minimal and remained close to the average value around the entire tube OD. The H\* contact pressure analysis predicted less contact pressure between the tube OD and the tube bore ID than the 2D FEA model predicted for every case. For example, in the case of feedwater line break,  $\Delta P$  across the tubesheet equal to 2650 psi, both the tube and the tubesheet at the temperature of 622.6°F, at a tubesheet radius of [ ]<sup>a,c,e</sup> inches, at an elevation of approximately 2 inches above the tube end weld, with a tube bore eccentricity of [ ]<sup>a,c,e</sup> inch, and zero residual contact pressure (0 psi) the 2D finite element model predicts an average tube-to-tubesheet (T/TS) contact pressure around the circumference of the tube of [ ]<sup>a,c,e</sup> psi. The H\* contact pressure analysis predicts a tube-to-tubesheet (T/TS) contact pressure of [ ]<sup>a,c,e</sup> psi for the same conditions, tube bore eccentricity, radius and elevation. Similarly for the case of NOP, with a  $\Delta P$  across the tubesheet equal to 1453 psi ( $P_{pri} = 2250$  psia,  $P_{sec} = 797$  psia), with both the tube and the tubesheet at 622.6° F, at a tubesheet radius of [ ]<sup>a,c,e</sup> inches, at a elevation approximately [ ]<sup>a,c,e</sup> inches above the tube end weld, with a tube bore eccentricity of [ ]<sup>a,c,e</sup> inch, and zero residual contact pressure (0 psi) the 2D finite element model predicts a maximum T/TS contact pressure of [ ]<sup>a,c,e</sup> psi. The H\* contact pressure analysis predicts a maximum T/TS contact pressure of [ ]<sup>a,c,e</sup> psi for the same conditions, tube bore eccentricity, radius and elevation. Therefore, the results of the H\* contact pressure analysis included in the H\* Integrator model are a reasonable estimate of calculated contact pressure available between the tube and the tubesheet during operating conditions based on conservative FEA results.

#### 6.4.7 Distribution of Tube-to-Tubesheet Contact Pressure as a Function of Tubesheet Elevation

Previous H\* submittals include data that showed a contact pressure profile that is similar to a typical bending stress profile through the thickness of the tubesheet. In that case, for a positive pressure difference between the primary and secondary faces of the tubesheet, the tubesheet will “bow” upward away from the channelhead. This deflection “pinches” the tubesheet bores at the primary surface of the tubesheet and acts to “open” the crevice at the top of the tubesheet. The change from the ALSP model to the 3D model also demonstrates this kind of behavior in the tubesheet deflection. See Figure 6-74 and Figure 6-75 for graphs of the deflection through the tubesheet at three tubesheet radii using the operating conditions in Table 6-8 for NOP and Table 6-8 for SLB.

The FEA results from the 3D models were obtained using the boundary conditions described in Section 6.2.2.2 and the procedure described in Section 6.4.3 to post-process the 3D FEA results into the required H\* analysis input format.



**Figure 6-74 TS Radial Displacement Under Combined Thermal and Pressure Loads During SLB**  
TTS = TS Elevation 21.0 inches, BTS = TS Elevation 0.0 inches

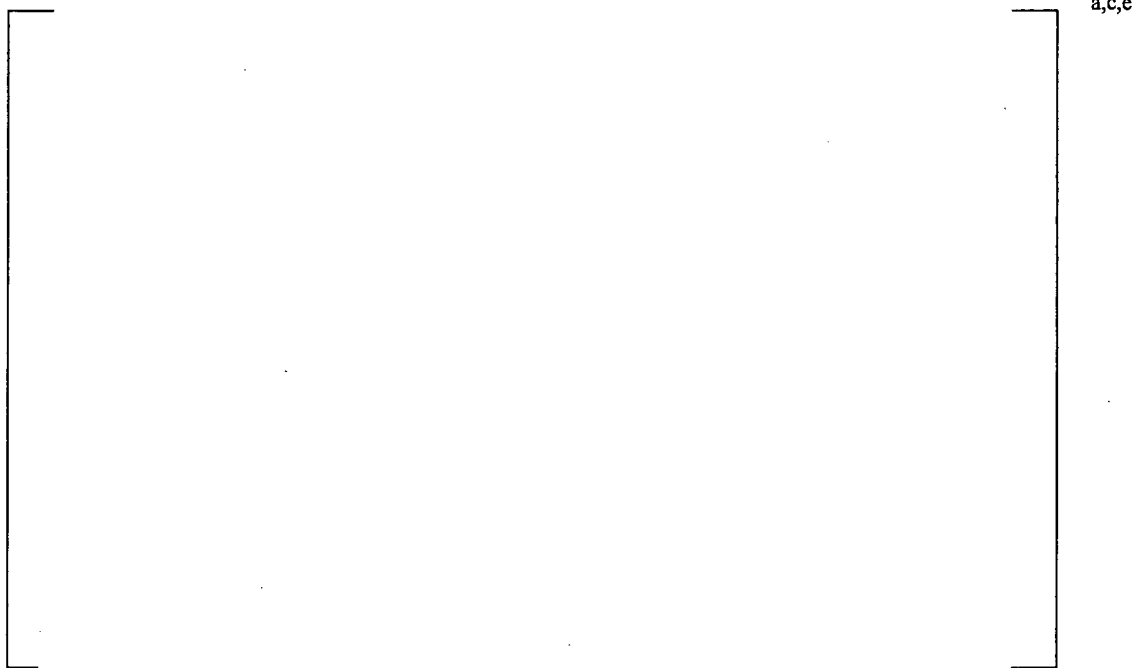


**Figure 6-75 TS Radial Displacement Under Combined Thermal and Pressure Loads for NOP  
TTS = TS Elevation 21.0 inches, BTS = TS Elevation 0.0 inches**

The tubesheet displacements in Figure 6-74 and Figure 6-75 show that the combined displacements for the NOP cases are larger than the combined displacement for the SLB case at each of the radii. The rates of increase of the combined tubesheet displacements for the SLB case are also greater than the rate of slope increase of the combined tubesheet displacements during NOP. The FEA results in Figure 6-74 and Figure 6-75 show that the tubesheet is “tighter” at the bottom of the tubesheet than at the top of the tubesheet and that the tubesheet is tighter at the SLB conditions than at NOP conditions. If actual SLB and NOP conditions are used to model the radial displacements in the tubesheet, the trend of the results in Figure 6-74 and Figure 6-75 remain but the magnitude of the displacements are different. Figure 6-76 and Figure 6-77 use the input data from Table 6-9 and Table 6-10 for NOP conditions and the input data from Table 6-11 for SLB. This data represents the bounding operating conditions from a single plant instead of the generic operating conditions from a postulated Model F plant.

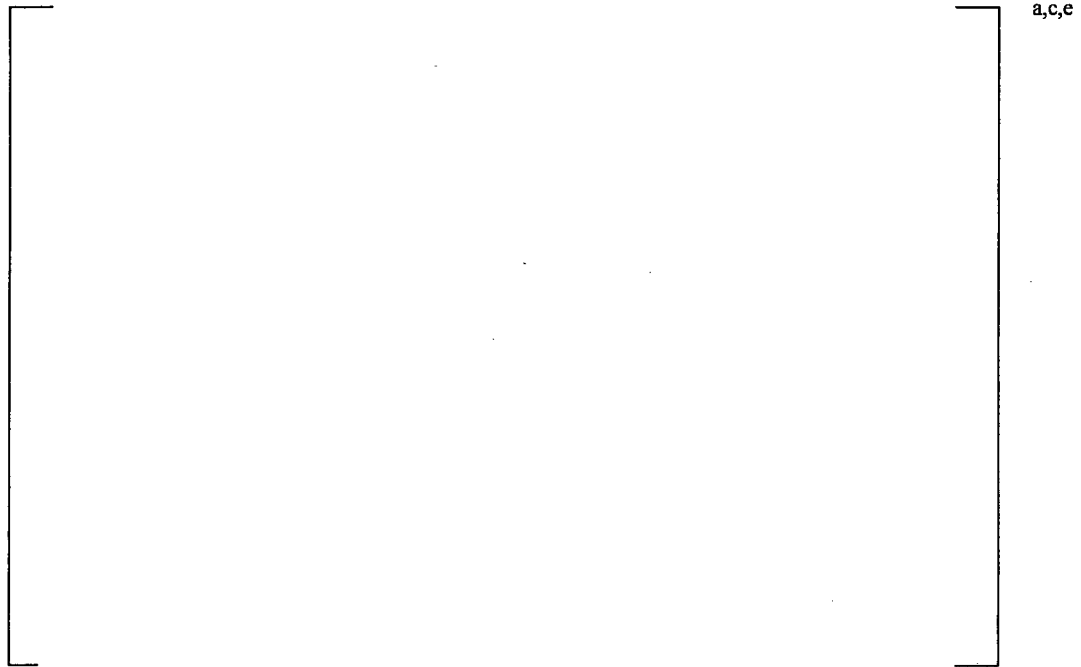


**Figure 6-76 Combined Thermal and Pressure Load Tubesheet Radial Displacements for NOP**  
**TTS = TS Elevation 21.0 inches, BTS = TS Elevation 0.0 inches**

The tubesheet displacements shown in Figure 6-76 and Figure 6-77 show that both the gradient of the tubesheet displacements as a function of tubesheet elevation and the magnitude of the radial tubesheet displacements in Figure 6-74 and Figure 6-75 are conservative relative to actual plant operating conditions.



**Figure 6-77 Combined Thermal and Pressure Load Tubesheet Radial Displacements for SLB**  
TTS = TS Elevation 21.0 inches BTS = TS Elevation 0.0 inches

The deflection profiles shown in Figure 6-74 through Figure 6-77 show that the contact pressure distribution between the tube and the tubesheet approximately follows the assumed bending stress profile (tight at the bottom of the tubesheet, looser at the top of the tubesheet). They also indicate that the contact pressure distribution for SLB conditions exceeds the contact pressure distribution for NOP conditions at some depth within the tubesheet for expected input operating conditions. See Figure 6-78 for a graph of the tube-to-tubesheet contact pressures during SLB and NOP conditions when the generic input for NOP conditions (Table 6-9 and Table 6-10) are used and the generic input conditions for SLB (Table 6-11) are used. It is concluded from Figure 6-79 that the contact pressure at SLB conditions exceeds that for NOP conditions. Although Figure 6-79 shows the axially distributed contact pressure at the limiting radial location, the same conclusions also apply for all other radial location in the tubesheet.

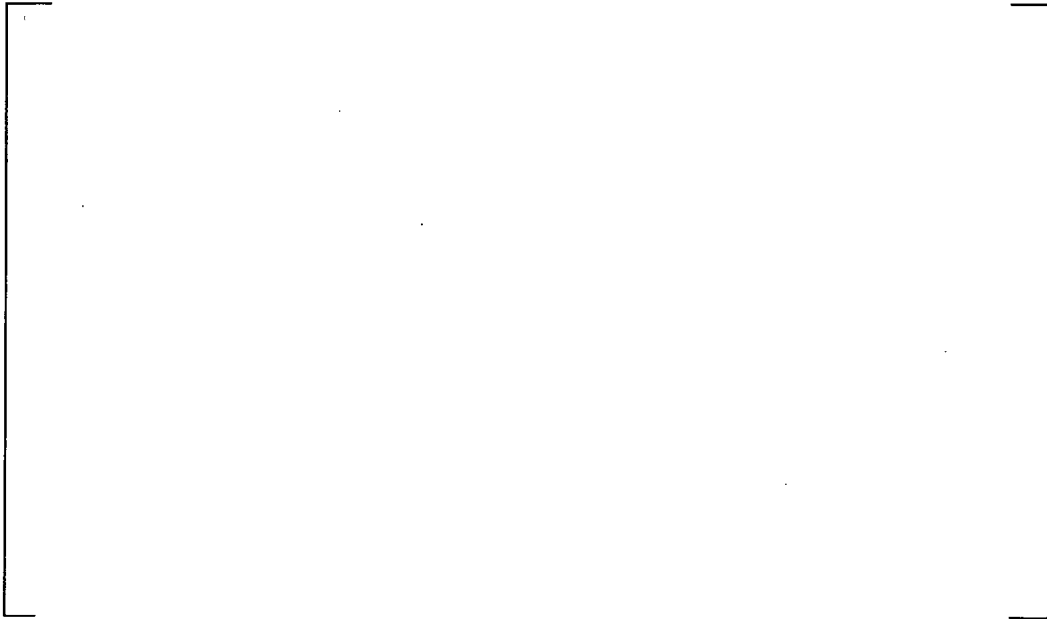


**Figure 6-78 Mean Contact Pressure Distribution Case for Point Beach Unit 1 Conditions at a TS Radius of [ ]<sup>a,c,e</sup> inches TTS = TS Elevation 0.0 inches BTS = TS Elevation 21.03 inches**

#### **6.4.8 Effect of Excluding Specimen 7 Crevice Pressure Data on Contact Pressure Results**

The crevice between the tube and the tubesheet is an important component of the H\* contact pressure analysis. Reference 6-28 documents data from a test whose purpose it was to determine the crevice pressure distribution assuming a primary-to-secondary leak in the expanded region of the tubesheet. The data from Reference 6-28 was included with a prior analysis of H\* (Reference 6-24) together with a basis for applying the test data. Subsequently, a recommendation was received from the NRC to apply the test data in a different fashion termed a “distributed,” or “depth-based” pressure distribution. The depth-based crevice pressure distribution has been adopted as the reference analysis case for H\*. See Reference 28 for a description of how the crevice pressure data is applied in the H\* analysis.

Crevice pressure and leakage tests are extremely difficult to perform, especially at elevated temperature, because the leakage is very small and difficult to measure even over an extended period of time. Some of the data, identified as Specimen 7, in Reference 6-28 appears counter-intuitive, suggesting a reversal of flow near the exit from the crevice. During a review of this data with the NRC Staff and ANL, it was concluded that the counter-intuitive data (from Specimen 7) in the crevice pressure experiment should be excluded from the final H\* contact pressure distribution analysis. In general, exclusion of the data from Specimen 7 results in less conservative results for H\*. The final analysis for H\* excludes the data from Specimen 7; however, the analysis to determine the limiting plant was based on the use of the entire data set, including Specimen 7. This was done to make sure that all of the collected test data was used in a conservative fashion when determining the limiting plant in the Model F fleet and any contact pressure related sensitivities (e.g., see Sections 6.2.4, 6.2.3, 6.2.5, 6.3, 6.4, 6.4.1 and 6.4.4). It was determined that the reduction in the mean H\* value as a function of tubesheet radius when the Specimen 7 data is excluded is small. The effect of excluding the Specimen 7 data on the associated contact pressure and

sensitivity studies can also be assumed to be small. Therefore, the conclusion from this analysis is that Model 44F H\* population is not affected by excluding the Specimen 7 crevice pressure data from the contact pressure analysis. Figure 6-79 compares the crevice pressure as a function of tubesheet elevation with the test data from Specimen 7 and Specimen 8 included and the crevice pressure distribution using only the Specimen 8 data. The resulting H\* distributions for the different crevice pressure distributions are shown in Figure 6-80.

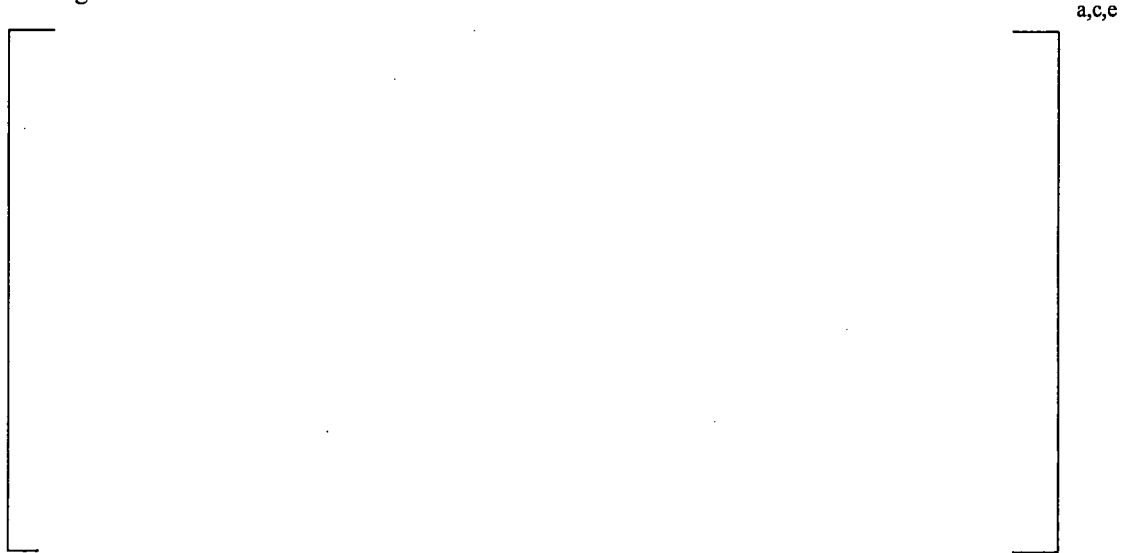


**Figure 6-79 Comparison of the Average Crevice Pressure Data as a Function of Depth Ratio for the Entire Crevice Pressure Data Set and the Data Set When Only Specimen 8 is Considered**



**Figure 6-80 Comparison of H\* for Different Crevice Pressure Data Input**

## 6.5 CONCLUSIONS

The results of the  $H^*$  contact pressure analysis demonstrate that there is sufficient contact pressure between the tube and the tubesheet due to thermal effects, pressure effects, tubesheet deflections and tube deflections to justify moving the primary pressure boundary and load path from the tube end weld to the tube-to-tubesheet expansion joint. The NOP contact pressure distribution is bounded by the SLB contact pressures throughout the tubesheet for the mean input case. The  $H^*$  contact pressure analysis results also show that the contact pressure increases from the top of the tubesheet to the bottom of the tubesheet. See Figure 6-78 for a graph of the contact pressure at the limiting tubesheet radius in the limiting Model 44F plant. See Table 6-25 and Table 6-26 for summaries of the mean contact pressure distributions in the limiting plant with Specimen 8 crevice pressure data input only. The limiting case, in the limiting sector, and throughout the tubesheet, is NOP Low- $T_{avg}$ . This case bounds all other load combinations and tubesheet displacement to produce the limiting  $H^*$  in the tube bundle. See Figure 6-1 for a graph of the mean value of  $H^*$  as a function of tubesheet radius. The significant conclusions in Section 6.0 are summarized in the list below:

1. The calculated mean value of  $H^*$ , [ ]<sup>a.c.e</sup> inches, is based on the limiting tube location at a radius of [ ]<sup>a.c.e</sup> inches in the limiting sector of the tubesheet. All other tubes will have a lower (i.e., better) value of  $H^*$ .
2. The reference structural model for the  $H^*$  analysis is a 3D FEA model that replaces the 2D ALSP model utilized in prior  $H^*$  evaluations. The 3D model shows that the results from the 2D model were conservative.
3. The 3D FEA model has been validated by comparing it to another model of the same structure, as well as a model by an independent organization, and achieving the same results.
4. The limiting tubesheet displacements in the bundle occur on the line that is perpendicular to the divider plate (referenced to the 0° face of the half symmetry tubesheet in the 3D FEA model). Tubesheet displacements at all other azimuthal positions in the bundle are less than the displacements on the zero degree (0°) face.
5. A greater value of  $H^*$  results when the divider plate is assumed to provide no support to the tubesheet. This conclusion applies for all radii on the tubesheet.
6. The effect of excluding Specimen 7 from the crevice pressure data is to slightly decrease the value of  $H^*$ .
7. Leakage channels in the crevice do not develop as a result of tubesheet bore dilation. The tube has been shown to remain in contact with the tubesheet bore for all predicted deformations of the tubesheet bore. The variation in contact pressure around the circumference of the tube is very small for the expected range of deformations.
8. The contact pressure between the tube and the tubesheet is greater during SLB conditions than at NOP conditions at all locations in the tubesheet, for all plants in the Model 44F fleet.
9. The bounding plant among the Model 44F population is Point Beach Unit 1. Point Beach Unit 1 meets all of the criteria established to define the bounding plant. In particular, Point Beach Unit 1 has the highest specified normal operating pressure differential among the candidate Model 44F plants.





## 6.6 REFERENCES

- 6-1 NEI 97-06, Rev. 2, "Steam Generator Program Guidelines," Nuclear Energy Institute, Washington, DC, May 2005 (issued for use by NEI on September 2, 2005 and confirmed by the NRC Staff as complying with TSTF-449 on October 3, 2005). Implementation is mandatory by March 2, 2006.
- 6-2 RIS 2007-20, NRC Regulatory Issue Summary 2007-20, "Implementation of Primary-to-Secondary Leakage Performance Criteria," August 23, 2007.
- 6-3 ASME Boiler and Pressure Vessel Code, Section 111, "Rules for Construction of Nuclear Power Plant Components," The American Society of Mechanical Engineers, New York, NY, 1989, No Addenda.
- 6-4 LTR-NCE-08-184, "Documentation of the Drawings and Input Data used in the creation of the FE Models of the Model 44F, D5 and F Steam Generators," October 31, 2008.
- 6-5 T. Slot, Stress Analysis of Thick Perforated Plates, 1972.
- 6-6 WTD-ED(SA)-70-037, "Influence of the Divider Lane on Tubesheet Stresses," September 1970.
- 6-7 *Divider Plate Cracking in Steam Generators: Results of Phase I: Analysis of Primary Water Stress Corrosion Cracking and Mechanical Fatigue in the Alloy 600 Stub Runner to Divider Plate Weld Material*. EPRI, Palo Alto, CA: 2007. 1014982.
- 6-8 A.P. Boresi, R.J. Schmidt, Advanced Mechanics of Materials, 6<sup>th</sup> Edition.
- 6-9 WTD-SM-75-072, "Temperature Distributions for Calculation of Secondary Skin Stress in D2-D3 Tubesheet Analysis," August 1975.
- 6-10 NCE-88-271 (Proprietary), "Assessment of Tube-to-Tubesheet Joint Manufacturing Processes for Sizewell B Steam Generators Using Alloy 690 Tubing," Westinghouse Electric, Pittsburgh, PA, November 1988.
- 6-11 Mark's Standard Handbook for Mechanical Engineers, 10<sup>th</sup> Ed., Editors: E.A. Avallone, T. Baumeister III, 2007.
- 6-12 WCAP-15932-P (Proprietary), Revision 1, "Improved Justification of Partial-Length RPC Inspection of the Tube Joints of Model F Steam Generators of Ameren-UE Callaway Plant," Westinghouse Electric Company LLC, Pittsburgh, PA, May 2003.
- 6-13 TID-26666, Vol 1, Design Data, Nuclear Systems Materials Handbook, ORNL, 1988.

- 6-14 WEST-13-402, Rev. 1, "An Evaluation of the Statistical Variability in Coefficient of Thermal Expansion Properties of SA-508 and Alloy-600," December 2008.
- 6-15 SM-94-58, Rev. 1, "Doel 4 Elevated Tubesheet Sleeve – ASME Code Evaluation and Effect of Tubesheet Rotations on Contact Pressure."
- 6-16 CN-SGDA-03-99 (Proprietary), "Evaluation of the Tube/Tubesheet Contact Pressures for Wolf Creek, Seabrook, and Vogtle Unit 1&2 Model F Steam Generators," Westinghouse Electric Company LLC, Pittsburgh, PA, September 2003.
- 6-17 SM-98-102 (Proprietary), Rev. 2, "Tube/Tubesheet Contact Pressures for Yonggwang 2," Westinghouse Electric, Pittsburgh, PA, November 1998.
- 6-18 Goodier, J., Schoessow, G., "The Holding Power and Hydraulic Tightness of Expanded Tube Joints: Analysis of Stress and Deformation," Transactions of the ASME, Vol. 65, July 1943.
- 6-19 STD-TP-1997-7951, Rev. 1, "Vogtle-1 SG 4 Tube-to-Tubesheet Joint Evaluation (Hydraulic Expansion Only to Determine Leakage and Loading Resistance)," Westinghouse Electric, Pittsburgh, PA, May 19, 1997.
- 6-20 CN-SGDA-03-99 (Proprietary), "Evaluation of the Tube/Tubesheet Contact Pressures for Wolf Creek, Seabrook, and Vogtle Unit 1&2 Model F Steam Generators," Westinghouse Electric Company LLC, Pittsburgh, PA, September 2003.
- 6-21 Wolf Creek Generating Station – Withdrawal of License Amendment Request on Steam Generator Tube Inspections (TAC No. MD0197)," United States Nuclear Regulatory Commission, Washington, D.C., February 28, 2008.
- 6-22 LTR-SGDA-03-129, "Responses to NRC RAIs on Partial-Length RPC Inspection of the Tubesheet Region of the Callaway Plant Steam Generators to AmerenUE Callaway (Class 2 Document)," June 2, 2003.
- 6-23 W. B. Middlebrooks, D. L. Harrod, and R. E. Gold, *Nuclear Engineering and Design* 143, 1993, pp. 159-169.
- 6-24 WCAP-16794-P, "Steam Generator Tube Alternate Repair Criteria for the Portion of the Tube Within the Tubesheet at the Vogtle Unit 1 & 2 Electric Generating Plants," October 2007.
- 6-25 Remaining Technical Issues Related to Technical Specification Amendment Request Regarding Steam Generator Tube Inspections Based on H\*/B\* Methodology, TAC No. MD0197, Wolf Creek Generating Station, Docket No. 50-482, January, 2008.
- 6-26 Reference Number Intentionally Not Used.

- 
- 6-27 WCAP-16145-P, "Justification for the Partial-Length Rotating Pancake Coil (RPC) Inspection of the Tube Joints of the Vogtle Units 1 & 2 Model F Steam Generators," October 2003.
- 6-28 LTR-SGDA-07-4 (Proprietary), "Letter Summary of Changes to B\* and H\* Analysis due to New Crevice Pressure and Divider Plate Data," Westinghouse Electric Company LLC, Pittsburgh, PA, January 17, 2007.
- 6-29 LTR-SGMP-09-17, "Analysis of Pressurized Tubesheet Local Stiffness."
- 6-30 CN-SGMP-08-3, "Residual Contact Pressure Between Steam Generator Tube and Tubesheet After Tube Expansion – Parametric Study."
- 6-31 Reference Number Intentionally Not Used.
- 6-32 WCAP-16228-P, "PWSCC Susceptibility Assessment of the Alloy 600 and Alloy 82/182 Components in Wolf Creek," March 2004.
- 6-33 D'Annucci, F., "Inspection of the Steam Generator Partition Plate," Proceedings of ICAPP '05, Seoul, Korea, May 15-19, 2005, Paper 5711.
- 6-34 MRP-EDF-SGPP02, "DAMPIERRE 1/2 NPP – Unit 1 – Chemical, Metallurgical and Mechanical Characterizations of the Weld Joining the Partition Stub, the Divider Plate and the Channelhead Bowl."
- 6-35 MRP-EDF-SGPP04, "CHINON B NPP – Unit 4 – Characterization of Indications Discovered on the SG #2 Stud / Partition Plate Weld Surface."
- 6-36 *Divider Plate Cracking in Steam Generators: Results of Phase II: Evaluation of the Impact of a Cracked Divider Plate on LOCA and Non-LOCA Analyses.* EPRI, Palo Alto, CA: 2008. 1016552.
- 6-37 Soler, A. et al., 1984, Mechanical Design of Heat Exchanger and Pressure Vessel Components, Arcturus Publishers, Cherry Hill, NJ.
- 6-38 Allam, M., Bazergui, A., Axial Strength of Tube to Tubesheet Joints, Journal of Pressure Vessel Technology, Volume 124, February 2002.
- 6-39 CN-SGMP-09-18, "Plant – Specific Finite Element Analyses of Model 44F Plants for H\*," April 2009.

## 7.0 RESIDUAL CONTACT PRESSURE

Residual Contact Pressure (RCP) is defined as the pressure between the tube and the tubesheet at room temperature resulting from the hydraulic expansion of the tubes into the tubesheet. Pull out tests have been performed to support prior submittals of the  $H^*$  justifications (Reference 7-1) and in conjunction with leakage tests to support return to power reports for plants that have experienced tube end damage due to failure of a split pin (Reference 7-3 and 7-4). These tests have been performed at both room temperature and at elevated temperatures. The tests utilized steel collars that simulated the stiffness and strength of unit cells of tubesheets with different dimensions of the square pitch and tube bore diameter.

Residual contact pressure derived from the measured pull out forces from tests that simulate the as-manufactured condition of the steam generators (SGs). All of the tests that have been performed to date have demonstrated that a positive value of RCP exists after the hydraulic expansions. However, the results from pull out test depend on a number of factors, including dimensional variations of the tubes and the tubesheet collars, surface finish variations, potential manufacturing artifacts in the tubesheet (collar) bore, process variables such as expansion pressures, etc. For elevated temperature pull out testing, the derivation of the RCP from the test data depends on the specific values of the coefficient of thermal expansion for the materials used for the test specimens that are generally not specifically known but fall within a small range (see Appendix B). As a result, elevated temperature pull out test data are not used for this evaluation. Nevertheless, data scatter is anticipated in the pull out tests and reduction of the test data to determine RCP due to the factors noted above. Uncertainty in the RCP value used was the source of staff concerns in prior submittal of  $H^*$  (Reference 7-1).

Another area of concern identified by the NRC staff was that only limited pull out data exists from which the residual contact pressures are estimated. The NRC staff stated in Reference 7-2 that insufficient information had been provided to establish whether the pull out test specimens used to determine residual contact pressure adequately envelop the range of values of these parameters which might be encountered for the expected range of the  $H^*$  value. Note that the prior analysis for  $H^*$  was very conservative and that larger values of  $H^*$  than provided in Section 6.0 were conservatively predicted. In prior submittals of  $H^*$ , the predicted  $H^*$  value was conservatively estimated using a 2-dimensional axisymmetric structural model, and temporary applications of  $H^*$  at 17 inches were approved (Reference 7-5). However, the pull out test specimen lengths were significantly shorter than the approved value of  $H^*$ , leading to questions if the force per unit length (F/L) calculations were reliable for the longer specified value of  $H^*$ .

To address these issues, a new pull out test program was initiated to support the development of  $H^*$  as described in this report. In addition, an analysis was performed to evaluate the uncertainties applicable to RCP (see Table 7-1). The purpose of the test program was to provide additional pull out data for longer test specimens than tested previously, which would be used to establish a conservative value of the expected mean RCP. The parallel analysis program provided the uncertainties that should be applied to the mean RCP determined from the pull out test program and prior pull out test data.

This section provides the results of the pull out test program and the results of the analytical uncertainty study the parameters that affect the RCP.

## 7.1 PULL OUT TEST PROGRAM

The objective of the pull out test program was to define a conservative mean value of residual contact pressure for use in the H\* analysis. Pull out tests provide load vs. displacement data for specimens of different lengths that represent both the range of potential values of H\* and the different tube diameters among the population of H\* candidates (11/16 inch, 3/4 inch and 7/8 inch). The RCP is calculated from the recorded pull out forces from these tests assuming the same coefficient of friction (0.2) that was assumed in Section 6.0 for the H\* structural analysis. This section, which summarizes the pull out test results and analysis for mean residual contact pressure, is currently in preparation. When completed, this section will provide the mean value of RCP that can be applied in the H\* justification, together with the uncertainty analysis provided in Section 7.2.

The reference value for RCP assumed in this report for H\* is assumed to be zero. The mean value of H\* provided in Section 6.0 and the probabilistic assessment in Section 8.0 are based on the assumption of zero residual contact pressure. Any positive value of RCP will reduce the mean value of H\* provided in section 6.0 and the probabilistic value of H\* discussed in Section 8.0.

## 7.2 ANALYSIS FOR UNCERTAINTIES IN RCP

### 7.2.1 Variables that Affect the Value of RCP

Table 7.1 summarizes the variables that impact the uncertainty of the RCP and that were considered in the calculations for RCP uncertainty.

For the component dimension variables, the mean values were determined from the applicable manufacturing drawings. The limits of the drawing tolerance were interpreted as  $[\ ]^{a,c,e}$  values and the  $[2\sigma]^{a,c,e}$  values were determined from this definition. This is conservative because component dimensions exceeding the drawing tolerances would be rejected. Since all components will meet the drawing dimensions unless documented by a manufacturing deviation notice as isolated cases, the limits of the drawing tolerances represent the total distribution of the variables.

For material properties,  $S_y$ ,  $E_T$  and  $E_{TS}$ , the limits of the material specification were conservatively interpreted as  $[\ ]^{a,c,e}$  values and the  $[ ]^{a,c,e}$  values were determined from this definition. This is conservative because materials exhibiting property values outside the specification would be rejected for use.

The Young's moduli,  $E_T$  and  $E_{TS}$ , are also parameters that directly affect the structural calculation for H\* in Section 6.0 and, consequently, the probabilistic evaluation for H\* in Section 8.0. The influence of the Young's moduli on both the structural analysis and on the RCP analysis is very small. Therefore, the Young's moduli of the tube and tubesheet materials are considered independently in the structural analysis and RCP analysis. No effort was made to coordinate the specific values of Young's modulus between the structural analysis and the analysis for RCP.

For the uncertainty analysis, the mean tube expansion pressure was conservatively assumed to be the minimum acceptable expansion pressure from the manufacturing specification for the Model F SGs. A  $[ ]^{a,c,e}$  standard deviation of the minimum acceptable expansion pressure was assumed to account for

expansion equipment instrumentation error. The manufacturing procedures prevent the as-built expansion pressure to be less than the lower tolerance of the specification. Tubes that initially did not meet the minimum expansion pressure were re-expanded at a higher pressure to assure compliance with the process specification. Therefore, the expansion pressure assumed for this study is a conservative, lower bound value when considering the absolute values of calculated residual contact pressures. Any expansion pressure greater than the assumed minimum value will result in an increase in the predicted residual contact pressure.

### 7.2.2 Structural Analysis Model

The analysis model to evaluate the contact stresses was a 2-dimensional plane strain finite element model using the ANSYS computer code (Reference 7-9). Both the tube and tubesheet are represented using the ANSYS [ ]<sup>a,c,e</sup> finite element, which is a 2-dimensional plane structural element. The model is a full 360° representation of the tube and tubesheet. The finite element mesh consists of [ ]<sup>a,c,e</sup> nodes about the circumference of both the tube and tubesheet. [ ]<sup>a,c,e</sup> elements are used radially through the tube wall and [ ]<sup>a,c,e</sup> elements are used radially through the tubesheet collar.

The contact interaction between the tube and tubesheet during hydraulic expansion is represented analytically as a [ ]<sup>a,c,e</sup>.

]<sup>a,c,e</sup>.

Figure 7-1 shows an overall view of the finite element model. This view shows the Model F model. The finite element models for Model D5 and 44F are similar; only the dimensions differ slightly. Figure 7-2 shows a close up of the tube region of the model.

#### 7.2.2.1 Dimensions, Boundary Conditions and Loads

The model simulates the unit cell representation of the tubesheet, using the same approach used in Section 6.0 to calculate contact pressure. The external dimensions of the collar that simulates the stiffness of the tubesheet unit cell is the same as that utilized in the pull out tests (Reference 7-9) for the different models of SG represented. The collar bore and tube dimensions are initially the mean values specified on Table 7-1.

Because there are no physical boundary conditions for the tube-to-tubesheet interaction, the boundary conditions in the finite element model are used to prevent singularity errors due to unimpeded rigid body motion during the analysis. As such, the boundary conditions were chosen to minimize the impact on the analysis results. On the outer circumference of the tubesheet collar, the four principal directions are set on [ ]<sup>a,c,e</sup>.

]<sup>a,c,e</sup>. This is shown in Figure 7-2. The pressure load is applied to the inside surface of the tube in [ ]<sup>a,c,e</sup>. The pressure load is [ ]<sup>a,c,e</sup>.

### 7.2.2.2 Solution Process

The hydraulic expansion process was simulated in ANSYS via a [

] <sup>a,c,e</sup>.

Residual contact pressure is the desired output for this parametric sensitivity study. Because of the symmetry of the geometry, boundary conditions and loading, the residual contact pressure is expected to be uniform around the circumference of the tube/tubesheet. However, the results show a slight variation in residual contact pressure distribution, which is a result of mathematical computations within ANSYS.

The average residual contact pressure reported was determined by averaging the minimum and maximum value calculated. Because the variation of the distribution around the circumference is small and is due to mathematical computations rather than a physical phenomenon, this averaging technique is judged to be a valid representation of the residual contact pressure.

### 7.2.3 Structural Analysis Results

The results of the contact stress parametric study are contained in Tables 7-2, 7-3, and 7-4 for the Model F, Model D5 and Model 44F, respectively. The parameter that most affects the residual contact pressure is the [

] <sup>a,c,e</sup>.

### 7.2.4 RCP Uncertainty Evaluation

The combined uncertainty of residual contact pressure, when all input variables are considered, is developed using an influence factor approach. In Tables 7-2, 7-3 and 7-4, the mean and two standard deviation values of contact stress (pressure) are provided for each input variable. Therefore, the necessary parameters are available to define a distribution of residual contact stress (residual contact pressure) for each variable. Tables 7-2, 7-3 and 7-4 show that the effect on RCP is different for positive or negative variations of individual parameters. Because it is of primary interest to determine the

minimum RCP, the individual distributions of RCP in each variable were based on only the parameter that would reduce the RCP. For example, on Table 7-2, the variation of RCP for a  $+2\sigma$  variation in tube OD is [ ]<sup>a,c,e</sup> psi, whereas the variation of RCP for a  $-2\sigma$  variation of tube OD is [ ]<sup>a,c,e</sup> psi. To establish the distribution of RCP for variation of tube OD, only the [ ]<sup>a,c,e</sup> psi variation is considered. The result of this approach is that the reduction of RCP is properly modeled, but that the potential increase in RCP may be over-estimated. Overestimating the RCP does not affect the conclusions for  $H^*$  because, while higher RCP reduces the value of  $H^*$ , only the lower tail of the  $H^*$  distribution is of interest in the probabilistic analysis of  $H^*$ .

Residual contact pressure cannot be less than zero. For this reason, the individual distributions of RCP for the eight significant variables were modeled as Weibull distributions. The Weibull distribution parameters,  $\alpha$  and  $\beta$ , were iterated until the distribution yielded the correct mean value of RCP and the correct value of standard deviation. Table 7-5 summarizes the Weibull distribution parameters along with the resulting mean and variance for each input variable. These values define the distribution of each influence function, which, if expressed as a cumulative distribution function (CDF) as shown in Figure 7-3, can be directly sampled using a Monte Carlo technique. The CDF for each variable is normalized by the predicted mean residual contact stress. The distribution of the final RCP variability is determined by the following equation:

$$[ ]^{a,c,e}$$

Where  $FRCP_i$  is the multiplier for the applicable mean RCP determined in Section 7.1, and  $v_{1i}$ ,  $v_{2i}$ ,  $v_{8i}$  are the influence factor values for the  $i^{\text{th}}$  pick.

One hundred thousand simulations for the RCP variability multiplier were performed. The resulting distribution of the variability multiplier is shown in Figure 7-4.

### 7.2.5 Application to $H^*$ Calculation

To apply the RCP distribution in Figure 7-4 to the  $H^*$  calculation, it is necessary to represent the RCP factor distribution in terms of  $H^*$ . This is readily accomplished by calculating  $H^*$  as a function of the RCP multiplier assuming that the mean value of RCP is known. As noted in Section 7.1, the mean value of RCP has not been finally determined from the test data. However, to illustrate the application to the  $H^*$  analysis, the estimate of mean RCP derived analytically in the RCP variability study is used. Based on this calculated value of mean RCP, [ ]<sup>a,c,e</sup> psi, an influence factor for  $H^*$  was calculated that can be sampled along with the influence factors for the variables that directly affect the calculation of  $H^*$  (see Section 8.0).

Figure 7-5 shows the influence of a mean value of RCP = [ ]<sup>a,c,e</sup> psi on the value of  $H^*$ . The cumulative distribution function from Figure 7-4 expressed in terms of the value of  $H^*$  is shown on Figure 7-5. If the multiplier on RCP from Figure 7-4 is zero, the value of  $H^*$  is the value calculated for zero RCP. A value of CDF equal to [ ]<sup>a,c,e</sup> (see Figure 7-4) represents the effect of the mean value of RCP on the value of  $H^*$ . As is seen from figure 7-5, the effective multiplier on  $H^*$  is approximately [ ]<sup>a,c,e</sup> for a mean value of RCP of [ ]<sup>a,c,e</sup> psi. This represents a reduction in the  $H^*$  value for zero RCP of approximately [ ]<sup>a,c,e</sup> inches. Smaller values of mean RCP will result in smaller reduction in the value of  $H^*$  and larger values of mean RCP will result in larger reduction.

It is concluded from this evaluation that the assumption of zero RCP for the reference value of  $H^*$  is extremely conservative. Depending on the value of mean RCP finally determined for the test data, the zero RCP value of  $H^*$  is estimated to include at least 1-2 inches of margin compared to a more realistic value of  $H^*$  that includes a real value of RCP.

### 7.3 REFERENCES

- 7-1 LTR-CDME-07-198, "Response to NRC Request for Additional Information Relating to LTR-CDME-07-02 P-Attachment and LTR-CDME-05-209-P of the Wolf Creek Generating Station (WCGS) Permanent B\* License Amendment Request," September 24, 2007.
- 7-2 NRC Letter, "Wolf Creek Generating Station-Withdrawal of License Amendment Request on Steam Generator Tube Inspections (TAC No. MD1097)," United States Nuclear Regulatory Commission, Washington, D.C., February 28, 2008.
- 7-3 CN-SGDA-03-99 (Proprietary), "Evaluation of the Tube/Tubesheet Contact Pressure for Wolf Creek, Seabrook, and Vogtle Unit 1&2 Model F Steam Generators," Westinghouse Electric Company, LLC, Pittsburgh, PA, September 2003.
- 7-4 DP-SGDA-03-1 (Proprietary), "Model D Tube-to-Tubesheet Joint Determination of Pull Out Resistance for H-Star (Program for Comanche Peak 2, Catawba Unit 2, Byron 2 and Braidwood 2," Westinghouse Electric Company, LLC, Pittsburgh, PA, 2003.
- 7-5 NRC Letter, "Braidwood Station, Units 1 and 2 – Issuance of Exigent Amendment Re: Steam Generator Tube Surveillance Program (TAC No. MC6757)," United States Nuclear Regulatory Commission, Washington, D.C., April 28, 2005.
- 7-6 1001191, "Steam Generator Degradation Specific Management Flaw Handbook," EPRI, Palo Alto, CA, January 2001.
- 7-7 ASME Boiler and Pressure Vessel Code, "Rules for Construction of Nuclear Power Plant Components," The American Society of Mechanical Engineers, New York, NY, 1989.
- 7-8 Begley, J.A., "Mechanical and Corrosion Properties of Ni-Cr-Fe Alloy 600 Related to Primary Side IGSCC," Final Report, EPRI Research Project S303-8, October, 1986.
- 7-9 CN-SGMP-08-3 (Proprietary), "H\* FEA Parametric Modeling," April 2009.
- 7-10 TP-CDME-08-1 (Proprietary), "Pull Out Test Program for H\*," Westinghouse Electric Company, LLC, Pittsburgh, PA, 2008.









a,c,e

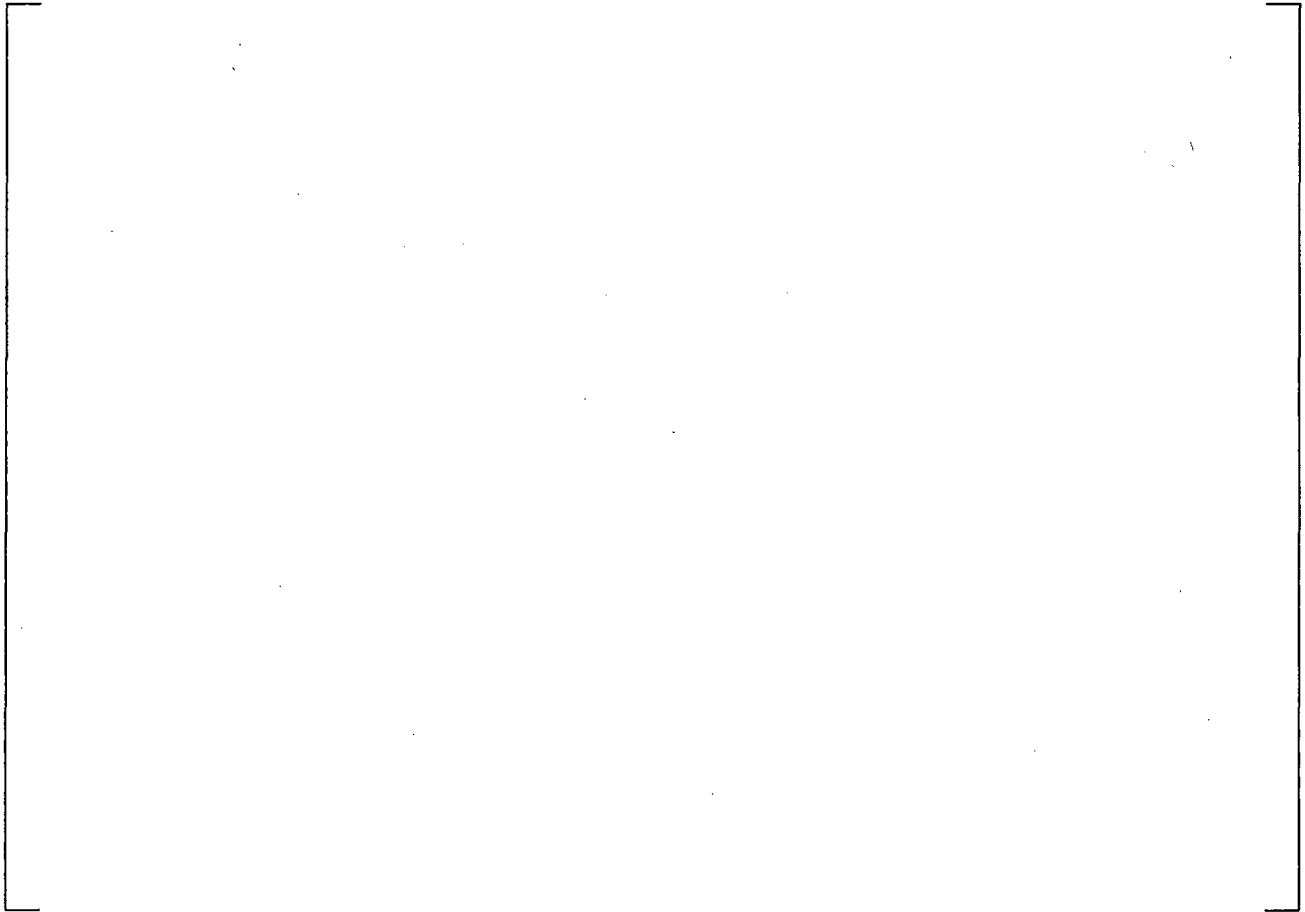


**Figure 7-1 Finite Element Model – Overall View**

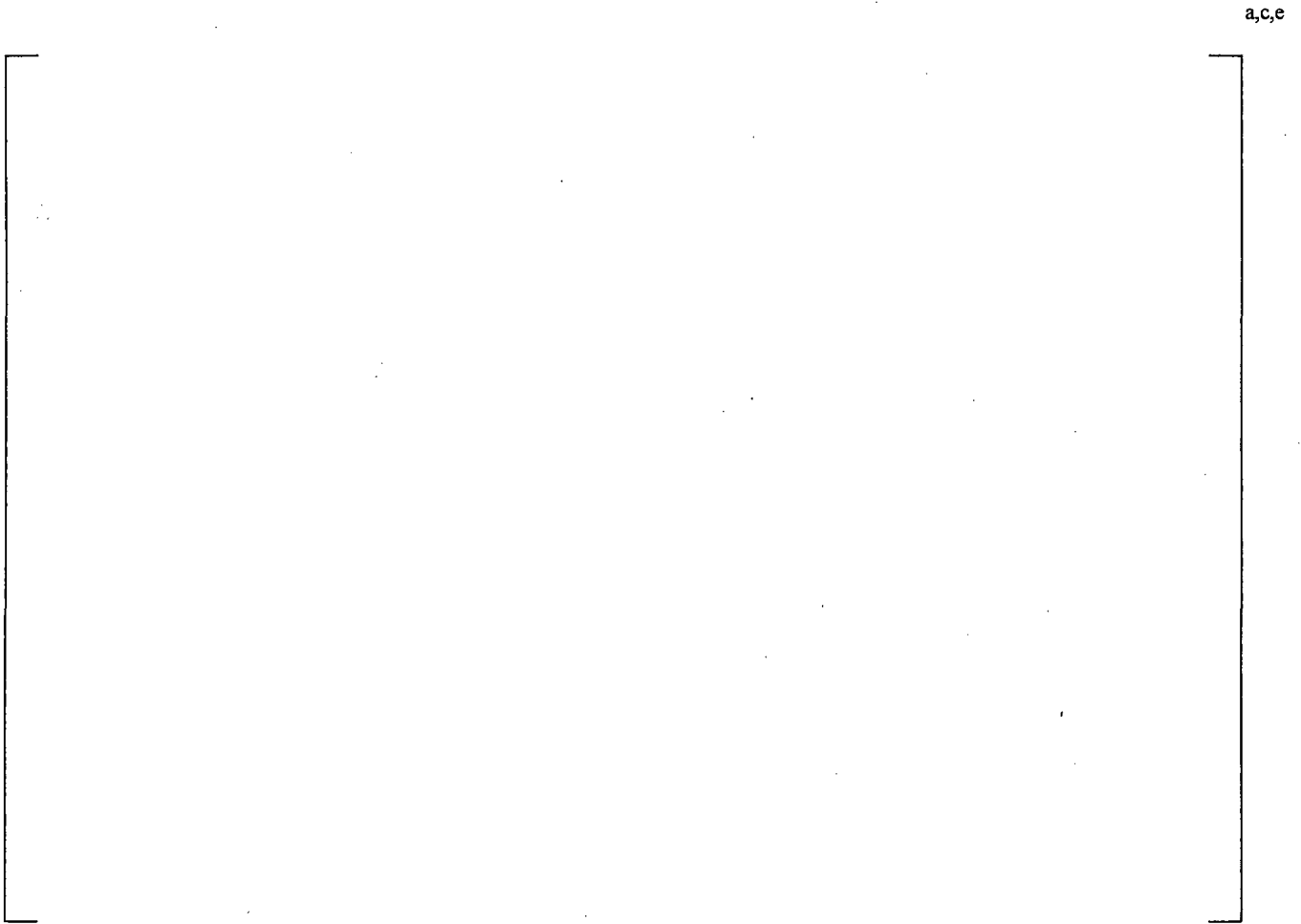


**Figure 7-2 Finite Element Model – Node Constraints**

a,c,e

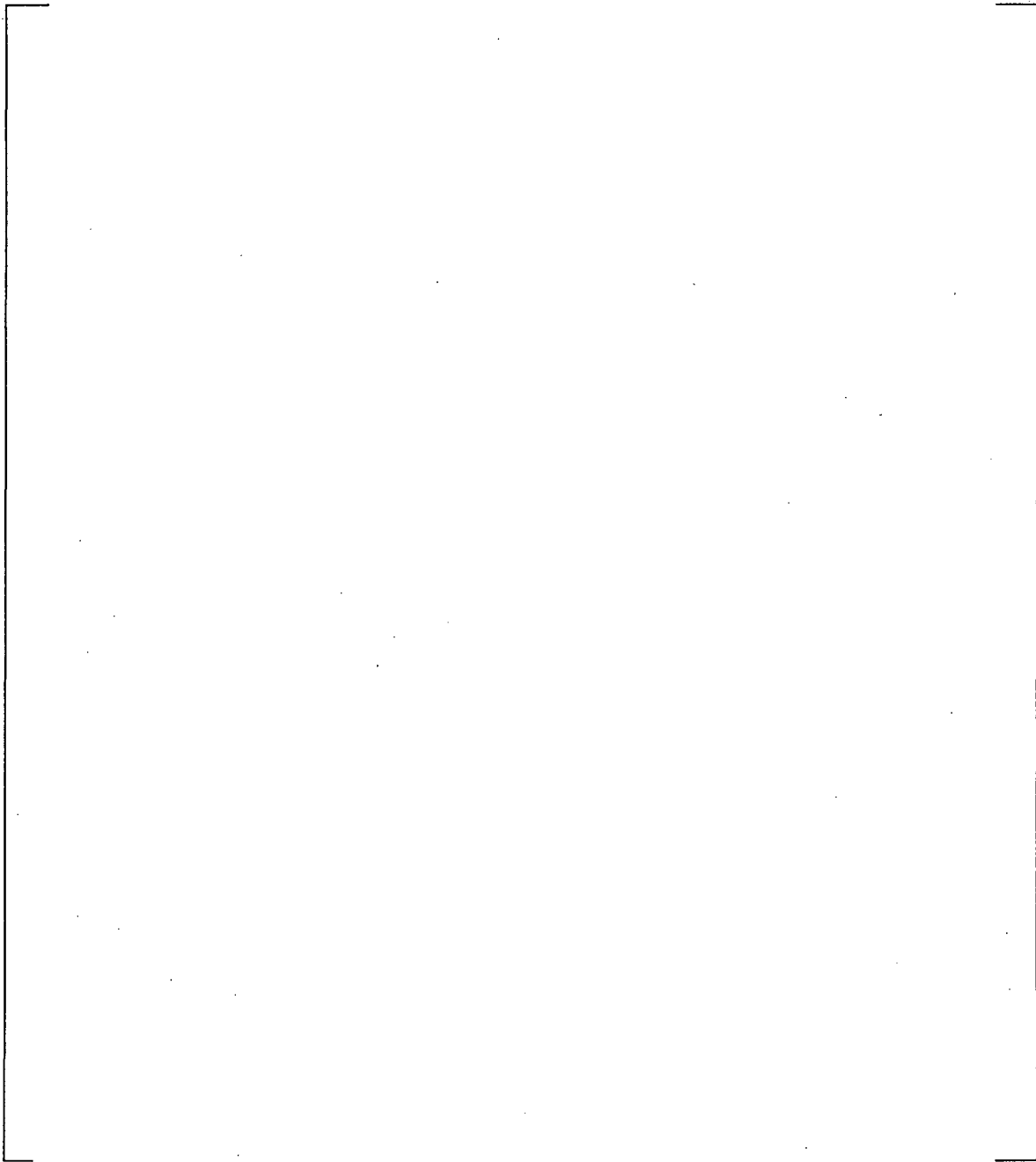


**Figure 7-3 Cumulative Distribution Functions of RCP Variables Factors**



a,c,e

**Figure 7-4 Composite Variability of Residual Contact Pressure**



a,c,e

**Figure 7-5 Illustration of Adjustment to  $H^*$  for Positive RCP**

## 8.0 DETERMINATION OF H\* AT THE REQUIRED PROBABILITY AND CONFIDENCE

The applicable probabilistic criteria for H\* were provided in Section 4.0 of this report. Each tube in the tube bundle must meet the H\* value with a probability of 95% at a confidence level of 50%. This definition is also known as a whole bundle analysis at 95/50.

Several approaches to meeting the probabilistic requirement are available. The EPRI Tube Integrity Guidelines (Reference 8-1) provide a simplified statistical approach under which the uncertainties on the mean prediction of H\* are combined as the square root of the sum of the squares (SRSS). The guidelines also provide for a fully probabilistic analysis utilizing a Monte Carlo sampling technique. While both methods are used in this report for developing the whole bundle H\* value at 95/50, the more simple and conservative method, SRSS, is the reference basis for determining the probabilistic value of H\*.

Section 6.0 of this report provides the structural basis for the limiting mean value of H\*, [ ]<sup>a,c,e</sup> inches, which includes the adjustment for the location of the bottom of the expansion transition (BET) and the adjustment for tubesheet NOP thermal distribution. Figure 6-1 provides the mean H\* value as a function of tubesheet radius within the limiting tubesheet sector for the bounding Model 44F steam generator (SG) plant. It was noted in Section 6.0 that the limiting mean value of H\* applies for the tube located at the limiting radius in the limiting sector of the tube bundle. Every other tube in the bundle would be expected to have a lower value of H\*. The H\* value for this limiting tube is utilized as the basis for the probabilistic evaluation included in this section.

### 8.1 PROCESS

#### 8.1.1 Effect of Crevice Pressure on H\*

Section 6.4.5 discusses the analysis iteration performed during the H\* calculation process to define the final H\* distance for a distributed crevice pressure ( $P_{crev}$ ) model referenced to the location of the predicted H\*. Referring to Figure 1-1, the H\* process diagram, the first prediction of H\* assumes that the postulated flaw exists at the bottom of the tubesheet. Thus, the crevice pressure distribution is initially applied assuming that it is distributed over the entire thickness of the tubesheet. The resulting prediction of H\* implies that the postulated flaw exists just below the predicted H\* distance. The final calculation of H\* assumes that the flaw is located at the initial predicted value of H\* and applies the crevice pressure distribution accordingly. This process adds a nominal length to the first H\* prediction because changing the crevice pressure axial location reference changes the contact pressure distribution above H\*.

The incremental value of H\* due to the application of the crevice pressure profile (see Figure 6-79) varies with the initial prediction of H\* but, within a small calculational uncertainty, has a single value for each H\* value. Multiple cases were evaluated in which the applicable input parameters identified in Section 8.1.2 were varied singly or in combination, an initial value of H\* was calculated and the necessary adjustment due to the re-application of the crevice pressure distribution was determined. Figure 8-1 shows the resulting adjustment for crevice pressure for the range of initially predicted values of H\* for the Model 44F SG. The characteristic of the  $P_{crev}$  adjustment curve is as expected. An initially predicted small value of H\* depends principally on contact pressure derived from thermally and pressure-

induced contact forces between the tube and the tubesheet with very little influence from the crevice pressure. Thus, the crevice pressure has little impact on the result and a small crevice pressure adjustment would be expected. As the initially predicted  $H^*$  length increases, the effect of the crevice pressure adjustment also increases because the thermal and pressure-induced contact pressures are proportionately less compared to the crevice pressure. Therefore, a larger impact of crevice pressure on the predicted value of  $H^*$  would be expected. At some value of initially predicted  $H^*$ , the slope of the crevice pressure adjustment begins to approach the initial crevice pressure distribution slope, based on the entire thickness of the tubesheet, and the relative adjustment due to the crevice pressure decreases to zero at the originally assumed distribution as the initial prediction of  $H^*$  approaches the full thickness of the tubesheet.

Because the  $P_{\text{crev}}$  adjustment is shown to be a function of the value of the first prediction of  $H^*$ , independent of parameter variations that result in the first predicted value of  $H^*$ , the adjustment for  $P_{\text{crev}}$  can be applied after the determination of the probabilistic value of  $H^*$  and is not a parameter in the probabilistic analysis. As a guideline, the data shown on Figure 8-1 were fit with a third order polynomial. The equation of the fit is shown on Figure 8-1; the fit is excellent with an  $R^2$  value of 0.98. Where data points fall above the data fit, the bounding values from the data are utilized to make the  $P_{\text{crev}}$  corrections to  $H^*$ .

### 8.1.2 Definition of Variables and Their Variability

The complete calculation for  $H^*$ , shown in the process diagram on Figure 1-1, depends on a number of input parameters whose value can vary. Not all of the variables affect every part of the calculation. Table 8-1 summarizes the input variables and their applicability to the separate models that are utilized in the  $H^*$  calculation process. Four input parameters directly affect the results of the contact pressure calculations: Young's modulus of the tubesheet and tube material ( $E_T$ ,  $E_{TS}$ ) and coefficient of thermal expansion (CTE) of the tube and tubesheet materials ( $\alpha_T$ ,  $\alpha_{TS}$ ). Variations in the tubesheet bore and the tube outer diameter and tube wall thickness do not directly affect the contact pressure calculations because the initial condition for the contact pressure calculations assume line-on-line contact between the tube and the tubesheet. However, geometric variability of the components is introduced into the calculations through the residual contact pressure (RCP) variability discussed in Section 7.0. The reference basis for the  $H^*$  calculations in this report is the assumption of zero residual contact pressure. All prior tube pull out testing has shown that there is a positive value for RCP. If a positive value of RCP is included in the  $H^*$  calculation, the value of  $H^*$  will decrease; thus, the assumption of zero residual contact pressure is conservative.

Table 8-2 summarizes the variables that affect the  $H^*$  calculations. The table includes the mean value of the variables, the predicted mean value of  $H^*$  and the resulting variability of  $H^*$  for perturbations of individual variables around their means. All of the material properties that are used as input variables in the  $H^*$  analysis are natural variables. An analysis parameter is considered to be a natural variable if the range of values that it is assumed to have is not affected by a process related to the analysis or is an intrinsic characteristic. For example, the CTE of Alloy 600 is not affected by the application of end cap loads on the tube and remains the same regardless of the volume of Alloy 600 that is present. Therefore, the CTE of Alloy 600 is considered an intrinsic material property and can be assumed to vary within a natural distribution of values. It is reasonable to assume that natural variables have normal (Gaussian) distributions because variations in material structures and properties (e.g., crystal structures, grain boundaries, etc.) are likely to be concentrated around some average value with an equal chance of being

either below the average or above it. For example, the distributions of the two most significant variables,  $\alpha_T$  and  $\alpha_{TS}$  were shown to be reasonably approximated by a normal distribution in the analysis of the coefficient of thermal expansion tests, Appendix B of this report.

The variation of  $H^*$  with respect to a known change of a single parameter over a defined range is called an influence factor. The concept of influence factors is well known in structural analysis and the application of the concept for the  $H^*$  analysis is the same. An influence factor was calculated for each of the relevant input parameters (i.e.,  $\alpha_T$ ,  $\alpha_{TS}$ ,  $E_T$ ,  $E_{TS}$ ) about a mean value determined from the ASME Code and a 1, or more, standard deviation variance based on established test data or reference literature [e.g., Appendix B, Reference 8-4]. The influence factors were calculated by repeating the entire calculation process shown in Figure 1-1, except the RCP calculations, by varying only one input variable at a time while holding all other inputs at their mean value. These calculations were repeated at different input parameter variances to account for possible non-normality of the resulting  $H^*$  influence factor distributions for each variable. It is seen from Table 8-2 that among the four variables affecting the value of  $H^*$ , the variation due to Young's Modulus,  $E$ , for both the tubesheet and tubing materials is very small compared to the variability of the coefficient of thermal expansion for both materials. Nevertheless, the variability in  $H^*$  due to all four properties was included in the probabilistic assessment.

### 8.1.3 Interaction Among the Applicable Variables

Application of the SRSS method of combining uncertainties assumes that each input parameter and the effect on  $H^*$  of varying that parameter, is independent of the other input parameters. The Monte Carlo influence factor approach also assumes that variables are independent. A variable is considered to be independent with respect to another variable if a change in that variable does not affect the variability of the other. With respect to  $H^*$ , a variable is independent if the characteristic of the change in  $H^*$  due to a variation of that parameter is not affected by a simultaneous change in another parameter. The characteristic variation of  $H^*$  in the four individual random variables affecting its value is shown in Figure 8-2. Each variable was changed from its mean value by a number of standard deviations while all other variables were held at their mean and the value of  $H^*$  was determined. Figure 8-3 shows the percent change in the "raw" mean  $H^*$  prediction plotted on the same scale to provide perspective on the significance of each variable. The raw mean  $H^*$  prediction is the predicted value of  $H^*$  before any adjustments are made for location of the BET, normal operating NOP thermal distribution (see Section 6.4.5) and crevice pressure adjustment.

Figure 8-3 shows that the most significant variables for  $H^*$  are the CTE of the tubesheet ( $\alpha_{TS}$ ) and of the tube materials ( $\alpha_T$ ). The tube CTE clearly dominates, resulting in approximately a [ ]<sup>a,c,e</sup>% increase in  $H^*$  from the mean if its value is approximately at its mean minus  $3\sigma$ . While the tubesheet material CTE is also significant, a mean plus  $3\sigma$  value for it results in approximately a [ ]<sup>a,c,e</sup>% increase in the value of  $H^*$  over its mean value. The remaining variables, the Young's Moduli of the tubesheet and tubing material are very weak variables, resulting in less than 3% increase in the  $H^*$  value at their means minus  $3\sigma$  values. [ ]<sup>a,c,e</sup>.

If the input variables are independent, their combined effect on  $H^*$  is expected to be a cumulative effect rather than a multiplicative effect. Figure 8-4 illustrates the expected effect of simultaneous variation of the CTE of the tube and the CTE of the TS, assuming true independence. From Figure 8-3, a -

$1\sigma$  variation of the CTE of the tubesheet results in a [ ]<sup>a,c,e</sup>% decrease in the value of  $H^*$ . Similarly, a  $+2\sigma$  variation of the CTE of the tubesheet results in approximately a [ ]<sup>a,c,e</sup>% increase in the value of  $H^*$ . Based on this logic, assuming the CTE of the tube and tubesheet to be independent, a family of curves was constructed to show the expected change in  $H^*$  when both the CTE of the tubes and the tubesheet are varied simultaneously, Figure 8-4. The difference between the individual curves is the constant offset from the mean  $H^*$  value for each different variation of both the tube and tubesheet CTE.

To determine if each of the variables affecting  $H^*$  are independent, a large number of influence factor calculations was performed in which two or more input parameters were varied over a wide range of their uncertainties. The result of these calculations is reflected in the variation of  $H^*$ . A matrix of interactions was considered for the four applicable variables for the determination of  $H^*$  as shown on Table 8-3.

Figure 8-5 shows the results of the interaction study for the coefficient of thermal expansion of the tubesheet and the coefficient of thermal expansion of the tube. The figure shows the percent variation from the calculated mean value of  $H^*$  when the coefficient of thermal expansion for the tube varies from  $+5\sigma$  to  $-5\sigma$  and when the coefficient of thermal expansion for the tubesheet is also varied from  $-1\sigma$  to  $+5\sigma$ . The shape of the curves is similar, suggesting that there are no discontinuities at which a value of  $H^*$  cannot be defined; however, the curves are rotated about the mean value of the tube CTE resulting in a convergence of the net effect on  $H^*$  when the CTE of the tubesheet is positively varied, and a divergence when the CTE of the tubesheet is negatively varied. If the variables were independent, a point-by-point difference of approximately [ ]<sup>a,c,e</sup>% change in  $H^*$  would be expected (see Figure 8-3) when the tubesheet CTE is at a value of mean  $+2\sigma$ . Over a  $3\sigma$  variation of the tube CTE, the point-by-point change in  $H^*$  is shown to vary (see Figure 8-5) from [ ]<sup>a,c,e</sup>% at mean tube CTE to [ ]<sup>a,c,e</sup>% at the mean minus  $3\sigma$  value of tube CTE. Therefore it is concluded that the tube CTE and tubesheet CTE have an interaction effect over a wide range of tube CTE variation.

Figures 8-2 and 8-3 show that the influence of Young's Modulus for both the tube ( $E_T$ ) and tubesheet ( $E_{TS}$ ) materials is essentially negligible. For a  $4\sigma$  variation of  $E_{TS}$ , the effect on  $H^*$  is less than [ ]<sup>a,c,e</sup>%. Similarly, for a  $4\sigma$  variation of  $E_T$ , the effect on  $H^*$  is less than [ ]<sup>a,c,e</sup>%. The effect of  $E_{TS}$  is greater than that of  $E_T$  because the structural response of the tubesheet and the tube-to-tubesheet contact pressure both involve this variable, whereas  $E_T$  is reflected in only the contact pressure calculation.

Figures 8-6 through 8-10 show the degree of interaction among the applicable variables:

- Figure 8-6: Interaction between  $\alpha_{TS}$  and  $E_{TS}$ . The slope of the curve for variation of  $E_{TS}$  alone (Figure 8-2c) is unchanged by a simultaneous  $1\sigma$  positive variation of  $\alpha_{TS}$ . The absolute difference between the two curves reflects only the effect of  $\alpha_{TS}$  on  $H^*$ . A negative variation of  $\alpha_{TS}$  would decrease the value of  $H^*$  and is of no consequence here.
- Figure 8-7: Interaction between  $\alpha_{TS}$  and  $E_T$ . The figure shows that there is no interaction between these variables. The curves are parallel and reflect only the impact of varying  $\alpha_{TS}$  on the value of  $H^*$ .
- Figure 8-8: Interaction between  $\alpha_T$  and  $E_T$ . The figure shows that there is no interaction between these variables. The curves are parallel and reflect only the impact of varying  $\alpha_T$  on the value of  $H^*$ .

- Figure 8-9: Interaction between  $\alpha_T$  and  $E_{TS}$ . The figure shows that there is no interaction between these variables.
- Figure 8-10: Interaction between  $E_T$  and  $E_{TS}$ . The figure shows that there is no interaction between these variables. The figure also shows that the Young's Moduli are extremely weak variables in regard to their effect on  $H^*$ .

It is concluded that  $\alpha_T$  and  $\alpha_{TS}$  are interdependent, however, the probability of achieving a combination of variables that would result in  $H^*$  being undefined is extremely low. Each of the other variables is independent and is not significantly affected by variation of any other variable as reflected by the predicted value of  $H^*$ .

The interdependence of  $\alpha_T$  and  $\alpha_{TS}$  requires special consideration to assure that a value of  $H^*$  exists, and is not excessively large, when an extremely unlikely combination of values of  $\alpha_T$  and  $\alpha_{TS}$  is considered. To address this issue, all of the input variables were set at their [ ]<sup>a,c,e</sup> value in the direction of increasing  $H^*$ , and a new  $H^*$  was calculated. The mean value of  $H^*$  for this very unlikely case increased by approximately [ ]<sup>a,c,e</sup> inches (excluding crevice pressure adjustment), indicating that  $H^*$  is tolerant to unlikely variations to the input parameters.

#### 8.1.4 Influence Factor Distributions

As noted in Figure 1-1 of this report, the calculation process for  $H^*$  is complex, involving 4 different models (only 3 if RCP is assumed to be zero). For this reason, it is not practicable to perform a classical Monte Carlo simulation in which multiple simulations are performed by randomly choosing values from the distributions of the input variables, performing a calculation for the dependent variable (in this case,  $H^*$ ) and rank ordering the solutions to determine the value at the desired probability and confidence level. To implement a classical Monte Carlo approach for  $H^*$  would require completing the entire structural calculation for the number of simulations desired (10K – 1M), including the 3D FEA analysis for tubesheet deflections and the  $H^*$  integration process, which is an extremely time and cost-intensive effort. However, the process can be made more practicable by developing distributions of  $H^*$  in each variable and then sampling these distributions using a Monte Carlo technique to determine the combined probability of  $H^*$  in all variables. This is termed the “Influence Factor Approach”.

To implement the influence factor approach, a best estimate (mean) value of  $H^*$  is calculated, assuming that all input variables are at their mean values (see Section 6.4.5). Subsequently, one variable at a time is perturbed by  $\pm 1\sigma$  (standard deviation) or greater and the corresponding values of  $H^*$  are determined. In this manner, individual distributions of  $H^*$  as a function of each variable are developed. It is assumed that the influence factor distributions are reasonably normally distributed; therefore, each  $H^*$  influence distribution is defined by the known mean value of  $H^*$  and the calculated variance of  $H^*$  from the perturbation of the input parameter. Thus, if an input parameter is varied by one standard deviation, the resulting  $H^*$  influence factor value would also be considered a  $1\sigma$  deviation. In this manner, because there are four parameters that affect the  $H^*$  calculation, four influence factor distributions are developed from which to sample to determine the final combined distribution of  $H^*$ .

The assumption that the individual influence distributions are essentially normally distributed appeared to be reasonable because the variables that affect the  $H^*$  calculation are all “natural” variables, which tend

to be normally distributed (see Table 8-1). Examination of Table 8-2 shows that the  $H^*$  influence factors are not truly normally distributed, particularly for the variable that has the most significant influence on  $H^*$  because the variations at multiple standard deviations are greater than the  $1\sigma$  variation multiplied by the number of standard deviations considered. For example, the variation of  $H^*$  for a  $5\sigma$  variations of  $\alpha_{TS}$  and  $\alpha_T$  are greater than five times the  $H^*$  variation for a  $1\sigma$  variation of  $\alpha_{TS}$  and  $\alpha_T$ . To address this, the distributions from which to sample were conservatively biased by basing them on only the influence function distribution that increased the value of  $H^*$  (see Figure 8-11). For example, for the variation of  $H^*$  for tubesheet coefficient of thermal expansion in Table 8-2, the  $H^*$  influence function was constructed using the positive variation result for  $H^*$ , 0.4 inch, to most accurately represent the influence function. Similarly, the influence distribution for the tube coefficient of thermal expansion was based on the negative variation result for  $H^*$ . This process biases the determination of the final  $H^*$  distribution to the conservative side (increased  $H^*$  length). This conservatively predicts the upper tail of the  $H^*$  distribution but slightly overpredicts the lower tail. This is acceptable because the lower tail of the distribution is not of interest. Influence factors were calculated in this manner for [ ]<sup>a,c,e</sup> parameter variations as shown in Table 8-2.



**Table 8-2 H\* Variables and Influence Factors**

a,c,e


**Table 8-3 Matrix of Variable Interaction Study for H\***

a,c,e


a,c,e



**Figure 8-1 Model 44F: Adjustment to  $H^*$  for Distributed Crevice Pressure Referenced to Initial Prediction of  $H^*$**



**Figure 8-2 H\* Variation of H\* with Individual Input Variables**

a,c,e



**Figure 8-3 Variability of H\*with All Relevant Parameters**



a,c,e

**Figure 8-4 Expected Variation of  $H^*$  When Both  $\alpha_T$  and  $\alpha_{TS}$  are Varied and are Independent**

a,c,e



Figure 8-5 Interaction Between  $\alpha_{TS}$  and  $\alpha_T$ .



**Figure 8-6 Interaction Between  $\alpha_{TS}$  and  $E_{TS}$**



**Figure 8-7 Interaction Between  $\alpha_{TS}$  and  $E_T$**



**Figure 8-8 Interaction Between  $\alpha_T$  and  $E_T$**

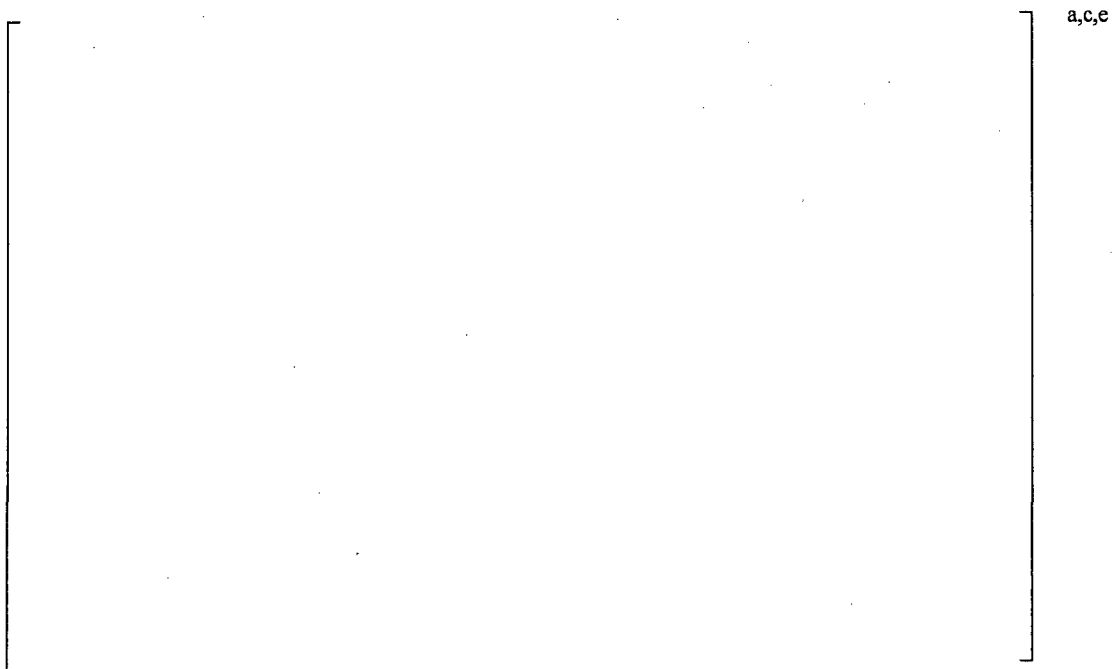


**Figure 8-9 Interaction Between  $E_{TS}$  and  $\alpha_T$**



**Figure 8-10 Interaction Between  $E_{TS}$  and  $E_T$**

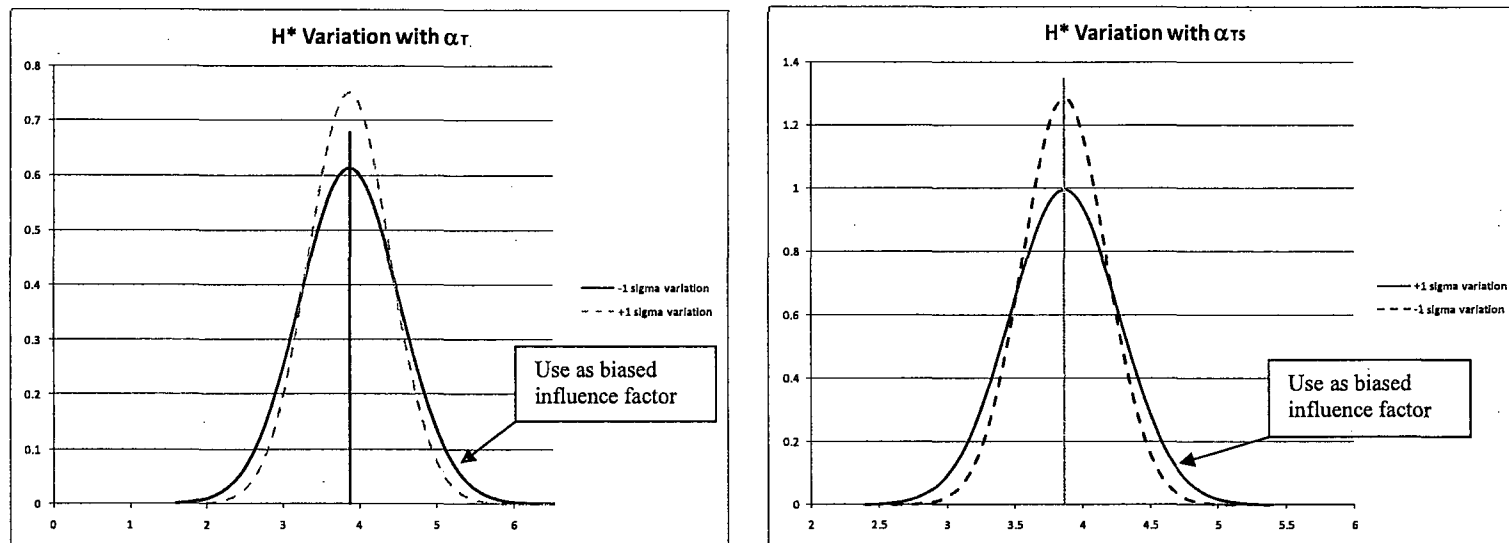


Figure 8-11 Illustration of Biased Influence Factors

## 8.2 CALCULATION OF PROBABILISTIC H\*

### 8.2.1 Square Root of the Sum of the Squares (SRSS) Approach

The Square Root of the Sum of the Squares (SRSS) approach is the reference approach for calculating the whole bundle value of H\* at 95% probability and 50% confidence.

The simplified statistical approach provided in Reference 8-1 permits combining the variability of multiple parameters by the square root of the sum of the squares (SRSS). This approach assumes that the variability of each parameter is reasonably approximated by a normal distribution. For the H\* calculation, this approach requires calculating the variation of the H\* influence factors for each input variable. An influence factor is defined as the variation in H\* from its mean value when each separate variable is perturbed while holding all other variables at their mean values. In other words, it is necessary to develop influence factors for each variable on H\* for the  $\pm n\sigma$  values of the variables where  $\sigma$  is the standard deviation and  $n$  is a multiplier chosen to represent the desired probability of occurrence of the variation. The choice of the value of  $n$  provides a basis for examining the assumption of normality of the distribution and investigating highly improbable occurrences of specific parameter variation, such as the assumption of specific tubesheet properties in recognition that the population of tubesheets is relatively small compared to the population of tubes. The results of varying one input at a time to determine the effect of such a variation on H\* are included in Table 8-2 and Figure 8-2.

As shown on Table 8-2, the H\* influence factors are reasonably represented by a normal distribution, except for  $\alpha_T$  which exhibits significant non-linearity with increased variation from the mean. For example, the H\* value for a  $5\sigma$  variation divided by 5 is [ ]<sup>a,c</sup> times greater than the  $1\sigma$  variation in the direction of increasing H\*. For this analysis, the H\* influence factor distributions were based on only the parameter variations that increased the value of H\*. These are called “biased influence factors” as discussed in Section 8.1.3 and illustrated on Figure 8-11. For example, on Table 8-2, a negative  $1\sigma$  variation of the coefficient of thermal expansion of the tube ( $\alpha_T$ ) results in a positive variation of H\* of 0.65 inch, whereas a positive  $1\sigma$  variation of  $\alpha_T$  results in a reduction of the value of H\* of -0.53 inch. To address the apparent non-normal distributions of the significant H\* influence factor, influence factors were calculated for a range of parameter variation up to  $5\sigma$  as shown on Table 8-2. No discontinuities of H\* in any of the input parameters were identified. For the H\* evaluation, only the variation in the direction of increasing H\* was considered for the influence factors for both the  $1\sigma$  and  $4.157\sigma$  parameter variation. The use of the  $4.157\sigma$  influence factors reasonably addresses the concern regarding the non-normality of the H\* influence factor distributions by examining the upper tail of the distribution. Calculations for determining the required single tube reliability were performed using standard functions in Excel® (Reference 8-3). Since the requirement for H\* is to achieve a whole bundle reliability of 95%, it is first necessary to calculate the required single tube reliability based on a bundle population of tubes equal to 3214. For this, the Excel® function BINOMDIST( $s, T, Pb, L$ ) is used, where

$s$  is the number of allowed failures = 0

$T$  is the number of trials = 3214

$Pb$  is the complement of the required single tube reliability that results in the desired whole bundle probability of 95% = approx.  $1.5960 \times 10^{-5}$

$L$  is a logical argument that directs the function to return the value of the cumulative distribution function, which is the probability that there are no more than  $s$  failures.

For the required whole bundle reliability (probability of success) of 95%, the function returns a value for the required single tube probability of failure (known as the individual term binomial distribution probability). For the required whole bundle reliability of 95%, the permitted single tube probability of failure ( $P_f$ ) is 1.5960E-5 for a bundle of 3214 tubes assuming no tubes are plugged.

The required single tube reliability ( $P_s$ ) is the complement of the permitted single tube probability of failure:

$$P_s = 1 - P_f = 1 - (1.5960 \times 10^{-5}) = 0.9999840$$

The Excel® function NORMSINV® returns the number of standard deviations required to achieve a desired reliability,  $R$ , of a single tube. When considering a single tube, the necessary multiplier on the combined variance is 1.645 to achieve a 95% probability at 50% confidence (Reference 8-2). For the single tube reliability required to achieve a whole bundle reliability of 95% probability at 50% confidence, the function returns a value of 4.157 as the multiplier on the standard deviation.

Figure 8-12 shows the variation of the required single tube reliability, expressed in numbers of standard deviations from the mean as a function of number of tubes in the bundle to meet the 95% whole bundle reliability criterion. Hypothetically, if the bundle consisted of only a single tube, the multiplier required to meet 95% reliability is 1.645. For a full complement of 3214 tubes, the multiplier is 4.157.

Two different evaluations were made to develop the 95/50 value for the full bundle using the SRSS approach and to develop the sensitivity of  $H^*$  to the input variables.

1. The SRSS combined result based on the  $1\sigma$  variation of  $H^*$  in all four input variables was multiplied by 4.157 to determine the full bundle 95/50  $H^*$  value.
2. The SRSS combined result based on the  $4.157\sigma$  variation of  $H^*$  in all four input variables was calculated directly. This approach takes into account that the  $H^*$  influence factors, in particular,  $\alpha_T$ , are not true normal distributions as noted above.

Table 8-4 summarizes the  $H^*$  probabilistic predictions including the adjustment for applying the crevice pressure to the depth of the initially predicted  $H^*$  value. Cases S-1, S-2, S-3 and S-4 are the results for the different evaluations.

**Case S-0:** For this evaluation, the influence factors for  $H^*$  were determined for  $1\sigma$  variation of each variable affecting the  $H^*$  calculation as summarized in Table 8-2. Because it was noted that the variations of  $H^*$  were not true normal distributions in each variable, the deviation of each variable was chosen in the direction that maximized the value of  $H^*$ , i.e., using the biased influence factors. For example, considering the two most influential variables, the coefficients of thermal expansion ( $\alpha$ ) of the tubesheet and tubing material, the positive variation of the tubesheet  $\alpha$  and the negative variation of the tube  $\alpha$  were chosen. Although much less significant, the same process was applied for the variation of Young's Modulus for both materials. The resulting combined  $H^*$  variance, [ ]<sup>a,c,e</sup> inch by the SRSS method,

was determined. When multiplied by the factor 1.645, the resulting increase from the mean of the predicted  $H^*$  value is [ ]<sup>a,c,e</sup> inches. When the adjustment is made for the crevice pressure referenced to the initially predicted value of  $H^*$  (see Figure 8-1), the final value of  $H^*$  is [ ]<sup>a,c,e</sup> inches. This value is the 95% probability, 50% confidence value of  $H^*$  for a single tube.

Case S-1: For this evaluation, the biased influence factors from Case S-0 were utilized. To extend the evaluation to include the full tube bundle complement of 3214 tubes, the applicable multiplier for the single tube analysis is 4.157. The resulting increase from the predicted mean  $H^*$  value is [ ]<sup>a,c,e</sup> inches. When the adjustment is made for the crevice pressure distribution referenced to the predicted  $H^*$ , the final value of  $H^*$  for the entire bundle at 95% probability and 50% confidence is [ ]<sup>a,c,e</sup> inches.

Case S-2: As noted above, influence factors for  $H^*$  were calculated based on parameter variances of  $4.157\sigma$ . Only the variations that would increase the value of  $H^*$  were considered. It is seen from Figure 8-2 and Table 8-3 that the most significant influencing variable is the tube  $\alpha$ . The predicted result for  $H^*$  for a variation of  $\alpha_T$  of  $4.157\sigma$  is greater than 4.157 multiplied by the  $1\sigma$  variability of  $H^*$ . However, the variation of  $H^*$  at a  $4.157\sigma$  variation of the tubesheet  $\alpha_{TS}$  is only slightly greater than 4.157 times the  $1\sigma$  variation of  $H^*$  in the tubesheet  $\alpha$ . When the adjustment is made for the crevice pressure distribution referenced to the predicted  $H^*$ , the final value of  $H^*$  for the entire bundle at 95% probability and 50% confidence is 13.31 inches. This case is the recommended value of  $H^*$  at 95% probability and 50% confidence for the entire bundle of 3214 tubes.

Case S-3: This case replicates Case S-2 except that the biased influence factors are based on  $5\sigma$  variations of each of the input parameters. The predicted value of  $H^*$  for this case is [ ]<sup>a,c,e</sup> inches. The  $H^*$  probability for this case is far in excess of 95/50 for a tube population of 3214 tubes. Application of  $5\sigma$  parameter variations is well in excess of the required parameter variation,  $4.157\sigma$ , to satisfy the 95% whole bundle probability requirement. This case shows that  $H^*$  is not highly sensitive to extreme parameter variations and validates the recommended  $H^*$  value of 13.31 inches from Case S-2 above.

Case S-4: Because there is interaction between  $\alpha_{TS}$  and  $\alpha_T$ , this case arbitrarily assumes that both  $\alpha_{TS}$  and  $\alpha_T$  and the respective Young's moduli are at their  $2\sigma$  values in the direction of increasing  $H^*$  to define a very conservative biased mean value of  $H^*$ . The influence factors at  $4.157\sigma$  were combined by SRSS and added to the mean determined as noted above. After adjusting for  $P_{crev}$ , the resulting value of  $H^*$ , [ ]<sup>a,c,e</sup> inches, significantly exceeds the whole bundle probability requirements of 95% at 50% confidence. This case further demonstrates that even at highly improbable input parameter combinations, a value of  $H^*$  exists.

## 8.2.2 Monte Carlo Sampling Approach to Calculating the Probabilistic Value of $H^*$

The process described in this section, based on a Monte Carlo sampling technique, was utilized to provide a check of the method described in Section 8.2.1.

A Monte Carlo sampling process was utilized, using the commercially available program "@RISK," to develop the final  $H^*$  distribution for all parameters combined (Reference 8-5). The biased influence factors developed for each variable are randomly sampled to develop the final  $H^*$  distribution. The combined distribution is defined by the following equation:

$$[ \quad ]^{a,c,e} \quad (8-1)$$

where  $v_i$  is the randomly sampled value of  $H^*$  from each individual influence factor distribution.

Table 8-4 summarizes the results of various Monte Carlo cases considered.

Case M-0: Because the  $-1\sigma$  variation of each variable results in a different variation in  $H^*$  than the  $+1\sigma$  variation (see Table 8-2), effectively there are two possible influence distributions for each variable. Hence, a total of eight influence distributions can be constructed. For this case, the distributions that were constructed from the  $+1\sigma$  variable variation were sampled; 10,000 simulations were performed and the final  $H^*$  distribution was constructed. The results of this simulation are presented in Table 8-4. The final  $H^*$  value, [ ]<sup>a,c,e</sup> inches, represents the 95% probability at 50% confidence value of  $H^*$  for this particular set of inputs after the adjustments for BET and crevice pressure have been made. Because the input variations chosen are arbitrary, there is no physical significance to this result, except to provide information on the sensitivity of  $H^*$  to variations of the input parameters.

Case M-1: This case is the same approach as Case M-0 except that the influence distributions from all of the  $-1\sigma$  variations of the input variables were utilized. The results of this simulation are presented in Table 8-4. The final  $H^*$  value, [ ]<sup>a,c,e</sup> inches, represents the 95% probability value of  $H^*$  for this particular set of inputs. Because the inputs chosen are arbitrary, there is no physical significance to this result, except to provide information on the sensitivity of  $H^*$  to variations of the input parameters. The case demonstrates the greater influence of the negative variation of  $\alpha_T$  on  $H^*$ .

Cases M-0 and M-1 were initial analyses to scope the sensitivity of  $H^*$  to variations in the input parameters. Comparing the  $H^*$  results for these influence factor variations leads to two observations:

1. At a 1 to 2 sigma variation of the input parameters, the change in the predicted  $H^*$  value is not significantly sensitive to the variations of the input parameters in either the positive or negative direction, and,
2. The variation of  $H^*$  is principally driven by the value of  $\alpha_T$ . The results of these initial analyses suggested the conservative path for evaluating the probabilistic value of  $H^*$ , which was to bias all of the influence function in the direction of increasing  $H^*$ .

Case M-2: The eight possible influence distributions from Cases 1 and 2 were reduced to four by selecting only those that resulted in an increased value of  $H^*$  as suggested by Cases M-0 and M-1. For example from Table 8-2 for the  $\pm 1\sigma$  variations of the variables, the influence distributions were based on the following parameter variations:

$E_{TS}$ : $-1\sigma$ variation	Results in 0.04 inch increase in $H^*$
$\alpha_{TS}$ : $+1\sigma$ variation	Results in 0.40 inch increase in $H^*$
$E_T$ : $-1\sigma$ variation	Results in 0.01 inch increase in $H^*$
$\alpha_T$ : $-1\sigma$ variation	Results in 0.65 inch increase in $H^*$

This set of influence parameters are referred to as the “biased influence factors” because all of the variable variations were chosen to maximize the H\* value.

Using the influence distributions determined from the mean H\* [ ]<sup>a,c,e</sup> inches, including the BET and applicable NOP temperature distribution adjustments and the standard deviations noted above, 100K simulations were performed to determine the combined H\* distribution. The 95% probability value was chosen from the resulting combined distribution. This case represents a conservatively biased estimate of a single tube H\* value at 95% probability and 50% confidence. The final calculated value of H\* for this case is [ ]<sup>a,c,e</sup> inches.

Case M-3: As an extension of Case M-2, the final H\* distribution from case M-2 was sampled 3214 times, and the resulting H\* values were rank ordered from high to low. The maximum value of H\* from this sampling was determined to be [ ]<sup>a,c,e</sup> inches as shown on Table 8-4. This case is not a complete extreme value evaluation but it provides insight into the combined distribution of H\*, particularly when compared to Cases M-2 and M-4.

Case M-4: This case is a further extension of Case M-2 and Case M-3. The distribution from Case M-2 is sampled similarly to Case M-3, except that the sampling of the Case M-2 results is repeated 1000 times. The maximum values from each of the 1000 repeats of the 3214 samples from the distributions are recorded and rank ordered. From this ranking, the 950<sup>th</sup> value is chosen, which is the 95% probability at 50% confidence of the distribution of extreme values. This case represents a true extreme value evaluation for the case when all the influence factors are conservatively biased in the direction of a greater H\*. The resulting value of H\* is [ ]<sup>a,c,e</sup> inches. Comparing this value with that from Case M-3 shows that there is very little change in the value of H\* when 1000 samples of the maximum values are taken compared to only a single sample.

Case M-5: This case considers the biased influence factors for the 4.157 $\sigma$  variation from Table 8-2 divided by 4.157 to give equivalent 1 $\sigma$  factors that take into account the non-normality of the influence factor distributions. Monte Carlo sampling from each influence distribution was performed 100,000 times to determine the resulting distribution of H\*, and the 95% probability, 50% confidence value is reported from this distribution. It is noted that each of the 100K simulations assumes a new value for the tubesheet properties. Interaction effects are included because the 4.157 $\sigma$  variations were used that already partially include the effective interactions among the variables. The predicted whole bundle H\* value at 95/50 is [ ]<sup>a,c,e</sup> inches. This case is a whole bundle case because it is based on the parameter variation of 4.157 $\sigma$ ; a single tube analysis would be based on 1.645 $\sigma$  to demonstrate 95% probability, 50% confidence. When compared to Case M-2, this case illustrates the effect of the non-normality of the influence factors.

Case M-6: Recognizing that there is a limited population of tubesheets among the H\* candidate plants, this case provides an extreme value H\* assuming a limited population of tubesheets. An iterative sampling scheme was applied in which the tubesheet properties were sampled once and, while holding the tubesheet properties at that chosen value, the tube properties were sampled 3214 times and the maximum value of the resulting H\* was recorded. This process was repeated for 1000 random picks of tubesheet properties. The recorded 1000 maximum H\* values were rank ordered and the 950<sup>th</sup> value was selected. This value, [ ]<sup>a,c,e</sup> inches, represents the extreme value of H\* at a probability exceeding 95% at 50% confidence for the entire bundle of 3214 tubes assuming a limited population of tubesheets.

This case demonstrates that  $H^*$  is not significantly sensitive to extremely conservative assumptions. It validates the SSRS-based recommended value of  $H^*$  of 13.31 inches because it represents a significantly higher level of confidence, but does not provide a significantly larger value of  $H^*$ .

Case M-7: The conservatism of this case defines it as a bounding case which cannot reasonably occur. The mean value of  $H^*$  is the basis for this calculation; however, the variability of the parameters at  $2\sigma$  biased in the direction of increasing  $H^*$  is assumed. Thus, this case exceeds the whole bundle case based on  $4.147\sigma$  divided by 4.157. For example:

Parameter	$\alpha_T$	$E_T$	$\alpha_{TS}$	$E_{TS}$
4.157 $\sigma$ Value/4.157	1.65	.014	0.52	0.03
Value used in Case M7	1.73	0.03	0.76	0.04

Thus, case M7 essentially approximates a  $5\sigma$  variability case.

The influence factor distributions are sampled 100K times to develop the  $H^*$  distribution. The  $H^*$  distribution was sampled 3214 times, and that sampling was repeated 1000 times. The maximum values from each of the 1000 replicates of 3214 samples were retained and rank ordered. The 950<sup>th</sup> rank value, [ ]<sup>a,c,e</sup> inches (before the  $P_{crev}$  correction), represents the 95% probability at 50% confidence of the extreme value of this biased case. Because the influence factors were based on the actual  $2\sigma$  values, this case includes an interaction effect between the two principal variables,  $\alpha_T$  and  $\alpha_{TS}$ .

After the correction for the effect of crevice pressure referenced to the location of the predicted  $H^*$  is added, the final value of  $H^*$  for this extremely conservative case is [ ]<sup>a,c,e</sup> inches. This case exceeds the requirement of 95% probability at 50% confidence for the whole bundle by a significant margin.

### 8.3 SUMMARY AND CONCLUSIONS

The input variables that affect the calculations for tubesheet displacement, tube-to-tubesheet contact pressures and residual contact pressure were defined. The variation of these parameters was previously defined in Section 6.0. Only four parameters, the coefficient of thermal expansion for the tubesheet and the tube material and the Young's Modulus of the tubesheet and the tube material, affect the calculation of  $H^*$  if it is assumed that the residual contact pressure is zero. The impact of variability of each of these parameters on  $H^*$  was determined. Two approaches were utilized to determine the probabilistic value of  $H^*$  that meets the requirement of 95% probability at 50% confidence for all of the 3214 tubes in the Model 44F tube bundle, combination of uncertainties by the square root of the sum of the squares (SRSS), and a Monte Carlo sampling method.

The following conclusions were reached:

1. The recommended 95/50 whole bundle value of  $H^*$  is 13.31 inches (Case S-2). This value meets the requirements of whole-bundle based 95% probability at 50% confidence, and is the most conservative of all of the results obtained from various different assessments of  $H^*$  that did not intentionally bias the results for the purpose of evaluating the sensitivity of  $H^*$  to parameter

variations. It is based on the use of the SRSS method of combining uncertainties. The uncertainties are based on variation of the individual parameters of 4.157 standard deviations from their respective mean values.

2. An assessment of the extreme value of  $H^*$  for all of the tubes (3214 for a Model 44F SG) in a SG tube bundle shows that the extreme value of  $H^*$  based on the use of variances biased to maximizing the value of  $H^*$  (Case M-4) is enveloped by the recommended value of  $H^*$ .
3. Four input parameters affect the value of  $H^*$ : The coefficients of thermal expansion of the tubesheet and tubing materials and the Young's moduli for the tube and tubesheet materials. The parameter that most influences the  $H^*$  value is the coefficient of thermal expansion of the tubing material (A600) and the second most important variable is the coefficient of thermal expansion of the tubesheet material (SA508). Variations of Young's Modulus of both materials have only minor influence on the value of  $H^*$ .
4. Two of the input variables, the coefficients of thermal expansion of the tube material and of the tubesheet material, are interdependent. An analysis showed that the other input parameters independently affect the value of  $H^*$  without regard to the variation of any other parameter. The interdependence of the coefficients of thermal expansion is significant only at extremely low probabilities of occurrence.
5. The 95/50 value of  $H^*$  is moderately sensitive to extreme variations of the input parameters as shown by the distribution of results for all of the cases considered.
6. If the number of tubesheet samples is reduced to account for the limited population of tubesheets among the  $H^*$  candidate plants, the extreme value of  $H^*$  of [ ]<sup>a,c</sup> inches (Case M-6). This result validates the recommended value of 13.31 inches because the extreme value case reflects a significantly higher confidence but not a significantly larger value of  $H^*$ .
7. The recommended value of  $H^*$  is based on the mean value of  $H^*$  for the single worst tube in the bundle at [ ]<sup>a,c</sup> inches radius in the sector of tubes shown to have the limiting  $H^*$  values. All other tubes will have a lesser value of  $H^*$ .

#### 8.4 REFERENCES

- 8-1 EPRI 1012987, Revision 2, Steam Generator Integrity Assessment Guidelines; July 2006.
- 8-2 LTR-SST-05-19, Rev. 1, "System State Equivalency Testing Not Required for Windows XP SP-2," June 20, 2005.
- 8-3 Microsoft Excel Function Reference; Document Number AB26298-0392; Microsoft Corporation; Redmond, WA.
- 8-4 ID-26666, Vol. 1, Design Data, Nuclear Systems Materials Handbook, ORNL, 1988.

8-5 LTR-SGMP-09-55, "Monte Carlo Analyses in Support of the H-Star Program,"  
Westinghouse Electric Company LLC, Pittsburgh, PA, April 20, 2009.



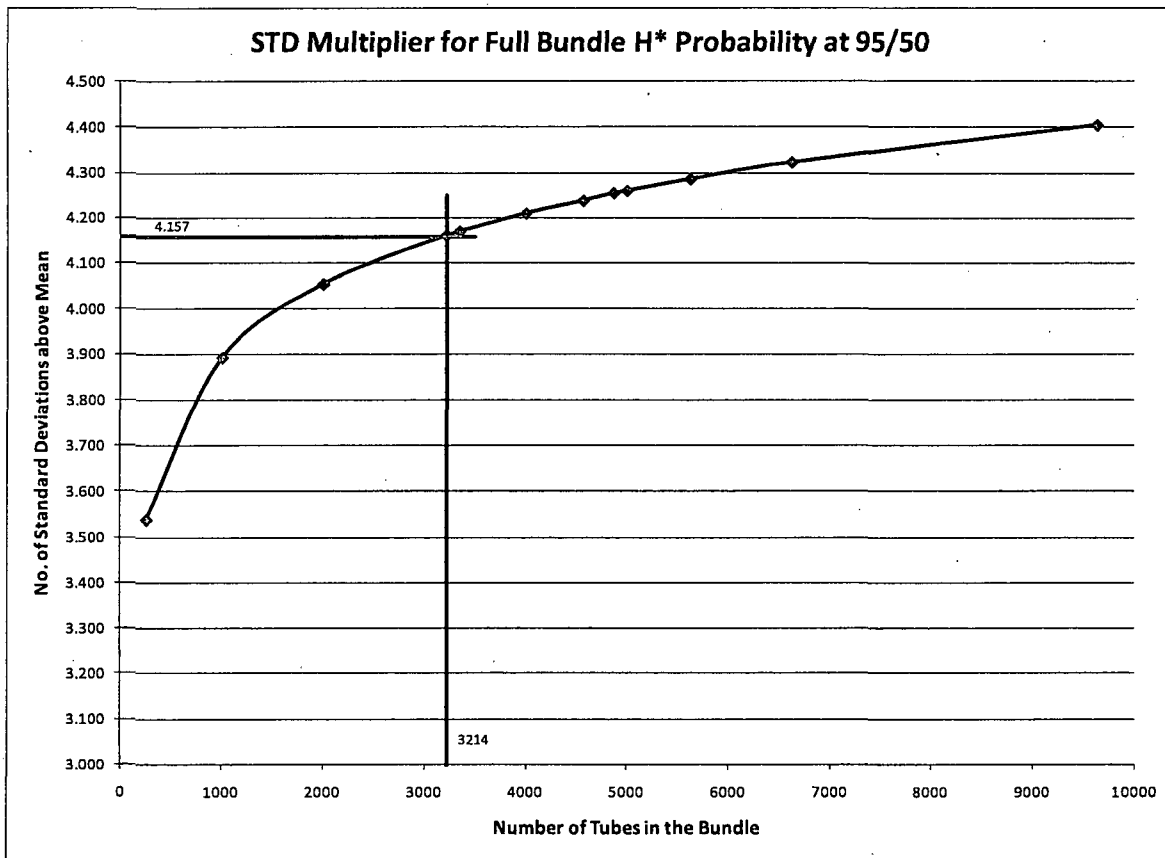


**Figure 8-12 Single Tube Required Reliability, Expressed as Number of Standard Deviations from the Mean to Meet a Whole-Bundle (3214 Tubes) Reliability of 95%**

## **9.0 LEAK RATE ANALYSIS OF CRACKED TUBE-TO-TUBESHEET JOINTS**

Leakage considerations were addressed in prior H\*/B\* technical justifications (e.g., Reference 9-10) by B\*. B\* was defined as the length of undegraded tubesheet expansion region at which the resistance to leakage under postulated accident conditions was the same as the leak resistance during normal operating conditions (NOP). This permitted the accident condition leakage rate to be bounded by a factor of 2 on the normal operation leak rate from degradation at or below the B\* distance from the top of the tubesheet. The B\* justification was based on a correlation of loss coefficient with contact pressure between the tube and the tubesheet.

A test-by-test analysis of the data has been completed to address the data scatter (see Figure 9-2) in relating the loss coefficient to tube joint contact pressure (References 9-1 and 9-2). The test-by-test analysis of the available leakage data has shown that there is no correlation between loss coefficient and contact pressure for the conditions tested (see Section 9.3.3). Therefore, the analysis basis of this report is that there is no correlation between loss coefficient and contact pressure for the conditions of interest for the SG expansion region. The original leakage analysis approach called B\* and the approach utilized in the justification of the interim alternate repair criteria (IARC) (Reference 9-3) have been revised. The current approach to the leakage analysis is described in Section 9.1.

To address NRC RIS-2007-20 (Reference 9-4) regarding the definition and treatment of the limiting accident condition, the current analysis provides detailed evaluation of the pressure-time histories of the postulated accident conditions and develops an overall leakage factor (ratio) for accident leakage to normal operating leakage for each H\* candidate plant (Section 9.1). This section also provides a rationale for calculating the time-integrated leak rate, based on the time histories of the postulated accident conditions, that effectively reduces the leak rate factors for two of the three applicable transients (i.e., steam line break, locked rotor and control rod ejection) to account for the time at temperature and pressure.

The applicable leak rate factor for the limiting transient, defined as the transient that results in the highest leakage factor, is determined to be equal to, or less than, 2.03 for all of the H\* candidate plants.

### **9.1 LEAKAGE ANALYSIS METHODOLOGY**

#### **9.1.1 Development of Overall Leakage Factor**

The underlying theoretical basis for the leakage analysis is the Darcy formulation of leakage through a porous medium (Reference 9-8). There has been general concurrence among the industry and the NRC and its consultants that the Darcy model is the correct and conservative model for potential leakage in the tubesheet expansion region for hydraulically expanded tubing. The Darcy model for leakage is discussed in detail below.

In Reference 9-5, the NRC Staff provided their evaluation of the potential for the normal operating leak rate to increase under steam line break (SLB) conditions. Making the conservative assumption that loss coefficient and fluid viscosity are constant under both normal operating and steam line break conditions,

the NRC Staff concluded that the ratio of steam line break leakage rate to normal operating leakage rate is equal to the ratio of steam line break pressure differential to normal operating pressure differential times the ratio of the effective crevice length under normal operating conditions ( $l_{NOP}$ ) to effective crevice length under steam line break conditions ( $l_{SLB}$ ). Effective crevice length is defined as the crevice length above the  $H^*$  distance for which there is positive contact pressure between the tube and the tubesheet. Using various values of ratio ( $l_{NOP}:l_{SLB}$ ) determined from previous  $H^*/B^*$  analyses, the NRC Staff concluded that a factor of 2.5 conservatively bounds the potential increase in leakage from the lower-most 4 inches of tubing that would be realized in going from normal operating to steam line break conditions (Reference 9-5).

A ratio of the Darcy equation for flow through a porous medium is used to calculate the estimated increase in leakage during design basis accidents that model primary-to-secondary leakage for each of the  $H^*$  plants. The Darcy model for describing axial flow in a porous medium is:

$$Q = \frac{\Delta p}{12\mu Kl} \quad (9-1)$$

Where:

$Q$  is the flow rate of the fluid through the porous medium,

$\Delta p$  is difference in pressure (or driving head) acting to force the fluid through the porous medium,

$\mu$  is the viscosity of the fluid,

$K$  is the loss coefficient for the flow through the porous medium and

$l$  is the axial length of the medium.

In lieu of the  $B^*$  approach, which requires a value of the leak loss coefficient, the expected increase in leakage during an accident event relative to normal operating conditions can be defined using a ratio of Equation (9-1) for the different operating conditions. The resultant Darcy flow equation ratio can be separated into four "subfactors" as follows:

$$\frac{Q_{DBA}}{Q_{NOP}} = \frac{\Delta p_{DBA}}{\Delta p_{NOP}} \frac{\mu_{NOP}}{\mu_{DBA}} \frac{K_{NOP}}{K_{DBA}} \frac{l_{NOP}}{l_{DBA}} \quad (9-2)$$

Making the assumption that the loss coefficient is constant under normal operating and design basis accident conditions reduces the ratio of design basis accident leakage rate to normal operating leakage rate to three subfactors. The assumption of constant loss coefficient is supported by test-by-test regression analysis results for loss coefficient as a function of contact pressure for both Model D5 and Model F leakage test specimens (see Figures 9-15 and 9-16). The overall leakage factor is equal to the ratio of design basis accident pressure differential to normal operating pressure differential multiplied by the ratio of dynamic viscosity at normal operating conditions to dynamic viscosity at design basis

accident conditions multiplied by the ratio of effective crevice length under normal operating conditions ( $l_{NOP}$ ) to effective crevice length under design basis accident conditions ( $l_{DBA}$ ). The ratio of the leak rates is shown in Equation (9-3):

$$\frac{Q_{DBA}}{Q_{NOP}} = \frac{\Delta p_{DBA} \mu_{NOP} l_{NOP}}{\Delta p_{NOP} \mu_{DBA} l_{DBA}} \quad (9-3)$$

Recall that “effective crevice length” is defined as the length of positive contact between the tube and the tubesheet (above  $H^*$ ). It is shown in Section 6.0 that there will always be positive contact pressure between the tubes and the tubesheet during all plant conditions for each tube over the entire length of the tubesheet thickness. Therefore, the effective crevice length ratio,  $l_{NOP}/l_{DBA}$ , is 1.0 above the previously calculated  $H^*$  length for each transient condition that models primary-to-secondary leakage. Consequently, during a postulated design basis accident, the expected increase in leakage is only a function of the increase in pressure differential that occurs across the tubesheet and the ratio of the dynamic viscosity between normal operating and the design basis accident conditions during the plant transient and Equation (9-3) further simplifies to Equation (9-4).

$$\frac{Q_{DBA}}{Q_{NOP}} = \frac{\Delta p_{DBA} \mu_{NOP}}{\Delta p_{NOP} \mu_{DBA}} \quad (9-4)$$

### 9.1.2 Viscosity Subfactor

The viscosity ratio subfactor in Equation (9-4) is determined from the applicable temperatures and pressures for the conditions of interest. Figure 9-1 shows the relationship between dynamic viscosity as a function of temperature and pressure. To facilitate determining the viscosity factor ratio analysis, a third order polynomial fit to dynamic viscosity data (Figure 9-1) was used to develop the appropriate leakage factors for each of the plant conditions. The fit accurately represents the variability of dynamic viscosity with temperature. The viscosity ratio subfactor is utilized for determining the final leakage factor discussed below. It can be seen from Figure 9-1 that dynamic viscosity decreases with increasing temperature. An increase in temperature relative to normal operating plant conditions or no load plant conditions would result in an increase in leakage during a postulated design basis accident (DBA).

### 9.1.3 Discussion on Porous Medium

For the tube-to-tubesheet joint, the porous medium is defined as the interaction between the asperities of the surface finishes of the tubesheet bore and the tube outside surface. The as-manufactured tube outside diameter (OD) has a relatively smooth finish (10 rms finish), and the as-manufactured finish of the tubesheet bore is controlled to a 250 rms surface finish. During the tube expansion process, the peaks of the surface asperities of the respective components are deformed, creating a randomly distributed porous interface over the length of the tube expansion.

For this analysis, the resistance of the porous medium to leakage is assumed to be uniform around the circumference of the tube. Confirmatory testing (STD-MC-06-11, page 33, Reference 9-6) and results

published in the Journal of Pressure Vessel Technology, August 2006, Volume 128, Issue 3, pp. 408-413 (Reference 9-7) both show that “circumferential bands” of leakage are principally the leakage mode for tubes expanded into tubesheets. This suggests that the actual leakage mechanism is a tortuous path of relatively high flow resistance rather than the assumed circumferentially, evenly distributed porous medium flow resistance. Additionally, three-dimensional finite element analysis (3D FEA) results in Section 6.0 show that the degree of tubesheet bore ovalization that occurs due to tubesheet bow is negligible compared to the asperity height of the original 250 rms surface finish of the tubesheet bore during all plant conditions. The analysis also shows that there is no loss of contact around the perimeter of the tube. The tube follows the ovalization of the tubesheet bore due to internal pressure, temperature and bending effects (see Section 6.2.5). Therefore, it is concluded that the assumption of circumferentially uniformly distributed porous medium is appropriate and conservative for application to the leakage evaluation and that channeling of flow due to tubesheet hole ovalization does not occur.

## **9.2 DETERMINATION OF LIMITING CONDITIONS FOR H\* LEAKAGE CALCULATION**

### **9.2.1 Background**

Primary-to-secondary leakage is assumed to occur in several design basis accidents for the Model 44F SG (e.g., steam line break (SLB), locked rotor, and control rod ejection). The radiological dose consequences associated with this assumed leakage are evaluated to ensure that they remain within regulatory limits (e.g., 10 CFR Part 100, 10 CFR 50.67, GDC 19). The accident-induced leakage performance criteria are intended to ensure the primary-to-secondary leak rate during any accident does not exceed the primary-to-secondary leak rate assumed in the accident analysis.

### **9.2.2 Pressure-Time Histories for Accidents that Model Primary-to-Secondary Leakage**

As noted in Reference 9-4 (NRC RIS-2007-20, “Implementation of Primary-to-Secondary Leakage Performance Criteria”), implementing the accident-induced leakage performance criteria requires an analysis of the condition of the SG tubing during a SG inspection to calculate the magnitude of the primary-to-secondary leakage which could potentially occur for each of the design basis accidents. The calculated leak rates for each design basis accident should not exceed the value assumed in the corresponding accident analyses.

To make such a comparison for the H\* plants, a study was completed to define the loading conditions on the tubes for each of the design basis accidents that model primary-to-secondary leakage for each SG type involved in the H\* program (Reference 14). In addition to the SLB/FLB<sup>1</sup> accidents, the transients that were evaluated include:

- Reactor Coolant Pump Locked Rotor – Dead Loop
- Reactor Coolant Pump Locked Rotor – Active Loop(s)
- Control Rod Ejection

<sup>1</sup>The postulated feedline break is not part of the licensing basis for plants with Model 44F SGs. The postulated FLB is only applicable to plants with Model F and D5 SGs

Transient response data was considered for all of the H\* plants as follows:

Model F	Model D5	Model 44F and 51F
Wolf Creek	Byron 2 / Braidwood 2	Turkey Point 3 and 4
Vogtle Unit 1 and 2	Catawba Unit 2	Point Beach 1
Millstone 3	Comanche Peak 2	H.B. Robinson 2
Seabrook		Indian Point 2
Salem 1		Surry 1 and 2
Vandellos 2		

Examples of the transients input data from Reference 9-13, the SLB transient pressure and temperature versus time histories for the Model 44F SGs are shown in Figures 9-3, 9-3a, 9-3b, 9-4, 9-4a and 9-4b taken from Reference 9-12. Similar transient input data for the other DBA events noted above are also available in Reference 9-12. Table 9-2 provides a summary of the corresponding peak RCS pressures achieved during the transients (References 9-12 and 9-13).

Plant-specific operating conditions are used to generate the overall leakage factor ratios that are to be used in the condition monitoring/operational assessments as discussed in Section 9.4. The plant-specific data provide the initial conditions for application of the transient input data. The results of the analyses of the plant-specific inputs, to determine the bounding plant for each model of SG, are contained in Section 6.0 of this report.

### 9.2.3 Limiting Temperature Conditions

For the Model 44F SGs, the postulated SLB for a two loop or three loop plant results in a cooldown event and the subsequent temperatures in the reactor coolant system do not exceed the temperatures at plant no load conditions (discussed further in Section 9.2.3.1 below). Therefore, an increase in leakage due to the viscosity subfactor in the Darcy equation discussed above will not occur.

The other design basis accidents, such as a postulated locked rotor event and a control rod ejection event, are conservatively modeled using the design specification transients to result in increased temperatures in the SG hot and cold legs for a period of time. Dynamic viscosity decreases with increasing temperature. Therefore, referring to the Darcy model, and holding the other parameters constant, leakage would be expected to increase, due to decreasing viscosity, for the duration of time that there is a rise in reactor coolant system (RCS) temperature during these transients (see Section 9.5 for a discussion on the impact of time integration of leak rate on acceptable leakage). Table 9-1 provides a summary of the transient temperature increase above normal operating conditions that is considered in this leakage analysis in the hot and cold legs of the SGs for each model SG [References 9-12 (Model F, 44F, 51F) and Reference 9-13 (Model D5)]. The locked rotor and control rod ejection are of very short duration, for which the H\* leakage calculations employ a time integrated leakage approach (see Section 9.5 below).

### 9.3 LEAK RATE TESTING

#### 9.3.1 Description of Testing

A test program was conducted with the primary objective to characterize leakage across simulated tube-to-tubesheet hydraulically expanded SG tube samples and to establish a crevice loss coefficient as discussed above (References 9-8 and 9-9). The testing applied representative primary-to-secondary side pressure differential conditions to determine the leak rates across the simulated SG tube expansion. Two types of testing were conducted on the SG tube samples (Reference 9-10):

- 1) To determine leak rates at normal operating conditions, and
- 2) To determine leak rates under simulated accident conditions.

The tests on the Model F samples and on the Model D5 samples were completed at different times and using different test set-ups. The Model F specimen tests (in CY 1997) were performed using a stand-alone system whereas the tests for the Model D5 samples were completed in an autoclave (CY 2003). Schematics of the two test systems are provided in Figure 9-7 for the Model F samples and Figure 9-8 for the Model D5 samples.

##### 9.3.1.1 Model F Testing Configuration

The design of the test samples modeled key features of the Model F tube-to-tubesheet joint for leakage tests as follows:

A steel collar, with an outside diameter of approximately [ ]<sup>a,c,e</sup> inches, was utilized to simulate the radial stiffness of a Model F tubesheet unit cell. The length of the test collars was [ ]<sup>a,c,e</sup> inches longer than the thickness of the SG tubesheet. The length of the hydraulic expansion was 16.5 inches. This allowed for the introduction and collection of leakage in unexpanded sections of the tube, while retaining the desired expansion lengths. The collars were drilled to the nominal design inside diameters with the surface finish based on SG manufacturing drawing tolerances.

[

] <sup>a,c,e</sup>.

Model F A600TT tubing with a yield strength within the range of that of the tubes in the operating plants, which ranges from [ ]<sup>a,c,e</sup> was used. The tubing used was from a certified heat and lot conforming to ASME SB163, Section III NB Class 1.

The intent of the leakage portion of the test program was to determine the leakage resistance of simulated Model F tube-to-tubesheet joints, without the tube-to-tubesheet weld or the effect of the [

] <sup>a,c,e</sup> (see Figure 9-7). The welds were a feature of the test specimen design and made no contribution to the hydraulic resistance. All of the leak tests conducted for the Model F test specimens discharged to atmospheric pressure, 15 psia.

The testing was performed according to a test procedure which outlined two types of leak tests as follows:

1. Room temperature primary-to-secondary side leak tests were performed on all test samples, [ <sup>a,c,e</sup>
2. Elevated temperature primary-to-secondary leak tests were performed using an [ <sup>a,c,e</sup>

These tests were performed following the room temperature primary-to-secondary side leak tests on the chosen samples.

### 9.3.1.2 Model D5 Testing Configuration

The test samples modeled key features of the Model D5 tube-to-tubesheet joint for leakage tests. The following hardware was used:

Model D5 tubesheet simulating collars, matching the radial stiffness of a Model D5 tubesheet unit cell, with an outside diameter of approximately [ <sup>a,c,e</sup> inches were used. The length of the test collars allowed the introduction of fluid in an unexpanded section of the tube. The surface finish and run-out tolerances of the tubesheet unit cell simulants were based on factory tolerances specified for the tubesheet drilling operation. The length of hydraulic expansions ranged from 3 to 12 inches.

[

] <sup>a,c,e</sup>.

The average yield strength for the SG Alloy 600TT tubing in the Model D5 plants is [ ] <sup>a,c,e</sup> ksi. The Alloy 600 tubing used for these tests was from certified heats conforming to ASME SB163, Section III Class 1. The intent of the leakage portion of the test program was to determine the leakage resistance of simulated Model D5 tube-to-tubesheet joints, disregarding the effect of the [ ] <sup>a,c,e</sup>.

The design hydraulic expansion pressure range for the Model D5 steam generators is [ ] <sup>a,c,e</sup>. This value is conservatively in the lower end of the range of expansion pressures used for the Model D5 SGs. Figure 9-9 shows the details of the configuration for the leak test. The test equipment consisted of a make-up tank (MUT), primary water autoclave (AC1) and a secondary autoclave (AC2) connected by insulated pressure tubing. Two specimens were installed into the secondary autoclave to minimize set-up time and variability across test runs. The primary water autoclave was run with deoxygenated primary water containing specified amounts of boron, lithium, and dissolved hydrogen to simulate the reactor primary coolant. The primary chemistry conditions were controlled in the make-up tank and a pump and backpressure system allowed the primary water to re-circulate from the make-up tank to the primary water autoclave. The primary autoclave had the normal controls for heating, monitoring pressure and safety systems including rupture discs. Figure 9-8 shows the entire test system with key valves and pressure transducers identified. In addition to the normal controls for heating, monitoring pressure, and maintaining safety, the secondary autoclave was outfitted with water cooled condensers that converted any steam escaping from the specimens into room temperature water. The pressure in the secondary side in the main body of the secondary autoclave, was monitored by pressure transducers. For most tests, the leakage was collected in a graduated cylinder on a digital balance connected to a computer so that the amount of water could be recorded as a function of time. For some normal operating condition tests, the leakage was calculated based on changes in the secondary side pressure. All relevant autoclave temperatures and pressures were recorded at regular time intervals with an automatic data acquisition system.

Primary-to-secondary leak tests were performed on all test samples, using simulated primary water chemistry as the pressurizing medium. Test pressure differences of 2850-to-15 psid, 2250-to-800 psid, and 1900-to-15 psid conditions were used, at 600°F.

The room temperature primary-to-secondary side leak tests were performed using the autoclave simply as a test sample holding device, again with simulated primary water as the pressurizing/leakage medium. Test pressures of 2835-to-0, 1900-to-0 and 1450-to-0 psid, (all values nominal) at room temperature, were used.

For all tests, the fluid pressure was applied to the tube inside diameter (ID) and concurrently to the tube-to-collar interface, to simulate a perforation of the tube wall due to corrosion cracking. All of the elevated temperature primary-to-secondary side leak tests were performed using an autoclave, with simulated primary water as the pressurizing/leakage medium. In the case of the 800 psid back pressure tests, the leakage was collected in the autoclave as it issued from the tube-to-collar crevice. In the

remainder of the autoclave tests, the leakage was collected in the autoclave as it issued from the tube-to-collar crevice but it was piped to a condenser/cooler and weighed on an instrumented scale.

### 9.3.2 Leak Test Results

The room temperature and elevated leak test results for the Model F samples are provided in Tables 9-3 and 9-4.

The Model F test results considered different expansion pressures for the test specimens as well as different initial inner diameters for the collars. As noted above, the hydraulic expansion length in the samples was 16.5 inches. The magnitude of leakage can best be described as primary-to-secondary weepage, ranging from 16.6 drops per minutes (dpm) to 240 dpm at room temperature to 0 dpm to 53 dpm at elevated temperatures, using data with hydraulic expansion pressures within the range of the as-built expansion pressures. The average leak rates at room temperature and elevated temperatures were 118.2 dpm and 13.25 dpm, respectively, using data with hydraulic expansion pressures within the range of the as-built expansion pressures. The Model F leak rate results are provided in the form of pressure differential and leak rate ratios in Table 9-3 (room temperature) and Table 9-4 (elevated temperature). The same data are shown graphically in Figures 9-10 through 9-13. These figures demonstrate that the use of the Darcy equation for flow is appropriate as it is shown that it is conservative to assume that primary-to-secondary leakage increases linearly with pressure differential at both room temperature and elevated temperature (see Figures 9-10 and 9-11). The dotted line in Figures 9-12 and 9-13 represents a linear increase in leakage ratio as a function of pressure differential ratio. The room temperature test data falls below the dotted line in Figure 9-12. For the most part, the elevated temperature data also falls below the dotted line in Figure 9-13. Those data points that do not fall below the dotted line can be attributed to leak rate measurement error associated with test specimens that resulted in very low levels of leakage (i.e., leakage on the order of 6 to 20 dpm). Test specimens that resulted in greater amounts of leakage (i.e., leakage upwards of 1420 dpm) always resulted in increased leakage within that predicted by the Darcy flow equation.

Similar results were obtained for the Model D5 test specimens.

### 9.3.3 Loss Coefficient Evaluation

A theoretical model (see Reference 20) developed at Argonne National Laboratory suggests that leakage loss coefficient is correlated with the contact pressure between the tube and the tubesheet. The data shown in Figure 9-2 display significant scatter and, collectively, do not lend themselves to a strong argument that a correlation exists between loss coefficient and contact pressure for the conditions tested (representative of SG operating and transient conditions). It was recommended that the test specimens that included sufficient pressure differential data points be individually analyzed to determine if there is a correlation between loss coefficient and contact pressure and the degree of correlation.

The results of this study are presented in Figure 9-14 for the Model D5 test specimens and Figure 9-15 for the Model F test specimens. For both sets of data, it is seen from these figures that no significant correlation can be established between loss coefficient and contact pressure. The contact pressures for the tests were calculated using the equation used to calculate the local effects due to the interaction of the tube and the tubesheet hole for the determination of  $H^*$  that is discussed in Section 6.41 of this

document. The crevice pressure profiles were matched to test conditions with  $P_{sec}$  assumed at the exit of the expansion length. The Model D5 test conditions used to calculate the contact pressures were: Normal Operation (2250 psi) and FLB (2800 psi). The Model F test conditions used to calculate the test sample contact pressures were: SLB (2650 psi) and "Other (Tested at Hydrostatic Test Pressure)" (3100 psi). Average crevice pressures were used resulting from the crevice pressure profile for both the Model D5 and Model F test specimens. The average crevice pressures used for the Model D5 specimens were [ ]<sup>a,b,c</sup> psi for NOP and [ ]<sup>a,b,c</sup> psi for the FLB condition (2800 psi). The average crevice pressures used for the Model F specimens for the SLB profile were [ ]<sup>a,b,c</sup> psi and [ ]<sup>a,b,c</sup> psi for the higher pressure profile (3800 psi).

As noted above, the leakage data from the Model F and Model D5 leakage tests show significant scatter. The most difficult parameter to measure in these tests is the leakage. In the high temperature tests, leakage is collected after condensation. Further, for all the tests, the leakage is extremely small, measured in drops per minute over an extended period of time. Consequently, test data scatter is expected even for tests on the same specimen at differential pressure conditions. As a result, no significance is attached to an apparent minor decrease in loss coefficient with increasing contact pressure noted in Figures 9-14 and 9-15.

The results of this study confirmed the assumption in the H\* leakage analysis that the loss coefficient is not strongly correlated to contact pressure for the conditions of interest applicable to the SGs.

#### 9.4 DEVELOPMENT OF FINAL LEAKAGE FACTORS

Plant-specific leakage factors are provided for each H\* candidate plant to establish the expected leakage during each of the accident condition loadings that model primary-to-secondary leakage. The limiting (largest) leakage factor can be established based on the calculated results and will vary from plant to plant. The normal operating conditions for each plant are defined in Reference 9-21.

Equation (9-4) is used to calculate both the steam line break and feedwater line break<sup>1</sup> leak rate factor for each H\* plant. The pressure differentials used to calculate the steam line break/feedwater line break leakage subfactors for substitution in Equation (9-4) are contained in Table 9-6. Conservatively, the maximum feedwater line break pressure differential for a Model F plant is used to calculate the SLB leakage factor for the Model 44F steam generators (Reference 9-14). Additionally, the pressure differential ratio associated with the High  $T_{avg}$  condition is used to calculate the leakage factor (which results in a higher leakage factor than if the low  $T_{avg}$  pressure differential was used). As discussed in Section 9.2.3.1 above, a viscosity ratio of 1.0 is used for the SLB transient as the SG hot or cold leg temperatures do not exceed the normal operating temperature condition.

The pressure differentials and temperatures used to calculate the leakage factors for the H\* plants for the locked rotor and the control rod ejection can be determined using Tables 9-1, 9-2, 9-5 and 9-6. Conservatively, the maximum SG tube hot leg temperature conditions from the active loops and the maximum pressure differential from the dead loop (Models F, 51F, 44F) or active loop (Model D5) (whichever is the greatest) as defined by the SG design specification transients are used to calculate the

<sup>1</sup>Feedline break is not part of the licensing basis for plants with Model 44F steam generators.

leakage factor for the locked rotor event. The SG hot leg temperature (also defined by the design specification design transient) is combined with the maximum pressure differential to calculate the control rod ejection leakage factor for each of the H\* plants.

Table 9-7 identifies the individual components of the calculation process utilized to develop the final applicable leakage factors for the candidate plants by providing a listing of the pressure differential and viscosity subfactors that are used in the development of the plant-specific overall leakage factors for each of the faulted events that model primary-to-secondary leakage (Reference 9-14). The limiting locked rotor leakage factor for the Model 44F SGs occurs in the SG hot leg. Therefore, only the hot leg overall leakage factor is included in Table 9-7 for each H\* plant. The same is true for the control rod ejection event leakage factor.

The process utilizes Equation (9-7), applying the appropriate assumptions and adjustment factors as follows:

- Loss coefficient is assumed to be constant
- Dynamic viscosity appropriate for the condition is used (set to 1 for SLB)
- Maximum DBA pressure differentials are used
- Effective crevice length ratio is 1.0 (contact between the tube and tubesheet is assured for NOP and DBA conditions)
- Circumferential separation of the tube is assumed at H\*

Adjustments of the leak rate factors in Table 9-7 have been made to account for the time duration of the locked rotor and control rod ejection transients (see Section 9.5). As discussed in Section 9.5, the locked rotor leakage factors are divided by 2 and the control rod ejection transient leakage factors are divided by 6 to account for the brief duration of the transient (e.g., see Figure 9-16 for the locked rotor and control rod ejection transient).

The effective leakage factors for H\* leakage analysis for all H\* candidate plants are less than or equal to 2.03 (factor bounds both hot leg and cold leg leakage). Table 9-7 summarizes the leak rate factors for all of the H\* candidate plants for all of the relevant transients. No leakage factor is required for the locked rotor or control rod ejection event as all of the adjusted leakage factors included in Table 9-7 are less than 1.0.

## 9.5 CONDITION MONITORING/OPERATIONAL ASSESSMENT IMPACT

This section discusses the use of the leakage factors in the Condition Monitoring (CM) and Operational Assessment (OA). For example, for Turkey Point Units 3 and 4, for a postulated SLB, a factor of [ ]<sup>a,c</sup> (see Table 9-7) will be applied to the normal operating leakage associated with the tubesheet expansion region in the condition monitoring (CM) and operational assessment (OA). Specifically, for the CM assessment, the component of leakage from the prior cycle from below the H\* distance will be multiplied by a factor of [ ]<sup>a,c</sup> and added to the total leakage from any other source and compared to the allowable accident-induced leakage limit. For the OA, the difference in the leakage between the allowable leakage limit and the accident leakage from sources other than the tubesheet expansion region

will be divided by [ ]<sup>a,c,e</sup> and compared to the observed operational leakage. If necessary, an administrative limit (for operational leakage) will be established to ensure the allowable accident leakage limit is not exceeded.

For transients other than a postulated steam line break, most plants on a case basis can take advantage of the fact that the length of time that the differential pressure across the tubesheet exceeds the normal operating pressure differential is less than [ ]<sup>a,c,e</sup> seconds. Figure 9-16 is a typical locked rotor and control rod ejection transient  $\Delta P$  response for a Model 44F plant. Referring to Figure 9-16, the typical Model 44F plant exceeds the normal operating pressure differential for much less than [ ]<sup>a,c,e</sup> seconds. As the accident-induced leakage performance criteria (AILPC) is defined in gallons per minute, the leak rate for a control rod ejection event can be integrated over a minute to compare to the limit. Time integration permits an increase in acceptable leakage during the time of the peak pressure differential by approximately a factor of [ ]<sup>a,c,e</sup> because of the short duration of the elevated pressure differential. This translates into an effective reduction in leakage factor by that same factor of [ ]<sup>a,c,e</sup> for the locked rotor event (i.e., the amount of leakage associated with a factor of [ ]<sup>a,c,e</sup> increase in leakage rate for [ ]<sup>a,c,e</sup> seconds is equal to the amount of leakage associated with a leakage factor of 1 for one minute). Therefore, for the locked rotor event, the leakage factor identified in Table 9-7 of [ ]<sup>a,c,e</sup> (for Turkey Point Units 3 and 4) is adjusted downward to a leakage factor of [ ]<sup>a,c,e</sup>.

The same process can be applied to the leakage factor for a postulated control rod ejection event. In that case, the length of time that the pressure differential is greater than the normal operating pressure differential is less than [ ]<sup>a,c,e</sup> seconds. Therefore, for the control rod ejection event, the leakage factor identified in Table 9-7 of [ ]<sup>a,c,e</sup> (for Turkey Points Units 3 and 4) is adjusted downward by a factor of 6 to [ ]<sup>a,c,e</sup>.

## 9.6 FINAL LEAKAGE FACTOR DETERMINATION

Based on a review of Table 9-7 and implementation of the time integrated approach discussed above, it is concluded that the limiting leakage factor for all design basis accident conditions is bounded by a factor of 2.03 (factor bounds both hot leg and cold leg leakage). This factor, although determined for a Model F, bounds the plant-specific leakage factor for all plants. It is recommended that all H\* plants adopt this factor for consistency of application of H\*. With one exception, no leakage factor is required for the locked rotor or control rod ejection event as all of the adjusted leakage factors included in Table 9-7 are less than 1.0. The one exception is if a plant has a locked rotor with stuck-open SG PORV event as part of its licensing basis. It is judged that the leakage factor for this event is bounded by the leakage factor of 2.03 for a postulated FLB/SLB event.

## 9.7 LIGAMENT TEARING DISCUSSION

The fundamental assumption for calculating H\* is that there is a circumferential sever at the H\* distance. While the structural analysis (pull out) is based on this assumption, an additional concern may apply for the leakage evaluation. Since the leakage factors discussed above apply to "observed" leakage, which may be in part determined by an axial or circumferential crack, it is necessary to consider the effect of a postulated accident on the sources of the observed leakage. The potential for ligament tearing of circumferential and axial cracks below H\* are addressed in References 9-15 and 9-17 and are evaluated below.

### 9.7.1 Circumferential Cracks

One of the concerns that must be addressed in dealing with cracks in SG tubes is the potential for ligament tearing to occur during a postulated accident when the differential pressure is significantly greater than during normal operation. While the strength evaluations demonstrate a resistance to pull out in excess of  $3\Delta P$  for normal operation and  $1.4\Delta P$  for postulated accident conditions, the potential for ligament tearing to significantly affect the leak rate predictions needs to be addressed.

Ligament tearing considerations for circumferential tube cracks that are located below the  $H^*$  depths within the tubesheet are significantly different from those for potential cracks at other locations. The reason for this is that  $H^*$  has been determined using a factor of safety of three relative to the normal operating pressure differential and 1.4 relative to the most severe accident condition pressure differential. Therefore, the internal pressure end cap loads which normally lead to an axial stress in the tube are not transmitted below about  $1/3$  of the  $H^*$  depth. This means that the only source of stress acting to extend the crack is the primary pressure acting on the flanks of the crack. Since the tube is captured within the tubesheet, there are additional forces acting to resist the opening of the crack. The contact pressure between the tube and the tubesheet results in friction-induced shear stress acting opposite to the direction of the crack opening. Moreover, the pressure on the flanks is compressive on the tube material adjacent to the plane of the crack, hence a Poisson's ratio radial expansion of the tube wall in the immediate vicinity of the crack plane is induced, increasing the contact pressure and also acting to restrain the opening of the crack. In addition, the differential thermal expansion of the tube is greater than that of the carbon steel tubesheet, thereby inducing a compressive stress in the tube below the  $H^*$  length.

A scoping evaluation of the above effects was performed by ignoring the forces that resist the crack opening, and simply looking at the effect of the pressure acting to open the crack. If a  $360^\circ$  through-wall crack is considered, the stress from the pressure on the flanks is 0.209 (20.9%) (this is the ratio of the material area of the tube to the OD section area) of the stress that would result from an end cap pressure load for the same pressure. The primary pressure during normal operation and during a postulated FLB accident is 2250 and 2575 psia, respectively. The actual pressure difference is 325 psi or 14.4% of that applied during normal operation.

The magnitude of the effect can also be used to conservatively estimate the ligament thickness of tube material affected. Using the ASME Code specified minimum yield [

]<sup>a,c,e</sup>.

In summary, considering the worst-case scenario, the likelihood of ligament tearing from radial circumferential cracks resulting from an accident pressure increase is small since at most, only 8% of the

cross-sectional area is needed to maintain tube integrity. Also, since the crack face area will be less than the total cross-sectional area used above, the difference in the force applied as a result of normal operating and accident condition pressures will be less than the 43 lbs associated with the above numbers. Therefore, the potential for ligament tearing is considered to be a secondary effect of essentially negligible probability and should not affect the results and conclusions reported for the H\* evaluation. The leak rate model does not include provisions for predicting ligament tearing and subsequent leakage, and increasing the complexity of the model to attempt to account for ligament tearing has been demonstrated to be unnecessary (Reference 9-15).

### 9.7.2 Axial Cracks

Axial ligament tearing may occur during a postulated accident when the differential pressure across the tube wall is significantly greater than during normal operation. Ligament tearing is accounted for in the strength evaluations that demonstrate a resistance to pull out in excess of 3 ΔP for normal operation and 1.4 ΔP for postulated accident conditions.

The tube area required to resist tearing due to an axially oriented crack can be calculated using traditional mechanics. It is conservative, in this case, to neglect the forces that would act to keep a crack closed and compress the flanks in the ligament so that tensile tearing would become unlikely. This includes the far field axial stress on the tube cross section generated by internal pressure end cap loads which would act to close the ligament and any cracks above the H\* depth. The axial orientation of the damage in the tube means that the required area of the tube cross section to resist tearing and damage should be based on the local strength of the material around the crack. This is in contrast to the typical method used to compare what percent of the area is required to resist ligament tearing in circumferentially damaged tubes based on the amount of force applied to the damaged tube cross section.

The allowable ratio of the applied stress on a tube cross section to the limiting stress the tube cross section can support may be defined as:

$$n = \frac{\sigma_{APPLIED}}{\sigma_{LIMIT}} \quad (9-5)$$

where  $\sigma_{APPLIED}$  is the stress applied to the cross section under either the normal operating condition or a steam line break and  $\sigma_{LIMIT}$  is either the ASME Code minimum tensile yield stress of the tube material (used to predict yield in the ligament) or the ASME Code minimum ultimate tensile strength of the tube (used to predict rupture and tearing of the ligament). The significant properties of the tube cross section are defined as:

$$A_{INITIAL} = \pi(r_o^2 - r_i^2) \quad (9-6)$$

$$A_{MIN} = \pi(r_o^2 - r_{min,i}^2) \quad (9-7)$$

$$t = r_o - r_i \quad (9-8)$$

$$R_M = \frac{r_o + r_i}{2} \quad (9-9)$$

where  $A_{INITIAL}$  is the cross-sectional area of the tube in the undamaged state,  $A_{MIN}$  is the minimum cross-sectional area required to resist ligament tearing,  $t$  is the thickness of the tube wall,  $R_M$  is the mean radius of the tube,  $r_o$  is the outer radius,  $r_i$  is the initial inner tube radius and  $r_{min,i}$  is the minimum inner radius of the tube in the damaged configuration that can still resist ligament tearing.

In the case of an axial crack, the largest local stress contributing to the damage in the tube is the hoop stress acting on the tube due to the internal pressure. The hoop stress acting on the tube cross section is calculated using the following relationship:

$$\sigma_{HOOP} = \frac{Pr}{t} = \frac{PR_M}{t} = \frac{SP_{LIMIT}R_M}{t} \quad (9-10)$$

Where  $S$  is the given safety factor used in the analysis for conservatism and  $P_{LIMIT}$  is the limiting internal pressure that will initiate tearing in the tube. The limiting state in the tube material where the ligament will still hold occurs when the applied loading is equal to the allowable loading that the damaged cross section can bear, or when  $n = 1$ , as shown below.

$$n = 1 = \frac{\sigma_{APPLIED}}{\sigma_{LIMIT}} \rightarrow \sigma_{LIMIT} = \sigma_{APPLIED} \quad (9-11)$$

The applied stress can be written as:

$$\sigma_{APPLIED} = \frac{F_{LIMIT}}{A_{MIN}} \quad (9-12)$$

$$F_{LIMIT} = \sigma_{HOOP} A_{INITIAL} \quad (9-13)$$

where  $F_{LIMIT}$  is the force applied to the cross section by the limiting internal pressure. Substitution of Equations (9-11) and (9-13) into Equation (9-12), and rearranging to solve for  $A_{MIN}$ , gives:

$$\sigma_{LIMIT} = \frac{\sigma_{HOOP} A_{INITIAL}}{A_{MIN}}$$

$$\sigma_{LIMIT} A_{MIN} = \sigma_{HOOP} A_{INITIAL} \rightarrow A_{MIN} = \frac{\sigma_{HOOP} A_{INITIAL}}{\sigma_{LIMIT}} \quad (9-14)$$

Substitution of the definitions for  $t$ ,  $R_M$ ,  $\sigma_{HOOP}$  and  $A_{INITIAL}$  into the equation for  $A_{MIN}$  yields

$$A_{MIN} = \left( \frac{r_o + r_i}{2} \right) \left( \frac{1}{r_o - r_i} \right) \frac{SP_{LIMIT}}{\sigma_{LIMIT}} \pi (r_o^2 - r_i^2) \quad (9-15)$$



## **9.8 REVIEW OF LEAK RATE SUSCEPTIBILITY TO TUBE SLIPPAGE**

### **9.8.1 Background**

As noted in Section 2.1, the potential for incremental slippage under temperature and pressure cycles was one of the remaining technical issues at the end of 2007. Incremental slippage is not considered a credible event because among the possible operating conditions of the steam generators, it is not considered possible to develop a credible argument that slippage has a significant potential to occur. The following summarizes the justification that tube slippage is extremely unlikely.

### **9.8.2 Assessment of the Potential for Tube Slippage**

The justification for H\* shows that tube pull out will not occur under the greater of 3 times the normal operating pressure differential or 1.4 times the steam line break pressure differential. The principal mechanism – although not the only one – that retains the tube in the tubesheet is differential thermal expansion between the tube and tubesheet that causes radial contact forces between the tube and tubesheet, resulting in axial friction forces. The assumed coefficient of friction is conservatively chosen as a lower bound of values that the literature provides, (Section 6.2.2.3.3). The H\* analyses are steady state analyses that assume the limiting forces and temperatures occur simultaneously, and are, therefore a conservative representation of the actual operating conditions in the SG.

The postulated mechanisms for tube slippage, pressure and temperature cycles, do not realistically represent the actual operating characteristics of the steam generator. Implicitly, it is postulated that a significant pressure cycle can occur while the contact forces between the tube and tubesheet are at a minimum. In fact, the pressure cycles that can occur are principally dependent on the temperature conditions of the system. It is not possible to incur a significant pressure cycle without the SGs being at a temperature greater than room temperature. The pull out loads considered in the H\* structural justification cannot occur without the system temperatures for the conditions considered also occurring. The pull out loads for H\* also include significant safety factors of 3 at NOP and 1.4 at DBA conditions and margin against these already conservative loads is demonstrated by the H\* analysis. Thus, it is concluded that a pressure cycle cannot occur without a concurrent temperature increase.

Temperature cycles by themselves cannot result in a mechanism that would apply axial loads and thus, tend to move the tube out of the tubesheet. The classical thermal ratcheting mechanism requires unrestrained axial differential thermal expansion between two components and a mechanism that prevents restoration of the axial motion upon cooldown to its initial starting position. If such conditions existed, repeat of this cycle could result in incremental motion between the two components.

In the SG, since the heat source for the tube is the primary coolant, it could be assumed that the tube expands axially more than the tubesheet for a give temperature increase. This would require a further assumption that there is not friction between the tube and the tubesheet, because the greater growth of the tube occurs radially as well as axially, resulting in much higher contact forces and axial friction forces. It could also be assumed that a tube, once moved axially, is restrained from returning to its initial position upon cooldown by an interaction with the tube support plates. However, this assumption would apply to many tubes, not only an isolated tube among many, because it is based on accumulation of deposits, which is a generalized bulk condition for larger areas of the tube bundle. Therefore, either there is no

mechanism that prevents restoration of the tube to its initial condition, or the axial growth cannot occur because the tube is restrained by the bulk of the tube bundle.

Therefore, the following conclusions are reached:

1. Pressure cycles without concurrent temperature increases, which result in significant restraining forces, are not a credible event.
2. Temperature cycles do not have a credible potential to result in "ratcheting" of the tube out of the tubesheet, because there is no credible mechanism to prevent axial thermal growth from restoration or, alternatively, differential axial ratcheting is prevented by the condition of the tube bundle.
3. The analysis provided in this report provides a conservative assessment that the tubes cannot move in the tubesheet under the worst-case loading conditions, assuming a very large degree of conservatism in the inputs to the analysis.
4. Incremental motion of the tubes due to pressure or temperature cycles is not considered a credible assumption.

### 9.8.3 Assessment of Leakage Potential Under Postulated Tube Slippage

Addressing the four subfactors discussed in Section 9.1.1 above, used to determine the overall leakage factor, there is no change in the pressure and temperature of the fluid due to postulated tube slippage; therefore, the pressure differential and the viscosity ratios do not change. Additionally, the assumption that loss coefficient is constant during all plant conditions remains unchanged; therefore, the loss coefficient ratio above  $H^*$  remains equal to one. It is judged that there would be an insignificant reduction in radial contact pressure due to an end effect at the point of separation of the tube. The same local end effect would be present during both NOP and accident conditions so that the net effect would not require a change to the conservative assumption of a constant loss coefficient. Concerning effective crevice length (i.e., tube hydraulic expansion length with positive contact pressure), if incremental slippage were to occur, the location of the separation in the tube relative to the top of the tubesheet after slippage would be the same during both NOP and at postulated accident conditions. The length of hydraulic expansion with positive contact pressure above the separation is the same during both plant conditions and no change in the ratio of effective crevice length during normal operating and postulated accident condition is required. Therefore, no increase in leakage would occur due to incremental slippage.

Concerning the potential for the occurrence of sudden slippage during accident conditions, this circumstance is not considered to be a credible event for the same reasons that ligament tearing is not considered to be a credible event, and is, in fact, a substantial part of the entire justification of  $H^*$ . As discussed in Section 9.7.1 above,  $H^*$  has been determined using a factor of safety of three relative to the normal operating pressure differential and 1.4 relative to the most severe accident condition pressure differential. Therefore, the internal pressure end cap loads which normally lead to an axial stress in the tube are not transmitted below about 1/3 of the  $H^*$  depth. The only source of load acting to push the separated tube out of the tubesheet is the primary pressure acting on the flanks of the separated tube.

Since the tube is captured within the tubesheet, there are additional forces acting to resist the upward movement of the separated tube. The contact pressure between the tube and the tubesheet results in friction-induced shear stress acting opposite to the direction of travel of a tube. Moreover, the pressure on the flanks is compressive on the tube material adjacent to the plane of the separation, hence a Poisson's ratio radial expansion of the tube wall in the immediate vicinity of the crack plane is induced, acting to restrain the upward movement of the tube. No sudden upward motion of a separated tube is anticipated. As is the case with postulated incremental slippage during normal operating conditions, none of the four subfactors discussed in Section 9.1.1. used to define the overall leakage factor change.

Based on the above, no change in the leakage factors for the design basis accident conditions will occur as a result of slippage of a tube.

#### **9.8.4 Conclusions Regarding Tube Slippage**

It is not considered necessary to monitor for tube slippage for the following reasons:

1. The assumption required to result in the conditions required to apply axial loads to the tubes without also causing constraint against axial motion are not credible.
2. No credible mechanism exists that would restrain a tube from returning to its initial axial position after postulated differential axial motion. Indeed, the conditions necessary for this, (i.e., locked TSPs) would prevent differential axial motion of a single, or several tubes.
3. The value of  $H^*$  is based on the limiting loads and operating conditions, either normal operating conditions or design basis accident conditions. Therefore, if normal operating conditions define the most conservative value of  $H^*$ , by definition, the limiting design basis accident condition cannot cause tube slippage. Conversely, if the design basis accident conditions define the most conservative value of  $H^*$ , there cannot be a worse condition that would cause tube slippage.
4. Incremental slippage does not affect the calculated leakage factors; sudden slippage is not considered to be a credible event.

**9.9 REFERENCES**

- 9-1 LTR-CDME-07-72, "Response to NRC Request for Additional Information Relating to LTR-CDME-05-209-P of the Wolf Creek Generating Station (WCGS) Permanent B\* License Amendment Request," Westinghouse Electric Company LLC, Pittsburgh, PA, April 24, 2007.
- 9-2 LTR-CDME-07-198, "Response to NRC Request for Additional Information Relating to LTR-CDME-07-72 P-Attachment and LTR-CDME-05-209-P of the Wolf Creek Generating Station (WCGS) Permanent B\* License Amendment Request," Westinghouse Electric Company LLC, Pittsburgh, PA, September 24, 2007.
- 9-3 LTR-CDME-08-11 P-Attachment, Rev. 3, "Interim Alternate Repair Criterion (ARC) for Cracks in the Lower Region of the Tubesheet Expansion Zone," Westinghouse Electric Company LLC, Pittsburgh, PA, June 3, 2008.
- 9-4 RIS-2007-20, NRC Regulatory Issue Summary 2007-20, "Implementation of Primary-to-Secondary Leakage Performance Criteria," August 23, 2007.
- 9-5 NRC Letter, "Wolf Creek Generating Station – Issuance of Amendment Re: Revision to Technical Specification 5.5.9 on the Steam Generator Program (TAC No. MD8054)," United States Nuclear Regulatory Commission, Washington, D.C, April 4, 2008.
- 9-6 STD-MC-06-11-P, Rev. 1, "Pressure Profile Measurements During Tube-to-Tubesheet Leakage Tests of Hydraulically Expanded Steam Generator Tubing," Westinghouse Electric Company LLC, Pittsburgh, PA, August 30, 2007, page 33.
- 9-7 Journal of Pressure Vessel Technology, August 2006, Volume 128, Issue 3, pp 408-413.
- 9-8 TH-98-37, Rev. 1, "Vogtle/Yonggwang Tubesheet Crevice Leakage," Westinghouse Electric, Pittsburgh, PA, November 11, 1998.
- 9-9 CN-SGDA-03-119, Rev. 1, "Calculation of Loss Coefficient for Model D5 Steam Generators," Westinghouse Electric Company LLC, Pittsburgh, PA, June 15, 2004.
- 9-10 WCAP-16794-P, "Steam Generator Tube Alternate Repair Criteria for the Portion of the Tube Within the Tubesheet at the Vogtle Unit 1 & 2 Electric Generating Plants," Westinghouse Electric Company LLC, Pittsburgh, PA, October 2007.
- 9-11 Not used.
- 9-12 System Standard 1.3F, Rev. 0, "NSSS Design Transients," Westinghouse Electric, Pittsburgh, PA, March 1978.

- 
- 9-13 System Standard 1.3, Rev. 2, "NSSS Design Transients," Westinghouse Electric, Pittsburgh, PA, April 1974.
  - 9-14 LTR-RCPL-09-41, "Technical Support for the H\* Leakage Analysis," Westinghouse Electric Company LLC, Pittsburgh, PA, March 2009.
  - 9-15 CN-SGDA-05-54 (Proprietary), "H\* Ligament Tearing for Models 44F and 51F Steam Generators," Westinghouse Electric Company LLC, Pittsburgh, PA, November 2005.
  - 9-16 EPRI Tube Integrity Tools Theory Manual, Final Report, May 2006.
  - 9-17 LTR-SGDA-06-108 (Proprietary), "Data and Analysis Methodology in Support of Axial Ligament Tearing Model," Westinghouse Electric Company LLC, Pittsburgh, PA, June 29, 2006.
  - 9-18 WCAP-15932-P (Proprietary), Rev. 1, "Improved Justification of Partial-Length RPC Inspection of Tube Joints of Model F Steam Generators of Ameren-UE Callaway Plant," Westinghouse Electric Company LLC, Pittsburgh, PA, May 2003.
  - 9-19 WCAP-9230, "Report on the Consequences of a Postulated Main Feedline Rupture," Westinghouse Electric, Pittsburgh, PA, January 1978.
  - 9-20 ANL Progress Report, September 2008.
  - 9-21 CN-SGMP-09-7, "Design and Faulted Transient Primary-to-Secondary Side Pressure Differential Calculations to Support H\*," Westinghouse Electric Company LLC, Pittsburgh, PA, March 2009.

**Table 9-1 Reactor Coolant System Temperature Increase Above Normal Operating Temperature Associated With Design Basis Accidents**  
 (References 9-12 and 9-13)

SG Type	Steam Line/Feedwater Line Break <sup>1</sup>		Locked Rotor (Dead Loop)		Locked Rotor (Active Loop)		Control Rod Ejection	
	SG Hot Leg (°F)	SG Cold Leg (°F)	SG Hot Leg (°F)	SG Cold Leg (°F)	SG Hot Leg (°F)	SG Cold Leg (°F)	SG Hot Leg (°F)	SG Cold Leg (°F)

a,c,e

\* Best estimate values for temperature during FLB<sup>1</sup>/SLB are used as discussed in Section 9.2.3.1.

<sup>1</sup> FLB is not part of the licensing basis for Model 44F SGs

**Table 9-2 Reactor Coolant Systems Peak Pressures During Design Basis Accidents**  
 (References 9-12 and 9-13)

SG Type	Steam Line Break (psia)	Feedwater Line Break (psia) <sup>1</sup>	Locked Rotor (psia)	Control Rod Ejection (psia)	a,c,e

<sup>1</sup> FLB is not part of licensing basis for Model 44F SGs

**Table 9-3 Model F Room Temperature Leak Rate Test Data**

a,c,e

Test No.	EP-31080	EP-30860	EP-30860	EP-29799	EP-31330	EP-31320	EP-31300	

**Table 9-4 Model F Elevated Temperature Leak Rate Test Data**

Test No.	EP-31080	EP-31080	EP-30860	EP-30860	EP-29799	EP-29799	EP-32800	EP-32800	EP-31300	EP-31300	

a,c,e







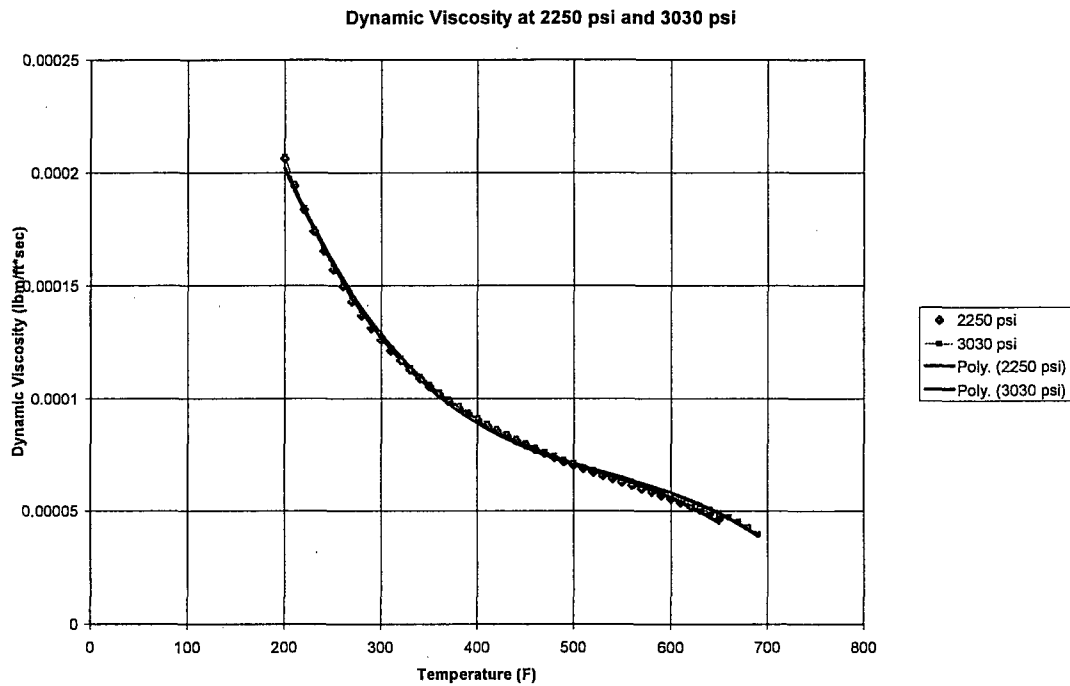


**Figure 9-1 Dynamic Viscosity as a Function of Temperature**

Note: Dynamic viscosity data from [Isothermal Properties of Water, National Institute of Standards and Technology, Online Database, webbook.nist.gov](http://webbook.nist.gov).

a,c,e



**Figure 9-2 Plot of Model D and Model F Total Data Set for 70°F and 600°F**  
(Reproduced from Reference 9-10)

a,c,e



**Figure 9-3 Model 44F SLB RCS Pressure-Time History Graph for a 2 Loop Plant**

a,c,e



**Figure 9-3a Model 44F SLB RCS Temperature-Time History Graph For a 2 Loop Plant (Hot Leg)**

a,c,e



**Figure 9-3b Model 44F SLB RCS Temperature–Time History Graph For a 2 Loop Plant  
(Cold Leg)**

a,c,e



**Figure 9-4 Model 44F SLB RCS Pressure-Time History Graph For a 3 Loop Plant**



**Figure 9-4a Model 44F SLB RCS Temperature-Time History Graph For a 3 Loop Plant (Hot Leg)**



**Figure 9-4b Model 44F SLB RCS Temperature-Time History Graph  
For a 3 Loop Plant (Cold Leg)**

**Figure 9-5 This Figure Intentionally Left Blank**

**Figure 9-6 This Figure Intentionally Left Blank**

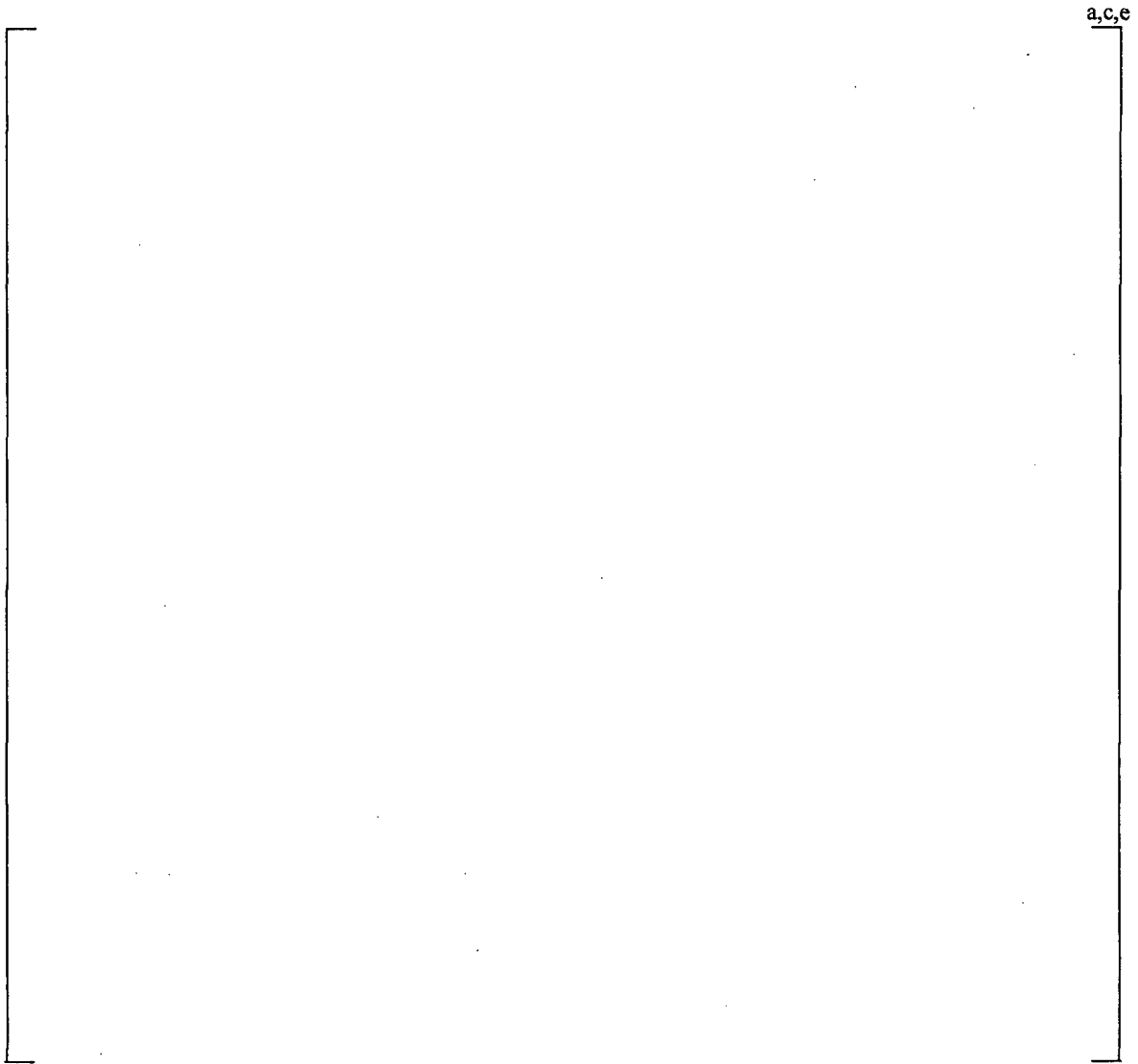


**Figure 9-7 Example Leakage Test Schematic (Model F Testing Only)**

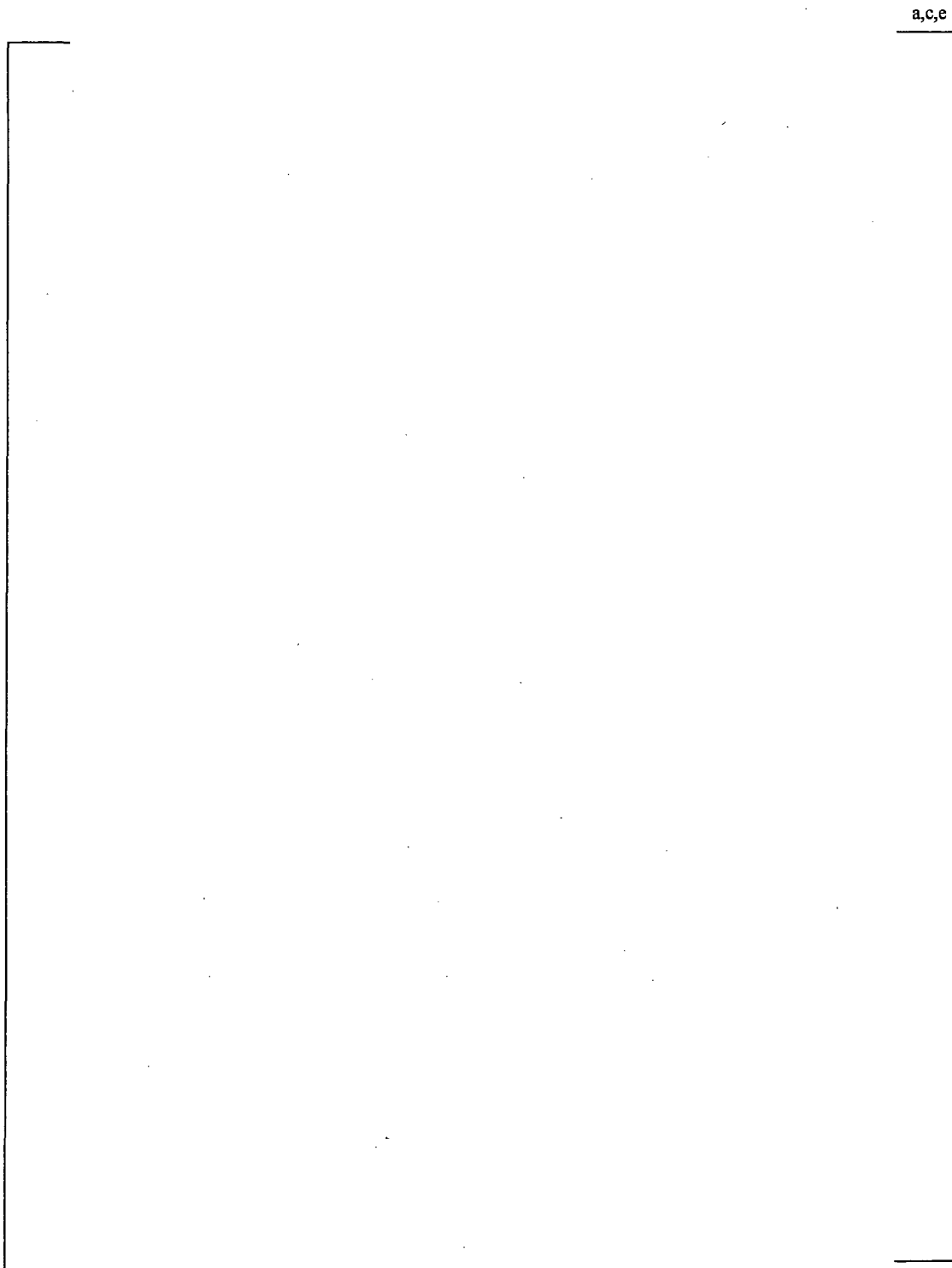


**Figure 9-8 Schematic for the Test Autoclave Systems for Leak Rate Testing (Model D5 Testing Only)**

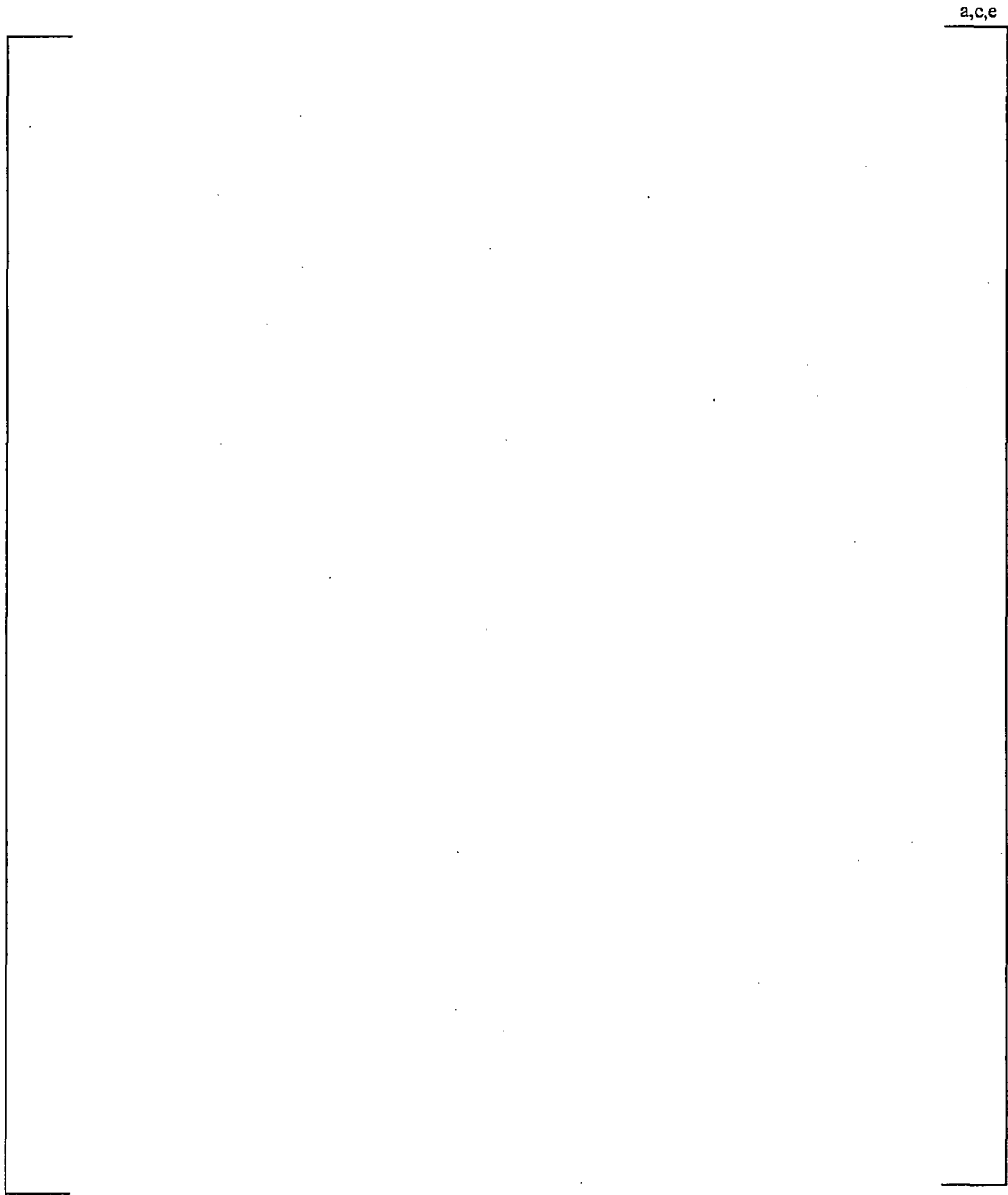


**Figure 9-9 Example Tube Joint Leakage Test Configuration**

a,c,e



**Figure 9-10 Model F Room Temperature Leak Rate Test Results**  
(Curves shown correlate with expansion pressures noted in the legend)



**Figure 9-11 Model F Elevated Temperature Leak Rate Test Results**  
(Curves correlate to expansion pressures shown in the legend)

a,c,e



**Figure 9-12 Model F Room Temperature Leak Rate Ratio Versus Differential Pressure Ratio Comparison**

(Curves correlate with expansion pressures in legend)



**Figure 9-13 Model F Elevated Temperature Leak Rate Ratio Versus  $\Delta P$  Ratio Comparison (600°F)**



a,c,e

**Figure 9-14 Results of Test-by-Test Loss Coefficient (K) Regression on Contact Pressure for Model D5 Test Specimens**

a,c,e

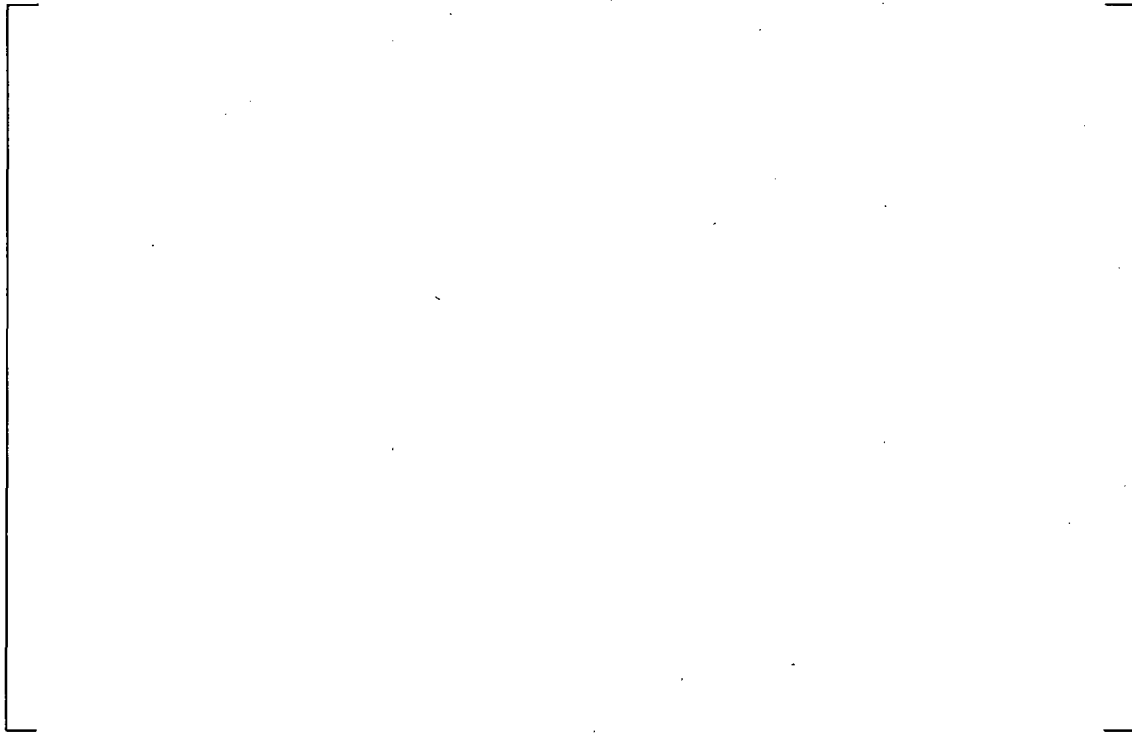


**Figure 9-15 Results of Test-by-Test Loss Coefficient (K) Regression on Contact Pressure for Model F Test Specimens**

a,c,e



**Figure 9-16 Typical Reactor Coolant Pump Locked Rotor and Control Rod Ejection Delta P for Model 44F SGs**

## 10.0 SUMMARY AND CONCLUSIONS

This report provides a technical justification for re-defining the primary pressure boundary in the steam generators (SG). The original design methods that are reflected in the applicable American Society of Mechanical Engineers (ASME) Code Stress Reports for the Model F, Model D5, Model 44F and Model 51F SGs rely on the tube end welds as the pressure boundary without taking credit for the hydraulic expansion joint between the tubes and the tubesheet. The technical justification provided in this report provides a conservative analysis that shows that the hydraulic expansion joint is capable of functioning as the primary pressure boundary without relying on any aspect of the tube end weld, either as a structural restraint for retaining the tubes in the tubesheet or as a barrier against unacceptable leakage. The title of the technical justification is H\* (H-star).

Since 2004, when stress corrosion cracking (SCC) in the tubesheet expansion region was first reported among SGs with hydraulically expanded thermally treated Alloy 600 (A600TT) tubing, multiple plants have inspected throughout the full thickness of the tubesheet with rotating pancake coils (RPC). Since the first report of SCC in the tubesheet expansion region, only one other plant identified SCC in the tubesheet expansion region above the tube-end welds as an isolated incident. However, although not great in number, additional indications of SCC have been reported since the Spring 2008 outages at or within 1 inch of the ends. Unless an alternate repair criterion (ARC) is approved, industry guidelines require that tubes with crack-like indications be plugged and that the inspection scope be expanded, potentially including all SGs in the plants. H\* provides a conservative technical justification that a length of undegraded tube, measured from the top of the tubesheet, provides structural and leakage integrity in accordance with the industry requirements without relying on the tube end welds or the lower several inches of the tubes to provide these functions. The value of H\* defines the necessary length of undegraded tubing. Application of H\* permits keeping acceptable tubes in service, reduces the inspection requirements and requirements for inspection expansions without any impact on public safety.

### 10.1 RECOMMENDED VALUE OF H\*

The recommended value of H\* for application to the Model 44F SGs is 13.31 inches. The interpretation of this recommendation is that inspection with a qualified probe to detect stress corrosion cracking in the tubesheet region is required only from the top of the tubesheet (TTS) to 13.31 inches below the TTS. For practical purposes, it is assumed that the tube below the H\* value does not exist, or that any degradation below 13.31 inches from the TTS is acceptable, provided that there is no degradation observed in the span from the TTS to 13.31 inches below the TTS.

### 10.2 H\* CONCEPT AND EVOLUTION

In concept, H\* is similar to other technical justifications that have been licensed for implementation, such as F\* (for hard rolled tubesheet joints), W\* (for explosively expanded tubesheet joints using the WEXTEx process), and C\* (for explosively expanded tubesheet joints using the Combustion Engineering "Expansion" process). The technical bases for all of these alternate repair criteria (ARC) are similar in that the interaction forces between the tube and tubesheet resulting from the initial expansion process and from the thermal and pressure-induced forces under normal operating conditions (NOP) and design basis accident (DBA) conditions are relied upon to prevent tube pull out and to limit leakage from the primary

to the secondary side of the SG to acceptable limits. The difference among the H\*, F\*, W\* and C\* ARC lies in the relative tightness of the tubesheet joints achieved by the original manufacturing processes.

This technical justification was preceded by other analyses which had the same objective of replacing the tube end weld as the primary pressure boundary with the hydraulic expansion joint. The prior analyses have undergone extensive reviews, and the lessons learned from these reviews are incorporated into the current analysis. A summary of prior technical review issues is provided in this report to capture the lessons learned and to provide comprehensive documentation of the evolution of H\* to its current embodiment.

### **10.3 DESIGN REQUIREMENTS**

The applicable design requirements are those specified in industry performance criteria contained in NEI 97-06, Revision 2 and its sub-tier mandatory and recommended guidelines. The specific design requirements applicable to the H\* analyses are:

1. The applicable loads shall be the greater of 3 times the normal operating pressure differential or 1.4 times the accident-induced pressure differential across the tube.
2. DBA (other than a tube rupture) induced primary-to-secondary leakage shall not exceed the leakage assumed in the accident analysis applicable to the specific plants that implement H\* in terms of total leakage rate and leakage rate for an individual SG.
3. It is required that the recommended value of H\* for every tube in the bundle meets a statistical probability of 95% at 50% confidence. This is known as the "whole bundle" probability.

Because the industry guidelines are designed to address prevention of tube burst, they do not directly apply to the tubesheet expansion region where burst is not possible due to the constraint provided by the tubesheet. Nevertheless, the criteria to prevent burst are conservatively applied by treating "failure to meet H\*" as a burst.

### **10.4 DESIGN CONDITIONS**

Several different models of SGs are among the H\* candidate population. These include the Model F, Model D5, Model 44F and Model 51F SGs. Except for the Model 51F SGs, multiple plants are represented among each sub-population. The approach utilized in this justification is to consider the design and operating conditions for each plant and to define the plant with the most limiting conditions for H\* among each sub-population. Consequently, four reports for H\* are provided that have large overlap of contents for methodology, but specific content for each model of SG. This report is specific to the Model 44F SG.

For all models of SGs, the design and operating conditions for normal operation and all design basis accidents that include leakage are evaluated. These include steam line break (SLB), feedwater line break (FLB), control rod ejection (CRE) and locked rotor (LR). The limiting conditions among these are the basis for the applied loads to the tubes and for the end cap loads.

The population of plants with Model 44F SGs includes 2-loop and 3-loop plants. The bounding plant is a 2-loop plant because of the specific operating conditions of that plant that include a significant power uprating. Therefore, the results in this report are significantly more conservative for the other Model 44F plants than the significant conservatism already included for the bounding plant.

## 10.5 MATERIAL PROPERTIES

The principal factor that enables  $H^*$  is differential thermal expansion between the tube and the tubesheet. It is assumed that, as a minimum, the as-manufactured condition of the tubes in the tubesheet have zero clearance contact with the tubesheet after the hydraulic expansion process. As the temperature increases to operating conditions, the tube material, thermally treated Alloy 600 (A600TT), expands more than the tubesheet material (SA508), resulting in a significant increase in the contact forces between the tubes and the tubesheet.

Extensive testing summarized in Section 3.0 and Appendix B show that differential thermal expansion between the tube and the tubesheet will always occur, even at significant levels of uncertainty for both materials simultaneously. The tests performed under the  $H^*$  program significantly increased the available database for coefficient of thermal expansion (CTE) for A600 and SA508 materials. The data also show that the use of the mean values of CTE from the ASME Code (2007 edition) to determine the limiting  $H^*$  value is conservative. The standard deviations of CTE for A600 and SA508 are 2.33% and 1.44%, respectively, of the at-temperature mean value. (A standard deviation of [ ]<sup>a,c,e</sup> % is conservatively used for the CTE of SA508 in the structural analysis of the tubesheet.) The data also imply that the bulk of this uncertainty is the result of measurement error, and that the true variance of these properties is actually much smaller than the values noted above. Reductions of the variance of CTE to represent the true values would result in a significant decrease in the recommended value of  $H^*$ .

## 10.6 RESIDUAL CONTACT PRESSURE

Prior, and current, test data show that the hydraulic expansion process results in a positive value of contact pressure between the tubes and the tubesheet. However, the technical justification in this report conservatively assumes that the contact pressure due to only the hydraulic expansion process, known as residual contact pressure (RCP), is zero. (Test data provided in Section 7.0 show that positive RCP exists for hydraulic expansions. Negative values of RCP are not possible.) The assumption of zero RCP is conservative because any value of RCP will reduce the recommended value of  $H^*$ .

## 10.7 STRUCTURAL ANALYSIS

The structural analysis included in this report is a significant evolution from the prior analyses. The current analysis is based on a three-dimensional (3D) finite element analysis (FEA) of the tubesheet complex, which includes the tubesheet, stub barrel, channelhead and divider plate. Prior analyses utilized a two-dimensional axisymmetric model to calculate the tubesheet radial and axial deflections. The current 3D FEA approach shows that  $H^*$  results prior to 2008 were significantly conservative. The 3D FEA analysis results were compared against an independently created model of the same geometry and shown to provide essentially the same results when the same inputs were utilized.

The mean value of  $H^*$  is calculated to be 3.87 inches (including adjustments the location of the bottom of the transition and for the applicable thermal distribution correction) for the limiting operating condition, NOP. This value applies to the limiting radius in the worst sector of the tubesheet, which is the sector of tubes in approximately a 5 degree arc from the perpendicular to the divider plate. All tubes at other locations in the tubesheet have a smaller value of  $H^*$ . This is a significant conservatism because the probabilistic evaluation is based on this worst-case mean value of  $H^*$ .

There is much conservatism included in the structural analysis as summarized in Section 1.0. The following are the most significant conservatisms:

1. The mean value of  $H^*$  is based on the location of the limiting radius of the tubesheet in the limiting sector of the tubesheet for the limiting SG operating condition. All other locations on the tubesheet have a lower value of  $H^*$ .
2. The analysis assumes that the divider plate has no connection to the tubesheet. It is shown that this assumption results in the largest values of  $H^*$ .
3. The value of the coefficient of friction utilized is 0.2. A significantly greater coefficient of friction could be justified based on the available literature. A greater coefficient of friction would result in a smaller value of  $H^*$ .
4. Boundary conditions are applied to yield the most conservative (largest) values of  $H^*$ .
5. The conditions of the bounding plant in the population of Model 44F SGs are used for all Model 44F plants.

## 10.8 LEAKAGE ANALYSIS

The leakage analysis is based on application of the Darcy model for flow through a porous medium. The approach used is to determine the ratio of accident-induced leakage to the observed leakage under normal operating conditions. These ratios are termed "Leakage Factors". The applicable maximum leakage ratio for all plants is 2.03 and is based on the peak pressure differential from a postulated FLB event for a Model F SG, which is shown to be a plant cooldown event when taking credit for operator action. The maximum leakage ratio for the Model 44F population is 1.82.

The leakage factor is applied to the normal operating leakage that is associated with the tubesheet expansion region in the condition monitoring and operational assessments. No increase in the accident-induced leakage assumed in the safety analysis results with the implementation of the leakage factor approach; however, an adjustment to the administrative shutdown leakage limit may be required depending on the NOP leakage observed and the possible sources of leakage in the SG. The leakage factor for a postulated FLB bounds the leakage factor required for a postulated SLB event because the pressure differential across the tubesheet is greater during a postulated FLB versus a SLB event; both events result in a plant cooldown event. For most plants, due to the short duration of the transients, no leakage factors are required for a postulated locked rotor or control rod ejection events. The leakage factor for a postulated FLB is conservatively used for those plants with a locked rotor with a stuck open SG power operated relief valve (PORV) as part of the licensing basis.

It is important to note that the implementation of  $H^*$  does not require that the maximum leakage factor be used by plants that have a lower leakage factor; however, the maximum factor provides a conservative basis for performing the condition monitoring and operational assessments.

## 10.9 PROBABILISTIC ANALYSIS

Four input parameters directly affect the calculation of  $H^*$  if it is assumed that RCP is equal to zero. Other variable parameters are introduced if a non-zero value of RCP would be included in the analysis. The applicable variables are the CTE of the tube and tubesheet materials (A600 and SA508) and Young's Moduli of the tube and tubesheet materials. Sensitivity analyses have shown that the variation of Young's Modulus of both the tube and tubesheet materials has insignificant effect on  $H^*$ . The principal variable affecting  $H^*$  is the CTE of the tube material, A600.

Sensitivity analyses also indicate that there is an interaction between the CTE of the tube and tubesheet materials when expressed as a variation of  $H^*$ . The effect of the interaction is that the value of  $H^*$  increases more when both parameters are varied than the cumulative effect on  $H^*$  when each parameter is varied separately. However, even for extreme variations of these parameters (3 to 4 standard deviations from the mean in the direction of increasing  $H^*$ ), a value of  $H^*$  exists; thus, there is no credible event that would invalidate the  $H^*$  concept. No other interactions among the four effective parameters were identified.

Standard binomial statistical analysis shows a 4.157 standard deviation ( $\sigma$ ) variance is required to achieve 95% probability at 50% confidence for a population of 3214 tubes, i.e., the full tube complement of a Model 44F SG. The variations of  $H^*$  were calculated for a number of assumptions of parameter variations up to and including 5 standard deviations and also specifically including 4.157 standard deviations. These sensitivity analyses showed that the variation of  $H^*$  was not linear for the parameter input assumptions made.

Both a simplified statistical approach and a fully probabilistic approach using a Monte Carlo simulation technique were applied for the  $H^*$  analysis as permitted by the industry Integrity Assessment Guidelines for meeting the probabilistic criteria of 95% probability at 50% confidence for every tube in the tube bundle. In the simplified statistical approach, the uncertainties are combined by the square root of the sum of the squares (SRSS) method. In the fully probabilistic approach, simulations are performed by randomly sampling from influence functions of  $H^*$  for each of the four variables that directly impact the  $H^*$  calculations, assuming that RCP is equal to zero.

The change in  $H^*$  due to positive variation of a parameter may be different than the change in  $H^*$  due to a negative variation of the same parameter. In the probabilistic analysis of  $H^*$ , only the parameter variations that adversely affect the value of  $H^*$  (i.e., increase the value of  $H^*$ ) were conservatively used.

The SRSS is the preferred approach to determining the 95/50 whole bundle value of  $H^*$  because of its simplicity. Using the 4.157 ( $\sigma$ ) parameter input variation of  $H^*$  directly, the 95% probability at 50% confidence value of  $H^*$  for the whole bundle is 13.31 inches.

Different extreme value analyses were performed based on the Monte Carlo simulation approach under various assumptions of parameter variability and sampling schemes that recognized that the number of

tubesheets in the population of H\* candidate plants is limited. All of the extreme value cases considered exceed the probabilistic requirement of 95/50 for the entire bundle. Therefore, although some of these extreme value cases yielded H\* values slightly greater than the recommended value of H\* of 13.31 inches as expected, the results from all of the extreme value cases support the recommended value of 13.31 inches.

#### **10.10 TUBE SLIPPAGE**

The technical justification for H\* concludes that at a high level of confidence at the value of H\* specified, 13.31 inches for the top of the tubesheet, the tubes are fully restrained against motion under very conservative design conditions and very conservative analysis assumptions. Therefore, tube slippage is not a credible event for any tube in the bundle. It is concluded, based on the analyses in this report, that no significant technical case can be made that monitoring for tube slippage is necessary.

## APPENDIX A TUBE PULL OUT TESTING DATA

In reviewing Wolf Creek Nuclear Operating Corporation's request for a license amendment for H\*/B\*, the NRC staff determined that the utility had not provided information which was necessary to support a conclusion that the tubes would have adequate integrity if flaws were to occur in the region of the tube not inspected. One area of concern identified by the NRC staff was that only limited pull out data exists upon which the residual contact pressures are estimated. The NRC staff stated in Reference A-1 that WCNOG had not provided information to establish whether the pull out test specimens used to determine residual contact pressure adequately envelop the range of values of these parameters which might be encountered in the Wolf Creek Generating Station steam generators. In particular, in item numbers 4 and 5 identified in Reference A-1, the NRC staff requested test specimen dimensions for R12C08, R11C08, R12C07, R11C07, R10C08, and R10C07 similar to what has been provided for tube pull out specimens 33625-09 through 33625-15 in response to RAI numbers 1 and 2 in LTR-CDME-07-72. Additionally, the NRC staff requested the yield strength for each of the eight test specimens.

The objective of this appendix is to provide all available information (References A-2, A-3, A-4, and A-5) for each of the fourteen room temperature test specimens previously used to establish residual contact pressure in the development of the H\* criterion. Information on wall thicknesses and yield strength is provided for the test specimens for 1 1/16, 3/4 and 7/8 inch outer diameter tubes in Tables A-1, Model F Test Specimens, Table A-2, Model 44F and 51F Test Specimens and Table A-3, Model D5 Test Specimens.

### References:

- A-1 NRC Letter, "Wolf Creek Generating Station – Withdrawal of License Amendment Request on Steam Generator Tube Inspections (TAC No. MD1097)," United States Nuclear Regulatory Commission, Washington D.C., February 28, 2008.
- A-2 NCE-88-271, "Assessment of Tube-to-Tubesheet Joint Manufacturing Processes for Sizewell B Steam Generators Using Alloy 690 Tubing," November 1988.
- A-3 STD-DP-1997-8015, Rev. 0, "Data Package for Leak Testing of Vogtle Unit 1 Steam Generator Tube-to-Tubesheet Joint for STD-TP-1997-7951 Rev. 1," June 18, 1997.
- A-4 DP-SGDA-05-2, "Data Package for H-Star Pull Test of 7/8 Inch Tubing from Simulated Tubesheet PA-MS-0199 WOG Program for Steam Generator Models 44F and 51F," November 30, 2005.
- A-5 DP-SGDA-03-1, "Model D5 Tube-to-Tubesheet Joint Determination of Pullout Resistance for H-Star Program for Comanche Peak 2, Catawba 2, Byron 2 and Braidwood 2," August 11, 2003.



**Table A-2 Model 44F and 51F Test Specimen Pull Out Data (7/8 Inch Diameter Table)**

Specimen Number	Test Temperature (°F)	R <sub>i</sub> (a) (in)*	R <sub>o</sub> (b) (in)*	R <sub>o</sub> (c) (in)	Expansion Length (in)	Pull out Force (lbf)**	F/L (lbf/in)**	Tube Yield Strength (ksi)	Hydraulic Expansion Pressure (psi)	a,b,c

**Table A-3 Model D5 Test Specimen Pull Out Data (3/4 Inch Diameter Tubes)**

Specimen Number	Test Temperature (°F)	R <sub>i</sub> (a) (in)	R <sub>o</sub> (b) (in)	R <sub>o</sub> (c) (in)	Expansion Length (in)	Pull out Force (lb)**	F/L (lb/in)*	Tube Yield Strength (ksi)	Hydraulic Expansion Pressure (psi)

a,b,c

---

**APPENDIX B**  
**AN EVALUATION OF THE STATISTICAL VARIABILITY IN**  
**COEFFICIENT OF THERMAL EXPANSION PROPERTIES OF SA-508**  
**AND ALLOY-600**

Report No. WEST-13-402, Rev. 1  
Project No. WEST-13  
December, 2008

**An Evaluation of the Statistical  
Variability in Coefficient of  
Thermal Expansion Properties of  
SA-508 and Alloy-600**

*Prepared for:*

Westinghouse Electric Corp.  
Waltz Mill, PA  
PO Number 4500272299

*Prepared by:*

Structural Integrity Associates, Inc.  
Centennial, Colorado

*Prepared by:*



Peter C. Riccardella

Date: 12/24/08

*Reviewed by:*



Dilip Dedhia

Date: 12/24/08

*Approved by:*



Peter C. Riccardella

Date: 12/24/08

**REVISION CONTROL SHEET**

Document Number: WEST-13-402

Title: An Evaluation of the Statistical Variability in Coefficient of Thermal Expansion Properties of SA-508 and Alloy-600

Client: Westinghouse

SI Project Number: WEST-13

Quality Program:  Nuclear  Commercial

Section	Pages	Revision	Date	Comments
All	All	0	10/17/08	Initial Issue
2,3 3 4 Appendix	2-2, 2-3, 3-1, 3-2 3-3, 3-4, 3-5, 3-13, 3-14 4-1 A-1 to A-6	1	12/24/08	Revised to delete PMIC data for SA-508 from analysis Revised to address strain hardened A-600 retests Revised conclusions for above changes New Appendix: justification for excluding PMIC SA-508 data

Table of Contents

<u>Section</u>	<u>Page</u>
<b>1.0 INTRODUCTION.....</b>	<b>1-1</b>
<b>2.0 CTE DATA AND DATA SOURCES .....</b>	<b>2-1</b>
<b>3.0 ANALYSES .....</b>	<b>3-1</b>
3.1 Statistical Analysis of Uncertainties .....	3-1
3.2 Evaluation of Within-Heat Variability.....	3-2
3.3 Effect of Strain Hardening on Alloy-600 CTE.....	3-3
3.4 Overall Mean versus ASME Code Curves .....	3-3
<b>4.0 CONCLUSIONS .....</b>	<b>4-3</b>
<b>5.0 REFERENCES.....</b>	<b>5-3</b>
<b>APPENDIX A .....</b>	<b>3</b>

List of Tables

<u>Table</u>	<u>Page</u>
Table 1-1 Sources of CTE Data Used in the Evaluation .....	2-2

List of Figures

<u>Figure</u>	<u>Page</u>
Figure 2-1. CTE Data from various sources for A-508 Low Alloy Steel.....	2-3
Figure 2-2. CTE Data from Various Sources for Alloy 600.....	2-4
Figure 2-3. Plots of New ANTER Data for Two Heats of A-508 (Typical) .....	2-5
Figure 2-4. Plots of New ANTER Data for Two Heats of Alloy 600 (Typical).....	2-6
Figure 3-1. Normal and Lognormal Probability Plots for A-508 CTE Residuals and Associated Linear Curve Fits .....	3-3
Figure 3-2. Recommended Normal Distribution of CTE Data for SA-508.....	3-3
Figure 3-3. Normal and Lognormal Normal Probability Plot for Alloy 600 CTE Residuals and Associated Linear Curve Fit .....	3-3
Figure 3-4. Recommended Normal Distribution of CTE Data for Alloy 600.....	3-3
Figure 3-5. Comparison of Within-Heat Scatter of Multi-Sample Tests on a Heat of SA-508 (upper plot) with Multiple Tests of a Single Sample from the Same Heat (lower plot).....	3-3
Figure 3-6. Comparison of Within-Heat Scatter of Multi-Sample Tests on a Heat of Alloy 600 (upper plot) with Multiple Tests of a Single Sample from the Same Heat (lower plot).....	3-3
Figure 3-7. Illustration of the Apparent Effect of Strain Hardening on Alloy 600 CTE Data. Heat Means of Strain Hardened versus Non Strain Hardened Data – Initial Testing.....	3-3
Figure 3-8. Further Study of the Effect of Strain Hardening on Alloy 600 CTE Data: Means of Strain Hardened versus Non Strain Hardened versus Repeat Strain Hardened Tests .....	3-3
Figure 3-9. Compilation of CTE Data from Various Sources for Alloy 600, with Original Test Data Replaced by Repeat Strain Hardened Test Data (Plot is indistinguishable from Figure 2-2 thus demonstrating that strain hardening has a negligible effect.) .....	3-3
Figure A-1 – Raw Test Data (in Micro-strain) from several SA-508 CTE Tests.....	3
Figure A-2 – Expanded View of Low Temperature End of Figure A-1.....	3
Figure A-3 – CTE Computed from Test Data of Figure A-1 .....	3

## 1.0 INTRODUCTION

The ASME B&PV Code (Section II) [1] provides material properties for use in design and analysis of pressure vessels and other components, including thermo-physical properties such as thermal expansion, thermal conductivity and thermal diffusivity. Variability in these properties is recognized, and the Code states that these properties are considered typical, and should be considered to have an associated uncertainty of  $\pm 10\%$  [1, 2]. However, the meaning of this uncertainty range is not defined in statistical terms.

The purpose of this report is to document a statistical evaluation of Coefficient of Thermal Expansion (CTE) data for SA-508 Grade 2 and thermally treated Alloy-600 tube material. Data obtained from a number of sources are included in the evaluation, including literature sources as well as extensive new laboratory CTE data developed specifically for this purpose. The evaluation results in recommended statistical distributions of this property for the two materials.

This study was performed to support the technical justification for re-defining the primary pressure boundary from the tube-end weld to the hydraulic expansion joint in Westinghouse designed steam generators with hydraulically expanded tubing. Because this technical justification relies significantly on differential thermal expansion between the tube and the tubesheet, and regulatory acceptance criteria are stated in terms of probabilities, it is necessary to establish the mean and probabilistic variability of the CTE.

## 2.0 CTE DATA AND DATA SOURCES

Figures 2-1 and 2-2 present compilations of CTE data for the two materials compared to the current ASME Section II curve with  $\pm 10\%$  error bands. Data are reported from various sources listed in the figure legends and represent mean CTE between 70°F and the plotted temperature. A summary of the various data sources is provided in Table 1.

Data were obtained from several literature sources, as identified in Table 1. The current ASME Section II design curves are assumed to represent a single data set, even though they likely represent means of several data sets. In addition to the literature data, the analyses considered

extensive new CTE testing performed specifically for this program under contract to Westinghouse by ANTER laboratories [5]. These tests included multiple samples from nine heats of Alloy-600 steam generator tubing plus four heats of A-508 low alloy steel. The Alloy-600 heats were tested in both the as-received form as well as in a strain hardened condition performed to simulate that produced by hydraulic tube expansion. In all, over 100 new CTE tests were performed at ANTER on thirteen heats of material.

Typical plots of the new ANTER data for A-508 and Alloy 600 materials are contained in Figures 2-3 and 2-4.

Table 1-1 Sources of CTE Data Used in the Evaluation

<b>Alloy-600:</b>	<b>SA-508 Grade 2:</b>
<b>Literature Data Sources:</b> ASME Section II, 2007 Edition [1] Specialty Metals Datasheet [3] Aero SM Handbook [3] Mil Handbook 5 [3] NSMH Values[3] Miscellaneous Datasheets [3] ANL ANTER [7] ANL PMIC [6]	<b>Literature Data Sources:</b> ASME Section II, 2007 Edition [1] ANL ANTER [7]
<b>New ANTER Data [5]:</b> 9 heats (3 to 4 samples each) Multiple Tests (single sample) Strain Hardened Specimens (Same 9 heats, 3 to 4 samples each)	<b>New ANTER Data [5]:</b> 4 heats (10 samples each) Multiple Tests (single sample)

An additional dataset for SA-508, provided by ANL and tested at Precision Measurements and Instruments Corporation (PMIC) in both air and vacuum [6], was found to be highly inconsistent with the balance of the data for this material. An assessment of these data was performed, starting with the raw data, and is documented in Appendix A. This assessment concluded that there are anomalies in the data that make it virtually unusable, and that dataset was therefore excluded from this analysis.

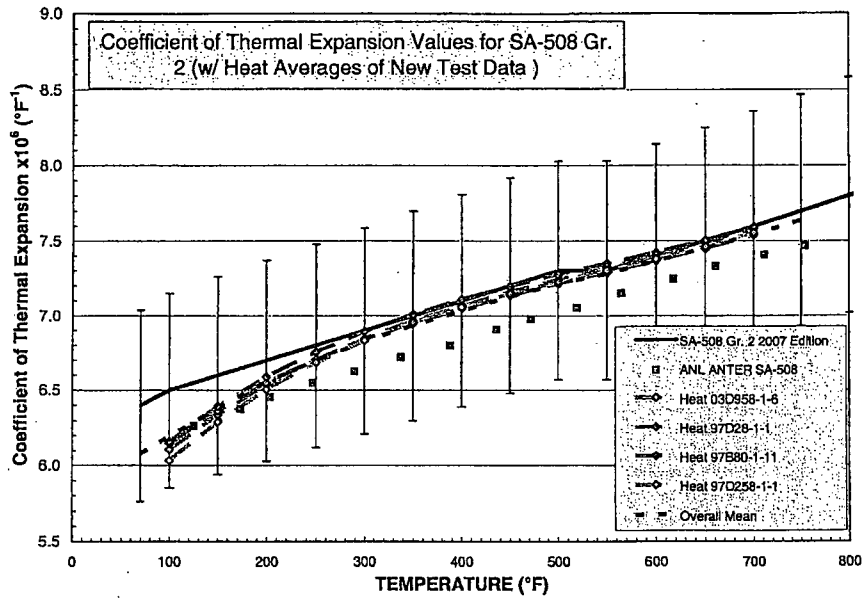


Figure 2-1. CTE Data from various sources for A-508 Low Alloy Steel

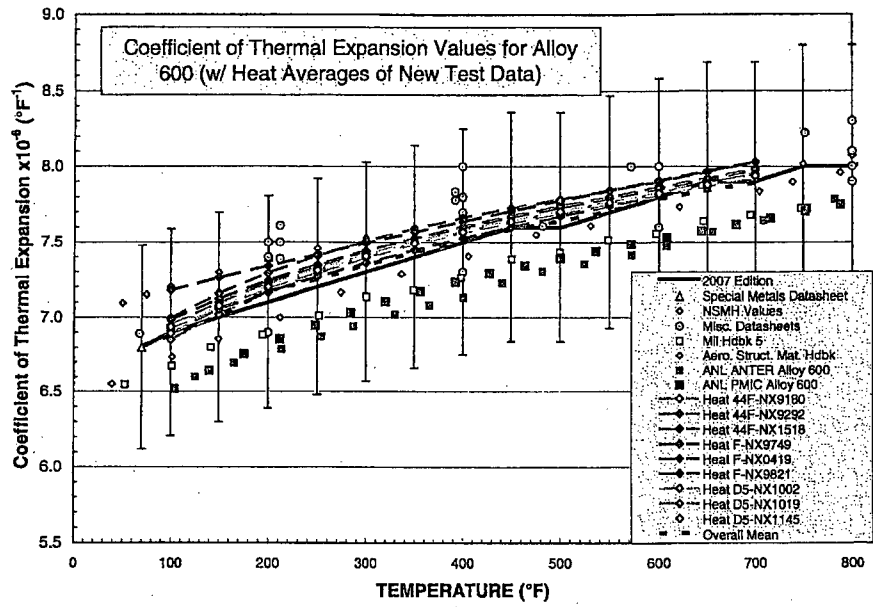


Figure 2-2. CTE Data from Various Sources for Alloy 600

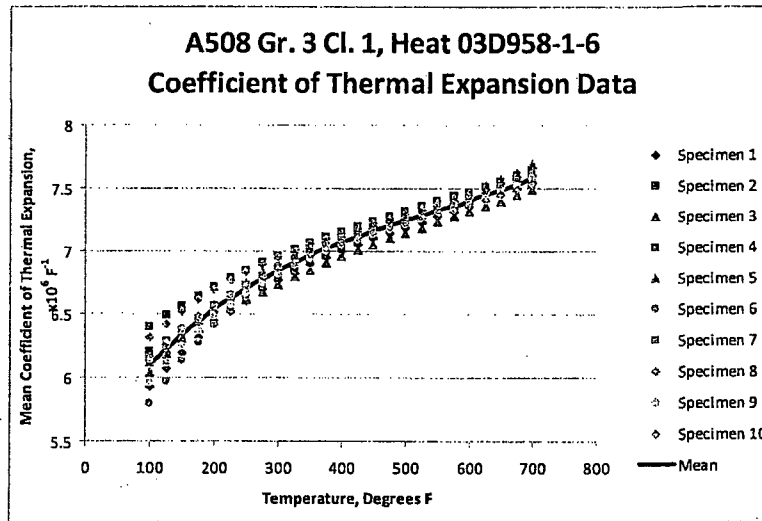
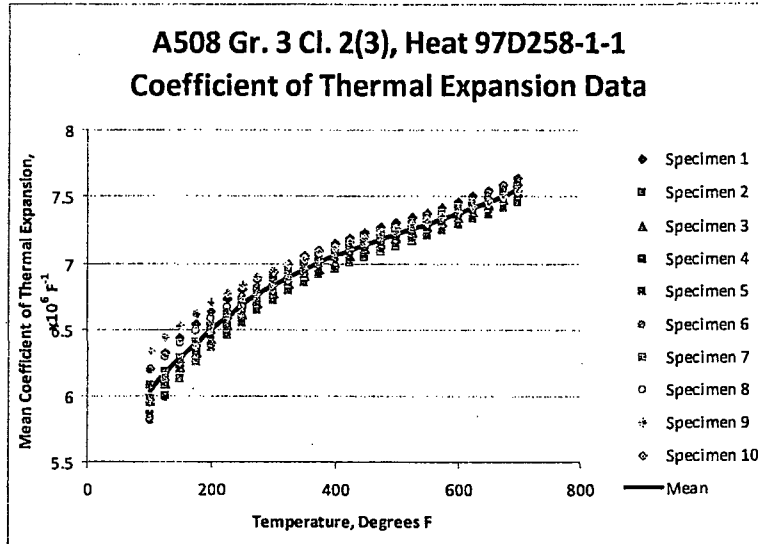


Figure 2-3. Plots of New ANTER Data for Two Heats of A-508 (Typical)

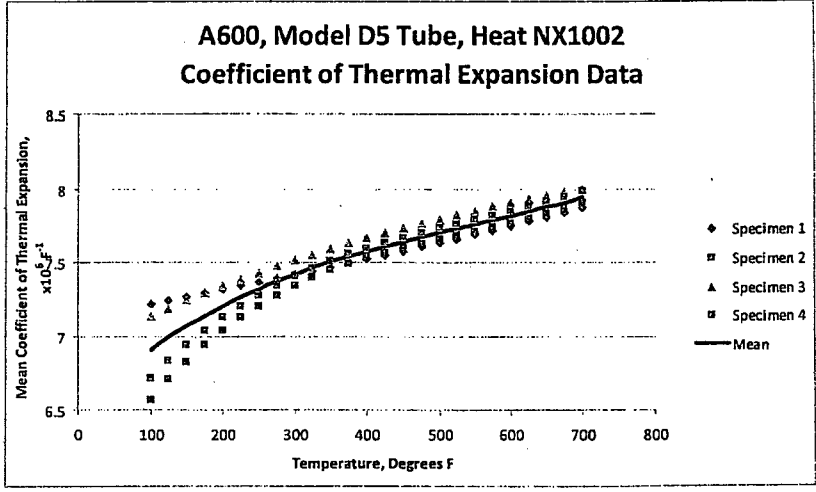
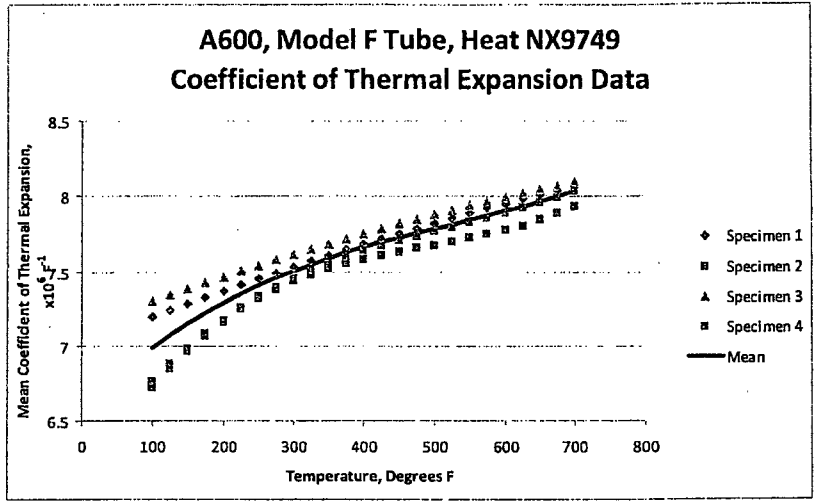


Figure 2-4. Plots of New ANTER Data for Two Heats of Alloy 600 (Typical)

### 3.0 ANALYSES

#### 3.1 Statistical Analysis of Uncertainties

The data in Figures 2-1 and 2-2 were evaluated using a standard probability plotting technique [4], which is a graphical technique for assessing whether or not a data set follows a given distribution such as normal or lognormal. The CTE data were assessed in terms of their deviations (or residuals) from the overall means of the data for each material at the applicable temperature. Data points were selected at approximately 50°F intervals for each curve, in the temperature range of interest (70°F to 700°F).

The residuals between each individual data point and the applicable overall mean of the data were computed, sorted and plotted as a probability plot in which:

- Vertical axis: Ordered residual values
- Horizontal axis: Order statistic medians for the distribution  
[e.g. Norm Inverse of F; where  $F = (n - 0.3) / (N + 0.4)$ ; N is the total number of data points, and n is the nth data point in the ordered set]
- Analyzed each material individually (A-600: 227 points; SA-508: 82 points)
- Probability plots were developed in this manner for normal and log normal distribution types for each material.

The normal probability plot, generated from the SA-508 dataset of Figure 2-1 (82 data points) is illustrated at the top of Figure 3-1. The correlation coefficient associated with a linear fit to the data is 0.8958, and the mean of the data is very close to zero (0.00044), indicating a good fit to a normal distribution. A lognormal probability plot of the same data is also illustrated at the bottom of Figure 3-1. Review of the two plots indicates that the lognormal distribution gives essentially the same correlation coefficient (0.8964). The normal distribution is recommended because physical data such as CTE are expected to be normally distributed and because the log normal fit introduces the added complexity of having to adjust the original data set to eliminate logarithms of negative numbers (approximately half of the residuals are negative).

The resulting normal distribution for SA-508 is illustrated, along with the residual data, in Figure 3-2. The standard deviation of the residuals is  $0.099 \times 10^{-6}$  in/in/°F, or 1.44% of the mean CTE value for the material at the midpoint temperature (Mean CTE at 400°F =  $7.035 \times 10^{-6}$  in/in/°F).

A similar normal probability plot, generated from the Alloy 600 dataset of Figure 2-2 (227 data points) is illustrated at the top of Figure 3-3. The correlation coefficient associated with the linear fit to the data is 0.9325, and the mean of the data is again close to zero (0.014), indicating a good fit to a normal distribution. A lognormal probability plot of the same data is also illustrated at the bottom of Figure 3-3. In this case the lognormal distribution is a worse fit (correlation coefficient = 0.8909). The normal distribution is again recommended.

The resulting normal distribution for Alloy 600 is illustrated, along with the residual data, in Figure 3-4. The standard deviation of the residuals is  $0.175 \times 10^{-6}$  in/in/°F, or 2.33% of the mean CTE value for the material at the midpoint temperature (Mean CTE at 400°F =  $7.525 \times 10^{-6}$  in/in/°F).

### 3.2 Evaluation of Within-Heat Variability

Examination of the detailed ANTER test data in Figures 2-3 and 2-4 indicates that there was considerable variability in the test results from different samples from the same heats of material, especially at low temperatures (below ~300°F). This "within-heat" variability was not included in the foregoing statistical analyses, because it was judged to be the result of measurement inaccuracy, and not a true material variability, especially at the lower temperatures, in which the amount of physical growth of the samples from 70°F to the indicated temperature challenged the measurement accuracy of the test equipment. Based on this judgment, the data plots in Figures 2-1 and 2-2 and the statistical analyses of Section 3.1 utilized the mean curves of the new ANTER data for each heat of material.

In order to confirm this judgment, a series of additional tests was run, in which a single sample from one heat each of the two materials was tested multiple times to obtain an estimate of testing uncertainty. The results of these "multiple" tests are compared to the prior "multi-sample" results for the same heats in Figures 3-5 and 3-6. It is seen from these figures that the variability in the multiple tests was essentially equivalent to that of the multi-sample tests. Standard

deviations of the data at two temperatures (100°F and 600°F) are indicated in the figures and are comparable for the two cases. Also apparent in the figures is significantly greater variability in the lower temperature regime due to the aforementioned higher measurement uncertainty there. (e.g. Figure 3-7, the standard deviations at 100°F are more than three times those at 600°F).

Based on these additional tests, and the data comparisons presented in Figure 3-7, is concluded that the within-heat variability observed in the multi-specimen test data is solely attributable to testing uncertainty, and that utilizing the heat means in the statistical analyses of Section 3.1 is an appropriate approach.

### 3.3 Effect of Strain Hardening on Alloy-600 CTE

A second set of Alloy 600 specimens were machined from the same nine heats of tubing material, but these were hydraulically expanded into split collars, sized to be typical of the tubesheet bore diameter, before CTE testing, to simulate the strain hardening that occurs in tubesheet ends of steam generator tubes hydraulically expanded into the tubesheet as applied in Westinghouse steam generators. The apparent strain hardening effect on CTE from this initial set of tests is illustrated in Figure 3-7. It is seen from this figure that the variability is about the same in the strain hardened versus non-strain hardened data, but that the means of the strain hardened data tended to be somewhat lower than those in the non-strain hardened results, especially in the higher temperature regime (open data points versus solid points connected by dashed lines in Figure 3-7).

Cold working during hydraulic expansion, however, creates a large increase in dislocation density. Dislocation interactions during deformation create interstitial atoms and vacancies in the atomic lattice. At 600°F, dislocations, interstitials and vacancies tend to rearrange themselves via diffusion. Vacancies and interstitials mostly disappear and dislocations form relatively stable networks. It was thus hypothesized that this effect caused the downward shift in CTE values at temperatures above 350°F in the initial thermal expansion tests of cold worked tubing, and that retesting might yield results more closely resembling the non-strain hardened results, since the specimens will have been heated to >600°F (simulating to the first cycle of

steam generator operation after hydraulic expansion). Under this scenario reheating to 600°F would not lead to further changes in CTE.

To test this hypothesis, the samples from three of the strain hardened heats of Alloy 600 tubing were retested using identical equipment and procedure as the initial strain hardened tests. The results are illustrated in Figure 3-8, which contains three CTE plots for each of the retested Alloy 600 heats. Examination of this figure indicates that the repeat strain hardened test results, in all cases, lie on or very close to the original, non-strain hardened data, thus confirming the above hypothesis. In the cases where there is a small deviation in the test results, the repeat strain hardened tests fell above rather than below the original non-strain hardened results, and were much closer to the non-strain hardened results at the higher temperatures which are of primary interest.

The direction of cold working has no effect on the density of dislocations, interstitials and vacancies that are produced by the cold work. Since the repeat tests demonstrated essentially no effect of cold work on CTE, the results are also independent of cold work direction.

Figure 3-9 is a re-plot of all of the Alloy 600 data, with the non-strain hardened results replaced by the strain hardened results for the three heats that were retested in the strain hardened state. The figure is indistinguishable from Figure 2-2. The statistical analysis discussed in Section 3.1 above was re-performed for Alloy 600 using the data in Figure 3-9 rather than Figure 2-2. The revised statistical distribution, about a new overall mean curve, is virtually identical to that developed based on the non-strain hardened data. (Standard Deviation = 0.176 or 2.34%, Correlation Coefficient of Fit to Normal Distribution = 0.9268).

#### 3.4 Overall Mean versus ASME Code Curves

Review of Figures 2-1 and 2-2 indicates that the ASME Code CTE curves are a reasonable representation of the overall mean curves of the data. For SA 508, the overall mean is consistently about 1% lower than the Code curve for the entire temperature regime, except for at lower temperatures (<300°F), at which it is ~4% lower. Since a higher tubesheet CTE is conservative with respect to steam generator tube to tubesheet interface pressure (results in lower

interface pressure), it is deemed reasonably accurate and conservative to continue to use the ASME Code values.

A similar observation may be drawn for Alloy 600,, based on both the non-strain hardened data (Figure 2-2) and the strain hardened repeat tests (Figure 3-9). The overall means of the data are consistently higher than or equal to the ASME Code curve except for one small region at 650°F. In this region the Code curve exhibits a discontinuity which is believed to be due to truncating the data to two significant figures, which was done in later Code editions, while the overall mean of the data is a smooth curve. Nonetheless, the difference between the Code curve and the overall mean in this region is very small.. Use of a lower tube CTE for the Alloy 600 tubes is conservative with respect to steam generator tube to tubesheet interface pressure (results in lower interface pressure).and thus it is deemed reasonably accurate and conservative to continue to use the ASME Code values.

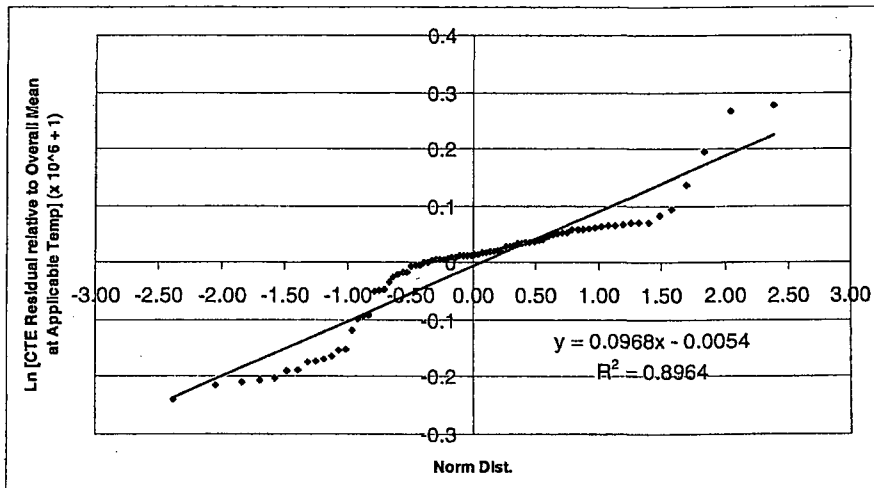
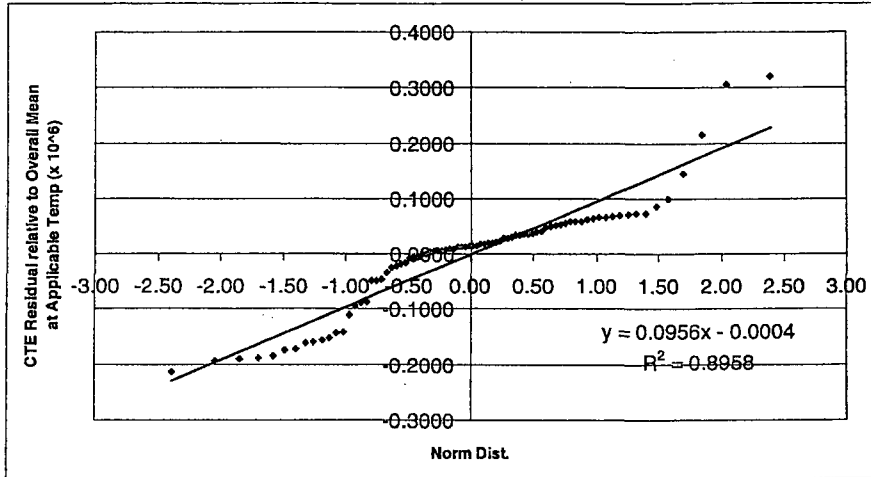


Figure 3-1. Normal and Lognormal Probability Plots for A-508 CTE Residuals and Associated Linear Curve Fits

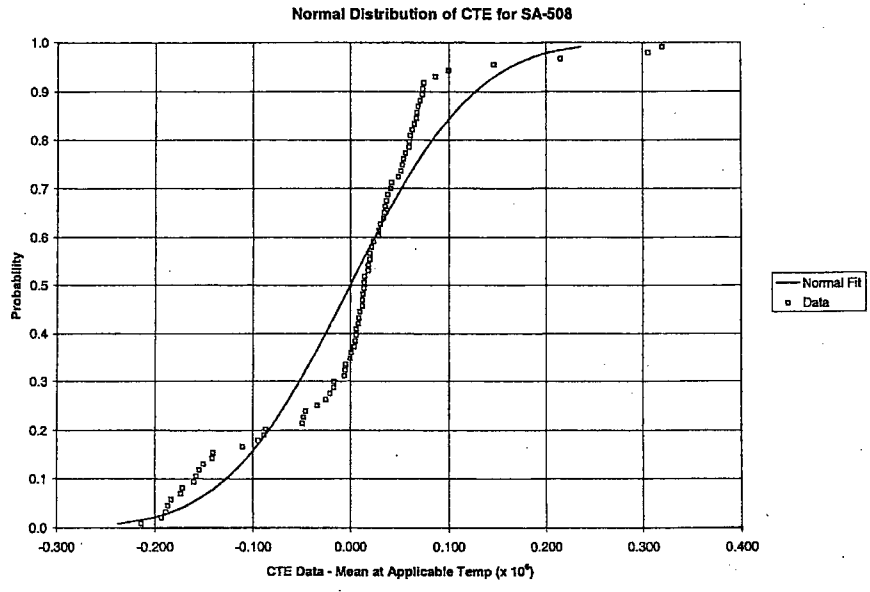


Figure 3-2. Recommended Normal Distribution of CTE Data for SA-508

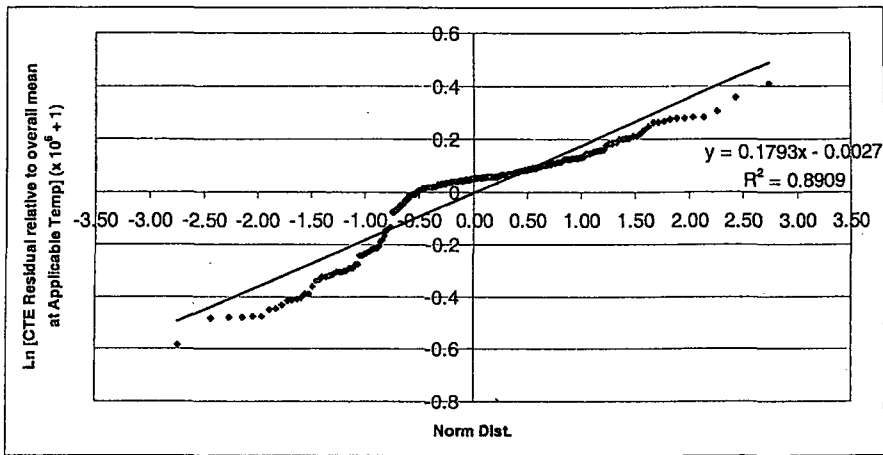
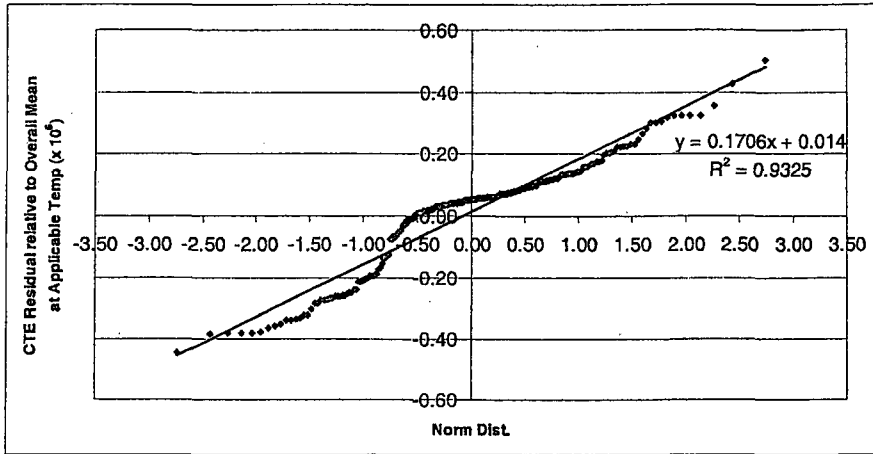


Figure 3-3. Normal and Lognormal Normal Probability Plot for Alloy 600 CTE Residuals and Associated Linear Curve Fit

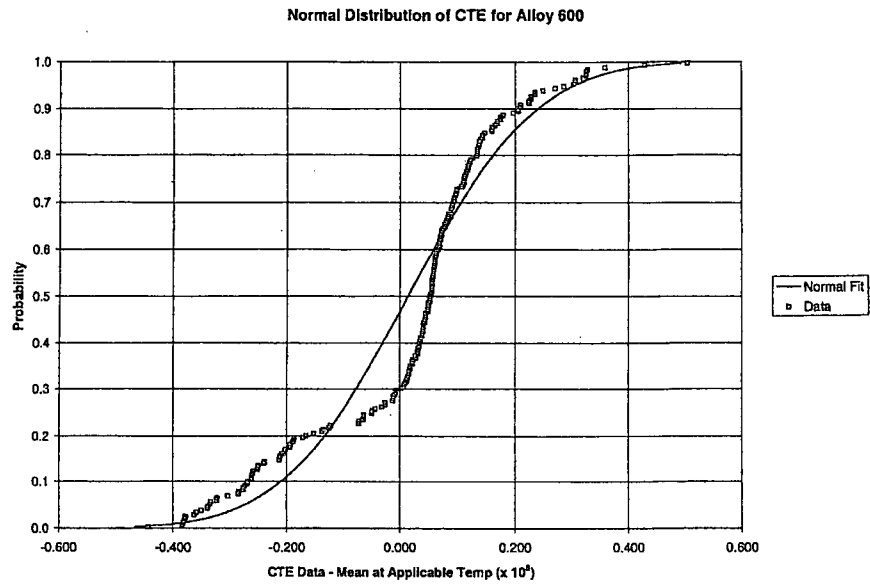


Figure 3-4. Recommended Normal Distribution of CTE Data for Alloy 600

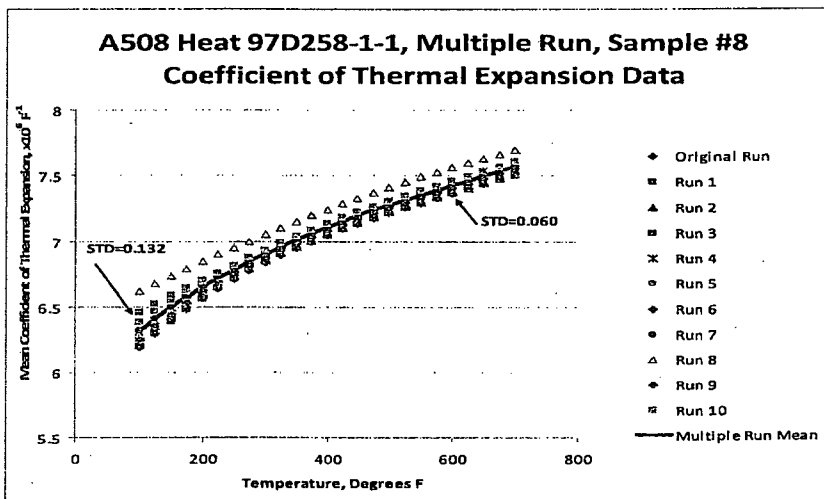
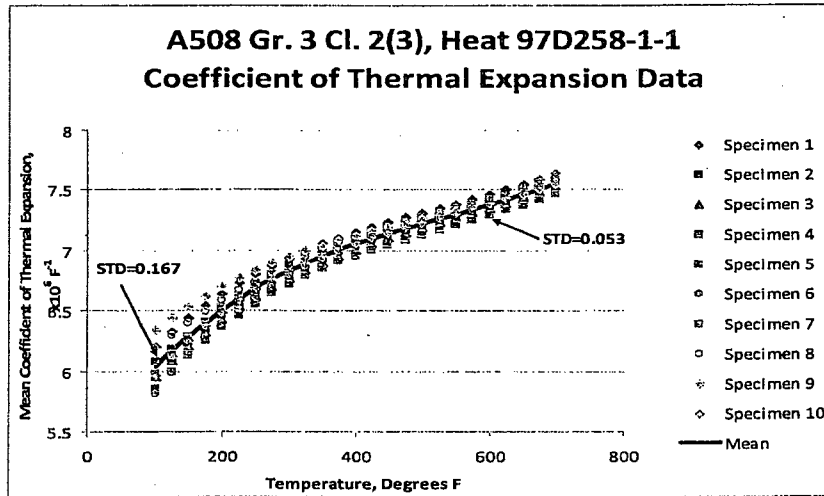


Figure 3-5. Comparison of Within-Heat Scatter of Multi-Sample Tests on a Heat of SA-508 (upper plot) with Multiple Tests of a Single Sample from the Same Heat (lower plot)

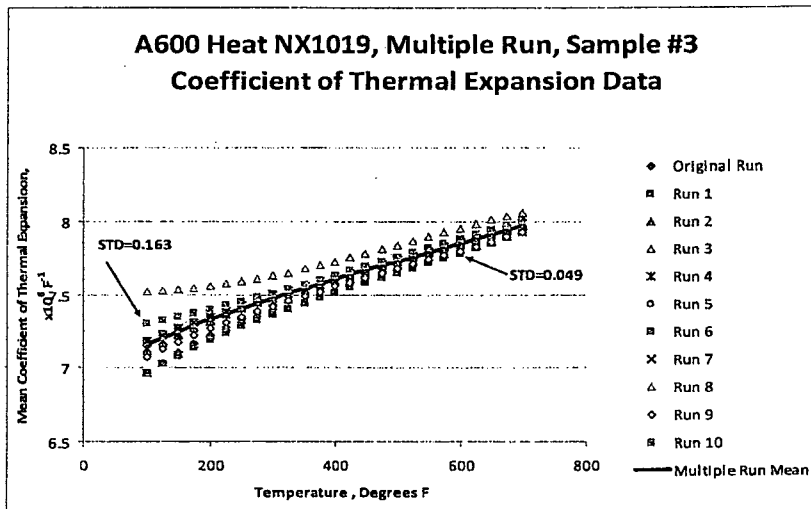
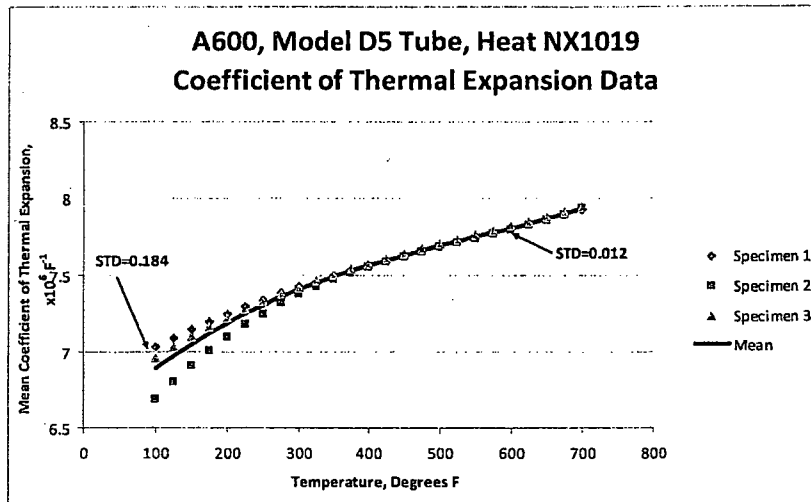


Figure 3-6. Comparison of Within-Heat Scatter of Multi-Sample Tests on a Heat of Alloy 600 (upper plot) with Multiple Tests of a Single Sample from the Same Heat (lower plot)

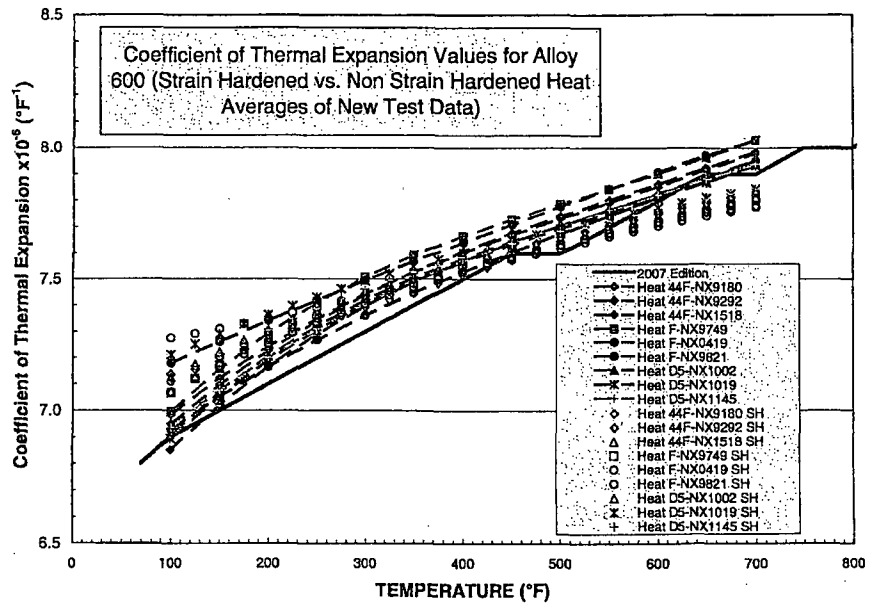


Figure 3-7. Illustration of the Apparent Effect of Strain Hardening on Alloy 600 CTE Data.  
Heat Means of Strain Hardened versus Non Strain Hardened Data – Initial Testing

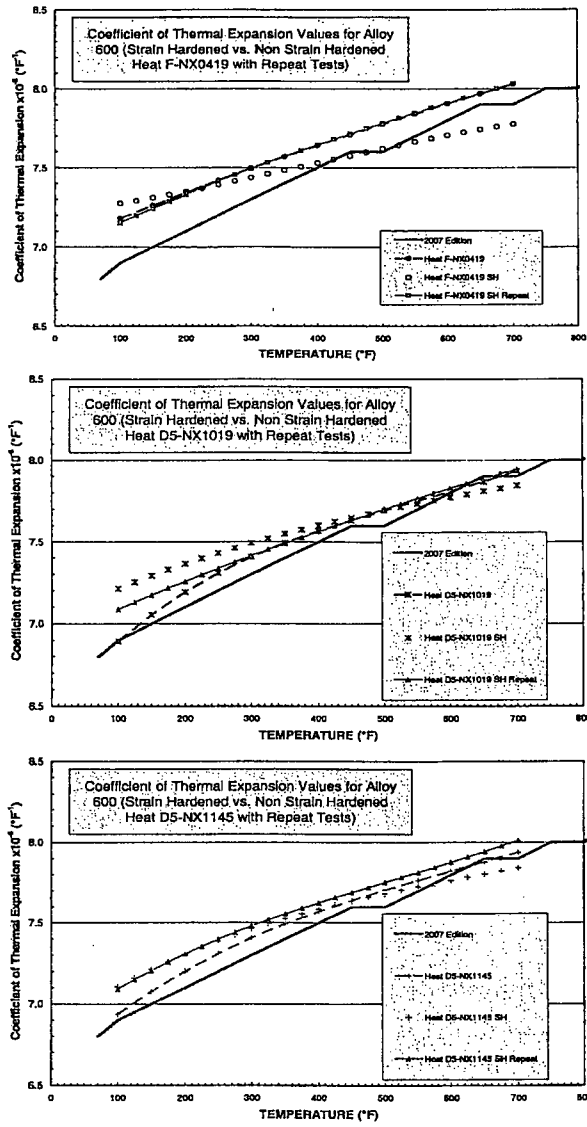


Figure 3-8. Further Study of the Effect of Strain Hardening on Alloy 600 CTE Data: Means of Strain Hardened versus Non Strain Hardened versus Repeat Strain Hardened Tests

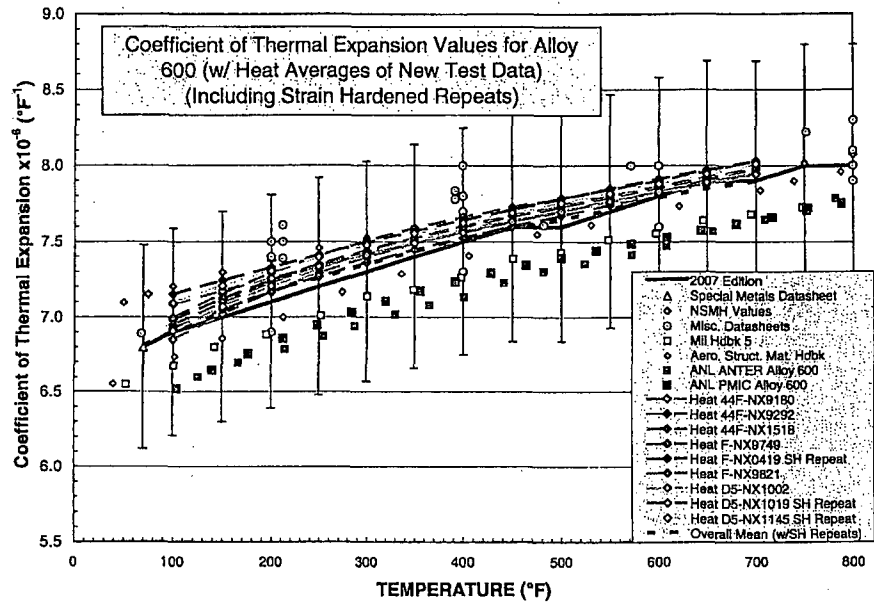


Figure 3-9. Compilation of CTE Data from Various Sources for Alloy 600, with Original Test Data Replaced by Repeat Strain Hardened Test Data (Plot is indistinguishable from Figure 2-2 thus demonstrating that strain hardening has a negligible effect.)

#### 4.0 CONCLUSIONS

The analyses presented in this report result in recommended statistical distributions of CTE for use in Monte Carlo analyses of steam generator tube pullout depths ( $H^*$ ). The recommendation is a normal distribution about the ASME Section II (2007 Edition) curves for SA-508 Grade 2, with a standard deviation of  $0.099 \times 10^{-6}$  in/in/°F, or 1.44% of the Code CTE values. For Alloy 600, the recommendation is a normal distribution with a standard deviation of  $0.175 \times 10^{-6}$  in/in/°F, or 2.33%. In the case of Alloy 600, an evaluation was also performed of the effect of strain hardening due to hydraulic expansion of the tubes into the tubesheet. Strain hardening was found to have a negligible effect on CTE as it was demonstrated that the CTE of the strain hardened specimens returned to its non-strain-hardened value after a single exposure to the typical normal operating temperature, 600°F.

The study also found that, compared to the overall means of the CTE data, it is reasonably accurate and conservative to use the ASME Code CTE curves [1] for these two materials as the mean values about which the above statistical variations occur. The following table summarizes the recommended values of CTE for use in the probabilistic analysis for  $H^*$ :

Material	Mean CTE	Standard Deviation
SA-508	2007 Edition of ASME Code, Section II, at desired temperature	1.44% of mean value at desired temperature
A600	2007 Edition of ASME Code, Section II, at desired temperature	2.33% of mean value at desired temperature

## 5.0 REFERENCES

1. ASME Boiler and Pressure Vessel Code, Section II. Part D, Subpart 2, 2007 Edition
2. "Thermophysical Properties of Ferrous Structural Alloys", R.A. Moen, Hanford Engineering Development Laboratory, HEDL-TME 78-47, EC-79b,h, April, 1978
3. Presentation: "Coefficient of Thermal Expansion and Other Material Property Uncertainties", Chris Hoffman, Westinghouse, Jan. 15, 2008
4. Chambers, John, William Cleveland, Beat Kleiner, and Paul Tukey, (1983), "Graphical Methods for Data Analysis", Wadsworth.
5. Transmittals of ANTER Laboratories Test Data, J.T. Kandra to P.C. Riccardella, 7/18/2008 thru 10/10/2008.
6. Precision Measurements and Instruments Corporation, THERMAL EXPANSION MEASUREMENTS OF AN ALLOY 600 TUBE AND A508 STEEL ROD SPECIMEN, Argonne National Laboratory, 7A-09505, September 18, 2007
7. ANTER Laboratories, Inc, TRANSMITTAL OF TEST RESULTS, Transmittal #: PR27988-52336 to Argonne National Laboratory, April 27, 2007

## APPENDIX A

### RATIONALE FOR EXCLUDING PMIC SA-508 DATA FROM CTE STATISTICAL EVALUATION

One of the data sets originally used in the CTE statistical evaluation was data obtained from ANL based on testing performed at Precision Measurements and Instruments Corporation [A1]. These data were not consistent with the balance of the data collected for SA-508 low alloy steel. To ascertain the source of the inconsistency, an assessment of these data was performed, starting with the raw data tabulated in Reference [A2]. Two sets of CTE data are presented for SA-508 material in [A2], one for a sample tested in a vacuum and a second for a sample tested in air. The raw data from these tests are plotted in Figure A-1, in terms of measured expansion (in micro-strain) versus temperature in °F. Also shown on the plot are data for the same SA-508 material performed for ANL by ANTER Laboratories Inc [A3], as well as a sampling of more recent CTE tests performed by ANTER for Westinghouse [A4-A6].

Figure A-1 indicates that the data sets tested by ANTER, including both the original tests for ANL as well as the more recent tests for Westinghouse, all lie in a fairly tight band. The PMIC air data deviates from that band at the low temperature end, while the PMIC vacuum data shows an even more significant deviation. Figure A-2 presents an expanded view the low temperature range (0 to 200°F) of the data in Figure A-1. It is seen from this figure that the two sets of PMIC data both exhibit offsets (or dead-bands) at the start of the tests, in which essentially no expansion was measured. The offset in the air data is ~15°F while the offset in the vacuum data is greater than 40°F. Since CTE is generally computed relative to an unexpanded room temperature state (70°F), these offsets have a significant impact on the CTE values computed from the data, especially at the low temperature end. Figure A-3 illustrates this effect, in terms of average CTE between room temperature and the indicated temperature computed from the raw data. It is seen from this plot that the PMIC vacuum data deviates over the entire temperature range, due to the large offset at the start of the test. Based on these observations, it is concluded that the PMIC data vacuum could not be used in the statistical analyses of this report without adjusting for the observed offsets in the raw data.

It was determined in discussions with Argonne National Laboratories, the sponsor of the PMIC CTE tests on the SA-508 material, that the sequence of testing was performed first in vacuum (increasing the temperature then decreasing temperature), then in air. In the initial vacuum test, the material was exposed to a temperature of approximately 700°C. Exposure of the material to this temperature changes the microstructure of the material and invalidates subsequent tests on the same specimen. Therefore, the data for the sample in vacuum taken in the temperature decreasing mode and the air environment data are excluded a priori. The PMIC vacuum data from the increasing temperature tests remains suspect in that the raw data exhibits the large offset at the start of the tests, observed in Figures A-1 and A-2. The resulting CTE computed for this sample thus deviates from the remaining available data for SA-508 by a large degree.

Because of this, and because the new testing performed in support of this effort produced sufficient of data for the statistical analysis, it was decided to exclude the PMIC SA-508 data from the study..

**References:**

- A1. Precision Measurements and Instruments Corporation, "Thermal Expansion Measurements of an Alloy 600 Tube and A508 Steel Rod Specimen", Final Report, Argonne National Laboratory Purchase Order Number 7A-09505, September 18, 2007
- A2. 13159 Argonne National Lab CTE Data-LVDT-Final.xls, Transmitted by E-mail, Emmett Murphy to Daniel Mayes, January 9, 2008
- A3. ANTER Laboratories Inc, Transmittal of Test Results, Transmittal # PR27988-52336, Renee Jacobs-Fedore to Saurin Majumdar, April 27, 2007
- A4. ANTER Laboratories Inc, Transmittal of Test Results, Transmittal # PR28355-52514, Renee Jacobs-Fedore to Joseph Kandra, July 15, 2008
- A5. ANTER Laboratories Inc, Transmittal of Test Results, Transmittal # PR28355-52514a, Renee Jacobs-Fedore to Joseph Kandra, July 17, 2008
- A6. ANTER Laboratories Inc, Transmittal of Test Results, Transmittal # PR28355-52514b, Renee Jacobs-Fedore to Joseph Kandra, July 25, 2008

Thermal Expansion of SA508 Steel  
Comparison of Raw Data from Several Sources

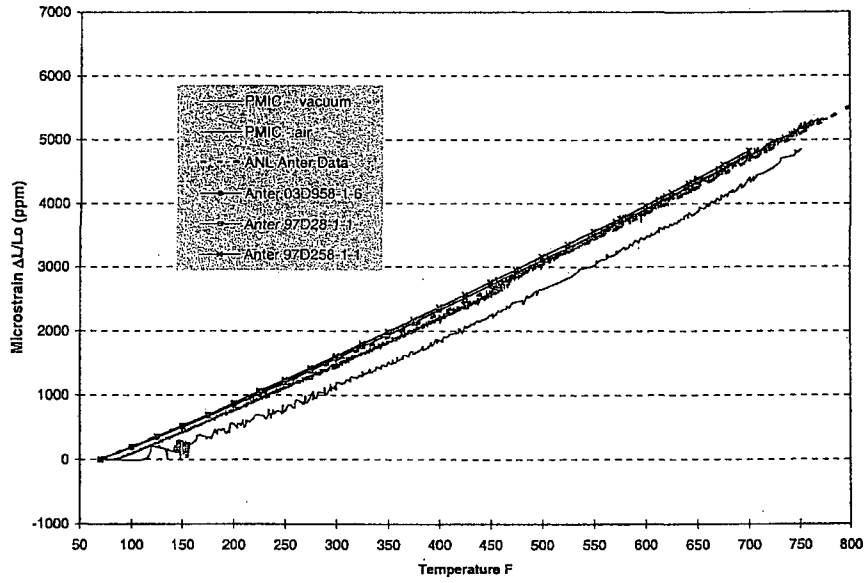


Figure A-1 – Raw Test Data (in Micro-strain) from several SA-508 CTE Tests

Thermal Expansion of SA508 Steel  
Comparison of Raw Data from Several Sources

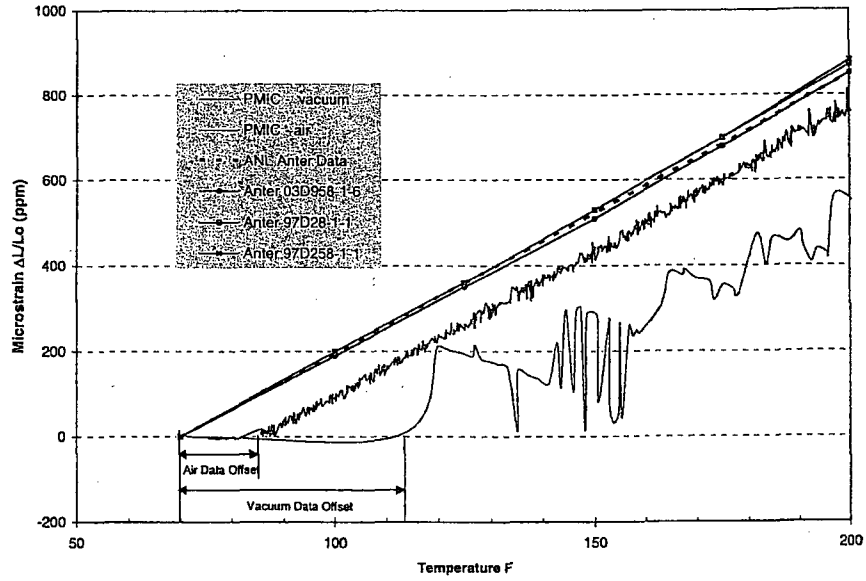


Figure A-2 – Expanded View of Low Temperature End of Figure A-1

Thermal Expansion of SA508 Steel  
CTE Computed from Raw Data

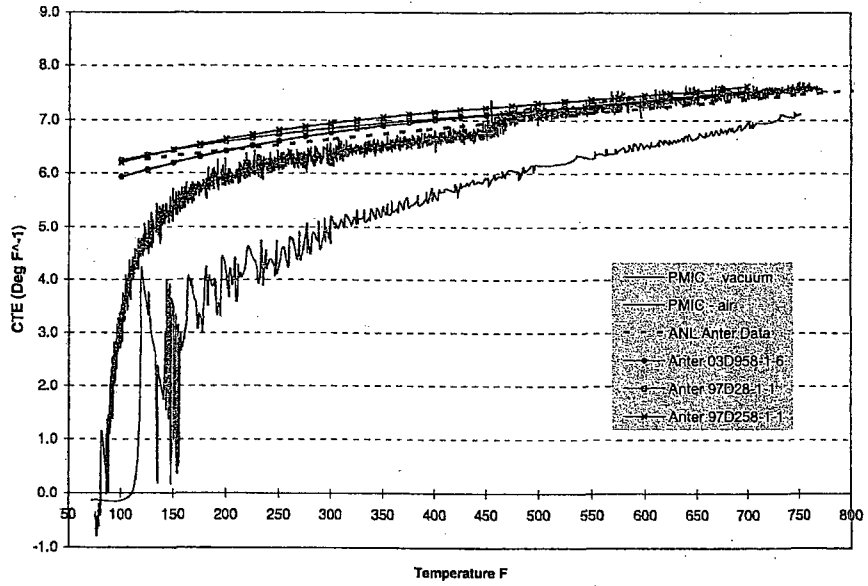


Figure A-3 – CTE Computed from Test Data of Figure A-1

**ENCLOSURE 6**

Copy of the Proprietary WCAP-17091-P, Rev. 0 dated June 2009,  
H\*: Alternate Repair Criteria for the Tubesheet Expansion Region in Steam Generators with  
Hydraulically Expanded Tubes (Model 44F).

(WCAP-17091-P, Rev. 0 is 356 Pages)